

THE UNIVERSITY *of* EDINBURGH

This thesis has been submitted in fulfilment of the requirements for a postgraduate degree (e. g. PhD, MPhil, DClinPsychol) at the University of Edinburgh. Please note the following terms and conditions of use:

- This work is protected by copyright and other intellectual property rights, which are retained by the thesis author, unless otherwise stated.
- A copy can be downloaded for personal non-commercial research or study, without prior permission or charge.
- This thesis cannot be reproduced or quoted extensively from without first obtaining permission in writing from the author.
- The content must not be changed in any way or sold commercially in any format or medium without the formal permission of the author.
- When referring to this work, full bibliographic details including the author, title, awarding institution and date of the thesis must be given.

White micas in subducted crust: their role in the subduction zone nitrogen cycle and as a tracer of fluid processes

Benedict Harris

A thesis submitted to the
University of Edinburgh
for the degree of
Doctor of Philosophy



THE UNIVERSITY
of EDINBURGH

School of Geosciences
University of Edinburgh

January 2024

Declaration

I declare that this thesis has been composed solely by myself and that it has not been submitted, in whole or in part, in any previous application for a degree. Except where stated otherwise by reference or acknowledgement, the work presented is entirely my own.

Benedict Harris, January 2024

Acknowledgements

Firstly I would like to acknowledge the support of my primary supervisors Cees-Jan de Hoog and Ralf Halama. Cees-Jan provided me with continual support and guidance on every aspect of the project, and many excellent constructive criticisms which greatly improved my work. Ralf's great knowledge of nitrogen geochemistry provided me with many important ideas and his willingness to read anything I sent at short notice was always greatly appreciated. Thank you also to my secondary supervisor Simon Harley who always checked up on me whenever we met and provided a very useful sanity check on what I was writing when I was finishing up my thesis. I would also like to acknowledge a few other people who helped with various aspects of the project. Hans-Peter Schertl and Yi-Xiang Chen, who provided me with samples and helped me to develop some of the ideas in the Dora-Maira chapter. Samuel Angiboust, Alberto-Vitale Brovarone, Maureen Feinemann and Ray Burgess who all generously provided me with samples when I was unable to do my own fieldwork during the Covid pandemic. Toby Boocock, who taught me how to run bulk nitrogen analyses and gave me some great ideas to think about as I was developing that chapter, even whilst he was approaching the end of his own PhD. Finally Mike Hall, Ivan Febbrari, Chris Hayward, Nicola Cayzer and the other technical staff of the Grant Institute who keep the facilities running without which I would not have been able to do any of this.

Lastly I would like to thank my partner Sarah who has been a constant source of support and encouragement throughout my PhD, especially during these last few months that I was writing up my thesis.

Abstract

Subduction is the primary mechanism for transferring volatiles from the Earth's surface to the mantle. White micas (muscovite, phengite, paragonite) can be significant mineral hosts for a number of volatiles, including water, nitrogen, boron and halogens, in a range of subducted crustal lithologies. This thesis explores the role of white micas in transporting nitrogen and other fluid-mobile elements in subducted crust, and, more generally, their utility as a recorder of fluid-rock interaction, through the study of formerly subducted and subsequently exhumed metamorphic rocks.

I present the first *in situ* measurements of N concentrations in minerals from subduction-related rocks, using secondary ion mass spectrometry. Mineral N concentrations in a suite of rocks representing formerly subducted oceanic crust confirm that white micas contain the highest N concentrations of any common high pressure mineral. However, when the concentrations and modal abundances of each mineral are accounted for, omphacite, amphiboles and chlorite also host a significant fraction of the N budget in some samples. The role of paragonite as a host for N, and other volatile elements, may be underappreciated compared to phengite, which is the more common white mica phase. Comparison of bulk rock N concentrations with mineral N concentrations reveals that non-mineral hosts for N such as fluid inclusions can also be significant.

By comparing the behaviour of N to other fluid mobile elements in samples that record high pressure fluid-rock interaction, I am able to place constraints on the fluid-mica partition coefficient of N at high pressure. These are the first natural constraints on this parameter and they suggest that the assumption made by some previous studies, that N behaves similarly to Rb, is incorrect, and N is in fact more fluid mobile. The stability of micas during fluid-rock interaction has a major effect on the retention or loss of N, B and other mica-hosted trace elements during subduction. I also present the first inter-mineral partition coefficients amongst white micas, omphacite, Na-Ca amphiboles and chlorite, showing that N partitions strongly into white micas over a range of subduction-related pressure-temperature conditions.

Through several case studies of rocks that record high pressure fluid-rock interaction, I demonstrate that the analysis of *in situ* N concentrations, B concentrations and B isotopes, and other fluid-mobile element concentrations in white micas can be an effective tracer of fluid sources in high

pressure rocks, particularly for sediment-derived fluids. These tracers are then applied to a suite of formerly subducted oceanic crustal rocks and show that fluid-mediated N transfer from sediments into oceanic crust during subduction appears to be a relatively common process, but some samples can also retain N that was acquired during seafloor alteration. Different styles of seafloor alteration may increase or decrease the ability of oceanic crust to retain N during subduction, depending on their effect on the high pressure mineralogy.

Lay summary

Water and nitrogen at the surface of the Earth are two of the essential ingredients that enabled life to begin and evolve on our planet. Over millions of years the abundances of these elements can change as they are exchanged between the surface and rocks deep within the Earth. Subduction zones are areas where rocks from the surface sink into part of the deep Earth called the mantle. These subducting rocks carry water and nitrogen within their constituent minerals. Over time subduction zones transfer water and nitrogen from the surface into the deep Earth. As the subducting rocks sink these minerals transform into different minerals due to the increase in pressure and temperature. During these reactions water is released, which causes melting in the surrounding mantle. These melts migrate upwards towards the surface and erupt at volcanoes in places such as Japan and Indonesia. Nitrogen can also be released alongside water and returned to the atmosphere via these volcanoes. The extent to which water and nitrogen that enters the subduction zone is returned to the surface via volcanoes, or stored in the deep mantle, is one of the key factors that has determined how the abundance of water and nitrogen at the surface has changed over the Earth's history, and yet it is poorly understood.

In some rare places, rocks that were subducted into the deep Earth have returned to the surface and can be collected and studied. This thesis investigates such rocks to find out how nitrogen and other elements behave during the mineral reactions that occur during subduction. I do this by analysing and comparing the chemistry and ratios of different isotopes within the minerals that formed at different stages of these reactions. This enables us to predict how much nitrogen is lost during mineral reactions and returned to the surface, compared to how much is retained in the new minerals and stored in the mantle.

Contents

1 Chapter 1: Introduction **14**

1.1 Dehydration of the subducting slab 15

1.2 The role of white mica 17

1.2.1 White mica stability 18

1.3 The geological nitrogen cycle and behaviour of nitrogen 20

1.3.1 The role of subduction zones 23

1.3.2 Nitrogen studies in subducted crust 24

1.3.3 Methods for analysing nitrogen 26

1.4 Boron as a tracer of fluid processes 27

1.4.1 The subduction zone boron cycle 27

1.4.2 Boron studies in subducted crust 28

1.5 Thesis aims and chapter outline 30

1.6 Thesis style 32

2 Chapter 2: Methods **33**

2.1 Bulk rock major and trace element concentrations 33

2.2 Bulk rock nitrogen concentrations and nitrogen isotopes 33

2.3 Mineral major element concentrations 34

2.4 Mineral nitrogen, volatile and trace element contents 35

2.5 Mineral boron isotopes 41

2.6 Mineral modal abundances 44

3 Chapter 3: The behaviour of nitrogen during high pressure fluid-rock interaction 46

3.1 Preface 46

3.2 Abstract 46

3.3 Introduction 47

3.4 Geological background and sample descriptions 50

3.4.1 Lago di Cignana, Italy . . . 50
3.4.2 Raspas Complex, Ecuador . . . 50
3.4.3 Jenner, California . . . 52
3.5 Analytical methods . . . 54
3.6 Results . . . 54
3.6.1 Major element mineral chemistry and N, B, Li concentrations in white mica . . . 54
3.6.2 N, B, Li concentrations in other minerals . . . 56
3.6.3 Bulk nitrogen contents . . . 57
3.7 Discussion . . . 57
3.7.1 Residency of nitrogen and implications for global nitrogen recycling . . . 57
3.7.2 Fluid rock interaction: a simple system . . . 62
3.7.3 Fluid-rock interaction: growth of new phases . . . 66
3.7.4 Fluid-rock interaction in other samples . . . 70
3.8 Conclusions . . . 72
3.9 Post-script . . . 73

4 Chapter 4: Tracing fluid sources during polymetasomatism 74

4.1 Preface . . . 74
4.2 Abstract . . . 75
4.3 Introduction . . . 75
4.3.1 Geological background . . . 77
4.4 Analytical techniques . . . 82
4.5 Sample descriptions and major element compositions . . . 82
4.6 Mineral trace element and isotope compositions . . . 87
4.6.1 Trace elements and H_2O . . . 87
4.6.2 Boron isotopes . . . 88
4.7 Discussion . . . 91
4.7.1 Element mobility during whiteschist prograde metamorphism: implications for fluid sources . . . 91

4.7.2 Effects of retrograde fluid addition . . . 96
4.7.3 Boron isotope constraints on metasomatic fluid compositions . . . 97
4.7.4 Comparison with previous evidence for fluid compositions . . . 100
4.7.5 The differing records of tourmaline and phengite boron isotopes . . . 102
4.8 Wider implications . . . 104
4.9 Conclusions . . . 105
4.10 Post-script . . . 106

5 Chapter 5: Partitioning, distribution and sources of nitrogen in subducted oceanic crust 107

5.1 Preface . . . 107
5.2 Introduction . . . 107
5.3 Samples . . . 111
5.4 Analytical methods . . . 111
5.5 Results . . . 113
5.5.1 Bulk rock major and trace elements . . . 113
5.5.2 Mineral major and trace elements . . . 115
5.5.3 Mineral boron isotopes . . . 118
5.5.4 Mineral modes . . . 118
5.6 Discussion . . . 121
5.6.1 Effects of seafloor and subduction-related alteration . . . 121
5.6.2 Nitrogen partitioning between HP minerals . . . 127
5.6.3 Mineral contributions to reconstructed bulk nitrogen concentrations . . . 134
5.6.4 Comparison of measured and reconstructed bulk nitrogen . . . 136
5.6.5 Boron isotope constraints on the origin of nitrogen enrichment . . . 147
5.7 Implications for nitrogen recycling . . . 151
5.8 Conclusions . . . 153
5.9 Post-script . . . 155

6 Chapter 6: Conclusions and further work 156

6.1 Recommendations for further work 159

A Appendix A: Data **162**

A.1 Data for Chapter 3 162

A.2 Data for Chapter 4 173

A.3 Data for Chapter 5 183

B Appendix B: Additional methods **194**

B.1 Ellenbergerite mode calculation - Chapter 4 194

B.2 Grain boundary trace element calculation - Chapter 5 195

List of Figures

1 Subduction zone volatile cycle schematic - Chapter 1 15

2 Altered oceanic crust pseudosection - Chapter 1 19

3 SIMS calibration of N contents - Chapter 2 38

4 SIMS calibration of N contents - Chapter 2 39

5 SIMS N backgrounds - Chapter 2 40

6 SIMS B isotope calibration 43

7 Sample photomicrographs and BSE images - Chapter 3 53

8 Major and trace element data - Chapter 3 56

9 Boron and N data - Chapter 3 57

10 Bulk K_2O and N contents - Chapter 3 61

11 N-K-Na data for chlorite - Chapter 3 62

12 N-B-Li modeling for samples LC-3 - Chapter 3 65

13 Equilibrium phase diagrams for sample SEC16-1 - Chapter 3 69

14 Geological map of the Dora-Maira Massif - Chapter 4 79

15 Dora-Maira P-T path - Chapter 4 81

16 Thin section photomicrographs - Chapter 4 83

17 Mica major element chemistry - Chapter 4 85

18 SIMS trace element data - Chapter 4 89

19 SIMS B isotope data - Chapter 4 90

20 Whiteschist metamorphic history schematic - Chapter 4 93

21 Boron isotope disequilibrium plot - Chapter 4 103

22 Sample SEM images - Chapter 5 112

23 Immobile element plots - Chapter 5 114

24 Bulk N–δ^{15}N data - Chapter 5 116

25 Bulk K-N data - Chapter 5 117

26 Mineral N data - Chapter 5 119

27 Mineral B isotope data - Chapter 5 121

28 Major element metasomatism plots - Chapter 5 122
29 Bulk K–Na–N–Rb and mica mineralogy plot - Chapter 5 124
30 P-T conditions and mica mineralogy plot - Chapter 5 125
31 Trace element metasomatism plots - Chapter 5 126
32 N-B-Li cross correlation plots - Chapter 5 128
33 N-B-Li partitioning plots (all samples) - Chapter 5 129
33 Figure 33 continued 130
34 N-B-Li partitioning plots (selected samples) - Chapter 5 131
34 Figure 34 continued 132
35 Partition coefficient P-T correlations - Chapter 5 134
36 Mineral modes and N distribution - Chapter 5 136
37 Reconstructed and measured bulk K, Rb, N concentrations - Chapter 5 137
38 Bulk N discrepancy versus mineral modes - Chapter 5 140
39 Mineral N-Cl correlations - Chapter 5 144
40 Boron and N isotope covariation - Chapter 5 148
41 Boron isotope covariation with other geochemical indicators - Chapter 5 150
42 Grain boundary porosity model - Appendix B 196

List of Tables

1 N and B composition of key geochemical reservoirs - Chapter 1 22

2 Commonly used abbreviations - Chapter 1 32

3 Mineral modes and N concentrations, and calculated bulk N concentrations - Chapter 3 58

4 Inter-mineral partition coefficients for Li, B and N - Chapter 3 59

5 Experimental N partitioning data - Chapter 3 67

6 Sample location and mineralogy - Chapter 4 82

7 SIMS trace element data - Chapter 4 86

8 Trace element redistribution calculations - Chapter 4 95

9 Sample information - Chapter 5 113

10 Whole rock major element and N data - Chapter 5 114

11 Mineral N data - Chapter 5 120

12 Mineral modal abundances - Chapter 5 120

13 N-B-Li partition coefficients - Chapter 5 135

14 Literature bulk and mineral N comparison - Chapter 5 146

15 EPMA major element data for Chapter 3 - Appendix A 163

16 EPMA major element data for Chapter 3 - Appendix A 164

17 EPMA major element data for Chapter 3 - Appendix A 165

18 SIMS trace element data for Chapter 3 - Appendix A 166

19 SIMS trace element data for Chapter 3 - Appendix A 167

20 SIMS trace element standards for Chapter 3 - Appendix A 168

21 SIMS trace element standards for Chapter 3 - Appendix A 169

22 SIMS trace element standards for Chapter 3 - Appendix A 170

23 SIMS trace element standards for Chapter 3 - Appendix A 171

24 Mineral modal abundances for Chapter 3 - Appendix A 172

25 EMPA major element data for Chapter 4 - Appendix A 174

26 EMPA major element data for Chapter 4 - Appendix A 175

27 SIMS trace element data for Chapter 4, session 1 - Appendix A 176

28 SIMS trace element data for Chapter 4, session 2 - Appendix A 177
29 SIMS trace element data for Chapter 4, session 3 - Appendix A 178
30 SIMS B isotope data for Chapter 4, session 1 - Appendix A 179
31 SIMS B isotope data for Chapter 4, session 2 - Appendix A 180
32 SIMS B isotope data for Chapter 4, session 2 - Appendix A 181
33 SIMS B isotope standards for Chapter 4 - Appendix A 182
34 XRF trace element data for Chapter 5 - Appendix A 184
35 EDS major element data for Chapter 5 - Appendix A 185
36 EDS major element data for Chapter 5 - Appendix A 186
37 EDS major element data for Chapter 5 - Appendix A 187
38 SIMS trace element data for Chapter 5 - Appendix A 188
39 SIMS trace element data for Chapter 5 - Appendix A 189
40 SIMS trace element data for Chapter 5 - Appendix A 190
41 SIMS trace element standards for Chapter 5 - Appendix A 191
42 SIMS B isotope data for Chapter 5 - Appendix A 192
43 SIMS B isotope standards for Chapter 5 - Appendix A 193

1 Chapter 1: Introduction

The presence of volatiles such as water, carbon and nitrogen at the Earth's surface was essential to the emergence and survival of life. Subduction zones are the primary location where water and other volatile elements (e.g. C, N, halogens) are transferred from the Earth's surface to the mantle. Understanding the behaviour of volatile elements during subduction is therefore a critical part of constraining the evolution of volatiles at the Earth's surface over geological history, and therefore of understanding the conditions under which life evolved.

Subduction zones occur where oceanic lithosphere sinks beneath the overriding plate, which can be either oceanic or continental. Three main lithologies make up the oceanic lithosphere: sediments, mafic oceanic crust, and depleted lithospheric mantle. Fresh crust and depleted mantle formed at mid-ocean ridges have low concentrations of all volatiles. Hydrothermal alteration of crust and mantle by comparatively volatile-rich seawater-derived fluids forms two new lithologies: altered oceanic crust (AOC) and serpentinites; which are enriched in volatiles compared to fresh lithosphere. Sediments deposited on top of the crust often contain high concentrations of volatiles acquired from seawater or organic material. This package of sediments, AOC and serpentinized mantle, along with its volatile inventory, is what enters the subduction zone in the downgoing slab (Bekaert et al., 2021; Halama and Bebout, 2021).

When the altered oceanic lithosphere is subducted it undergoes a series of dehydration reactions, where hydrous minerals break down, releasing aqueous fluids into the rock. Many volatile elements are also fluid mobile elements (FME), meaning that they exist in significant concentrations in the fluid phase in equilibrium with the rock. If there is sufficient permeability in the rock then these fluids can be expelled from the slab, taking other volatile and fluid-mobile elements with them. The transfer of aqueous fluids from the subducting slab into the mantle wedge is inferred to be the main driver of the melting that generates arc magmas (e.g. Wyllie, 1988) and there is abundant evidence in the composition of these magmas for the transfer of other volatile components from the slab to the mantle wedge (e.g. Fischer et al., 1998; Plank and Langmuir, 1993; Ryan and Langmuir, 1993; Sasaki and Ishihara, 1979; Staudacher and Allègre, 1988; Varekamp et al., 1992; Zellmer et al., 2015). Some amount of volatiles can be retained in minerals within the slab and returned to the convecting

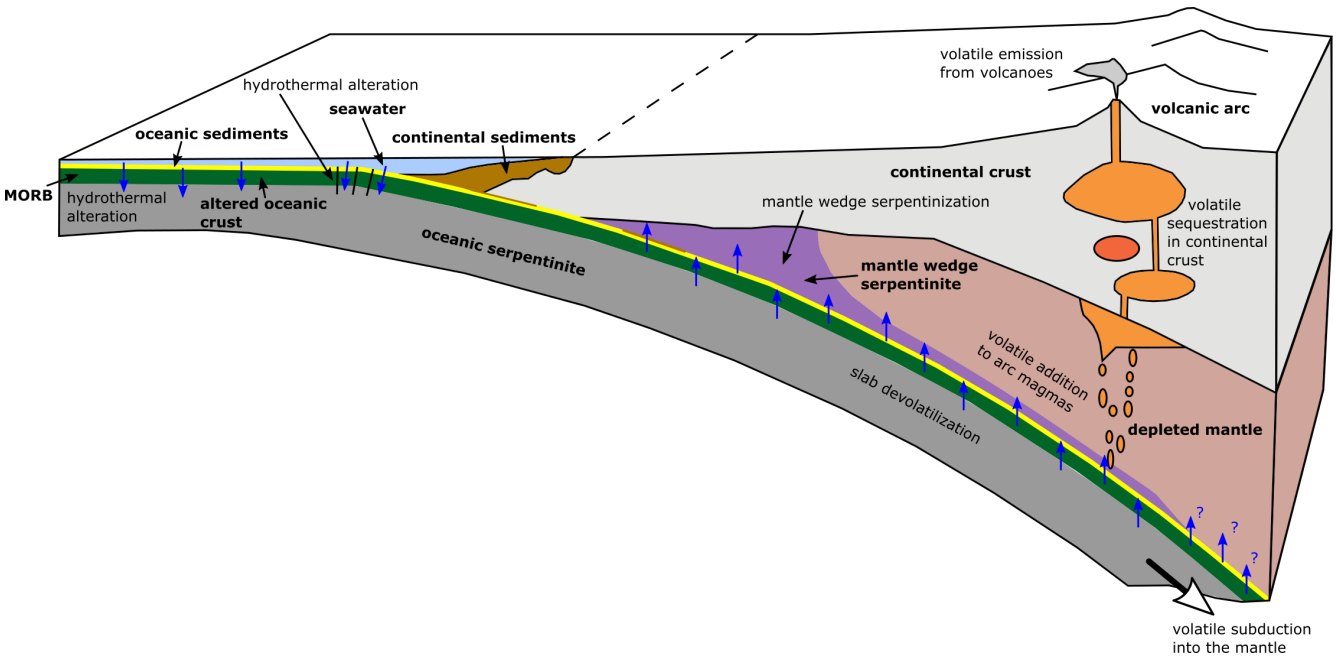


Figure 1: Schematic diagram showing the major volatile reservoirs and volatile mobilization processes involved in subduction. Modified after De Hoog and Savov, 2018.

mantle. There is evidence for these subducted crustal volatiles in the mantle from the compositions of some ocean island basalts (OIB, e.g Hanyu et al., 1999; Mohapatra and Murty, 2000; Perfit et al., 1980) and mantle diamonds (e.g. Cartigny et al., 1998). The main processes relating to subduction zone volatile recycling are illustrated in Figure 1.

The concentrations of many volatiles typically decrease from sediments to AOC to serpentinites, but since the volumetric proportions of these lithologies increases in the same order, all three can make a significant contribution to the budget of volatiles entering the subduction zone. This thesis primarily focuses on AOC.

1.1 Dehydration of the subducting slab

The thermal structure of subduction zones has a significant effect on whether volatiles are released from the subducting slab into the mantle wedge, or are retained and subducted into the mantle. Alongside the bulk composition of the subducting rocks, pressure-temperature (P-T) conditions are the main control on the mineralogy of the subducting slab. This in turn controls which metamorphic reactions take place and how much, and at what depth, fluids are released. Additionally, different minerals have different capacities to host volatiles within their crystal structure, which means that

the fluid-rock partitioning behaviour changes with the rock mineralogy.

Average geothermal gradients in subduction zones range from ~5–15 °C km^{-1}, although recent modelling shows that there is significant variation in the local geothermal gradient within a single subduction zone, both with depth from the Earth's surface, and depth within the slab (i.e. the distance from the slab-mantle wedge interface) (e.g. Gerya et al., 2002; Peacock, 2020; Syracuse et al., 2010; van Keken et al., 2018). Most modern subduction zones are thought to fall at the lower end of this range of geothermal gradients, but there are also examples of warm, modern subduction zones and warm subduction was likely more common in the Proterozoic, and possibly Archean, due to the higher global radiogenic heat production. An interesting point which is worth noting, but is beyond the scope of this thesis to address, is that there is a discrepancy between the average subduction geotherms predicted by most models and the P-T conditions recorded in exhumed subduction-related rocks (Penniston-Dorland et al., 2015; van Keken et al., 2018). Average conditions in rocks are 100–300 °C warmer than average conditions predicted by models at pressures < 2 GPa, whereas above 2 GPa, models and rocks agree fairly well. There is outstanding debate as to whether this reflects a deficiency of the models, or bias of the exhumed rock record towards warm subduction conditions, but it emphasises the need for studies of volatile behaviour in formerly subducted rocks, which can be compared with the behaviour predicted by models.

Numerous studies have modelled the mineralogical evolution of subducted oceanic crust, with many focusing on the depth and amount of water loss. They predict the mineralogical evolution of the crust along a subduction zone P-T path, either based on thermodynamic modelling or experimental phase equilibria. Based on the water content of each mineral, they then predict the amount of fluid remaining in the rock at any depth, assuming that any free fluid phase is immediately lost from the rock. Some models also then use trace element and/or isotope mineral/fluid partitioning data to predict how volatiles are extracted by these fluids (e.g. Konrad-Schmolke and Halama, 2014).

Chlorite, amphibole, lawsonite or epidote, and white mica are the main hydrous minerals in subducted oceanic crust (Hacker, 2008; Hernández-Uribe and Palin, 2019; Hernández-Uribe et al., 2020; Poli and Schmidt, 2002; Schmidt and Poli, 1998). Chloritoid and talc may also be important in some bulk compositions, primarily those that are enriched in Mg. Chlorite breaks down at shallow depths (< 50 km). Epidote is only stable along warmer geotherms and therefore also breaks down at

relatively shallow depths, since the temperature of epidote dehydration is reached at a shallow depth along such a geotherm. Amphibole persists to greater depths but is completely broken down by ~80 km even along cold geotherms. White mica is typically the only hydrous phase that is predicted to be stable at sub-arc depths (100 km), except along cold subduction geotherms, where moderate amounts of lawsonite and talc may persist to this depth. White mica therefore plays a key role in the transport of water to sub-arc depths and beyond.

1.2 The role of white mica

As well as being the main hydrous phase that is stable at sub-arc depths in the oceanic crust, white mica is an important host for a number of other volatiles and FME, including N, B, Rb, Cs, Ba, Be, F and Cl (e.g. Beaudoin et al., 2022; Busigny et al., 2003a; Domanik et al., 1993; Halama et al., 2017; Pagé et al., 2016; Sievers et al., 2017a; Sorensen et al., 1997). Since a number of these elements (notably B, Rb, Cs, Ba, N) are highly concentrated in mica relative to other phases, the amount of white mica present in the rock will have a substantial effect on the retention of these elements within the slab (Li et al., 2022; Marschall et al., 2007). For example, Marschall et al., 2007 suggested that subducted K-free MORB would lose 98% of its B by the time it reaches sub-arc depths and the B isotope composition would shift by ~35 ‰, whereas MORB with 5% white mica would lose only 65% of its B and the B isotope composition would shift by only ~10 ‰. Whilst the thermodynamic models used in this paper are now slightly outdated, and various assumptions could change the results somewhat, it illustrates the major effect that even small amounts of white mica can have on the behaviour of elements that are highly concentrated within it.

Nitrogen is an element for which white mica has been recognised to be a significant host in subducted rocks (Bebout et al., 2013; Bebout and Fogel, 1992; Busigny et al., 2003a; Halama et al., 2010, 2017; Li et al., 2014), but there is a lack of data on the behaviour of N in HP rocks, which prevents the development of models of N devolatilization. Nitrogen is a key element for the existence of life, and the behaviour of Earth's climate over geological history (Goldblatt et al., 2009), and subduction zone N cycling forms a key part of the geological N cycle which has regulated the amount of N in the atmosphere over time (see Section 1.3). A major part of this thesis is devoted to the investigation of N behaviour in white micas and coexisting minerals in subducted AOC. Boron is

a fluid mobile element which is concentrated in white micas, and is a useful tracer of subduction-related fluid processes (e.g. Konrad-Schmolke and Halama, 2014; Peacock and Hervig, 1999; Ryan and Langmuir, 1993). Both elements have stable isotope systems that exhibit significant fractionation between minerals and fluids and can be used as tracers of subduction zone fluids. The remainder of the introduction reviews the stability of white micas in metabasic rocks and the subduction zone geochemistry of N and B, before setting out the main research questions for the thesis.

1.2.1 White mica stability

White micas are stable over a wide range of P-T conditions and bulk compositions in HP subduction-related rocks. Their major element compositions can primarily be expressed with three end members: muscovite ($K_2Al_6Si_6O_{20}(OH)_4$), paragonite ($Na_2Al_6Si_6O_{20}(OH)_4$) and celadonite ($K_2(Mg, Fe^{2+})_2Al_2Si_8O_{20}(OH)_4$). Muscovite and celadonite form a continuous solid solution, defined by the substitution $2\,Al^{3+} \longleftrightarrow Si^{4+} + (Mg, Fe)^{2+}$, and micas with these compositions are called phengites (Rieder et al., 1998), a term which is used extensively in this thesis. The muscovite-celadonite substitution is used as a barometer, with Si and Mg + Fe^{2+} contents in phengites increasing with pressure (Coggon and Holland, 2002; Massonne and Schreyer, 1987; Ravna and Terry, 2004). Muscovite and paragonite are immiscible at low temperature, forming a solvus. This solvus widens with increasing pressure and increasing celadonite content, meaning that phengite and paragonite appear as separate phases at subduction zone P-T conditions (Guidotti and Sassi, 1976). Minor amounts of the Ca-mica margarite, and of trioctahedral micas (biotites *sensu lato*) can also be incorporated into white mica solid solutions.

An equilibrium phase diagram calculated for the average altered oceanic crust composition of Kelley et al., 2003 is shown in Figure 2. Phengite is stable everywhere up to 4 GPa except at high temperatures and low pressures (>400–500 °C, < 1.5 GPa, i.e. upper greenschist and amphibolite facies), where it is replaced by biotite. Under all but the warmest modelled subduction zone geotherms (van Keken et al., 2018), phengite will occur at all points along the P-T path. This fits with observations of subducted metabasic rocks, where biotite is common in amphibolites and some greenschists, but very rare in other metamorphic facies. The high pressure stability limit of phengite has been investigated experimentally. Pure phengite melts at 1075–1150 °C at 7 GPa (Domanik and Holloway,

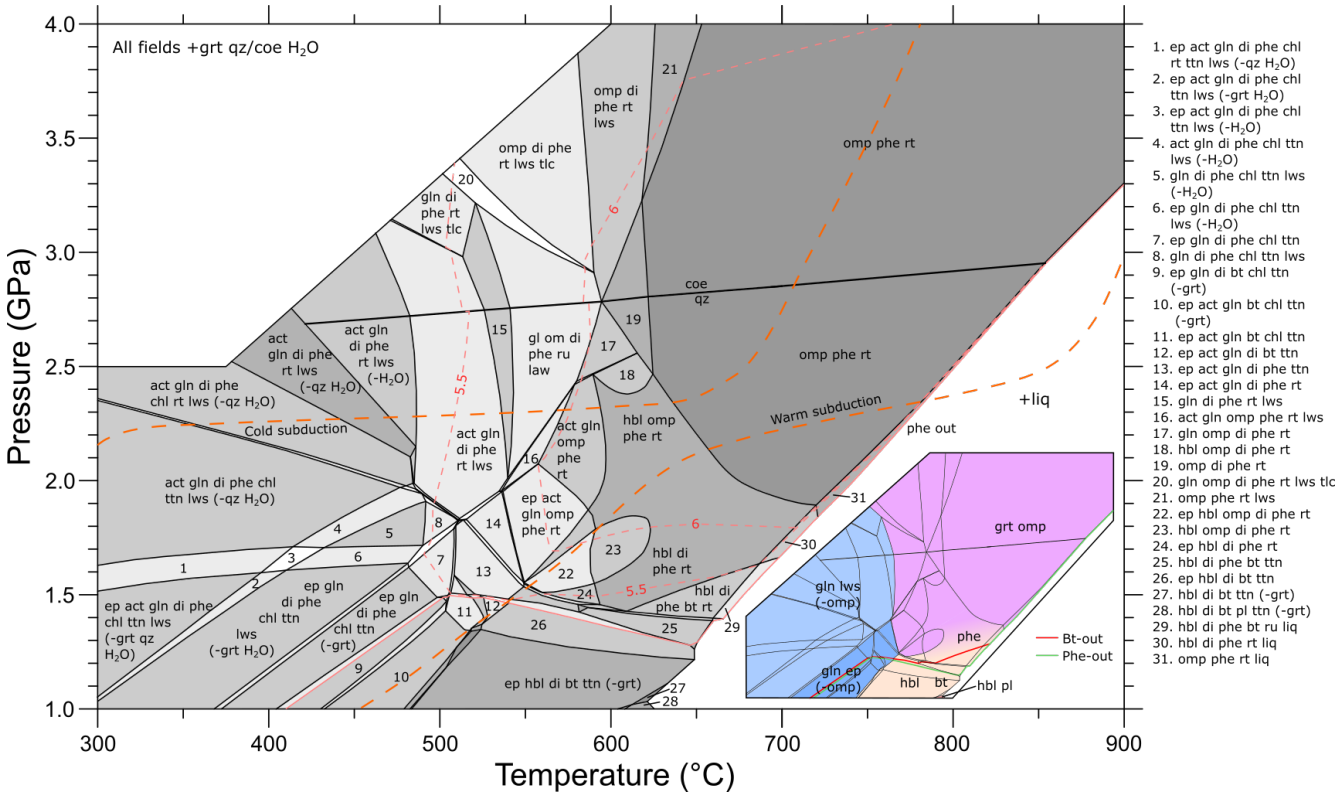


Figure 2: Equilibrium phase diagram for AOC calculated in the system Na_2O-CaO-K_2O-FeO-MgO-Al_2O_3-SiO_2-H_2O-TiO_2-Fe_2O_3 using THERMOCALC (Powell and Holland, 1988) and the ds62 thermodynamic database (Green et al., 2016; Holland and Powell, 2011). The bulk composition corresponds to the average altered oceanic crust of Kelley et al., 2003, with H_2O from loss on ignition (6.31 wt%) and $X_{Fe^{3+}} = 0.15$ (Cottrell and Kelley, 2011). The effect of fluid-melt miscibility at high pressures is not modelled. Red dashed lines show modal abundance (volume %) of phengite. Orange dashed lines show representative geotherms for the top of the slab for cold (central Japan) and warm (Cascadia) subduction zones (van Keken et al., 2018). The colour inset shows the fields of eclogite (grt + omp-bearing), blueschist (gln + lws/ep-bearing, omp-free) and amphibolite (hbl-bearing) assemblages, and the limits of phengite and biotite stability.

1996). However, for geologically relevant bulk compositions, the wet solidus terminates at a second critical end point (Poli and Schmidt, 2002; Schmidt et al., 2004), beyond which there is complete miscibility between aqueous fluids and melts, and phengite is able to dissolve into this supercritical fluid (Connolly and Galvez, 2018; Schmidt et al., 2004). In MORB-type compositions this occurs at $>$ 5–6 GPa (Kessel et al., 2005; Schmidt et al., 2004). The dissolution of phengite at such depths may result in its eventual disappearance from the crust, although this would be dependent on the availability of sufficient fluids.

In the absence of biotite or melt, phengite is the only K-bearing phase in these models and so phengite modal abundance is largely controlled by bulk rock K_2O. Small variations of volume%

mode with P-T are due to variations in phengite K_2O content. This is largely expected to be true in natural samples as well, although small amounts of K can be incorporated into other minerals such as amphibole (Schmidt, 1996), such that rocks with very low bulk K_2O may be mica-free in reality, whereas models predict small mica modes. AOC can contain up to ~8.0 wt% K_2O (and up to 7.0 wt% H_2O) as a result of hydrothermal alteration, although most samples fall in the range 0.1–2.0 wt% (Bach et al., 2003; Belgrano and Diamond, 2019; Coogan et al., 2017; Heft et al., 2008; Kelley et al., 2003; Staudigel et al., 1996). Compared to subduction of fresh MORB (0.16 ± 0.01 wt% K_2O, Gale et al., 2013), subducted AOC will therefore contain significantly more phengite.

In contrast to phengite, paragonite is not predicted to be stable in the average AOC composition modelled in Figure 2, or in subducted fresh MORB (Hernández-Uribe and Palin, 2019). Pure paragonite is stable only at pressures lower than 2.2–2.5 GPa, above which it dehydrates to form jadeite + kyanite + H_2O (Massonne and Sobiech, 2007). Hydrothermal enrichment of Mg in AOC may stabilise paragonite (Hernández-Uribe et al., 2020). Addition of small amounts of carbonate, which is also common during hydrothermal alteration, also appears to increase the stability of paragonite (Collins et al., 2015; Kerrick and Connolly, 2001; Li et al., 2012; Molina and Poli, 2000). There are a number of reports of paragonite-bearing blueschists and eclogites (Massonne and Sobiech, 2007 and references therein) but to my knowledge no study has systematically investigated the effects of bulk composition or other factors on the stability of paragonite in metabasic rocks, and its potential role as a host of volatiles has not yet been considered.

1.3 The geological nitrogen cycle and behaviour of nitrogen

The geological N cycle involves the transfer of N from the surface, where it primarily resides in the atmosphere, to the mantle. Nitrogen from the atmosphere is entrained in sediments and crust, which enter the subduction zone. There N can either be recycled into the mantle, or lost from the slab and enter the volcanic arc via melting in the mantle wedge. Nitrogen from the convecting mantle is returned to the atmosphere by volcanism at mid-ocean ridges (MORB) and ocean islands (OIB).

Nitrogen has a complex behaviour in geological systems because it can be present as a variety of different chemical species. The most important species are thought to be N_2, NH_3 (ammonia), NH_4^+ (ammonium), and N^{3-} (nitride) (in order of decreasing oxidation state: see below). Nitrogen

in minerals is thought to primarily be speciated as NH_4^+, substituting for K^+ and, to a lesser extent, Na^+ and Ca^{2+}. This is based on the high abundance of N in mica and feldspar mineral separates (Boocock et al., 2023b; Busigny et al., 2003b, 2004; Honma and Itihara, 1981; Jia, 2006; Pitcairn et al., 2005), and correlations between bulk K_2O and N in mica-rich rocks (Bebout et al., 2013; Bebout and Fogel, 1992; Busigny et al., 2003a; Li et al., 2021a; Sievers et al., 2017b). N_2 has also been demonstrated to reside in minerals such as cordierite and beryl, where there are large channels in the crystal structure that can accommodate neutrally charged species (Bebout et al., 2016; Palya et al., 2011; Wunder et al., 2015). N^{3-} minerals require extremely reducing conditions to form and occur only in meteorites, and perhaps the mantle (Adler and Williams, 2005), with one documented occurrence in an ultra-high pressure (UHP) ophiolitic chromitite from Tibet (Dobrzhinetskaya et al., 2009).

Nitrogen is considered to be a fluid mobile element. Thermodynamic modelling predicts that N in fluids should primarily be speciated as NH_4^+ or NH_3 in the upper mantle, whereas fluids in the mantle wedge are oxidised and should stabilise N_2 (Mikhail et al., 2017; Mikhail and Sverjensky, 2014). Most crustal fluids, including those in the subducting slab, are sufficiently oxidised that N_2 should be the dominant N species. However, modelling emphasises that fluid speciation of N is highly sensitive to temperature, pressure, redox state, pH and N concentration in the fluid, and some of these parameters are poorly constrained in natural samples. Recent experimental work has produced similar results to this thermodynamic modelling (Chen et al., 2019a). N_2 is observed in fluid inclusions in crustal rocks from a range of settings, including subducted crust (e.g. Andersen et al., 1991, 1989; Bottrell et al., 1988; Fu et al., 2003; Nishizawa et al., 2007; Správnitz et al., 2022). One study, which specifically looked for different N species in fluid inclusions, found that N_2 was the main species but NH_4^+ was also present in small amounts (Nishizawa et al., 2007). These rocks were sub-greenschist facies hydrothermal deposits so they may not be directly applicable to subduction zone conditions, but they seem to validate the results of thermodynamic models. A mixture of N_2 and NH_3 species in fluid inclusions has been documented in HP serpentinites, where they coexist with reduced carbon and sulphur species (CH_4 and H_2S) (Boutier et al., 2021; Vitale Brovarone et al., 2020).

Nitrogen has two stable isotopes, ^{14}N and ^{15}N, which are fractionated between different geochem-

ical reservoirs within the Earth (Table 1). Nitrogen isotope compositions ($\delta^{15}N = [(^{15}N/^{14}N)_{sample}/(^{15}N/^{14}N)_{air} - 1] \times 1000$) are measured relative to air, such that air has a value of 0 ‰. Significant N isotope fractionation occurs between minerals and aqueous fluids, with ^{14}N being preferentially partitioned into the fluid phase. The magnitude of fractionation depends on the speciation of N in the fluid, as well as temperature. A number of studies have looked at changes in N concentration and $\delta^{15}N$ in suites of rocks that have been metamorphosed to progressively higher grades. Loss of N and increase in rock $\delta^{15}N$ with increasing metamorphic grade has been observed in contact metamorphic (Bebout et al., 1999), regional metamorphic (Jia, 2006; Mingram and Bräuer, 2001; Plessen et al., 2010) and some subduction settings (Bebout and Fogel, 1992). The magnitude of the observed N loss and isotopic shift is generally consistent with N speciation as N_2 in the fluid, although a few studies have observed larger shifts which could indicate the presence of NH_3 (see review in Bebout et al., 2016).

	N (μg/g)	δ^{15}N (‰)	B (μg/g)	δ^{11}B (‰)
Seawater	0.01 – 1	0 – +20	4.5	+39.6
MORB	<0.01 – 9.5 (1.4)	-8.9 – +9 (-5)	0.4 – 2.5	-12.0 – 0.0 (-7.1)
AOC	1.3 – 75 (9.5)	-20.1 – +8.3 (+0.4)	1–200 (5.2)	-4.3 – +24.9 (+3.4)
Siliclastic sediments	30 – 8200	-0.9 – +8.5	60 – 160	-13.1 – +2.8
Chert/silicic ooze	18 – 2300	+2.5 – +7.7	50 – 150	-11.8 – +7.7
Carbonate sediments	62 – 580	+2.4 – +8.0	1 – 30	-5.0 – +26.0
Oceanic serpentinite	1.4–9.3	+3.4 – +15.0	10 – 91	+7 – +20
Depleted MORB mantle	0.01 – 0.3 (0.24)	-7 – -3 (-5)	0.06–0.08	-12.0 – 0.0 (-7.1)
Continental crust	1–3000 (60)	-15 – +15 (+5)	1–500 (11)	-16.0 – 0.0 (-9.4)

Table 1: Estimates of the B and N composition of some key geochemical reservoirs. Boron data from compilations by De Hoog and Savov, 2018; Marschall, 2018; Trumbull and Slack, 2018. Nitrogen data from Bebout et al., 2018; Johnson and Goldblatt, 2015; Li and Li, 2022, 2023a,b; Li et al., 2007, 2014. Average values in brackets where available.

Fresh MORB has low N concentrations (~1.4 μg/g, Table 1) and negative N isotope values ($\delta^{15}N$ = ~-5 ‰). Hydrothermal alteration of oceanic crust produces enrichment in N (1.3–75 μg/g). $\delta^{15}N$ (-20.1 – +8.3 ‰) is mostly elevated compared to MORB, which is attributed to addition of N sourced from seafloor sediments (18–8200 μg/gN, $\delta^{15}N$ = -0.9 – +8.5 ‰) and organic matter (10–3000 μg/gN, $\delta^{15}N$ = -3 – +7 ‰) (Busigny et al., 2005; Li et al., 2007). A smaller number of AOC samples display addition of N with strongly negative $\delta^{15}N$, which has been attributed to abiotic nitrogen reduction (Li et al., 2007). The amount of N carried into subduction zones by AOC is therefore at least an

order of magnitude higher than that carried by fresh MORB.

1.3.1 The role of subduction zones

A key parameter that influences the geological N cycle is subduction recycling efficiency, defined here as the percentage of N entering a subduction zone that is subducted into the mantle, beyond the volcanic arc. During prograde devoltilization, the N concentration in the slab is expected to decrease, and δ^{15}N to increase, as ^{14}N is preferentially partitioned into the fluid. These fluids will migrate into the mantle wedge and influence the composition of arc lavas and gases. Studies comparing the flux of N entering modern subduction zones with the flux of N expelled at volcanic arcs have produced a wide range of estimates, varying from almost complete subduction of N into the mantle, to almost complete recycling through the volcanic arc (e.g. Busigny et al., 2019; Elkins et al., 2006; Fischer et al., 2002; Füri et al., 2021; Labidi et al., 2021; Li and Li, 2022, 2023a; Li et al., 2023b; Mitchell et al., 2010; Zimmer et al., 2004). Whilst some of the variability between different subduction zones is likely related to real geological factors such as slab geothermal gradient and the variable composition of the crust entering the subduction zone, a significant amount of variability may be due to uncertainties in input and output fluxes. For example, two recent studies on the Central American Arc produced recycling efficiencies ranging from 0–30 % (Labidi et al., 2021) to 55–85 % (Li and Li, 2022), depending on data used for input and output fluxes. In particular, the output flux at arcs is hard to estimate since it is hard to disentangle the contribution of air contamination to volcanic gas emissions (Labidi et al., 2021), and there is uncertainty about the amount of N that is fixed into the igneous crust at arcs instead of being degassed (Boocock et al., 2023a; Füri et al., 2021; Li et al., 2023b). The relative contribution of sediments and mafic crust to the N budget entering the slab may vary significantly between subduction zones due to differences in N concentrations and thicknesses of the two components, particularly of sediments. Despite having a lower average N concentration, the mafic crust is generally much thicker than the overlying sediments and so on a global scale it appears that N fluxes from mafic crust and sediments are equal within a factor of two (Busigny et al., 2011; Li and Li, 2023a; Mallik et al., 2023). This emphasises the importance of the mafic crust in the subduction zone N cycle, which was somewhat overlooked in early studies due to its assumed low N concentration. The contribution of oceanic serpentinites is less well known since there are very few

N concentration data available, but a recent study by Li et al., 2023a suggests that the global flux might be 5–25% of that for sediments.

1.3.2 Nitrogen studies in subducted crust

An alternative method to constrain recycling efficiency is to study N in HP rocks that represent exhumed sections of the subducted crust. This allows a comparison between the N content of rocks which were subducted to sub-arc depths with their unmetamorphosed equivalents, to see how much, and at what depths, N was lost from the slab during subduction. Studies on metasediments suggest contrasting behaviour between the Western Alps (Bebout et al., 2013; Busigny et al., 2003a; Philippot et al., 2007), where concentrations of N and other FME did not change with increasing depth (as inferred from metamorphic pressure) up to around 90 km, and the Catalina Schist (Bebout and Fogel, 1992), where N and other FME concentrations in metasediments decrease with increasing depth and δ^{15}N increases. The former suggests that little N was lost during prograde metamorphism, whereas the latter suggests N loss into an aqueous fluid. The colder geothermal gradient in the Western Alps compared to the Catalina Schist has been suggested as the reason for the difference in behaviour. Little dehydration is suggested to have taken place during cold subduction in the Western Alps, and the mobility of any small amount of fluid produced was limited to the hand specimen scale. Only one study has looked at a suite of metabasic rocks with similar protoliths, but spanning a range of peak P-T conditions. Busigny et al., 2011 showed that metagabbros from the Western Alps exhibit little N and FME loss with increasing depth, similar to the behaviour observed for Western Alps metasediments.

Studying N in HP rocks also offers the opportunity to understand the processes that control N loss from the slab, such as N partitioning between minerals, fluids and melts, the capacity of different lithologies to transport N, and the magnitude of fluid fluxes associated with N transport. Understanding these processes would enable us to model the behaviour of N during subduction under different conditions such as variable geothermal gradients, subduction rates, and crustal compositions, which may have varied over Earth's history.

A number of studies have demonstrated that N can be redistributed between different lithologies within the slab. Halama et al., 2010 showed that eclogites from a variety of localities have N concen-

trations and δ^{15}N that overlap with unmetamorphosed AOC, but that some samples show other FME trace element signatures of sediment-derived material, raising the possibility that some of the N was in fact acquired from sediment-derived fluids inside the subduction zone. Metabasalts which exhibit significantly elevated N concentrations compared to unmetamorphosed AOC have been reported from several localities (Bebout, 1997; Li et al., 2021a; Mallik et al., 2023; Sievers et al., 2017b). Positive δ^{15}N and correlations of N with trace elements such as Ba, Rb, Cs have been used to argue that N was lost from sediments during devolatilization but then sequestered into these metabasalts. This suggests that the basaltic crust could act as a trap for sedimentary N, but the extent to which this occurs, and the factors that control it, remain unclear. It is also unclear whether this N was added during prograde subduction or during exhumation. If it was added during subduction, this trapped N could either be retained in the basaltic crust and subducted into the mantle, or could be released at greater depth by devolatilization of the basaltic crust itself.

Correlations of bulk N concentrations with K_2O, Rb and Cs in subducted metasediments suggest that white micas are the main host for N in these rocks (Bebout et al., 2013; Bebout and Fogel, 1992; Busigny et al., 2003a). Some correlations of N with these elements have been observed in subducted metabasic rocks but they are generally less strong, and are absent completely from some sample suites, particularly at lower N concentrations (< 10 μg/g bulk N, Halama et al., 2010, 2017; Li et al., 2021a; Mallik et al., 2023), suggesting that other minerals could also be significant hosts for N. There is very little data on the N concentrations in subduction-related micas (Busigny et al., 2003a; Li et al., 2014), and none for other minerals, because analysing N concentrations of individual minerals has been analytically challenging, and so no assessment has been made of the N partitioning between white micas and other minerals and their relative contribution to the N budget of subducted oceanic crust, taking into account their N concentrations and modal abundance.

Two studies have examined the behaviour of N in rocks interpreted to represent former fluid conduits that were active during subduction, by comparing the N concentrations in the conduit rocks with those in the unaltered wall rocks. Halama et al., 2017 demonstrated that phengite breakdown during a prograde fluid-induced blueschist-eclogite transition resulted in loss of N from the bulk rock. In a different sequence where phengite was stable during retrograde fluid-rock interaction, N was added to the rock from a sediment-derived fluid. Epstein et al., 2021 demonstrated up to 60% loss

of N from metasediments during fluid-rock interaction, with an associated increase in δ^{15}N, consistent with N partitioning into an aqueous fluid. Nitrogen was lost despite the stability of phengite and the growth of new paragonite during fluid-rock interaction. The stability of white mica clearly plays an important role in determining the behaviour of N during fluid-rock interaction. A number of experimental studies have determined mica-fluid partitioning coefficients for N at subduction zone P-T conditions. The reported partition coefficients are highly variable depending on the experimental conditions (e.g. Bos et al., 1988; Förster et al., 2019; Jackson et al., 2021; Kupriyanov et al., 2023; Li et al., 2015; Pöter et al., 2004). One reason for this may be the variable speciation of N in fluids, which is typically not well constrained in these experiments. Investigating fluid-rock partitioning in natural samples will help to determine which experimental data are most applicable to natural samples.

1.3.3 Methods for analysing nitrogen

One of the reasons for the lack of understanding of subduction zone N behaviour, is that most N data are for whole rock samples and little *in situ* data is available to understand N behaviour at the mineral scale. Busigny et al., 2003a and Li et al., 2014 analysed N concentrations and δ^{15}N in mineral separates by bulk combustion (see Section 2 for description of different analytical methods). Busigny et al., 2003a,b, 2004 used their bulk combustion data to calibrate analyses of N concentrations in white mica and biotite by Fourier-transform Infrared Spectroscopy (FT-IR), allowing *in situ* analyses with a ~100 μm beam size. Whilst these methods provide some useful data on N concentrations in minerals, neither of them can easily be adapted to measure concentrations of other FME in the same grains. Additionally, bulk analyses of mineral separates lack spatial resolution since multiple grains are required for each analysis. FT-IR is slightly better, but the 100 μm beam size is still relatively large compared to typical grain sizes in many HP rocks, allowing little spatial resolution within grains, and precluding the analysis of fine grained samples altogether. Füri et al., 2018, 2021 demonstrated that N concentrations down to ~1 μg/g can be analysed in silicate glasses by secondary ion mass spectrometry (SIMS), using a ~20 μm beam size. This offers the opportunity to achieve a significant improvement in spatial resolution compared to previous mineral analyses, and to measure other FME alongside N, which could provide additional constraints on the devolatilization history,

sources of metamorphic fluids, and partitioning behaviour of N during subduction. One of the main aims of this thesis is to conduct SIMS analyses of N in white micas and other minerals to investigate the processes controlling N recycling in subducted crust.

1.4 Boron as a tracer of fluid processes

Boron is a fluid mobile element which exhibits large stable isotope fractionation between different geochemical reservoirs and is therefore useful for tracing the source of geological fluids in subduction zones (De Hoog and Savov, 2018). White mica is a significant host of B, where it substitutes as a trace element for Si^{4+} or Al^{3+} (Leeman and Sisson, 1996). If white micas are present in a rock, they dominate the B budget, since their B concentrations are at least an order of magnitude higher than other common rock-forming minerals, with the exception of tourmaline (Domanik et al., 1993; Marschall et al., 2006a). Boron has two stable isotopes, ^{11}B and ^{10}B, which are strongly fractionated between different geochemical reservoirs within the Earth. ^{11}B is preferentially accommodated in trigonal coordination, whereas ^{10}B prefers tetrahedral coordination. The B concentrations and B isotope compositions ($\delta^{11}B = [(^{11}B/^{10}B)_{sample}/ (^{11}B/^{10}B)_{reference} - 1] \times 1000$) of some key reservoirs is given in Table 1 and spans ~60 ‰. This leads to significant B isotope fractionation amongst phases which differ in their B coordination. Boron resides in tetrahedral coordination in micas and most other silicate minerals. The mineral tourmaline is a notable exception, being the most common B-rich mineral (3–3.5 wt% B), where B forms a structural component and has trigonal coordination. Boron in aqueous fluids is present either as $B(OH)_3$, which has trigonal coordination, or $B(OH)_4^-$, which has tetrahedral coordination. The former is dominant in acidic to neutral fluids, whilst the latter becomes important in strongly alkaline fluids (Schmidt et al., 2005). Significant B isotope fractionation ($\Delta^{11}B_{a-b} = \delta^{11}B_a - \delta^{11}B_b$) therefore occurs between micas and tourmaline, and micas and acidic fluids, with micas having $\delta^{11}B$ values 10–15 ‰ lower than the coexisting fluid or tourmaline (Klemme et al., 2011; Kowalski et al., 2013; Wunder et al., 2005).

1.4.1 The subduction zone boron cycle

As shown in Table 1, the different lithologies entering the subduction zone have distinct B concentrations and isotopic signatures. Fresh MORB has low B concentrations (0.4–2.5 μg/g) and negative B

isotope values (δ^{11}B = -12.0 – 0 ‰). Seawater has a very heavy B isotope signature (+39.6 ‰), and hydrothermal alteration of oceanic crust by seawater-derived fluids produces enrichment in B (1–200 μg/g) and elevated δ^{11}B values (-4.3 – +24.9 ‰) compared to MORB. The same happens to oceanic serpentinites (10 – 91 μg/g, δ^{11}B = +7 – +20 ‰), formed by hydrothermal alteration of the oceanic lithospheric mantle (< 0.05 μg/g, δ^{11}B = -7 ‰). Carbonate sediments also have mostly positive δ^{11}B (-5.0 – +26.0 ‰), since they incorporate B from seawater, whereas siliciclastic sediments have largely negative δ^{11}B values (-13.1 – +2.8 ‰) due to the large B isotope fractionation between seawater and clays at low temperature. Continental crust has a range of δ^{11}B values (-16.0 – 0 ‰) with a peak around -8 – -10 ‰.

During prograde devolatilization, the B concentration and δ^{11}B of a rock is expected to decrease as fluid is lost from the rock, since ^{11}B preferentially partitions into the fluid (Konrad-Schmolke and Halama, 2014; Marschall et al., 2007). Arc lavas have elevated B/Nb ratios compared to the upper mantle, which implies that B is lost from the subducting slab and incorporated into the source of arc magmas (De Hoog and Savov, 2018; Ryan and Langmuir, 1993). Across-arc trends in lava compositions show systematic decreases in B/Nb and δ^{11}B with increasing depth to the slab for some arcs (Ishikawa and Nakamura, 1994; Turner et al., 2023), which has been interpreted to reflect the increasingly negative δ^{11}B and decreasing B concentration of fluids added to the mantle wedge from the dehydrating crust (Peacock and Hervig, 1999). Other arcs show more complex behaviour. For example, in the Kamchatka arc, δ^{11}B and B/Nb decrease with increasing slab depth initially, but then increase at 170–200 km depth, which was interpreted to reflect the release of isotopically heavy fluids from dehydrating oceanic serpentinite (Konrad-Schmolke et al., 2016). Boron isotopes have therefore proved a useful tool for tracing different sources of fluids entering the mantle wedge beneath arcs.

1.4.2 Boron studies in subducted crust

In addition to the B systematics of volcanic arcs, a number of studies have investigated the behaviour of B during subduction by studying formerly subducted rocks preserved in meta-ophiolites. Early SIMS studies showed that white mica contains an order of magnitude higher B concentrations than other common HP minerals in metabasalts and metasediments (Domanik et al., 1993; Nakano and

Nakamura, 2001), and that white micas and other minerals from a variety of localities and lithologies have negative δ^{11}B (-3 – -11 ‰, Peacock and Hervig, 1999), which are lower than the δ^{11}B of AOC and some sediments. The latter was interpreted as being consistent with B loss to an aqueous fluid during prograde devolatilization. More recent studies have demonstrated similar negative δ^{11}B in blueschists from the Mariana arc (Liu et al., 2022; Pabst et al., 2012). King et al., 2007 showed that lawsonite-albite and lawsonite-blueschist grade subducted melange material from the Catalina Schist has negative δ^{11}B (-12 – -3 ‰) consistent with devolatilized crust, but higher grade amphibolite-facies material has higher δ^{11}B (-4 – +4 ‰), which was interpreted to reflect assimilation of the isotopically heavy B lost from devolatilizing crust. This began to demonstrate the complexity of B transport within the subducted crust, whereby B released from one lithology may not be transported directly to the mantle wedge and could instead be sequestered somewhere else in the crust, either to be subducted into the mantle or to again be released at greater depth. On the other hand, this demonstrates the potential of B concentrations and isotopes to be used as tracers of fluid mobility within the subducted crust. Several studies have documented heavy B isotope signatures in HP tourmaline and white mica which would be in equilibrium with fluids having δ^{11}B = +10 – +30 ‰ (Angiboust et al., 2014; Halama et al., 2020; Marschall et al., 2006b; Ota et al., 2008). This likely traces the movement of fluids derived from oceanic serpentinite, as evidenced by the enrichment of Mg, Cr and Ni in eclogites with heavy δ^{11}B from Monviso (Angiboust et al., 2014). Other studies have documented B-rich fluids (100-1000s μg/g B) with lighter δ^{11}B (0 – +15 ‰, Guo et al., 2022; Sievers et al., 2017a), which likely derive from dehydration of sediments. The value of *in situ* analyses of individual minerals is demonstrated by numerous studies which show that different B isotope signatures may be preserved in different mineral generations, reflecting the evolution of fluid-rock interaction over time (e.g. Angiboust et al., 2014; Bebout and Nakamura, 2003; Guo et al., 2022; Halama et al., 2020; Konrad-Schmolke and Halama, 2014; Nakano and Nakamura, 2001; Sievers et al., 2017a; Xu et al., 2022). Relatively few studies have combined B concentrations and isotopes with analysis of other FME or isotope systems to trace different fluid sources (Angiboust et al., 2014; Chen et al., 2023b; Harvey et al., 2014; Menold et al., 2016; Sievers et al., 2017a). Given ranges in B concentrations and δ^{11}B of the different lithologies entering subduction zones, and the potential for generation of different B signatures at different depths, the combination of B with other FME will

yield additional constraints on fluid sources. For example, fluids with moderate B concentrations (~50–250 μg/g) and δ^{11}B in the range +5 – +15 ‰ could conceivably be sourced from serpentinites, AOC or sediments given the right conditions. The combination of *in situ* measurements of B and other FME such as N will be one of the aims of this thesis.

1.5 Thesis aims and chapter outline

Having reviewed the literature on the role of white mica as a carrier of volatiles in the subducted oceanic crust, and identified N and B as being elements of particular interest, I now give an outline of the main research question addressed by this thesis.

1. What is the significance of white mica as a host for N and other FME in subducted oceanic crust compared to other HP minerals, and to non-mineral hosts? How does the mineralogy of subducted rocks affect their ability to retain N and other FME during subduction?

2. How does N partition between different minerals at HP and can we place constraints on a) fluid-mineral, and b) inter-mineral partition coefficients for N in natural samples and compare these with experimental data?

3. Can we use coupled analyses of B isotopes, N and other FME to trace fluid sources within subducted crust, and disentangle processes such as seafloor alteration, devolatilization and HP fluid-rock interaction?

4. How are N and other mica-hosted FME redistributed between different lithologies in the subducting slab, and what are the implications of this for the recycling of these elements into the mantle?

Chapter 2 describes the analytical methods used in my work, since the several of the methods are common to multiple chapters.

Chapter 3 presents the first *in situ* N concentrations analysed by SIMS in HP rocks. I analyse a suite of samples which represent subducted oceanic crust that has undergone varying degrees of HP fluid-rock interaction. I discuss the importance of white micas as host for N compared to other minerals, and implications of the data for the N budget of subducted oceanic crust. Then I examine

the fluid-rock interaction history of two samples in detail. By comparing the behaviour of N to other FME I am able to place the first constraints on the fluid-mica partition coefficient for N in a natural system. I also explore how the stability of mica during fluid-rock interaction affects the loss of N from the rock.

Chapter 4 presents a case study of using *in situ* B isotopes, B concentrations and other FME concentrations (including N) to trace fluid sources in subducted rocks. I focus on the Dora-Maira whiteschists, which are highly metasomatised granites that form part of the subducted continental crust in the Western Alps. A number of previous studies have attempted to trace fluid sources responsible for metasomatism, using a variety of bulk rock and *in situ* geochemical data, but there is still a lack of consensus around the timing and sources of metasomatic fluids. I show that *in situ* B isotopes and B concentrations can be a useful tool to identify sediment-derived fluids. I also discuss the difference in the B isotope information recorded by white mica and tourmaline, and the mineralogical controls on the retention or loss of different FME during metamorphism and metasomatism.

Chapter 5 presents a larger dataset of SIMS N concentrations for subducted oceanic crust, alongside other FME concentrations, B isotopes, and bulk rock N concentrations and N isotopes. I provide a more extensive discussion of the different mineral hosts for N, exploring the differences between different metamorphic facies, and the effects of oceanic hydrothermal alteration on the HP mineralogy. These data are then used to calculate inter-mineral partition coefficients for N. I also compare the N concentrations in minerals, as determined by SIMS, to whole rock N concentrations, to assess the quality of the SIMS data, and examine the possible role of non-mineral hosts for N in HP rocks. Finally, I combine FME concentrations, N concentrations, N isotopes and B isotopes to identify the sources of N in subducted oceanic crust and distinguish the effects of seafloor alteration, devolatilization, and HP fluid-rock interaction.

Chapter 6 discusses how each research chapter helps to answer the four research questions set out above and suggests opportunities for further work.

1.6 Thesis style

Chapters 3 and 4 are published papers which are included with a short preface and post-script to explain their role within the thesis. Chapter 5 is written in paper format for consistency but has not yet been submitted for publication. Each chapter has its own introduction, including a review of the literature relevant to that chapter. In the case of the two published papers, a small amount of material may be repeated from the overall thesis introduction.

The details of the publications are given below:

Harris, B.J.R., De Hoog, J.C.M, Halama, R., 2022 The behaviour of nitrogen during subduction of oceanic crust: Insights from *in situ* SIMS analyses of high-pressure rocks. *Geochimica et Cosmochimica Acta* 321, 16–34, doi:10.1016/j.gca.2022.01.018

Harris, B.J.R., De Hoog, J.C.M, Halama, R., Schertl H-P., Chen Y-X., 2023 Multi-stage subduction-related metasomatism recorded in whiteschists from the Dora-Maira Massif, Western Alps. *Contributions to Mineralogy and Petrology* 178 (11), 76. doi:10.1007/s00410-023-02058-0

Mineral abbreviations are after Whitney and Evans, 2010. All other abbreviations are defined at their first usage, but a list of those most commonly used is given below. Chemical elements are referred to by their symbol, except at the beginning of sentences.

MORB	Mid-ocean ridge basalt
AOC	Altered oceanic crust
FME	Fluid-mobile element
LILE	Large ion lithophile element
P-T	Pressure-temperature
(U)HP	(Ultra-)high pressure
SIMS	Secondary ion mass spectrometry

Table 2: Commonly used abbreviations.

2 Chapter 2: Methods

This chapter details all analytical methods used in the thesis. Since there is overlap between the methods for different chapters, the methods sections of the published chapters have been combined and placed in this chapter, along with the methods for the unpublished chapter 5.

2.1 Bulk rock major and trace element concentrations

Whole rock major and trace elements in Chapter 5 were measured with a Panalytical PW2404 XRF spectrometer at the Grant Institute, School of Geosciences, University of Edinburgh, UK. Long term reproducibility of standards from this lab is 0.22–3.99% for major elements and 1.42–17.7% for trace elements.

2.2 Bulk rock nitrogen concentrations and nitrogen isotopes

Nitrogen contents and isotope values in Chapter 5 were measured on whole rock powders on a MAT253 Isotope Ratio Mass Spectrometer (IRMS) at the University of St Andrews Isotope Geochemistry (STAiG) laboratory, following the protocols developed in (Boocock et al., 2020). Sample powders were weighed into pre-cleaned quartz glass tubes together with ca. 1 g of CuO wire and evacuated overnight at 120 °C to remove air and volatile contaminants. After evacuation, the tubes were sealed with an oxypropane blowtorch and placed into a muffle furnace at 900 °C for 4 h, followed by 2 h at 600 °C to ensure total liberation of silicate-bound N and conversion to N_2. Combustion at 1050 °C was tested, as recommended by Li et al., 2021b, but resulted in sample powders reacting with the quartz tubes. After the heating step, the purified sample gasses were introduced into the mass spectrometer by a custom-built tube cracker line operating under continuous helium flow 50 ml/min (grade 5.0). USGS61 and USGS62 reference materials were used to calibrate measured isotopic ratios relative to atmospheric air ($\delta^{15}N = [(15N/14N)_{sample}/ (15N/14N)_{atmosphere} - 1] \times 1000$). The average reagent blank was 0.29 μg N, which equates to 0.4–6.6% of the sample peak area, with a $\delta^{15}N$ of -1.9 ‰. All analyses reported here are blank corrected. Basalt USGS BHVO-2 and serpentinite UB-N were used as secondary standards for quality control. Measured N concentrations for BHVO-2 (18.1

± 0.4 μg/g, n = 3) and UB-N (26.3 ± 1.1 μg/g, n = 2) are ca. 5–10% lower than published values (BHVO-2: 20.2–23.4, μg/g UB-N: 27.5 μg/g) due to the lower combustion temperature required for my samples. The δ^{15}N values for BHVO-2 (+1.8 ± 0.1 ‰, n = 3) and UB-N (+4.0 ± 0.3 ‰, n = 2) agree with published values (BHVO-2: 1.8–2.2 ‰, UB-N: 4.0 ‰, Boocock et al., 2023a, 2020, 2023b).

2.3 Mineral major element concentrations

For Chapter 3, most of the mineral major element concentrations were analysed using a JEOL JXA 8900R electron microprobe at the University of Kiel, Germany. These were analysed by my supervisor Ralf Halama as part of a previous research project (Halama et al., 2020 and other unpublished data). Elements were measured 15 s on peak and 7 s on background with an acceleration voltage of 15 kV, beam current of 15 na and beam diameter of 5 μm. Natural standards were used for calibration and a CITZAF matrix correction was applied. To complement this original dataset, additional analyses were carried out using a Cameca SX100 electron microprobe equipped with 5 wavelength dispersive spectrometers (WDS) at the Department of Earth Sciences, University of Cambridge, UK. Acceleration voltage was 20 kV, beam current was 20 nA and beam diameter was 5 μm. On-peak counting times (seconds) for elements were as follows (background time in brackets): K 10 (5), Na 10 (5), Mg 30 (15), Si 10 (5), Al 30 (15), Fe 40 (20), Ca 20 (10), Ti 60 (30), Mn 90 (45). A variety of synthetic and natural standards were used for calibration and a PAP matrix correction was applied. EPMA spots are located as close as possible to the corresponding SIMS spots. The source of each analysis (Kiel/Cambridge) is listed in Appendix A.1.

For Chapter 4, mineral major element concentrations were determined using a Cameca SX100 electron microprobe equipped with 5 wavelength dispersive spectrometers at the School of Geosciences, University of Edinburgh, UK. Acceleration voltage was 15 kV, beam current was 4 nA for major elements and 100 nA for minor elements. Beam diameter was 2 μm for anhydrous minerals and 5 μm for hydrous minerals. On-peak counting times (seconds) were as follows (background time in brackets). Major elements: K 20 (10), Na 20 (10), Ca 20 (10), Mg 20 (10), Fe, Si 20 (10), Al 20 (10). Minor elements: K 20 (10), Na 20 (10), Ca 50 (25), Mg 20 (10), Ti 60 (30), Mn 80 (40), P 20 (10), Zr 60 (30). A variety of synthetic and natural standards were used for calibration.

For Chapter 5, mineral major elements were measured by quantitative energy dispersive spectroscopy (EDS) using a Zeiss Sigma HDVP field emission scanning electron microscope (SEM) with an Oxford Instruments AZtec EDS X-ray analysis system at the Grant Institute, School of Geosciences, University of Edinburgh, UK. Accelerating voltage was 20 keV and the working distance was fixed at 7 mm. A cobalt standard was used for calibration. Mineral major elements were primarily used for calibration of the SIMS data (SiO_2) and estimation of the mineral modal abundances so EDS data were considered to be sufficiently accurate compared to the more commonly used EPMA technique.

2.4 Mineral nitrogen, volatile and trace element contents

The following is a description of the methods used for SIMS analysis of N, B, Li, F and Cl in Chapters 3 and 4. Full data for this session are given in Appendix Tables 18, 19, 20, 21, 22, 28 and 29. Nitrogen contents of minerals were determined *in situ* by SIMS at the Edinburgh Ion Microprobe Facility using a Cameca 7f-GEO with Hyperion source. Standard polished thin sections were cut to 25 mm rounds and gold-coated prior to loading into high vacuum (ca. 3×10^{-9} mbar). The sample surface was sputtered with a focused $^{16}O^-$ beam with a 18 nA beam current and an impact energy of 13.5 keV. Spot size was about 15 µm. One spot was analysed per grain, except where core and rim spots were analysed and reported separately. Prior to each analysis the analytical area was pre-sputtered for 120 s using a 15 µm beam raster to avoid background contamination. An effective field aperture of 20 µm was used to further reduce N backgrounds to <0.6 µg/g (see paragraphs below for details). Positive secondary ions sputtered from the sample were accelerated into a mass spectrometer and counted with an electron multiplier. An energy window of 50±20 V was applied to the secondary ion beam to reduce potential matrix effects. A mass resolution of 2000 (M/ΔM) was used to avoid interferences of $^{28}Si^{2+}$ and $^{12}CH_2{}^+$ on the $^{14}N^+$ signal, as well as $^{7}Li^{28}Si$ and $^{19}F^{16}O$ on ^{35}Cl. The mass calibration was updated at the start of each analysis using an automated peak centering routine on the ^{30}Si peak. The following isotopes were measured (total counting times per analysis in seconds in brackets): ^{7}Li (18), ^{11}B (30), $^{28}Si^{2+}$ (12), ^{14}N (60), ^{19}F (30), ^{26}Mg (12), ^{30}Si (12), ^{35}Cl (60). The ^{30}Si signal was used for internal standardisation using known SiO_2 contents measured by EPMA. As the wrong peak for ^{35}Cl was selected during the initial run, all analytical spots were repeated in a

separate routine measuring ^{26}Mg, ^{30}Si and ^{35}Cl only, with other analytical parameters kept identical to the original run.

Phengite mica 80-3 (71±19 µg/g N) and muscovite LMMN (186±11 µg/g N) were used for calibration of the N contents (Busigny et al., 2003b, 2004), St8.1.A9 basaltic glass for Cl (Lesne et al., 2011), Fba-5 basaltic glass for F (Guggino and Hervig, 2011), and GSD1-G basaltic glass for remaining elements (Jochum et al., 2005), the results of which are presented in Appendix A.1.

^{14}N count rates were low, equalling to a relative ion yield (RIY) compared to Si of ca. 0.002, which is why this element is not commonly measured, but signals were high enough to give acceptable counting statistics with the analytical conditions used. For example, for standard LMMN#2 (186 µg/g N), the ^{14}N count rate was ca. 35 counts per second, for a total of 2100 counts for the whole analysis (60s for ^{14}N) and a standard deviation of 2.2% based on counting statistics. This is nearly identical to the 1s uncertainty based on the 6 repeat cycles for each analyses (internal precision), which was 2.4%, indicating that analytical uncertainty was dominated by counting statistics. Repeatability (external precision) of this standard was 4.3% (n=16, see Appendix A.1), so about double the internal precision, which is probably mostly related to slight heterogeneity of the standard and/or instrumental factors. 1s uncertainties presented in the figures is based on the propagated uncertainty of the measurements (internal precision) and the uncertainty of the slope of the calibration line (Figure 3). The measurement of molecular species such as $^{14}N^{16}O$ or $^{28}Si^{14}N$ was explored in the course of this study, but did not yield any advantage, as with the positive secondary ion beam used in my setup the yield of these species was lower than the ^{14}N signal. This contrasts results in negative ion mode, where an advantage was observed (Füri et al., 2018), resulting in lower detection limits, but considering my ^{14}N count rates were sufficient for the material under investigation, I preferred to be able to analyse other fluid-mobile elements at the same time as N.

The two LMMN grains gave slightly different averages (187±22 and 153±7 µg/g, respectively, with n=20), the first grain containing areas with higher N contents (Figure 3). MgO contents (0.8 wt%) also showed about 10% variation, indicating some heterogeneity in this material (Figure 3). Multiple repeats of the Phe80-3 standard showed 13% variation (1s) in N content, which suggests some heterogeneity in this material as well, as it is much higher than the rsd for individual analyses (3%) and repeatibility of LMMN grain #2 (4%). Thus, the overall added uncertainty due to calibration

uncertainty is ca. 15%. Furthermore, I obtained a value of 17±0.4 µg/g N (n=2) on muscovite ms98973, for which no N data has been published. No certified N-free materials were available for extensive background evaluation, but a number of analyses of nominally N-free minerals (quartz and garnet) can be used to assess background contributions. Nitrogen concentrations in quartz ranged from 0.2–0.5 µg/g (n=3), and in garnet from 0.3–0.6 µg/g (n=4), with one outlier at 1.2 µg/g, suggesting that backgrounds are generally lower than 0.6 µg/g (Figure 5). The single outlier likely results from a spot overlapping with some more N-rich material. There was no systematic variation in background over time either during the first run (data for Chapters 3 and 4), when most of the analyses were carried out, or between the first and second runs (data for Chapter 5). Basaltic glasses GSD1-G and BCR2-G both showed concentrations of about 1.5±0.5 µg/g N. As it is possible that the glass reference materials GSD1-G and BCR2-G contain small amounts of N, no background correction was applied. Muscovite ms98973 (Dyar et al., 2001) was intended to be used as a secondary standard to detect potential matrix effects between basaltic glass and white mica, but I found that my concentrations for B (23–35 µg/g) and particularly Cl (31±13 µg/g) are very far from published values (180 and 700 µg/g, respectively; Dyar et al. (2001)), as well as highly heterogeneous. Fluorine was more homogeneous and my value of 12840 ± 45 µg/g is in reasonable agreement with the published value of 16800 µg/g Dyar et al. (2001). I also analysed two micas from Martin et al. (2015), namely JJE01-X-3 mica and MVE02-8-5 mica, to evaluate their use as potential N standards. However, although N contents were high, unfortunately they were also extremely heterogeneous for N, Li and B (see Appendix A.1).

N, B, Li, F, Cl, Rb, Cs and Sr in Chapter 5 was measured using a similar SIMS routine to that described above. The important differences are outlined below and full data for this session are given in Appendix Tables 38, 39, 40 and 41. For most samples a 22 nA beam current was used with a spot size of about 20 μm. The analytical area was pre-sputterred for 180s using a 30 μm beam raster. For fine grained samples the beam current was reduced to 10 nA, spot size to about 10 μm, and pre-sputtering to 120s with a 20 μm beam raster. In both cases, the secondary ion beam energy window was 50±20 V. The following isotopes were measured (total counting times per analysis in seconds in brackets for 22 and 10 nA beam currents respectively): ^{7}Li (30, 60), ^{11}B (40, 80), ^{14}N (100, 200), ^{19}F (50, 100), ^{23}Na (10, 20), ^{24}Mg (10 ,20), ^{27}Al (10 ,20), ^{30}Si (10, 20), ^{35}Cl (50, 100),

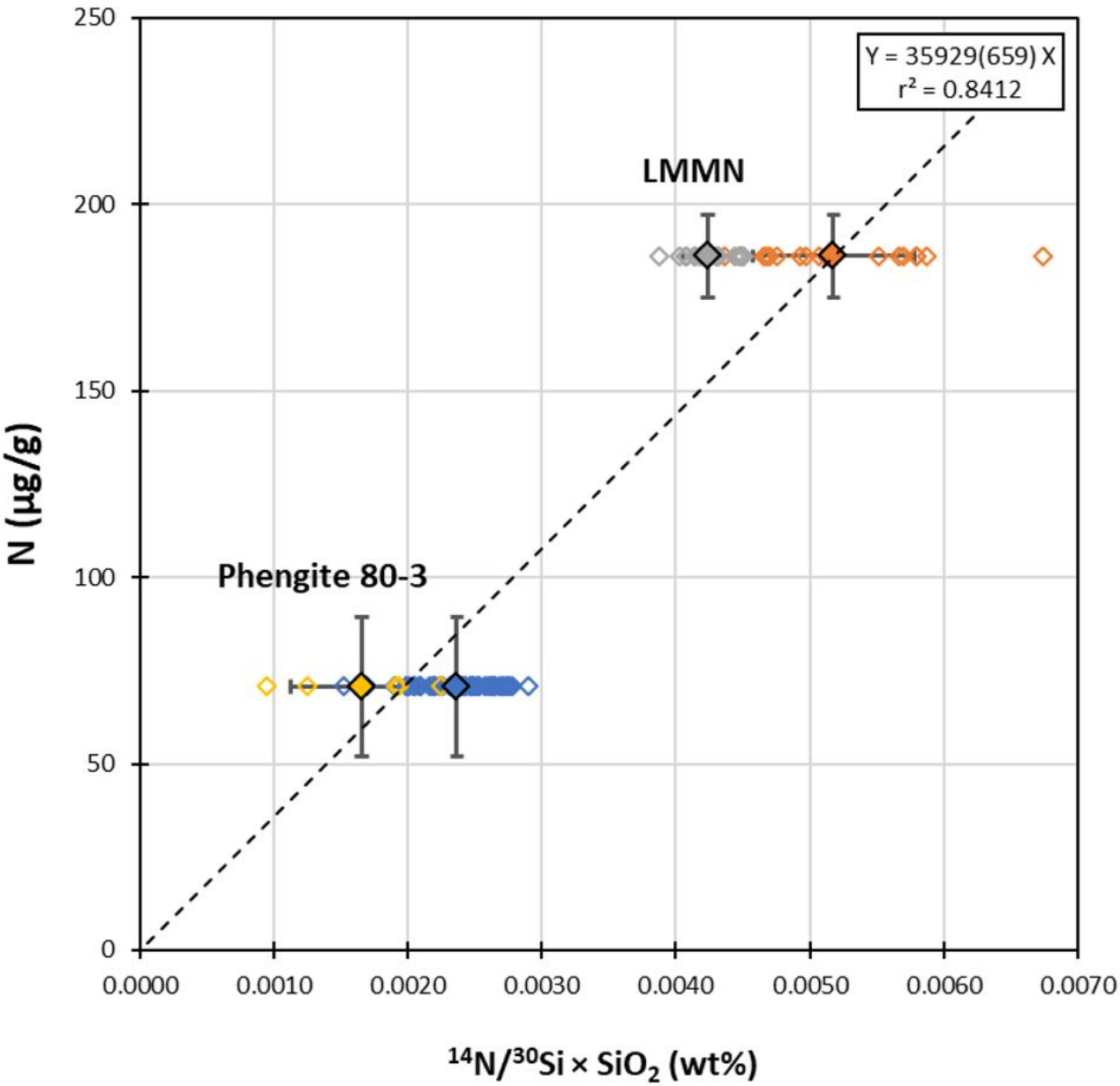


Figure 3: SIMS calibration of N concentrations for Chapters 3 and 4, based on two white mica standards (Phe80-3 and LMMN Busigny et al. (2003b, 2004)). All individual analytical spots (n=70) are indicated as well as averages with 1s uncertainties. The slope of the calibration slope is indicated, along with the 1s uncertainty in brackets.

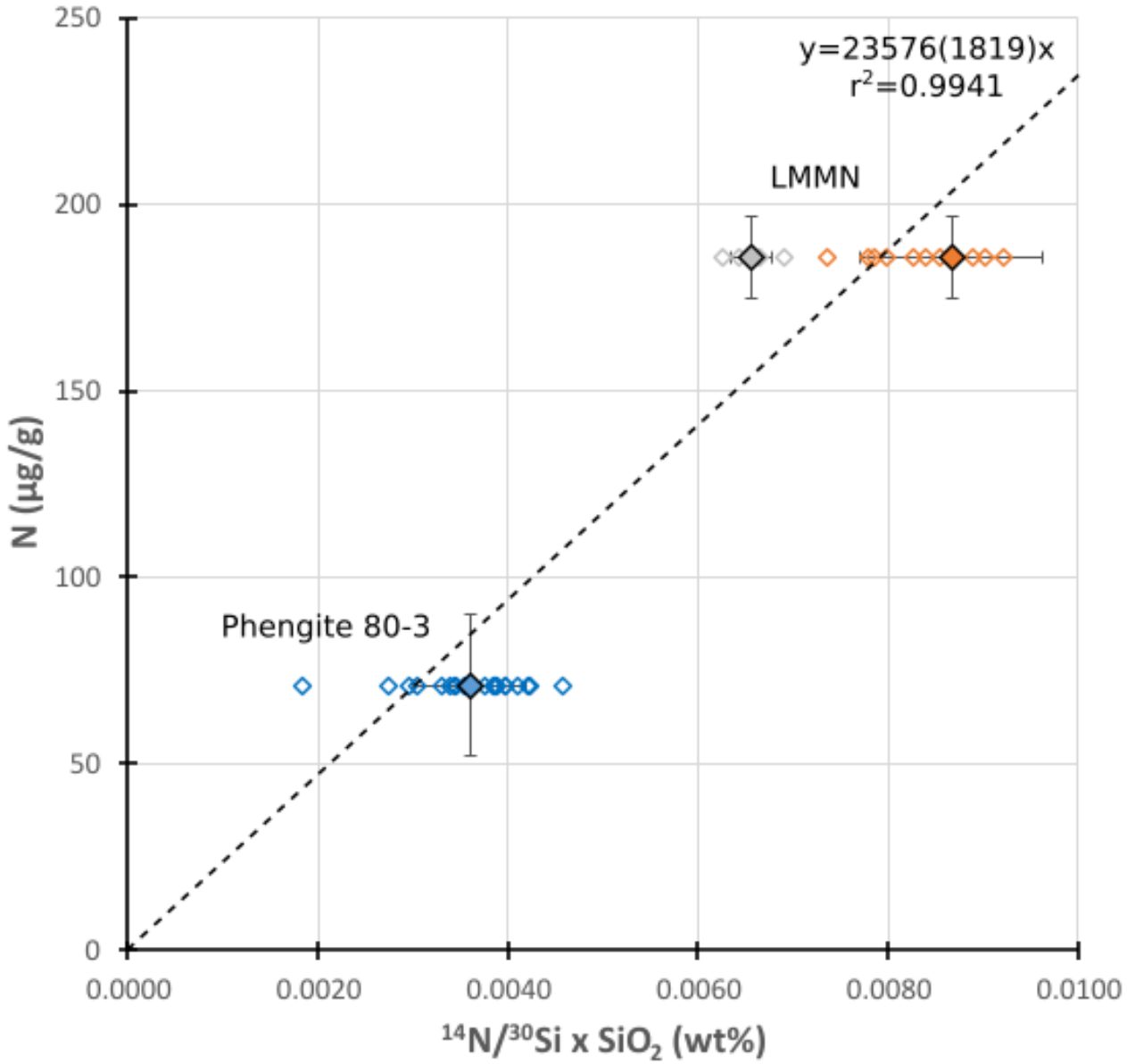


Figure 4: SIMS calibration of N concentrations for Chapter 5, based on two white mica standards (Phe80-3 and LMMN Busigny et al. (2003b, 2004)). All individual analytical spots (n=40) are indicated as well as averages with 1s uncertainties. The slope of the calibration slope is indicated, along with the 1s uncertainty in brackets.

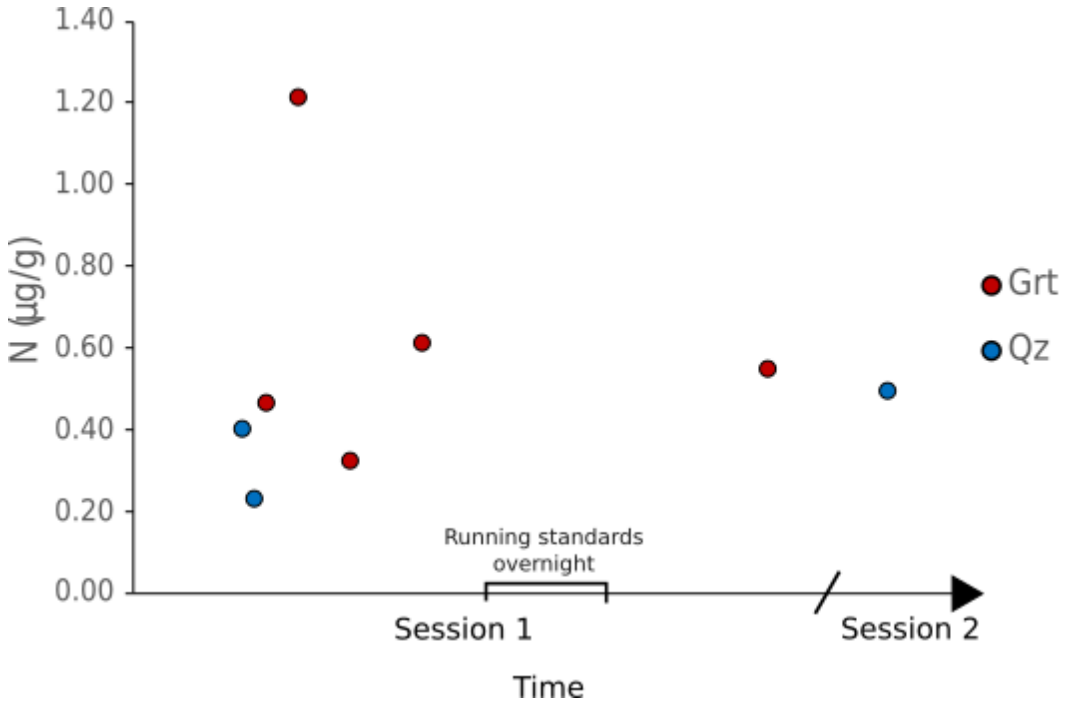


Figure 5: SIMS analyses of nominally N-free minerals used to assess background N levels.

^{39}K (10, 20), ^{84}Sr (50, 100), ^{85}Rb (50, 100), ^{88}Sr (40, 80), ^{133}Cs (80, 160). The same standards were used for calibration as the previous session. Repeatability (1sd) of the N concentrations of these standards was 16% for Phe80-3, 11% for LMMN#1 and 3% for LMMN#2, which is very similar to the previous session. The calibration curve for this session is shown in Figure 4. The difference in calibration slope is due to the differences in the analytical conditions.

B, Be, Li, Rb, Sr, Cs, F, and Cl in Chapter 4 were measured using a similar setup to that described for N. Beam current was 5 nA and spot size about 15 μm. The analytical area was pre-sputterred for 60s using a 10 μm beam raster. The following isotopes were measured (total counting times per analysis in seconds in brackets): ^{7}Li (40), ^{9}Be (40), ^{11}B (40), ^{19}F (40), ^{26}Mg (16), ^{30}Si (16), ^{35}Cl (60), ^{43}Ca (16), ^{47}Ti (24), ^{84}Sr (40), ^{85}Rb (40), ^{88}Sr (40), ^{133}Cs (40). As the wrong peak for ^{35}Cl was selected during the initial run, all analytical spots were repeated in a separate routine measuring ^{26}Mg, ^{30}Si and ^{35}Cl only, with other analytical parameters as detailed in the first N session. A variety of glass and mica standards were used for calibration, which is particularly important for halogens which experience strong matrix effects and accuracy benefits from matrix-matched standards. GSD1-G was used as the main calibration standard for elements other than halogens with preferred values from GeoReM (Jochum and Stoll, 2008), except B for which I adopted a value of 65 μg/g, following

Walowski et al., 2019.

2.5 Mineral boron isotopes

The following describes the methods used for SIMS analyses of B isotopes in phengite and tourmaline in Chapter 4. Full data for these sessions are given in Appendix Tables 30, 31 and 33. Boron isotopes in minerals were measured *in situ* by Secondary Ion Mass Spectrometry (SIMS) at the Edinburgh Ion Microprobe Facility, School of Geosciences, University of Edinburgh, UK, using a Cameca 7f-Geo equipped with a Hyperion RF oxygen source. Boron isotopes in minerals other than tourmaline were measured by sputtering the sample surface using a 20 nA $^{16}O^-$ primary beam in Kohler illumination mode and extracting the sputtered ions into the mass spectrometer. The analytical spot was about 25 μm wide. A single electron multiplier was used to count $^{10}B^+$, $^{11}B^+$ and $^{28}Si^{2+}$ signals sequentially for 8, 2 and 1 s, respectively, with 50 repeat cycles comprising a single analysis. Centering of the secondary beam relative to the field aperture and centering of the reference peak mass ($^{28}Si^{2+}$) were done in an automated routine prior to each analysis. A mass resolution of 1500 (M/ ΔM) was used to avoid ^{9}BeH and ^{10}BH interference peaks. Boron isotope ratios in phengite were corrected for instrumental mass fractionation using Phe80-3 phengite (δ^{11}B = -13.5 ‰; Pabst et al., 2012). In addition, GSD1-G basalt glass, B6 obsidian, ARM-3 andesite glass and GB4 obsidian were measured to monitor drift and relative offset of phengite compared to glass standards, which was -3 ‰ using values compiled in GeoReM (Figure 6). Reproducibility of the glass standards was 0.4–0.7 ‰ (1sd) whereas reproducibility of Phe80-3 was 1.6 ‰ (1sd, n=23), which suggests some minor heterogeneity of the Phe80-3 material. In addition, muscovite 98973 was measured as a secondary standard. Two rather different bulk values exist in the literature (-8.8 ± 0.3 ‰ Dyar et al., 2001 vs -20.00 ± 0.36 ‰ Codeço et al., 2019). The origin of this discrepancy is unknown, but I note that concentration of B and several other elements are heterogeneous and different from reported values (Section 2.4), suggesting further evaluation of this material is needed. I obtained a δ^{11}B value of -20.2 ± 0.3 ‰ (1se, n=12), which closely matches the value reported by Codeço et al., 2019 from bulk MC-ICP-MS analysis. Finally, mica MVE02-8-5 and JJE01-X-3 (Martin et al., 2015) were also measured, but both minerals are extremely heterogeneous exhibiting nearly 20 ‰ variations and are therefore less suitable as calibration materials. Boron concentrations were calculated using B/Si

ratios of samples and SiO_2 contents measured by EPMA, and standardized using GSD1-G glass.

Boron isotopes in tourmaline were measured using a similar setup except for using a ca. 100 nA beam, counting times of 4, 2 and 0.5 s for ^{10}B, ^{11}B and ^{30}Si, respectively, in 20 cycles and using a single Faraday Cup detector. Spot size was ca. 25 μm. Tourmaline dravite 108796 (my value -6.7 ± 0.5 ‰, reference value -6.6 ± 0.2 ‰), elbaite 98144 (my value -11.1 ± 0.4 ‰, reference value -10.5 ± 0.4 ‰) and schorl 112566 (my value -11.7 ± 0.3 ‰, reference value -12.5 ± 0.1 ‰) were used for calibration (Dyar et al., 2001). Small average offsets of 0.7–0.9 ‰ were measured for the latter two standards compared to the first, indicating a small matrix effect. As the analysed tourmalines were close to dravite this will have negligible effect on their accuracy. Typical internal precision was 0.1 ‰ (1s), whereas repeatability of standards was 0.3–0.5 ‰. My mean tourmaline boron isotope values for each sample matched from those of Xiong et al., 2022, measured by LA-MC-ICP-MS, within 1 ‰, which is well within the range of values within each sample (Appendix A.2).

A similar setup was used for SIMS analyses of B isotopes in micas, amphiboles, pyroxenes and chlorite in Chapter 5, using a Cameca 1270 at the Edinburgh Ion Microprobe Facility, School of Geosciences, University of Edinburgh, UK. This instrument has higher ion transmission and is therefore more suitable for analysing minerals with low B contents such amphiboles and pyroxenes. Full data are given in Appendix Tables 42 and 43. Analyses used a 40 nA beam with a spot size of ca. 25 μm, and counting times of 4, 2 and 1 s for ^{10}B, ^{11}B and ^{29}Si respectively. 50 repeat cycles were used for micas with B concentrations > 10 μg/g and 100 cycles for other minerals. Boron isotope ratios were corrected for instrumental mass fractionation using Phe80-3 phengite (Pabst et al., 2012) and ms98973 muscovite (Codeço et al., 2019) for micas, amph 21664 and amph 21805 (Pabst et al., 2012) for amphiboles and srp SY347 serpentine (Clarke et al., 2020) for chlorite, since no chorite reference materials are available. Instrumental mass fractionation for anhydrous pyroxene is assumed to be zero (Clarke et al., 2020). In addition, GSD1-G basalt glass, B6 obsidian and ARM-3 andesite glass were measured to monitor drift and relative offset of minerals compared to glass standards (Figure 6). Reproducibility of the glass standards was 0.4–0.8 ‰ (1sd) whereas reproducibilities were higher for mineral standards, which suggests some minor heterogeneity of these materials (Phe80-3: 3.0 ‰ (1sd, n=13), ms98973: 1.1 ‰ (1sd, n=3), amp 21664: 2.0 ‰ (1sd, n=10), amph 21805: 0.9 ‰ (1sd, n=15), SY347: 1.7 ‰ (1sd, n=6).

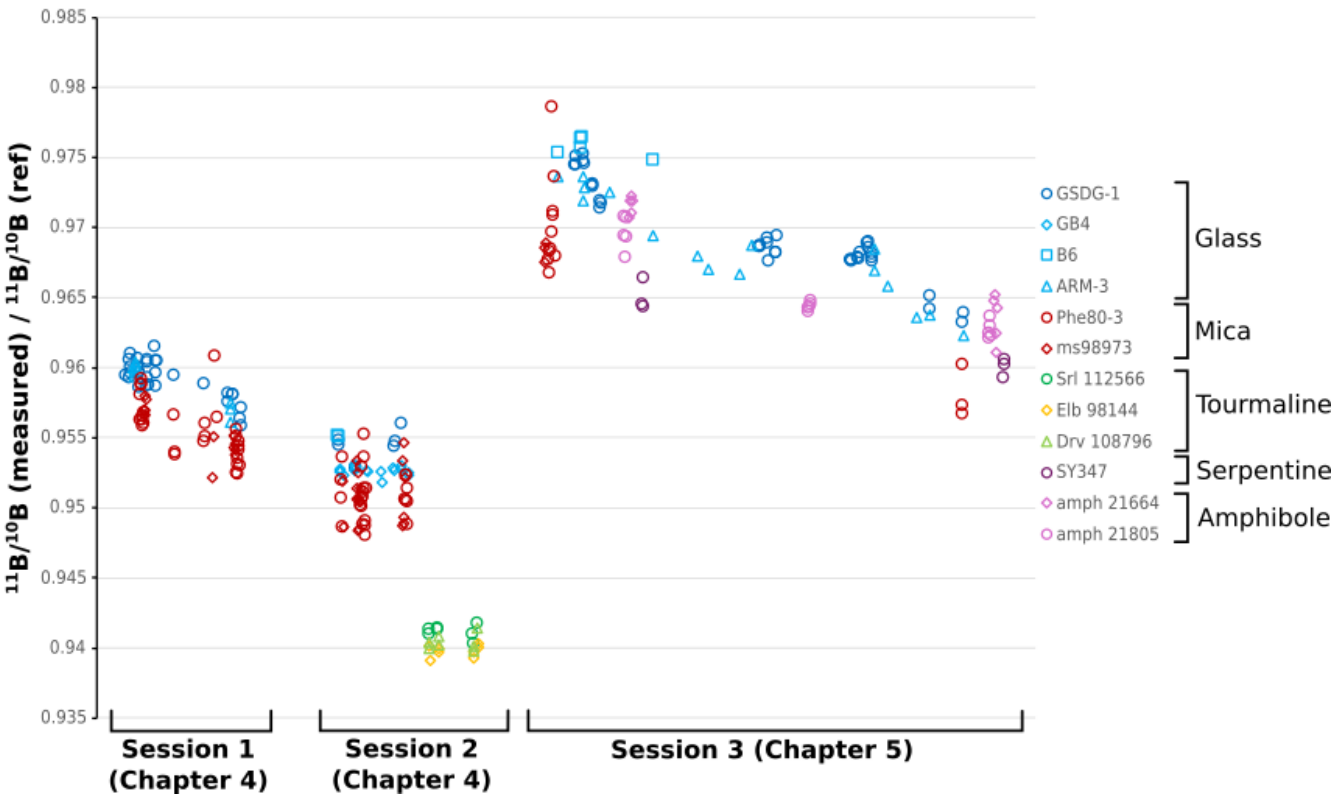


Figure 6: Comparison of measured vs. reference SIMS $^{11}B/^{10}B$ ratios for glass and mineral standards over the course of each analytical session. Differences between sessions are due to differences in the analytical conditions. Systematic drift during each analytical session was corrected for using the glass standards. The difference in instrumental mass fractionation between glasses and different minerals is visible in the offset between glass and mineral standards, and remains constant during each session.

2.6 Mineral modal abundances

Mineral modal abundances in Chapter 3 were determined by point counting 500 points on representative back scattered electron (BSE) or optical photomicrographs of each sample, using the software JMicroVision. Absolute uncertainties on mineral modes are calculated as $\sqrt{x}/x$, where x is the number of points. Only phengite, paragonite and chlorite modes were determined. These were relatively easy to assess since they are easily recognisable in either BSE images or optical photomicrographs.

In Chapter 5 I tried to get a more accurate estimate for the modal abundance of all minerals using powder X-ray diffraction (XRD). Mineral modal abundances were measured a Bruker D8 Advance XRD spectrometer at the Grant Institute, School of Geosciences, University of Edinburgh. The results were interpreted using the Bruker EVA software. Due to the complex mineralogy of the samples, the results were only semi-quantitative. The modal abundance estimates were further refined by using the mineral compositions (EDS and SIMS) to reconstruct the bulk composition (XRF). SiO_2, K_2O, Na_2O, MgO, CaO, Rb and Sr were used. Most of the selected elements were constrained to within 10% in most samples. Final modal abundances are shown in Figure 36 and listed in Appendix A.3. K_2O and Rb provide a good estimate of phengite abundance, since phengite these elements are strongly concentrated in phengite, and are also useful for constraining paragonite mode. Likewise, Sr is a good proxy for epidote. CaO, MgO, SiO_2 and Na_2O are all present in a number of phases but the ratios of elements differ between phases, which allows some differentiation. Further ground-truthing of the mineral modes was done by point counting on BSE images. Given the multi-method approach it is hard to estimate an uncertainty on the modal abundance. The largest source of error is probably the limited number of EDS/SIMS analyses of mineral compositions per sample, given that only 20-30 analyses were conducted on one thin section per sample, compared to bulk analysis on powders made from ~5 cm diameter rock samples. Average mineral compositions may therefore not be entirely representative of the sample at the hand specimen scale. This probably explains why there are some elements in some samples for which the mineral/bulk concentration comparison does not work as well (reconstructed and measured bulk concentrations differ by $> 10\%$). Calculating the mineral modes by a full inversion of all element concentrations without the use of additional constraints such as XRD and point counting does not work well, in part because some phases have similar compositions

(e.g. clinopyroxene and amphibole), and also probably because of this non-representative source of error.

3 Chapter 3: The behaviour of nitrogen during high pressure fluid-rock interaction

3.1 Preface

In this chapter I analyse a set of nine rocks from three localities, all of which have previously been interpreted to represent fragments of subducted oceanic crust. The samples were chosen because previous work has investigated the history of subduction-related fluid-rock interaction at these localities, and in some cases the specific samples that I studied. These samples therefore provide a useful opportunity to investigate the behaviour of N during fluid-rock interaction in settings where there are already constraints on the origin and timing of subduction-related fluids. I present the first SIMS data for N concentrations in minerals from HP rocks, and begin to answer questions 1 and 2 that were set out in the introduction. These questions are then further explored in Chapter 5.

This chapter was published in *Geochimica et Cosmochimica Acta* in 2022 (https://doi.org/10.1016/j.gca.2022.01.018) and is included here with minor typographic editing. The analytical methods have been removed and placed in Chapter 2 to avoid duplication across the chapters. All co-authors contributed comments during drafting, some of which were incorporated into the final text by myself.

3.2 Abstract

Understanding the Earth's geological nitrogen (N) cycle requires an understanding of how N behaves during dehydration of subducted crust. I present the first *in situ* measurements of N in silicate minerals by secondary ion mass spectrometry, focusing on high pressure rocks representing subducted oceanic crust. I investigate the distribution of N between mineral phases, and combine analyses of N with other trace and major elements in order to constrain the behaviour of N during fluid-rock interaction. The data confirm that white mica (phengite, paragonite) is the primary host for N, containing up to 320 µg/g, whereas minerals including clinopyroxene, amphibole and epidote contain < 5 µg/g N. Chlorite can also contain N (up to 83 µg/g) and may play a previously unrecognised role in subduction zone N cycling. Bulk rock N concentrations estimated from mineral N concentrations and

mineral modes are consistent with N concentrations measured by bulk combustion, which confirms that most N is hosted within silicate minerals and not along grain boundaries or in fluid inclusions. Bulk rock N contents correlate with K_2O ($N/K_2O = 19.3 \pm 2.0$). Using N/K_2O ratios and the average K_2O of altered oceanic crust, the flux of N subducted in oceanic crust is estimated to be $0.6 - 2.4 \times 10^{11}$ g/yr, which is consistent with but at the lower end of previous estimates. The data were also used to investigate the behaviour of N during fluid-rock interaction. Open system fluid-rock interaction modelling was used to model the evolution of N, B and Li contents during fluid-rock interaction in phengite from a garnet-phengite quartzite. By comparison to data for B and Li, the phengite-fluid partition coefficient for N was estimated to be 0.1–1.5. Separately, the growth of paragonite during fluid-rock interaction in a blueschist was shown to sequester N from phengite and limit bulk N loss to the fluid. The stability of white mica during fluid-rock interaction is therefore critical in controlling the behaviour of N. Nitrogen addition from sediment-derived fluids appears to be an important process in subduction zone rocks. Mafic crust can act as a sink for this N if white mica is stable. This work provides the first natural constraints on the fluid-mineral partitioning behaviour of N at subduction zone conditions and emphasises the complexity of N mobility within subduction zones, with redistribution between different phases and lithologies being important.

3.3 Introduction

The Earth's atmosphere is presently composed of 78% nitrogen and is essential for the habitability of the planet. There is considerable debate over the long-term evolution of the mass of N in the atmosphere (e.g. Avice et al., 2018; Barry and Hilton, 2016; Berner, 2006; Busigny et al., 2011; Mallik et al., 2018; Marty et al., 2013; Som et al., 2016, 2012; Wordsworth, 2016) and it is therefore necessary to quantify the flux of N between the surface and deep-seated reservoirs, primarily the mantle. Subduction zones are the primary locations where N from the Earth's surface is returned to the mantle, and therefore studies which explore the behaviour of N during subduction are of importance to resolving the long-term N cycle. Previous studies of N in subduction-related rocks have focused on whole rock analyses, with a particular focus on N isotopic work (e.g. Bebout et al., 2013; Busigny et al., 2011, 2003a; Epstein et al., 2021; Halama et al., 2014, 2010, 2017). Suites of subducted metasediments have shown little N loss up to 90 km depth in cold subduction zones

(Bebout et al., 2013; Busigny et al., 2003a), but substantial losses in warm subduction zones (Bebout and Fogel, 1992; Haendel et al., 1986; Mingram and Bräuer, 2001), with differing implications for the recycling of N over Earth's history. Basalts and gabbros representing oceanic crust (~1–30 µg/g N) have lower N contents than sediments (~100–2000 µg/g N) but the mass of subducted oceanic crust is an order of magnitude higher than of sediments. Considering average values for oceanic crust and sediment N concentrations, their contributions to the subducted N flux are comparable, although oceanic crust is less well constrained (Busigny et al., 2011; Halama et al., 2010; Li et al., 2007). Overall uncertainty in the global N recycling flux is on the order of 50–100% (Johnson and Goldblatt, 2015) due to the variable N contents of subducted lithologies and the lack of understanding of the processes controlling N recycling.

Nitrogen in rocks is primarily hosted as ammonium (NH_4^+), which substitutes for potassium and, to a lesser extent, sodium and calcium (Honma and Itihara, 1981). Micas are the dominant host of K in metasediments, and correlations between bulk K and N contents have been used to confirm that white micas are the main host for N (e.g. Bebout et al., 2013; Busigny et al., 2003a). High N contents of up to 1700 µg/g have been measured in micas from metasediments (Busigny et al., 2003b, 2004; Sadofsky and Bebout, 2000). For metabasic rocks that contain white mica, correlated bulk N, Cs and Ba concentrations also suggested that N resides in the mica (Halama et al., 2010). However, a weak correlation of N with $CaO + Na_2O$ in mica-free metabasic rocks may suggest that in these lithologies, N is hosted in Ca- and Na-bearing minerals (Busigny et al., 2011).

Nitrogen is regarded as a moderately fluid-mobile element. Several studies on rocks that have undergone extensive fluid-rock interaction have shown up to 60% loss of bulk N in metasomatised rocks compared to the country rock, in response to white mica dissolution or recrystallization during fluid-rock interaction (Epstein et al., 2021; Halama et al., 2017). Experimental data on fluid-mineral partition coefficients for N at subduction zone pressure-temperature conditions are sparse and values are not consistent between studies (Table 5, Förster et al. (2019), Jackson et al. (2021), Li et al. (2015), and Pöter et al. (2004)). There is agreement between these studies that increasing pressure leads to NH_4^+ becoming more compatible in both phengite and biotite, compared to an aqueous fluid, because NH_4^+ is thermodynamically favoured over N_2 at higher pressures (Förster et al., 2019; Jackson et al., 2021; Pöter et al., 2004). The effect of temperature is smaller but increasing temperature leads to

NH_4^+ becoming more compatible in phengite, compared to an aqueous fluid (Förster et al., 2019; Pöter et al., 2004), and less compatible in biotite (Förster et al., 2019; Jackson et al., 2021). The reasons for this are not fully understood. NH_4^+ is, overall, more compatible in biotite than muscovite over a wide range of P-T conditions, with values for $D_{NH_4^+}^{biotite-muscovite}$ from 1.5–4.2 (Busigny et al., 2004; Duit et al., 1986; Förster et al., 2019; Honma and Itihara, 1981; Pöter et al., 2004; Sadofsky and Bebout, 2000).

In situ data can provide new constraints on the partitioning of N between different minerals, reveal heterogeneities or zoning, and can be combined with thermodynamic and geochemical modelling to understand the behaviour of N during metamorphism and fluid-rock interaction. Previous *in situ* analyses of N contents were limited to a small number of measurements of large white mica and biotite grains in metasediments by Fourier transform infrared spectroscopy with a 100 µm beam size (Busigny et al., 2003a,b, 2004). Few studies have compared N contents of minerals to other major or trace elements, or to textural features of the samples. *In situ* analyses of other fluid-mobile elements (e.g. B, F, Cl, LILE) in subduction-related samples have been successful in constraining the inter-mineral partitioning behaviour of these elements, understanding their behaviour during metamorphic reactions and fluid-rock interaction, and constraining the amount of recycling of these elements into the mantle during subduction (e.g. Bebout et al., 2007; Clarke et al., 2020; De Hoog et al., 2014; Debret et al., 2016; Halama et al., 2020; Marschall et al., 2006a; Urann et al., 2020). In this study I aim to: 1) explore the residency of N in different minerals in a suite of high pressure rocks representing subducted oceanic crust; 2) combine *in situ* measurements of N concentrations with other trace and major elements to explore the behaviour of N during metamorphic fluid-rock interaction. Improved D values and mineral residency of N will allow more detailed modeling of N behaviour during subduction and eventually more accurate models of the long-term global N cycle in deep time.

3.4 Geological background and sample descriptions

3.4.1 Lago di Cignana, Italy

At Lago di Cignana, NW Italy, meta-ophiolites of the Zermatt-Saas Zone (ZSZ) are tectonically juxtaposed with a coesite- and diamond-bearing UHP metamorphic unit, the Lago di Cignana Unit (LCU) (Groppo et al., 2009). The LCU comprises eclogites, alongside metasediments including impure marbles and quartzites, and calcschists. Peak metamorphism of the LCU ocurred at ~600 °C, 2.7–3.2 GPa (Groppo et al., 2009; Reinecke, 1998), and was dated to 44 Ma by zircon U-Pb (Rubatto et al., 1998). The ZSZ comprises mantle serpentinites and eclogitic gabbros, which experienced a similar P-T-t history to the LCU (Groppo et al., 2009). REE patterns of eclogites from both the LCU and ZSZ indicate a MORB protolith (Dal Piaz et al., 1981; Halama et al., 2010).

The samples from Lago di Cignana have been described previously (Halama et al., 2020) but a brief description is reproduced here.

LC-3 is a garnet-phengite-quartzite (metachert) containing garnet, phengite and quartz as major phases, and accessory amphibole, biotite, rutile and opaques (Figure 7b). Garnet is euhedral, 100–500 μm in diameter and zoned, with Mn and Mg-enriched cores and Fe and Ca-enriched rims. Phengite occurs as 300–1500 μm flakes, which are preferentially aligned to define a weak foliation.

LC-1b is an eclogite containing garnet, omphacite, blue amphibole, epidote, paragonite and quartz. Paragonite occurs as needles, which are sometimes associated with rhombic pseudomorphs after lawsonite, formed during early retrograde decompression (Groppo et al., 2009).

LC-2a is a metagabbro. Omphacite, phengite, epidote, albite and chlorite are major phases, with accessory amphibole, titanite and rutile. This sample has been interpreted as showing pervasive retrogression into the greenschist-facies from a former high-pressure assemblage.

3.4.2 Raspas Complex, Ecuador

The Raspas Complex in southwest Ecuador exposes an high pressure terrane representing formerly subducted oceanic lithosphere (Arculus et al., 1999; Feininger, 1980). It includes eclogites and blueschists of the Raspas Formation, which occur alongside garnet-chloritoid-kyanite metapelites. All three lithologies record similar peak pressure-temperature conditions of 550–600 °C, 1.5–2 GPa

(Gabriele et al., 2003; John et al., 2010). The age of metamorphism was dated to ~130 Ma, using Lu-Hf methods (John et al., 2010). Lithological differences between the blueschists and eclogites are ascribed to differences in bulk composition, with the blueschists being enriched in K_2O and Al_2O_3, and depleted in CaO, MgO and FeO. Geochemical analysis of the eclogites suggests that their protoliths were typical mid-ocean-ridge-basalts (MORB), with LREE-depleted REE patterns. Blueschists show LREE-enrichment, which has been interpreted as evidence of a seamount-type protolith (John et al., 2010). The samples from the Raspas Complex have not been described individually, but descriptions of each lithology are given in John et al., 2010.

SEC16-1 is a blueschist containing garnet, Na-amphibole, phengite, paragonite, epidote, apatite, and calcium carbonate, with accessory chlorite (Figure 7a). Garnets (500–1500 μm) preserve an original euhedral outline but are sometimes corroded at the rims. A strong foliation is defined by preferential alignment of Na-amphibole, epidote, phengite and paragonite in the matrix. Epidote occurs also as elongate inclusions in garnet, which are aligned with the external foliation. Some apatite grains are elongate and aligned with the foliation. Chlorite occurs along fractures in garnet and at corroded rims.

SEC44-1 is an eclogite containing garnet, omphacite, phengite and quartz as major phases, and accessory Na-amphibole, rutile and apatite. Subhedral to euhedral garnets (100–600 μm) cluster in garnet-rich (up to 50 %) layers up to 3 mm thick. The matrix consists of subhedral omphacite and rutile, randomly oriented phengite flakes, which are often rectangular, and interstitial quartz. Intergrowths of lobate quartz with Na-amphibole occur in low abundance, usually in proximity to garnet.

SEC47-1 is an eclogite containing garnet, omphacite, phengite, quartz, Na-amphibole and epidote as major phases, with accessory rutile (Figure 7c). Subhedral to euhedral garnet (50–400 μm) occurs in garnet-rich (up to 80 %) layers up to 4 mm thick. Preferential alignment of epidote, Na-amphibole, omphacite and phengite define a weak foliation, which is sub-parallel to the garnet layering. Quartz and rutile also occur in the matrix.

3.4.3 Jenner, California

Eclogite and blueschist blocks at Jenner, California, occur as part of the Franciscan Complex, a subducted-related melange complex in NW California. Samples were collected just north of the mouth of the Russian River about 1.5 km west of Jenner. These blocks occur loose on the beach, or within a sandstone-shale-rich matrix, which is interpreted a a recent landslide deposit (Raymond, 2017). The presence of Mg-rich metasomatic rinds, and geochemical signatures within the blocks, have been used to infer a former serpentinite melange host (Errico et al., 2013). Enrichment in large ion lithophile elements (LILE) and low ϵ_{Nd} and δ^7Li values in some blocks has been used to infer an additional sediment-derived fluid source (Penniston-Dorland et al., 2010; Sorensen et al., 1997). Peak metamorphic assemblages in eclogite and blueschist facies are identified in the least retrograded samples and record conditions of ~450–500 °C, 1–1.5 GPa (Krogh et al., 1994). Prograde to peak garnet growth was dated to c. 158 Ma using Lu-Hf methods (Anczkiewicz et al., 2004). Many samples are retrograded to a lower temperature assemblage (~400 °C, 1 GPa), along a counterclockwise P-T path, which is attributed to secular cooling of the subduction zone. Whole rock major element and immobile trace element compositions are similar to MORB (Penniston-Dorland et al., 2010; Sorensen et al., 1997).

JEN12-03 is a blueschist containing garnet, Na-amphibole, omphacite, phengite, titanite, chlorite and quartz, with accessory iron oxides (Figure 7d). Three textural domains are identified. Rare omphacite-rich domains suggest a former eclogite facies assemblage. Large domains comprise a matrix of glaucophane, titanite, phengite, quartz and minor chlorite, with garnet occurring as porphyroblasts (up to 700 μm diameter). Garnets preserve an original euhedral outline but are corroded around the rims. A third domain is dominated by phengite flakes and fine grained chlorite. In all domains phengite occurs mostly as randomly oriented laths. Around 5 % of the phengite comprises rectangular to rhomboid grains, which are zoned in back scattered electron images.

JEN12-07 is a blueschist containing garnet, Na-amphibole, phengite, epidote and titanite, with accessory Fe-sulphides, apatite, quartz and chlorite. The matrix consists of aligned Na-amphibole, epidote, titanite and phengite, which define a foliation. Phengite also occurs as large (up to 500 µm) randomly oriented laths. Garnet occurs as 1–2.5 mm porphyroblasts with inclusions of Na-

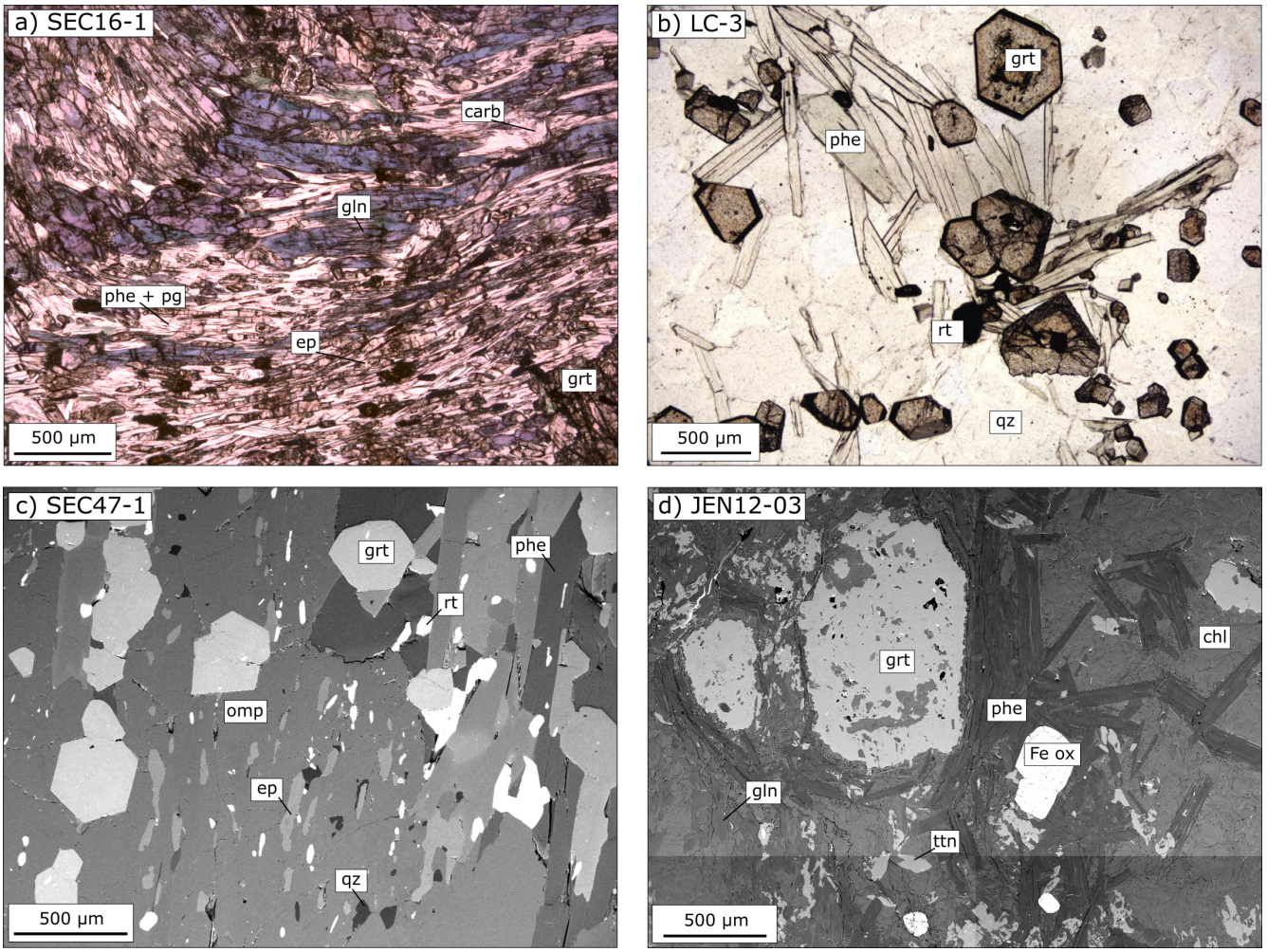


Figure 7: (a) Representative photomicrograph in plane polarised light of blueschist SEC16-1. (b) Representative photomicrograph in plane polarised light of garnet-phengite quartzite LC-3. (c) Representative back scattered electron image of eclogite SEC47-1. (d) Representative back scattered electron image of blueschist JEN12-03.

amphibole, epidote, titanite, quartz and chlorite, which preserve a foliation that is rotated relative to the external foliation.

JEN12-09 is an eclogite containing garnet, omphacite, phengite, epidote and titanite, with accessory chlorite, rutile, and quartz. The matrix consists of omphacite, phengite, epidote and titanite. Garnet occurs as 0.5–3 mm subhedral to euhedral porphyroblasts, containing inlcusions of omphacite, phengite, quartz and rutile. Chlorite occurs only on the rims of garnets. Phengite also occurs as up to 500 µm long grains in a 2 mm thick vein.

3.5 Analytical methods

The analytical methods are detailed in Chapter 2.

3.6 Results

3.6.1 Major element mineral chemistry and N, B, Li concentrations in white mica

3.6.1.1 Lago di Cignana

Garnet-phengite quartzite sample LC-3 contains phengite with Si contents from 6.85–7.00 p.f.u. and Na/(Na+K) from 0.02–0.06 (Figure 8). There is a strong negative correlation between Si p.f.u. and Na/(Na+K). Nitrogen contents occupy a narrow range from 10–21 µg/g, whilst B contents vary widely (85–329 µg/g). Lithium contents vary from 39–62 µg/g. Despite the wide range in B contents, there is no clear trend in [N] versus [B]. Lithium contents show an overall negative correlation with [B], and positive correlation with [N] (Figure 12).

Metagabbro sample LC-2a contains two populations of phengite with different major element chemistry (Figure 8). Six grains had Si contents from 6.67–6.77 p.f.u. and Na/(Na+K) = 0.10-0.12. Two grains had higher Si contents (6.84–7.03) and Na/(Na+K) = 0.04–0.12. The low Si population has [N] from 66–123 µg/g, [B] from 25-36 µg/g and [Li] from 55–64 µg/g. The high Si population has lower [N] (20–24 µg/g), higher [B] (48–49 µg/g) and lower [Li] (41–47 µg/g).

Eclogite sample LC-1b contains paragonite with a narrow range of Si contents (6.06–6.10 p.f.u.) and Na/(Na+K) = 0.94–0.97 (Figure 8). There is a negative correlation between Si p.f.u. and Na/(Na+K). Nitrogen contents vary from 15–47 µg/g, [B] from 13-24 µg/g and [Li] from 5-11 µg/g. There are no correlations between major and trace element concentrations.

3.6.1.2 Raspas

Eclogite sample SEC44-1 contains phengite with Si content ranging from 6.49–6.79 p.f.u., and Na/(Na+K) from 0.11–0.14 (Figure 8). Phengite grains are not zoned in major element chemistry. Nitrogen contents range from 147–244 µg/g and are not correlated with variations in major element chemistry. Boron contents range from 38–81 µg/g and Li contents from 19–48 µg/g. There

is a positive correlation between [N] and [B] with average [N]/[B] ~3.2 (Figure 9).

Eclogite sample SEC47-1 contains phengite with a narrow range of Si contents from 6.51–6.60 p.f.u., and Na/(Na+K) from 0.12–0.15 (Figure 8). Phengite grains are not zoned in major element chemistry. Nitrogen contents range from 37–83 µg/g, so are considerably lower than in sample SEC44-1. Boron contents vary from 50–77 µg/g and Li contents from 38–49 µg/g. Phengite grains show no significant intra-grain variation in [Li], [B] or [N]. There are no correlations between major and trace element concentrations.

Blueschist sample SEC16-1 contains phengite as well as paragonite. Phengite has Si contents from 6.64–6.80 p.f.u. and Na/(Na+K) from 0.06–0.14 (Figure 8). There is a negative correlation between Si content and Na/(Na+K). Phengite grains are not zoned in major element chemistry. N contents range from 117–243 µg/g, B contents from 30–92 µg/g and Li contents from 31–43 µg/g. There is a positive correlation between Si p.f.u. and [N], and Si p.f.u. and [B], and a negative correlation between Si p.f.u. and [Li]. Paragonite has Si = 5.98–6.00 p.f.u. and Na/(Na+K) = 0.92–0.96. Paragonite N contents range from 31–78 µg/g, [B] from 112–139 µg/g, and [Li] from 24–28 µg/g. One exceptional grain has higher Si p.f.u. and lower Na/(Na+K) than other paragonites, with Si = 6.11 p.f.u. and Na/(Na+K) = 0.76, but unexceptional trace element contents. There are no correlations between major and trace element concentrations in paragonite.

3.6.1.3 Jenner

Sample JEN12-03 contains phengite with a large range of Si contents from 6.61–7.00 p.f.u. Most grains have Na/(Na+K) from 0.01–0.03 and show no correlation between Na/(Na+K) and Si p.f.u. (Figure 8). Three low Si grains have much higher Na/(Na+K) from 0.09–0.11 and show a negative correlation between Na/(Na+K) and Si p.f.u.. Nitrogen contents range from 108–270 µg/g, [B] from 42–96 µg/g and [Li] from 13–33 µg/g. There are no correlations between trace and major element concentrations.

Sample JEN12-07 contains phengite with a large range of Si contents from 6.66–7.06 p.f.u. and Na/(Na+K) = 0.02–0.09 (Figure 8). There is a negative correlation between Si p.f.u. and Na/(Na+K). Nitrogen contents vary from 155–320 µg/g and are uncorrelated with Si p.f.u. Boron contents vary from 33–61 µg/g and [Li] from 6–38 µg/g. There is a positive correlation between [B]

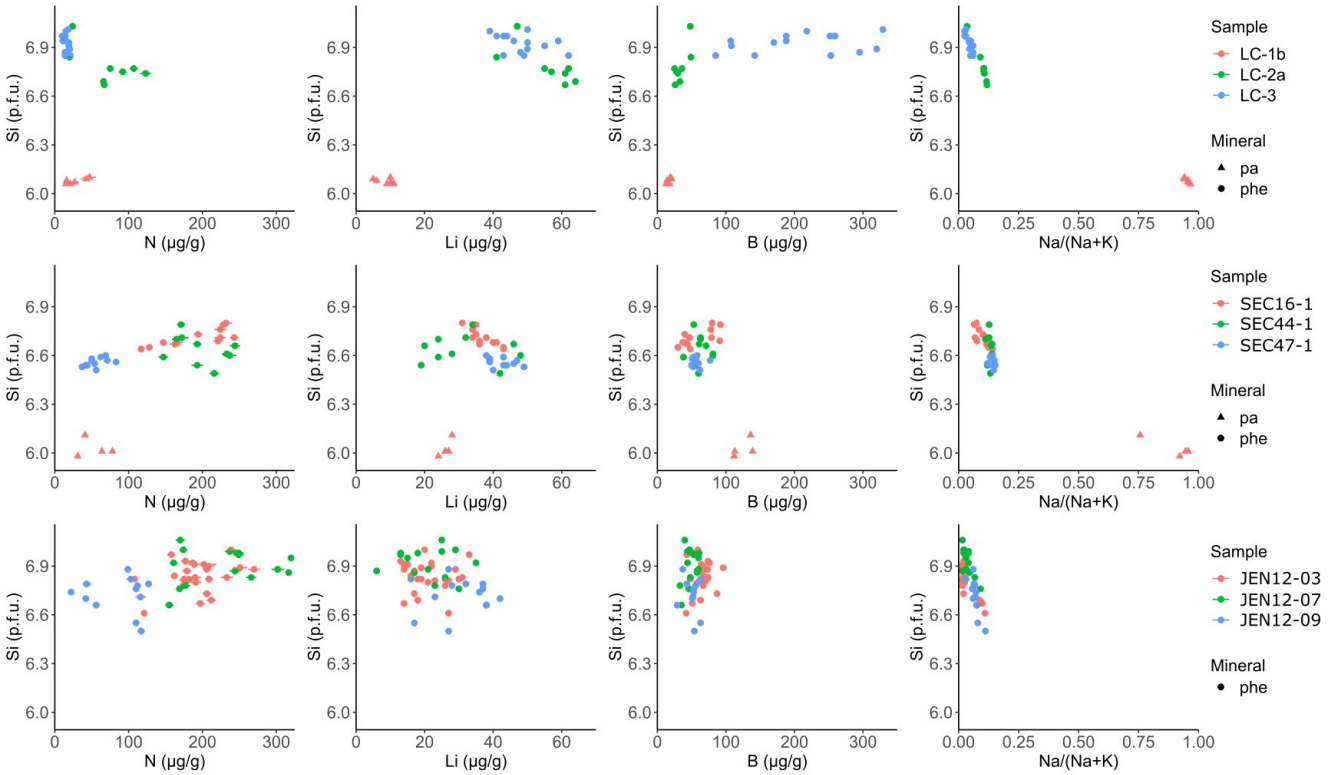


Figure 8: N, Li, B, Na/Na+K data vs Si p.f.u. for phengite and paragonite from each locality (top: Cignana, middle Raspas, bottom Jenner). 1s error bars are plotted. Where error bars are not shown, they are smaller than the size of the symbol.

and [N] with average [N]/[B] ~4.5 (Figure 9).

Sample JEN12-09 contains phengite with a large range of Si contents from 6.50–6.88 p.f.u., Na/(Na+K) from 0.03–0.11, and a negative correlation between Si p.f.u. and Na/(Na+K) (Figure 8). Nitrogen contents vary from 22–127 µg/g, [B] from 29–64 µg/g, and [Li] from 16–42 µg/g. There are no correlations between trace and major element concentrations.

3.6.2 N, B, Li concentrations in other minerals

Clinopyroxene, amphibole, epidote, titanite and garnet contain <5 µg/g N and B in all samples (see Appendix A.1). Garnet, epidote and titanite also contain <5 µg/g Li. Clinopyroxene and amphibole are significant hosts of Li varying from 46–142 µg/g in clinopyroxene, and 6–71 µg/g in amphibole. The N content of chlorite is variable between different samples. Chlorite which occurs in cracks and on the rims of garnet contains no detectable N, K or Na (JEN12-07, JEN12-09, SEC16-1, LC-2a). Chlorite which occurs in the matrix of sample JEN12-03 contains 10-83 µg/g N and minor amounts

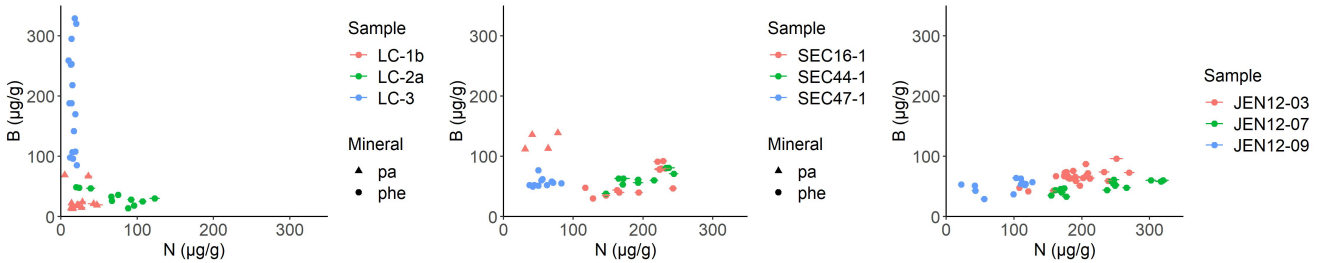


Figure 9: N vs B for phengite and paragonite from each locality (left: Cignana, middle Raspas, right Jenner). 1s error bars are plotted. Where error bars are not shown they are smaller than the size of the symbol.

of K (up to 0.32 wt%) and Na (up to 0.13 wt%). Coexisting phengite contains 108–270 µg/g N. Chlorite in all samples contains <5 µg/g B, and 29–140 µg/g Li but neither varies systematically with textural setting like N.

3.6.3 Bulk nitrogen contents

Bulk N contents of each sample were calculated to assess the variability of N contents in different protoliths (Table 3). For each sample, I combine the mean N concentration in each N-bearing phase with the modal abundance of that phase, and use a weighted average to calculate the bulk N concentration. The standard errors on mean mineral N concentrations are larger than the analytical uncertainty for all samples except LC-3, which indicates that variation in N concentrations is due to heterogeneity between grains, rather than analytical uncertainty. Mineral modes were estimated by point counting 500 points on representative back scattered electron or optical photomicrographs of each sample, using the software JMicroVision. Absolute uncertainties on mineral modes are calculated as $\sqrt{x}/x$, where x is the number of points. Bulk N contents range from 1.2–71 µg/g. Standard errors on mineral modes and N concentrations were propagated to calculate the uncertainty in bulk N contents.

3.7 Discussion

3.7.1 Residency of nitrogen and implications for global nitrogen recycling

Nitrogen typically occurs as NH_4^+ in crustal rocks, where it substitutes for K^+ in K-bearing minerals such as micas, and to a lesser extent for Na^+ and Ca^{2+} in minerals such as plagioclase (Honma and

Sample	LC-3	LC-2a	LC-1b	SEC16-1	SEC44-1
Lithology	Gt-phe quartzite	Metagabbro	Eclogite	Blueschist	Eclogite
Phe mode (vol%)	33	5		16	8
Phe N (µg/g)	10–21 (16)	20–123 (72)		117–243 (190)	147–234 (203)
Pa mode			5	16	
Pa N			5.5–47 (24)	31–78 (54)	
Chl mode		<1		<1	
Chl N		1.2–4.9 (3.6)		1.0–2.8 (2.1)	
Calculated bulk N	5.1	3.6	1.2	39	16
1s	±0.5	±0.9	±0.3	±4	±3
Measured bulk N				46	10
Sample	SEC47-1	JEN12-03	JEN12-07	JEN12-09	
Lithology	Eclogite	Blueschist	Blueschist	Eclogite	
Phe mode (vol%)	10	30	25	15	
Phe N (µg/g)	37–118 (61)	108–270 (193)	155–320 (229)	22–127 (88)	
Pa mode					
Pa N					
Chl mode		30		<1	
Chl N		10–83 (45)		0.0–9.2 (2.9)	
Calculated bulk N	5.6	71	57	13	
1s	±0.9	±10	±6	±2	
Measured bulk N	7.2				

Table 3: Mineral modes and N concentrations, and calculated bulk N contents for the nine samples in this study. N contents are given as a range followed by the mean in brackets. Three samples have measured bulk N contents (Halama et al., 2010), which are consistent with the calculated results. The procedure for calculating 1s uncertainties is described in Section 3.6.3 and the full data set is provided in Appendix A.1.

Itihara, 1981). White mica is the dominant K-bearing phase in most high pressure metabasaltic and metapelitic rocks up to ~9.5 GPa, 750–1000°C (Domanik and Holloway, 1996; Poli and Schmidt, 2002). Previous studies have used correlations between bulk K_2O and N contents to identify white micas as the main host for N (e.g. Bebout et al., 2013; Busigny et al., 2003a) in these rocks. Halama et al. (2010) reported bulk N concentrations for the three Raspas samples in this study. These values are consistent with my estimated bulk concentrations based on mineral modes (Table 3), which confirms that most N is hosted within the analysed minerals and not along grain boundaries or in fluid inclusions. Most samples contain a single white mica phase (phengite or paragonite), which is the dominant N-bearing phase in the sample. Sample SEC16-1 contains coexisting phengite (117–243 µg/g N) and paragonite (31–118 µg/g N), where N is preferentially partitioned into phengite. This is consistent with the large ionic radius of NH_4^+ (1.67 Å), which is closer to that of K^+ (1.64 Å) than Na^+ (1.39 Å) (Shannon, 1976; Sidey, 2016), and with previous data on the N partitioning between Na- and K-bearing minerals (Honma and Itihara, 1981). Nitrogen content of white micas is

	Li	B	N	n
SEC44-1				
Phe	19–48 (32)	38–81 (63)	147–244 (197)	10
Cpx	94–110 (104)	2.3–3.3 (2.9)	1.8–3.0 (2.4)	4
$D^{phe/cpx}$	0.31	22	81	
SEC47-1				
Phe	38–83 (46)	50–100 (61)	37–118 (61)	11
Cpx	142	3.0	3.0	1
Ep			1–2 (1.1)	2
$D^{phe/cpx}$	0.32	18	22	
$D^{phe/ep}$			55	
SEC16-1				
Phe	31–46 (37)	30–92 (59)	117–243 (190)	14
Pa	24–28 (26)	93–139 (119)	31–118 (66)	4
Gl	132–169 (151)	3.9–4.9 (4.4)	3.9–4.4 (4.1)	2
$D^{phe/pg}$	1.5	0.49	2.9	
$D^{phe/gl}$	0.25	13	46	
JEN12-09				
Phe	16–42 (30)	29–64 (51)	22–127 (88)	12
Cpx	46–55 (51)	1.2–1.3 (1.3)	1.5–1.9 (1.7)	2
$D^{phe/cpx}$	0.60	41	52	

Table 4: Inter-mineral partition coefficients for Li, B and N. Mineral compositions are given in µg/g as a range with a mean value in brackets. The number of analyses (n) is also listed. Partition coefficients are calculated from the mean values.

uncorrelated with Na/(Na+K) in most samples, which suggests that small variations in white mica Na/(Na+K) ratio do not exert a strong control on N partitioning behaviour.

My data suggest that white mica hosts >90% of the total N in all but two samples (LC-1b and JEN12-03). Omphacite, glaucophane/barroisite and epidote contain <5 µg/g N in all samples. Omphacite and/or glaucophane are the next most significant N hosts after mica due to their large modal abundance in most samples. Calculated inter-mineral partition coefficients for B and Li (Table 4) are similar to previously published values (Marschall et al., 2006a), which indicates that my values represent equilibrium partitioning and that my samples therefore can be used to investigate N partitioning. Partitioning values for N are variable between samples, due to the high N variability in phengite and the low N concentration in other minerals, but broadly indicate that N partitions strongly into phengite compared to other phases. Bulk K content controls white mica mode in metabasic rocks, and since N strongly partitions into white mica over other phases, the K content will

exert a strong control on the N budget of subducted oceanic crust. Figure 10 shows that reconstructed bulk K and N contents for mafic samples fall on a positive trend, with average N (µg/g)/K_2O (wt%) = 19.3 ± 2.0. The metachert sample LC-3 plots as an outlier. N/K_2O for subducted mafic rocks is an order of magnitude lower than for metasedimentary rocks (N/K_2O ~200, Busigny et al. (2003a)). My samples are representative of the basaltic upper oceanic crust, which has undergone hydrothermal alteration on the seafloor and subsequently been subducted. Using N/K_2O I can estimate the flux of N subducted in upper oceanic crust from the K_2O content and the mass of crust subducted each year (2×10^{16} g/yr, Peacock (1990)). If I assume all basaltic crust has a MORB-like K_2O content (0.16 wt% K_2O, Gale et al. (2013)), I calculate a flux of $6.2 \pm 0.6 \times 10^{10}$ g/yr using my average N/K_2O value of 19.3 ± 2.0. For average altered oceanic crust (AOC, 0.62 wt% K_2O, Kelley et al. (2003)) I calculate $2.4 \pm 0.2 \times 10^{11}$ g/yr. Busigny et al. (2011) calculated a N flux of 1.3×10^{11} g/yr for upper oceanic crust, based on the average N content of metabasalts, which is similar to my value assuming AOC but larger than my value assuming MORB-like crust. All my estimates are somewhat smaller than the flux attributed to subducted sediments (7.4×10^{11} g/yr, Busigny et al. (2003a)).

The only non-mica mineral with significant N is chlorite, for which N contents vary with textural setting. Chlorite forming rims around garnet contains very low [N] (typically <5 µg/g). This is consistent with it forming from retrograde breakdown of garnet, which contains <1 µg/g N. Chlorite which occurs in the matrix alongside N-rich phengite contains 10-83 µg/g N (sample JEN12-03). Chlorite from JEN12-03 also contains minor amounts of K + Na (Figure 11). Incorporation of minor K and Na in chlorite crystals by interlayering of chlorite and K-bearing phyllosilicates at the nanometre scale has been investigated in diagenesis and sub-greenschist facies metamorphism of mudstones and volcaniclastic sediments (Ahn et al., 1988; Lee et al., 1984). It is possible that this mechanism is partially responsible for incorporation of K, Na and N in my chlorites, but N/K_2O is much higher in chlorite than in co-existing phengite (chl: 370, phe: 18), which suggests excess N in the chlorite structure itself. Chlorite is structurally similar to the K and Na-bearing micas, with both minerals containing large interlayer cation sites. In micas these are filled by K^+ and Na^+ cations, whereas in chlorite they are vacant. A possible substitution reaction for N incorporation into chlorite is $NH_3\,(\text{fluid}) + OH^- \longrightarrow {NH_4}^+ + {O^{2-}}$, where ${NH_4}^+$ is incorporated in the vacant interlayer sites.

Chlorite is common in greenschist facies rocks across a wide range of bulk compositions and

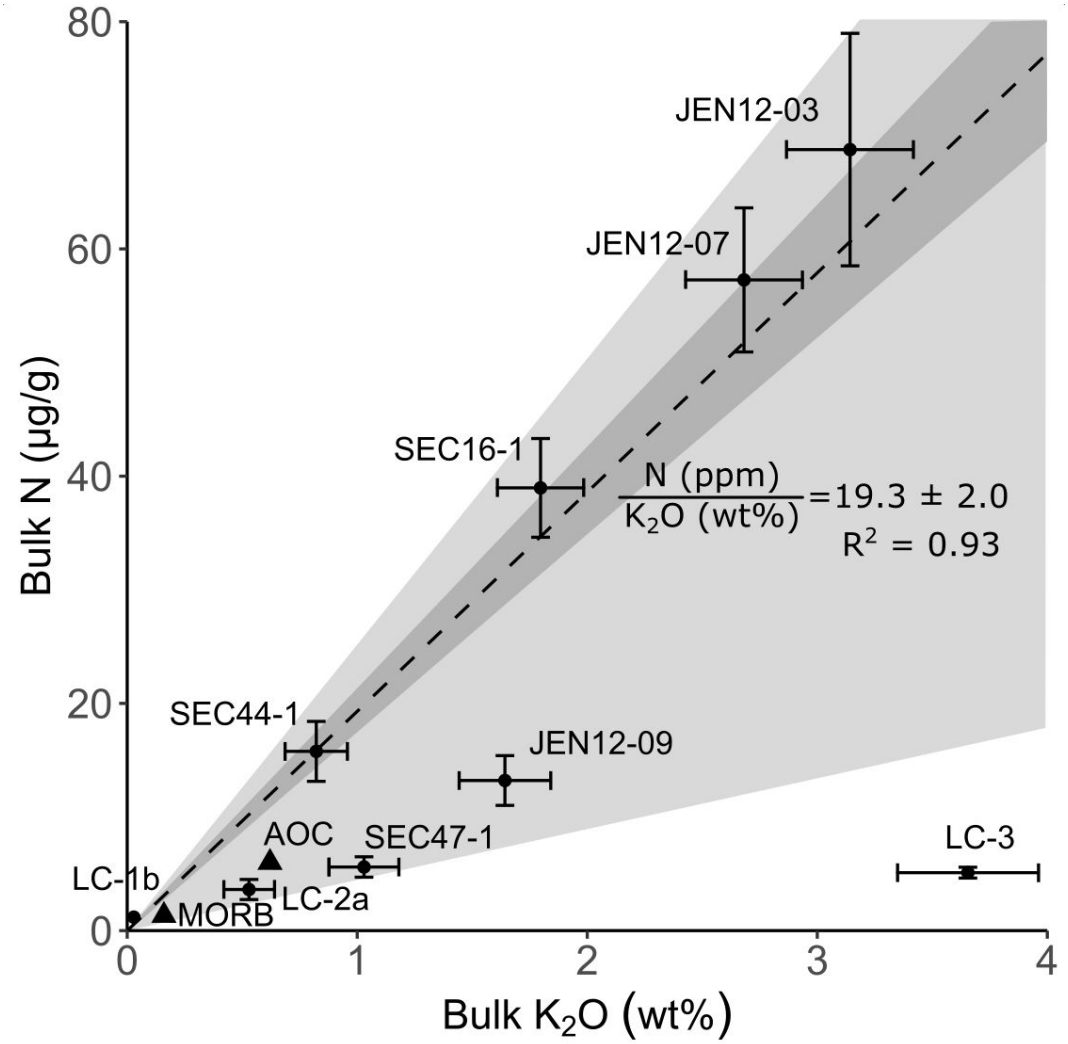


Figure 10: Calculated bulk K_2O and N contents for each sample. Average values for MORB and AOC (black triangles) are shown for comparison (Gale et al., 2013; Johnson and Goldblatt, 2015; Kelley et al., 2003). The average N/K_2O (excluding sample LC-3) is plotted as a dashed line with 1s uncertainty (dark grey). Upper and lower bounds are plotted in light grey.

therefore could potentially play an important role in subduction zone N cycling. However, it has received little previous attention as a possible host for N. Low-grade pelitic schists from the Erzgebirge massif displayed weak correlations between either chlorite or white mica mode and bulk N content, but a strong correlation between chlorite + white mica mode and bulk N content (Mingram and Bräuer, 2001), which supports chlorite being an important host for N. Chlorite also occurs in chlorite harzburgites, formed during serpentinite dehydration. Serpentinites typically have bulk N concentrations <5 µg/g (Halama et al., 2014; Philippot et al., 2007), but one chlorite harzburgite studied by Halama et al. (2014) has elevated N contents (~20 µg/g), which may be consistent with

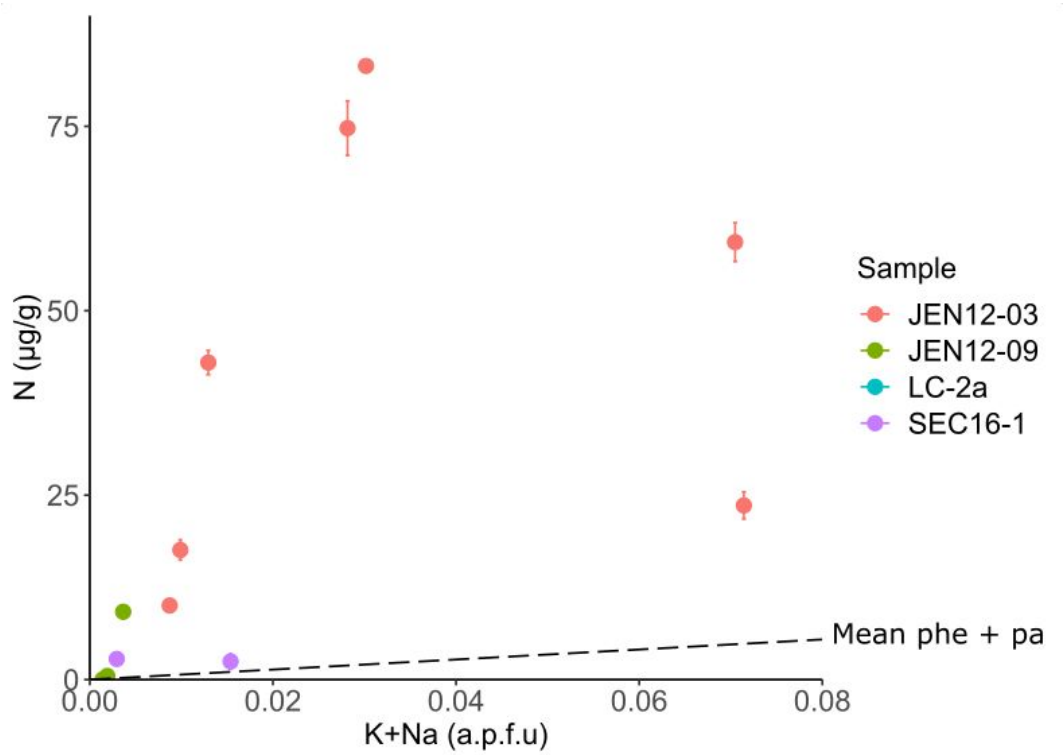


Figure 11: N versus K+Na plot for chlorite. Chlorites from sample JEN12-03 occur in the matrix alongside phengite, and have elevated K+Na and N contents. Chlorites from other samples occur as rims on garnets and contain little N, K or Na. A line showing the mean value for N/(K+Na) in phengite and paragonite is shown for comparison.

a role for chlorite as a host of N. More research is required to investigate the importance of chlorite as a host for N in different lithologies and the mechanism of N incorporation in chlorite.

3.7.2 Fluid rock interaction: a simple system

Sample LC-3 (Lago di Cignana garnet-phengite quartzite) was part of a previous study by Halama et al. (2020), who showed a strong positive correlation of B concentration and B isotopic composition, which was interpreted as resulting from addition of isotopically heavy B during peak metamorphic fluid-rock interaction with a serpentinite-derived fluid. I extend the fluid-rock interaction modelling approach of Halama et al. (2020) to include [Li] and [N] data and estimate the phengite-fluid partition coefficient for N. I modified the equation of Nabelek (1987) for open system fluid-rock interaction to replace the concentration of an element in the rock, with the concentration in phengite, multiplied by the modal abundance of phengite:

$$C^f_{phe} = DC_w - (DC_w - C^i_{phe})\ e^{-n/Dx_{phe}}$$

C^f_{phe} is the final concentration of the trace element in the phengite, C^i_{phe} is the initial concentration in the phengite, C_w is the concentration in the fluid, n is the fluid-rock ratio (by weight), x_{phe} is the modal abundance of phengite (33%), and D is the phengite-fluid partition coefficient. For B I use a partition coefficent of 0.7 (Marschall et al., 2006a). I used an initial B concentration in the phengite of 50 µg/g and concentration in the fluid of 1000 µg/g, based on the preferred interpretation of addition of B from a serpentinite-derived, B-rich fluid (Halama et al., 2020). Marschall et al. (2006a) reported a subsolidus partition coefficient for Li of 0.05, although higher values of 1 have been reported for suprasolidus experiments (Adam et al., 2014). I evaluate two different scenarios here to model the Li and B data and will subsequently use these constraints to model the combined [N]-[B] and [N]-[Li] data. For $D_{Li}^{phe-fl} = 0.05$, the [B]-[Li] data can be fitted using a Li concentration in the fluid of 800–1000 µg/g, and initial Li concentration in the phengite of 60–120 µg/g (Figure 12). For larger values of $D_{Li}^{phe-fl} = 0.5 - 1$, the [B]-[Li] data can be fitted with $[Li]_w = 0 - 20$ μg/g and $[Li]^i_{phe} \approx 65$ μg/g. Serpentinites typically contain <10 µg/g Li (Deschamps et al., 2012; Kodolányi et al., 2012; Lafay et al., 2013; Vils et al., 2008), and fluid inclusions representing serpentinite dehydration fluids also have <10 µg/g Li in both experiments and natural samples (Scambelluri et al., 2004; Spandler et al., 2014). Serpentinite-derived fluids are therefore expected to have low Li contents and the second scenario, with a value of $D_{Li}^{phe-fl} = 0.5 - 1$ is preferred. To model the [N]-[Li] data I therefore use $D_{Li}^{phe-fl} = 0.5$, $[Li]_w = 0$ μg/g and $[Li]^i_{phe} = 65$ μg/g, which allows the maximum range of D_N^{phe-fl} values that are consistent with the data.

To model the N data I consider a variety of theoretical scenarios and evaluate which are consistent with my data and independent constraints on fluid compositions. The [N]-[Li] data display a positive slope, which can be fitted with $[N]_w = 0$ μg/g, $D_N^{phe-fl} = 0.5 - 1.5$ and $[N]^i_{phe} = 17 - 20$ μg/g (Figure 12). These parameters also fit the [N]-[B] data. $D_N^{phe-fl} > 1.5$ is not consistent with the slope of the [N]-[Li] array for any range of other parameters. There is a trade-off between D and the concentration in the fluid, such that smaller values of D_N^{phe-fl} are consistent with the data if the fluid contains nitrogen (e.g. $D_N^{phe-fl} = 0.2$, $[N]_w = 50$ μg/g). There are no data available on the N contents of fluids derived

from serpentinite breakdown, but bulk serpentinites contain <15 µg/g N, and typically <5 µg/g N (Halama et al., 2014; Philippot et al., 2007). The major pulse of fluid release in serpentinites occurs during antigorite breakdown at 600–650 °C, which coincides with the P-T conditions inferred for fluid-rock interaction in this sample (Halama et al., 2020). The amount of fluid release is 6–13 wt%, depending on the serpentinite composition (Padrón-Navarta et al., 2013; Ulmer and Trommsdorff, 1995). Fluid release occurs over a narrow temperature interval so all fluid is likely to be pooled. Chlorite harzburgites produced from antigorite breakdown show a similar range of N contents to serpentinites (Halama et al., 2014), which suggests that the amount of N released during antigorite breakdown is relatively small. Based on these constraints I suggest that N contents in serpentinite-derived fluids are likely <100 µg/g, and may be much lower. Using this N concentration in the fluid, a lower bound of $D_N^{phe-fl} = 0.1$ is the minimum value of D_N^{phe-fl} which is consistent with the [N]-[Li] and [N]-[B] data. For a lower value of 10 µg/g N in the fluid, the data are fit by $D_N^{phe-fl} = 0.3$.

With $D_N^{phe-fl} = 0.1 - 1.5$ all the data can be explained by fluid-rock ratios of up to 0.1, which is similar to the values of 0.1–0.13 obtained from B isotope modelling (Halama et al., 2020). Note these values have been rescaled from the Halama paper because the effect of the modal abundance of phengite on modifying the bulk rock equations was not accounted for. A value of $D_N^{phe-fl} = 0.1 - 1.5$ is therefore considered the most consistent with my data and fluid composition constraints.

The reconstructed bulk N content for this garnet-phengite quartzite (sample LC-3) is 5 µg/g (Table 3). Siliceous ooze and chert, which are considered the likely protoliths, contain 18–78 µg/g bulk N in samples from the Western Pacific (Sadofsky and Bebout, 2004). If these values are taken as representative then this suggests that N was lost during subduction, consistent with the conclusions from my fluid-rock interaction modelling.

Reported subsolidus values for D_N^{phe-fl} range from 0.01 to ~10, depending on the experimental conditions (Table 5). Pöter et al. (2004) reported $D_{NH_4^+}^{muscovite-fluid} \approx 0.13$ at 0.4 GPa and $D_{NH_4^+}^{ms-fl} \approx 0.20$ at 1.5 GPa in the temperature range 400–600 °C. More recent experiments have focused on the partitioning behaviour at higher temperatures, during melting, but have produced substantially differing results in different experimental bulk compositions. Förster et al. (2019) report $D_{NH_4^+}^{phengite-fluid} \approx 10$ at 2 GPa, 750 °C (subsolidus) and 0.5–1 at 3 GPa, 800–850 °C (suprasolidus) during reaction of a metapelitic melt with dunite. Jackson et al. (2021) report $D_{NH_4^+}^{biotite-fluid}$=0.01–0.4 at 0.2–2.3 GPa,

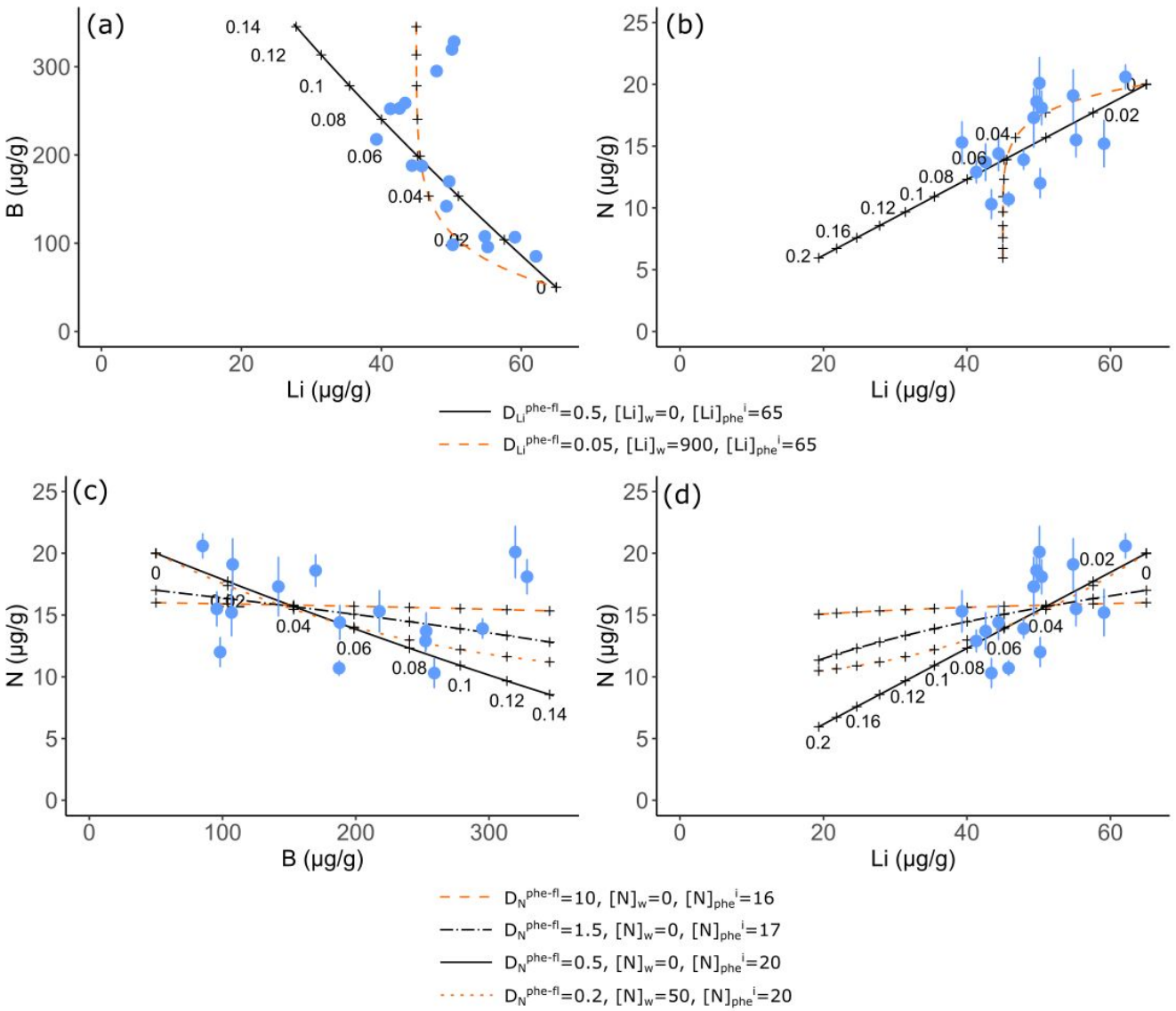


Figure 12: Fluid rock interaction modelling of phengite N-B-Li data from garnet-phengite quartzite (LC-3). Blue points are the measured data, and black lines show model outcomes for a range of different input parameters. 1s error bars are shown for N data. Error bars for B and Li are smaller than the size of the symbols. Boron input parameters were constrained from previous work (Halama et al., 2020). The top panel (a,b) shows two end member scenarios for Li modelling. The bottom panel (c,d) shows endmember scenarios for N modelling ($D_N = 10$ and $D_N = 0.2$) and two intermediate scenarios. See text for detailed explanation of modelling parameters (section 3.7.2).

725–925 °C during reaction of silicate minerals with hydrous fluids. NH_4^+ has also previously been assumed to behave similarly to Rb^+ (e.g. Busigny et al., 2003a; Mallik et al., 2018), which has a similar ionic radius (NH_4^+: 1.67 Å, Rb^+: 1.72 Å), and a D_{Rb}^{phe-fl} value of ~4–10 (Adam et al., 2014; Melzer and Wunder, 2000).

My value of $D_N^{phe-fl} = 0.1 - 1.5$ overlaps with the suprasolidus values of Förster et al. (2019). However, it is inconsistent with a single subsolidus value ($D_N^{phe-fl} = 10$) of Förster et al. (2019). and with the values of 4–10, based on the assumption that NH_4^+ behaves like Rb^+. Jackson et al. (2021) provide small values for $D_N^{biotite-fl}$ (0.01–0.4), which are mostly inconsistent with my value for D_N^{phe-fl}, when considering the consistent $D_N^{bt-phe} \approx 3$ reported by all studies. The subsolidus values of Pöter et al. (2004) ($D_N^{phe-fl} = 0.12 - -0.2$) fall at the bottom end of the range of values which are consistent with my data. The experimental data are either from similar temperatures but lower pressures to the Cignana case study (Pöter et al., 2004), or similar pressures but higher temperatures (Förster et al., 2019; Jackson et al., 2021). Extrapolation of the P-T effects reported by the Jackson study does not match my value for D_N^{phe-fl}, and therefore differences in P-T conditions are less likely to be the main factor for the discrepancy between my value and their work. Experimental and natural values for D_N^{phe-bt} are relatively consistent between multiple studies at different P-T conditions, whereas experimental values for D_N^{phe-fl} vary widely (Table 5), which suggests that variation may be a result of fluid-related factors. The difficulty of preserving N contents of experimental fluids during quenching may be a source of variation in the experimental results (e.g. Chen et al., 2019a). Nitrogen is present as NH_4^+ in both biotite and phengite, whereas N speciation in fluid varies between N_2, NH_3 and NH_4^+, depending on P, T, pH and fO_2 (Mikhail et al., 2017; Mikhail and Sverjensky, 2014) and therefore differences in fluid pH and fO_2 between experiments, and between experiments and my samples, are also possible reasons for the discrepancy.

3.7.3 Fluid-rock interaction: growth of new phases

Sample SEC16-1 (Raspas blueschist) contains phengite as well as paragonite. As both minerals are significant hosts for N and B, phengite compositions cannot be considered in isolation. Phengites show a decrease in [N] and [B] with decreasing Si p.f.u., an increase in [Li], as well as a increase in Na/(Na+K) (i.e. its paragonite component) whereas paragonite shows unsystematic variation in

	P (GPa)	T (°C)	$D^{\text{phe-fl}}$	$D^{\text{bt-fl}}$	$D^{\text{bt-phe}}$
Förster et al. (2019)	2	750	10		
Förster et al. (2019) *	3	800–1000	0.5–1.1	0.2–1.6	1.5–3.1
Pöter et al. (2004)	0.4	400–600	0.12–0.15		3.5
Pöter et al. (2004)	1.5	400–600	0.19–0.20		
Jackson et al. (2021) *	0.2–2.3	725–925		0.01–0.4	
Moine et al. (1994)	0.2	550		~0.5	
Honma and Itihara (1981) **	~ 0.4	~ 700			1.5–3.1
Duit et al. (1986) **	~ 0.5	500–700			2.2–4.2
Busigny et al. (2004) **					2.6–3.3

Table 5: Summary of available partitioning data for nitrogen between aqueous fluid and micas (phengite and biotite). Most data are from subsolidus experiments but data indicated with a * are from suprasolidus experiments. Some natural data on biotite-phengite partitioning are also included (**).

these elements (Figure 8).

I performed phase equilibria modelling in order to understand the mineralogical evolution of this sample and link this to the trace element behaviour. Calculations were performed using the Theriak-Domino software (de Capitani and Petrakakis, 2010; de Capitani and Brown, 1987) and the NCKFMASHTO + CO_2 system using an H_2O-CO_2 fluid in excess and the Holland and Powell (2011) thermodynamic database. The solution models used were: amphibole, clinopyroxene, white mica (Green et al., 2016); garnet, biotite, chlorite (White et al., 2014); epidote (Holland and Powell, 2011).

I calculated P-X(CO_2) and T-X(CO_2) equilibrium phase diagrams with variable X(CO_2) from 0 to 0.025, using the bulk composition for this sample reported in John et al. (2010) and an average MORB value of $X_{Fe^{3+}} = 0.16$ (Cottrell and Kelley, 2011). The effect of varying $X_{Fe^{3+}}$ from 0.05–0.25 moved field boundaries by only <1 kbar for all phases except epidote and therefore $X_{Fe^{3+}} = 0.16$ is considered suitable for this sample.

The observed assemblage occupies a field ranging from 1.5–1.9 GPa, 520–570 °C and X(CO_2) from 0.010–0.022 (Figure 13). This field is bounded by the disappearance of paragonite as X(CO_2) decreases, and the disappearance of garnet and epidote as X(CO_2) increases. John et al. (2010) previously calculated peak P-T conditions for the Raspas complex using conventional thermobarometry on garnet-omphacite-phengite assemblages. Peak P-T conditions of eclogites were 1.6–2.0 GPa and 550–650 °C. Garnet-omphacite-phengite domains in blueschists recorded slightly lower peak pressures

of 1.4–1.6 GPa and similar temperatures. According to my modelling, omphacite is only stable under these conditions at lower values of $X(CO_2)$ than are required to stabilise the observed blueschist assemblage, which has 16% paragonite. As mentioned above, the sample contains carbonate, and addition of CO_2 to the system stabilises paragonite. As $X(CO_2)$ increases across the observed assemblage field, the paragonite mode increases from 0 to 25%, and glaucophane mode decreases from 40 to 15% due to the (unbalanced) reaction glaucophane + CO_2 $\longrightarrow$ paragonite + (Fe,Mg,Ca) carbonate. The high paragonite mode observed in the sample can therefore be explained as a result of infiltration of a carbonate-bearing fluid.

As $X(CO_2)$ increases across the peak assemblage field, phengite Na/(Na+K) increases and Si content decreases. Phengite mode remains fairly constant, decreasing slightly from 16 to 14%. A range of phengite Si contents are observed in different phengite grains. These are interpreted as representing partial recrystallisation of phengite during interaction with a carbonate-bearing fluid, with the new domains having lower Si p.f.u. and higher Na p.f.u.. Trace element redistribution from other phases into phengite supports my interpretation. For example, the Li contents in phengite, which correlate with decreasing Si p.f.u., can be interpreted to reflect incorporation of Li from glaucophane breakdown, since glaucophane has high Li contents (132–169 µg/g). Although the preservation of variable phengite Si contents implies that full equilibrium was not reached during fluid-rock interaction (i.e. the reactant phases were not totally consumed), the assemblage, major and trace element data support the conclusion that interaction with a CO_2-bearing fluid occurred, likely during early retrograde metamorphism.

Decrease in phengite N content in SEC16-1 also correlates with decreasing Si content and increasing Na/(Na+K). This can be explained by the phengite recrystallisation discussed above. During paragonite growth, partial re-equilibration of phengite with the growing paragonite results in transfer of N from phengite to paragonite. Taking the phengite with the highest Si content to represent the initial phengite composition prior to fluid-rock interaction, I use the N content of this phengite (232 µg/g) to calculate the initial bulk N concentration of the sample. To calculate the final bulk N concentration I use the average N concentrations of all phengite and paragonite grains measured (190 and 53 µg/g respectively). The observed phengite and paragonite modes are around 16%. Using the method described in Section 3.6.3 I calculate the bulk N contents before and after fluid-rock

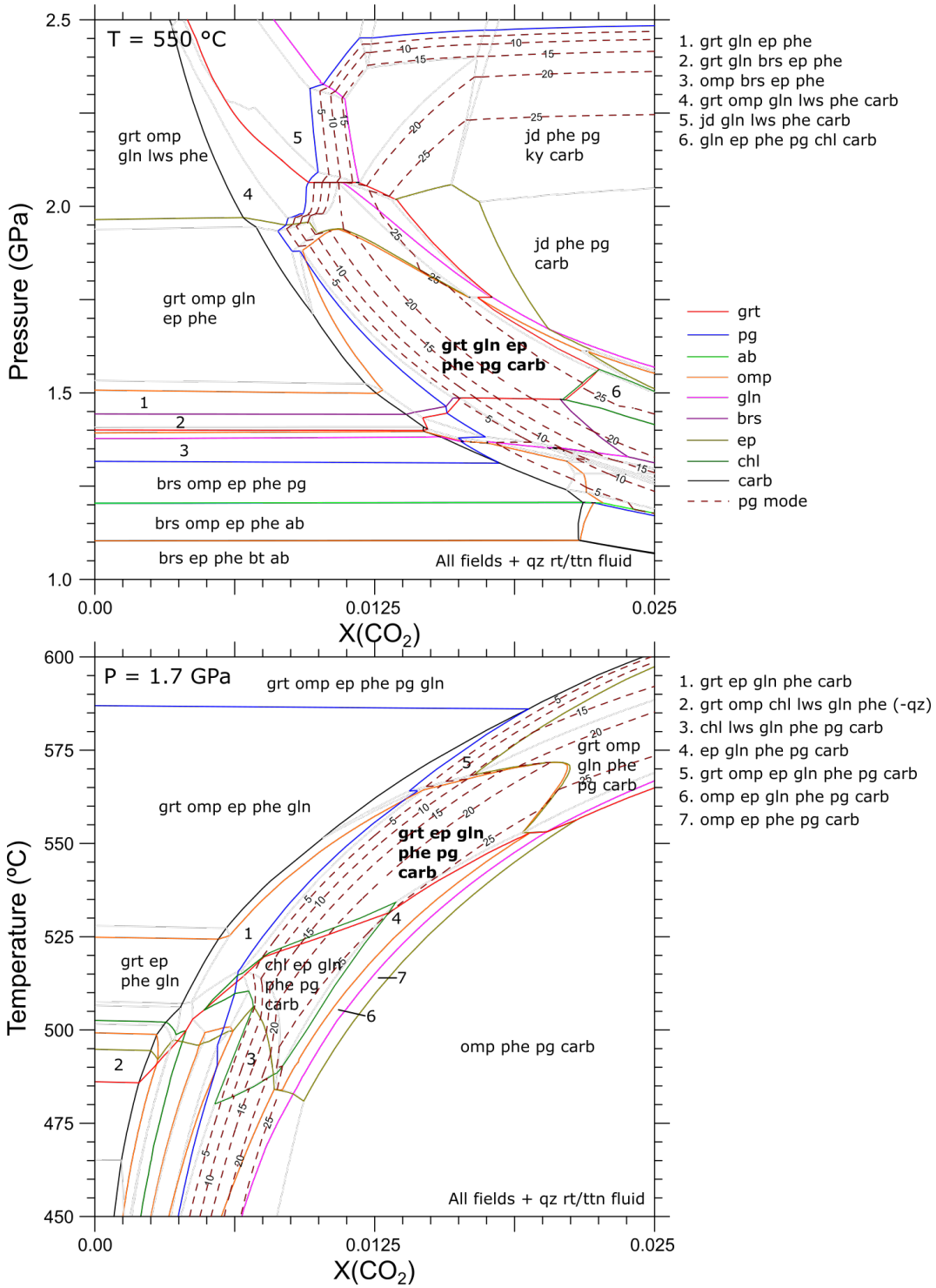


Figure 13: P-X(CO_2) and T-X(CO_2) equilibrium phase diagrams for sample SEC16-1. The observed assemblage is indicated in bold font. Gt = garnet, om = omphacite, jd = jadeite, gl = glaucophane (*sensu lato*), barroisite (*s.l.*), ep = epidote, phe = phengite, pa = paragonite, chl = chlorite, carb = carbonate, ab = albite, bi = biotite, law = lawsonite, ru = rutile, ttn = titanite.

interaction. The final bulk N content is 39 µg/g. For the conservative assumption that the phengite mode does not change during fluid-rock interaction, the initial bulk N is 37 µg/g. Accounting for the modelled decrease in phengite mode from 16 to 14%, the initial bulk is 42 µg/g. The decrease in N concentration seen in phengite in this sample can therefore be explained by redistribution of N between growing and dissolving phases during fluid-rock interaction, without any significant external input or loss of N from the rock. The uncertainty on the bulk [N] values was estimated to be ~15–20% by combining uncertainties on the mineral N concentrations and mineral modes. This conclusion is similar to Halama et al. (2017), who showed that the retention of N during fluid-rock interaction is strongly controlled by the stability or breakdown of white mica. A similar reaction (albite + CO_2 $\longrightarrow$ paragonite + aragonite) observed in calcschists from the Western Alps was associated with 60% loss of N from the bulk rock, with volumetric fluid-rock ratios of 3–4 (Epstein et al., 2021). The difference in N behaviour compared to my study may be explained by a lower fluid-rock ratio, or a different fluid composition. If I assume that the $X(CO_2)$ values which stabilise the observed assemblage (Figure 13) are representative of the fluid, and that all the CO_2 in the fluid was converted to carbonate minerals, I can estimate the minimum amount of fluid required to generate the modal abundance of carbonate observed. Using $X(CO_2)$=0.01–0.022 and a carbonate mode of 3–5 vol% gives a fluid-rock ratio of 0.2–0.9, which is indeed lower than for the Epstein study.

Phengite and paragonite are also the main B-bearing phases, so the same model can be applied to B as with N. The decrease in B contents with decreasing Si contents can be explained by redistribution of B into paragonite. The calculated final bulk B concentration is 28 µg/g, compared to an initial concentration of 15-17 µg/g depending on the estimate of the phengite mode. This suggests that in contrast with N, B has been added to the rock during fluid-rock interaction. This may explain why there is more scatter in the correlation of [B] with Si p.f.u., compared to [N], as individual grains have equilibrated to differing degrees with a B-rich fluid (Halama et al., 2020; Konrad-Schmolke and Halama, 2014).

3.7.4 Fluid-rock interaction in other samples

Calculated bulk N concentrations in Cignana mafic rocks (samples LC-2a, LC-1b) are very low. Sample LC-1b (1.2 µg/g N) falls within the range of N contents observed in fresh MORB, which

is generally <2 µg/g (Busigny et al., 2005; Erzinger et al., 1996; Li et al., 2007). Sample LC-2a has slightly higher N contents (3.6 µg/g), which may reflect a more hydrothermally altered protolith (Busigny et al., 2005; Li et al., 2007), or addition of minor N during subduction.

Sample LC-2a preserves variability in phengite major and trace element chemistry. The main population has constant Si p.f.u. but variable N contents (39–123 µg/g). There are two grains with higher, variable Si content, lower N (20–24 µg/g) and Li contents, and higher B content. The Si contents of these grains overlap with those from sample LC-3, which were interpreted to record peak metamorphism. Halama et al. (2020) previously interpreted B isotope data from LC-2a to suggest that B was lost during retrograde fluid-rock interaction. The observed lower B contents and lower Si contents in my analyses are consistent with this interpretation, where the low Si grains formed during retrograde recrystallization and the high Si grains preserve peak conditions. The elevated N and Li contents in low Si grains suggest that small amounts of N and Li were added during retrograde fluid-rock interaction.

Previous studies on eclogites and blueschists from Jenner have suggested a complex metamorphic history involving interaction with both sediment-derived (Penniston-Dorland et al., 2010; Sorensen et al., 1997) and serpentinite-derived fluids (Errico et al., 2013). Jenner samples show high bulk N contents (13–71 µg/g) compared to the range of both fresh MORB (< 2 µg/g) and altered oceanic crust (1–30 µg/g, Busigny et al. (2005) and Li et al. (2007)). The N concentrations in individual phengite grains are similar to those from Raspas, but the Jenner samples contain higher phengite modes, resulting in higher bulk N contents. High phengite mode is consistent with the bulk enrichment in K and other large ion lithophile elements documented by Sorensen et al. (1997) and attributed to interaction with a sediment-derived fluid. High N contents are also consistent with a sediment-derived fluid, since subducted sediments can have N contents up to 2000 µg/g (e.g. Li and Bebout, 2005; Sadofsky and Bebout, 2004). The positive correlation of N and B contents in phengite in samples JEN12-03 and JEN12-07 is also consistent with a sediment derived fluid, since sediments can also contain high B contents (e.g. Bebout et al., 2013; De Hoog and Savov, 2018; Romer et al., 2014). Negative correlation of [N] and [Li] in JEN12-07 and JEN12-09 suggests that these sediment-derived fluids may be Li-poor.

These samples demonstrate that addition of N during metamorphism appears to be a common

process in subduction-related mafic rocks, in agreement with recent work which found that N addition can occur as early as blueschist facies (Li et al., 2021a). These fluids are most likely sourced from dehydrating metasediments, as these are rich in N. Addition of N can be associated with either addition or loss of Li and B, which suggests that these fluids can be heterogeneous in their Li and B contents, possibly reflecting heterogeneity in the sediments themselves. Addition of N is seen in phengite with high Si contents, which implies that it occurred during deep subduction and is not a late-stage retrograde overprint. The presence of N and other fluid-mobile elements in sediment-derived fluids at depths of up to ~90 km (in the case of Cignana, see my modelling in Section 5.2) implies that these elements are at least partially retained to that depth, and can be mobilised and redistributed there, rather than being completely lost during shallow dehydration reactions. This emphasises the importance of understanding volatile element transfer between lithologies during subduction, not just the effects of prograde devolatilisation, and shows that mafic rocks may act as sinks for N and other volatiles during subduction-related metasomatism, if accompanied by growth of mica.

3.8 Conclusions

This study demonstrates the viability of *in situ* analyses of N in silicate minerals using SIMS. The data collected from a range of formerly subducted rocks show that N is dominantly hosted in white micas, compared to phases such as omphacite or Na-amphibole. Chlorite may have an additional role as a N host but more data are required to explore its role in a wider variety of localities and lithologies. Reconstructed bulk N contents based on mineral modes and N concentrations agree with bulk N contents measured by combustion, which confirms that most N is hosted in the major rock-forming minerals. Using the N/K_2O ratio in white micas, and the K-content of the subducted slab, I estimate the subducted flux of N in oceanic crust to be $0.6 - 2.4 \times 10^{11}$ g/yr, which is similar to or slightly smaller than previous estimates. A case study of fluid-rock interaction in a mineralogically simple garnet-phengite quartzite shows moderate N loss during fluid-rock interaction. Using open system fluid-rock interaction equations I show that N is a moderately fluid-mobile element under the P-T-X conditions experienced by this sample ($D_N^{phe-fl} = 0.1 - 1.5$). A second fluid-rock interaction case study shows the importance of white mica stability in controlling the N budget of rocks. White mica

growth during fluid-rock interaction can sequester N and prevent significant bulk N loss. My work provides constraints on the inter-mineral partitioning of N at subduction zone conditions and provides the first natural constraints on the fluid-mineral partitioning of N at these conditions. I emphasise the complexity of element mobility within subduction zones, with redistribution between different phases and lithologies being important, in addition to simple loss of volatiles during dehydration.

Acknowledgements

I thank M. Konrad-Schmolke for expert guidance at Jenner, T. John for assistance with Raspas samples, D. Wilde for help with sample preparation and I. Buisman for electron probe analyses. I also thank S. Mikhail, L. Li and an anonymous reviewer for comments which improved this manuscript. This work was supported by a NERC Doctoral Training Partnership grant (NE/S007407/1) and a NERC Ion Microprobe Facility grant (IMF709/0520).

3.9 Post-script

In this chapter I began to answer question 1 of the thesis by showing that white micas contain at least an order of magnitude higher N concentrations that coexisting HP minerals in subducted oceanic crust. I also identified chlorite as a potential host for N that has not been considered by previous studies. I build upon this work in Chapter 5, where the relatively contributions of different minerals to the N budget are assessed in greater detail.

I also addressed question 2a of the thesis by investigating the fluid-mica partition coefficient for N in natural samples. This was done by comparing the behaviour of N to other FME in a set of well studied samples where there were already existing constraints on the concentrations of other FME in the subducted-related fluids. I also began to address question 2b by providing some partitioning data for N between HP minerals, again comparing N to previously studied elements to verify that these minerals could preserve equilibrium partitioning. I expand upon this further in Chapter 5.

4 Chapter 4: Tracing fluid sources during polymetasomatism

4.1 Preface

This chapter presents a detailed case study of the mineralogical and fluid evolution of highly metasomatised, subduction-related rocks. This aims to address question 3 from the introduction, showing how coupled analyses of different FME in different minerals, including white mica, can be used to disentangle different processes controlling FME (re)-distribution during subduction.

I study the Dora-Maira whiteschists and their country rock metagranites, which form part of the formerly subducted continental crust preserved in the Western Alps. A number of studies have investigated the sources and timing of metasomatic fluids that infiltrated the whiteschists, but there is as yet no consensus. Part of the problem may be that different elements record different fluid compositions because they are hosted in minerals that grew at different times. Many studies only focused on one or two elements, and some studies only analysed whole rock data, which makes it harder to untangle the evolution of fluid compositions during subduction. With this in mind, I analysed the concentrations of B, N and other FME, and B isotopes, in micas and tourmalines from the whiteschists and their country rocks. The combination of different elements and minerals that grew at different times enabled me to offer some potential explanations for how to reconcile conflicting interpretations from previous studies.

This chapter was published in *Contributions to Mineralogy and Petrology* in 2023 (https://doi.org/10.1007/s00410-023-02058-0) and is included here with minor typographic editing. The analytical methods have been removed and placed in Chapter 2 to avoid duplication across the chapters. All co-authors contributed comments during drafting, some of which were incorporated into the final text by myself.

4.2 Abstract

Whiteschists from the Dora-Maira massif (Western Alps, Italy) are Mg and K-rich metasomatised granites which experienced ultra-high pressure metamorphism and fluid-rock interaction during Alpine continental subduction. The sources and timing of fluid infiltration are a source of significant debate. In this study I present boron (B) isotopes and other fluid-mobile trace element (FME) concentrations in various generations of phengite from whiteschists and their country rock protoliths to investigate the sources and timing of metasomatic fluid influx. Reconstructed bulk rock concentrations based on modal data and mineral compositions indicate that significant amounts B and other FME were added to the rock during prograde metamorphism, but that this fluid influx postdates the main Mg metasomatic event. High B concentrations (150–350 μg/g) and light δ^{11}B values (-16 to -4 ‰) recorded in phengite point to a B-rich sediment-derived fluid as the main source of B in the whiteschists. Further redistribution of FME during metamorphism was associated with breakdown of hydrous minerals such as talc, phlogopite and ellenbergerite. The source of the Mg-rich fluids cannot be constrained based on the B data in phengite, since its signature was overprinted by the later main B metasomatic event. Rare tourmaline-bearing whiteschists record additional information about B processes. Tourmaline δ^{11}B values (-6 to +1 ‰) are in isotopic equilibrium with similar fluids to those recorded by most phengite, but phengites in tourmaline-bearing samples record anomalous B isotope compositions that reflect later redistribution of B. This study demonstrates the utility of *in situ* analyses in unravelling complex fluid-rock interaction histories, where whole rock analyses make it difficult to distinguish between different stages of fluid-rock interaction. Polymetasomatism may result in decoupling of different isotopic systems, thus complicating their interpretation. The Dora-Maira whiteschists interacted with multiple generations of fluids during subduction and therefore may represent a long-lived fluid pathway.

4.3 Introduction

High pressure fluids are important agents for the transfer of fluid-mobile trace elements within the subducting slab and to the mantle wedge. (Ultra-)high pressure, (U)HP, rocks provide a record of the generation of such fluids and of the mobilization of trace elements within the slab. Two approaches

exist to recover (U)HP fluid compositions. Analysis of fluid inclusions trapped in (U)HP minerals provides direct constraints on fluid compositions (e.g. Ferrando et al., 2009; Hughes et al., 2021; Maffeis et al., 2021; Philippot et al., 1995), but are often rare and volumetrically small, which hampers their analysis. Alternatively, whole rock or mineral elemental and isotopic compositions, combined with fluid-rock partitioning data, provides an indirect method of constraining fluid compositions, and is applicable to a wider range of rocks (e.g. Busigny et al., 2003a; Halama et al., 2020; Harris et al., 2022; Konrad-Schmolke and Halama, 2014; Tian et al., 2019). *In situ* analyses of multiple fluid-mobile elements and isotope systems are particularly powerful for investigating the evolution of mineral and coexisting fluids during progressive stages of metamorphism and fluid-rock interaction (e.g. Bebout et al., 2007; Clarke et al., 2020; De Hoog et al., 2014; Debret et al., 2016; Halama et al., 2020; Harris et al., 2022; Urann et al., 2020).

The Dora-Maira whiteschists are continental rocks metamorphosed at UHP conditions during Alpine subduction of the European continental margin beneath the Adriatic Plate. They are characterized by extreme enrichment in Mg, and depletion in Na, Ca, Fe, and LILE relative to their country rocks (Chopin, 1984; Schertl et al., 1991; Schertl and Schreyer, 2008). They have been extensively studied after they revealed the first record of coesite in crustal rocks, indicating subduction to depths of at least 100 km (Chopin, 1984). The whiteschists represent a former fluid pathway which was active during continental subduction (Chen et al., 2023a; Chen et al., 2016; Ferrando et al., 2009; Tian et al., 2019; Xiong et al., 2022, 2021). Chopin, 1984 originally suggested an evaporitic protolith for the whiteschist. Most authors now regard the whiteschists as metasomatic alteration products of the orthogneiss and metagranite country rock by Mg-rich fluids (e.g. Ferrando et al., 2009; Gebauer et al., 1997; Schertl and Schreyer, 2008) but there is outstanding debate over the timing of metasomatic event(s) and the origin of metasomatic fluid(s). Oxygen and hydrogen isotope data have been used to argue that the metasomatic fluid was seawater-derived, but this has been interpreted as a signature of both pre-Alpine seafloor hydrothermal alteration (Gauthiez-Putallaz et al., 2016) and Alpine prograde dehydration of serpentinites (Chen et al., 2016) or altered oceanic crust (AOC) (Sharp et al., 1993). Gauthiez-Putallaz et al., 2016 proposed that Mg-metasomatism occurred on the seafloor where the Dora-Maira crust formed part of a hyper-extended continental margin sequence. Similar explanations have been proposed for whiteschists from the Monte Rosa nappe (Marger et al.,

2019; Pawlig and Baumgartner, 2001). Compagnoni and Hirajima, 2001 documented rare 'super-zoned' garnet with almandine-rich cores and pyrope-rich rims. The extreme compositional zoning shown is interpreted to be produced by a change in the whole rock bulk composition. Based on the inclusion assemblages in the almandine-cores they estimated the P-T conditions of formation to be $\sim$ 1.6 GPa and 600 °C, and concluded that subsequent Mg-metasomatism took place during Alpine subduction.

In this study I examine the mobility of trace elements during metasomatism and (U)HP metamorphic reactions. I combine *in situ* SIMS analyses of fluid-mobile elements (FME) and boron (B) isotopes in protolith and metasomatic minerals to address three main questions: 1) What were the sources of metasomatic fluids which interacted with the granitic rocks to produce whiteschist during subduction? 2) Do the unusual major element, trace element, and isotopic signatures all record interaction with the same fluid, or were there multiple periods of fluid influx? 3) To what extent was trace element distribution between minerals at different stages of metamorphism controlled by internal metamorphic reactions versus external fluid input? Boron isotopes are particularly suited to address the first two questions, since different subducted lithologies have distinct B isotope signatures (De Hoog and Savov, 2018).

4.3.1 Geological background

The Dora-Maira massif (DMM) forms one of the three Internal Crystalline Massifs within the Pennine Domain of the Western Alps (Chopin, 1984; Compagnoni and Hirajima, 2001) and exposes part of the European continental margin that was subducted and exhumed during the Alpine orogeny. It is now stacked within the Western Alps orogenic wedge, where it forms a dome roofed by normal-sense shear zones, which juxtapose the Monviso massif, and other units of the oceanic Piedmont zone (Lardeaux et al., 2006). The internal structure of the DMM consists of multiple thrust sheets, which experienced different peak pressure-temperature conditions during Alpine metamorphism (Figure 14). The Brossasco-Isasca Unit (BIU) in the southern DMM experienced peak UHP Alpine metamorphism at 730 °C, 4.0–4.3 GPa (Groppo et al., 2019 and references therein) and is divided into a polymetamorphic complex and a monometamorphic complex (Compagnoni et al., 1994). The polymetamorphic complex comprises almandine-kyanite-phengite metapelite with subordinate marble and eclogite, and

represents Variscan metamorphic basement, with partial Alpine HP metamorphic overprinting. The monometamorphic complex comprises garnet-biotite-phengite orthogneiss, with local occurrences of whiteschist lenses, garnet-jadeite quarzite, undeformed metagranite, and metapelite. This complex is interpreted as recording Permian granitoids intruded into the Variscan basement (Chen et al., 2017; Gebauer et al., 1997) and subsequently metamorphosed and deformed during Alpine subduction. The metapelite inclusions in orthogneiss are interpreted as xenoliths of the country rock (Compagnoni and Hirajima, 2001). Whiteschist is a term introduced by Schreyer, 1973 to describe magnesian rocks containing the high pressure assemblage talc + kyanite, with a bulk composition characterized by extremely high Mg/Fe ratio, very low Ca and Na, and high Al contents. In the BIU the whiteschists contain pyrope-rich garnets ($X_{Prp} > 0.9$) and have also been referred to as pyrope-quartzites in the literature (Chopin, 1984). The BIU whiteschists occur as decametric lenses within otherwise unremarkable orthogneiss. The contact between the lithologies is typically marked by alteration in the whiteschist. Whiteschists preserve an internal foliation which is truncated by the external foliation in the orthogneiss (Schertl et al., 1991), implying that they record a different stage of the BIU metamorphic and structural evolution.

The petrography of the whiteschists has been described in detail by Schertl et al., 1991. The matrix is mineralogically simple and consists of pyrope garnet, phengite, quartz (retrograde after coesite), kyanite, rutile, ± talc ± jadeite. Small pyrope and kyanite porpyroblasts contain inclusions of quartz, relict coesite, phengite, talc, rutile ± tourmaline. The presence of coesite was first described by Chopin, 1984 and confirms the UHP conditions experienced by the BIU. Decimetric pyrope megablasts consist of a core with a diverse inclusion assemblage, including several phases which do not occur in the matrix or small pyropes. These include Mg-chlorite, ellenbergerite, phlogopite and vermiculite, alongside kyanite and talc, which also occur in the matrix. Glaucophane, paragonite, muscovite, tourmaline, apatite, bearthite and Mg-dumortierite are rare inclusion phases. Magnesiochloritoid has also been found in megablasts from the Tapina locality (Simon et al., 1997). Quartz/coesite is absent from the megablast cores and phengite is extremely rare. Some megablasts contain a thin rim with similar composition and inclusion assemblage to the small pyropes. Occasionally various phengite schists occur, which are intercalated with the whiteschists (Schertl and Schreyer, 2008). These phengite schists have bulk compositions intermediate between the country

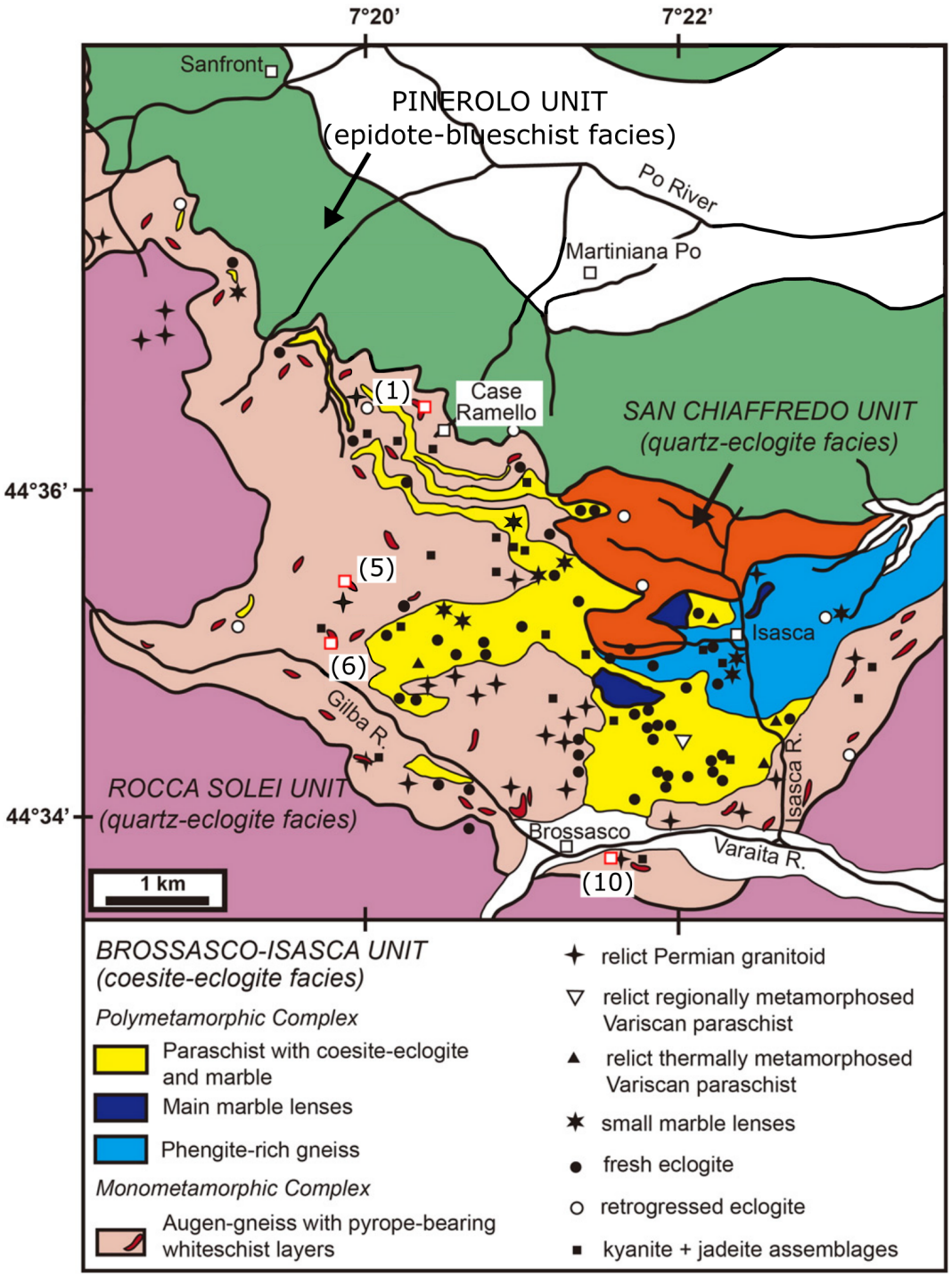


Figure 14: Geological map of the southern Dora-Maira Massif, showing sample localities, with locality numbers following Schertl and Schreyer, 2008. (1) DM5.2, DM6, DM1.1, 15597, 17478, 21437; (5) 20178, DM1b, 26405 (nearby) (6) 17618; (10) 17702. Modified after Chen et al., 2016, originally after Compagnoni and Rolfo, 2003.

rock orthogneiss and the whiteschists, and contain phengite, quartz ± phlogopite ± chlorite ± garnet ± kyanite ± tourmaline ± jadeite.

The Alpine P-T path of the BIU has been constructed from P-T estimates in multiple different lithologies (Figure 15). The earliest recorded stage of Alpine metamorphism is the growth of garnet cores in metapelites at 520–540 °C, 1.6–2.3 GPa (Groppo et al., 2019). Garnet mantles record slightly higher grade conditions (540–560 °C, 2.5–2.8 GPa), similar to the conditions suggested by Ferrando et al., 2009 for pyrope megablasts hosting ellenbergerite in whiteschists. Similar pressure estimates have also been recovered from phengite cores in marbles (Di Vincenzo et al., 2006). Growth zoning in clinopyroxene, garnet and phengite in eclogites records a similar prograde path (540–500 °C, 1.5 GPa; 570 °C, 2.5 GPa; 650 °C, 3.2 GPa; Nowlan et al., 2000). The peak metamorphic conditions (∼ 730 °C, 4.0–4.3 GPa) are well studied, with the best constrained estimates coming from metapelite garnet rims (Groppo et al., 2019), whiteschists (Hermann, 2003), and marbles (Castelli et al., 2007). Early retrograde decompression is recorded by phengite-talc-kyanite coronae in whiteschists (∼ 720 °C, 3.6–3.9 GPa, Hermann, 2003). Further decompression and cooling (670–700 °C, 2.5–3.0 GPa) is recorded by phengite-phlogopite-talc-kyanite coronae in whiteschists (Hermann, 2003) and retrograde assemblages in eclogites (Di Vincenzo et al., 2006; Groppo et al., 2007b), and marbles (Castelli et al., 2007). A major retrograde event, in response to a fluid influx, occurred at 600–650 °C, 1.1–1.5 GPa and is recorded by near-complete recrystallization in the orthogneiss (Di Vincenzo et al., 2006; Groppo et al., 2005), complete retrogression of pyrope in some whiteschists (Hermann, 2003), and also by assemblages in metapelites (Groppo et al., 2019), marbles (Groppo et al., 2007a) and eclogites (Di Vincenzo et al., 2006; Groppo et al., 2007b). Even lower grade assemblages (∼ 550 °C, 0.5–1.0 GPa) are preserved in calc silicates (Rubatto and Hermann, 2001).

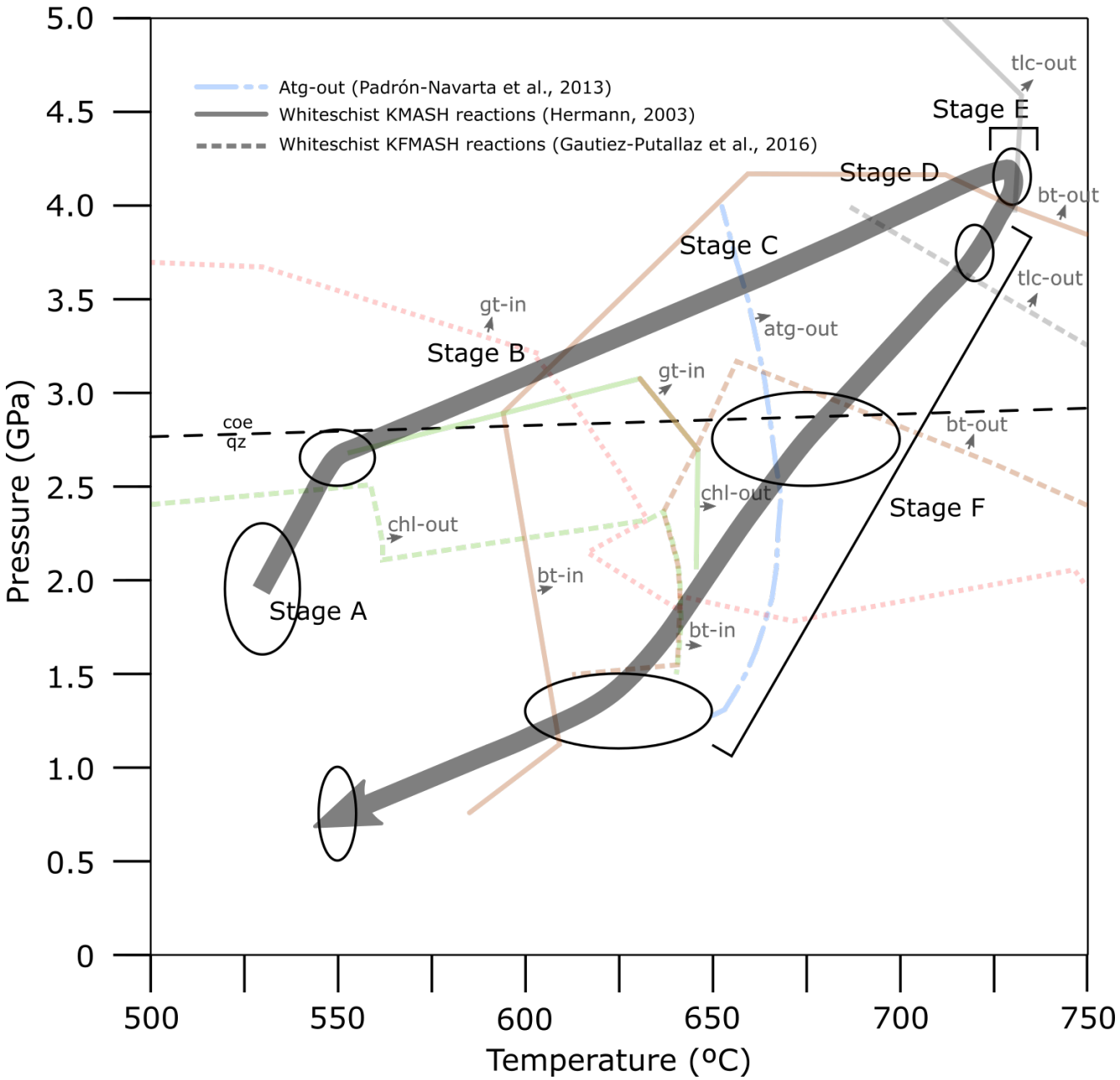


Figure 15: Summary of P-T path constrained from metapelite (Compagnoni and Hirajima, 2001; Groppo et al., 2019; Hermann, 2003), eclogite (Di Vincenzo et al., 2006; Groppo et al., 2007b; Hermann, 2003; Nowlan et al., 2000), whiteschist (Compagnoni and Hirajima, 2001; Ferrando et al., 2009; Ferraris et al., 2005; Gauthiez-Putallaz et al., 2016; Hermann, 2003), marble (Castelli et al., 2007; Di Vincenzo et al., 2006; Ferrando et al., 2017; Groppo et al., 2007a), calc silicate (Rubatto and Hermann, 2001) and orthogneiss (Di Vincenzo et al., 2006). Ellipses represent the uncertainty on P-T estimates for each point (see Geological background section). Stages, indicated by capital letters, correspond to stages of the whiteschist mineralogical evolution and are discussed later. Key mineral growth and breakdown reactions in the whiteschists (see discussion) are shown in the K_2O–MgO–Al_2O_3–SiO_2–H_2O (Hermann, 2003) and K_2O–FeO–MgO–Al_2O_3–SiO_2–H_2O (Gauthiez-Putallaz et al., 2016) systems. Also shown is the breakdown of antigorite (Padrón-Navarta et al., 2013), which has been proposed as a source of Mg-rich fluids.

4.4 Analytical techniques

The analytical methods are detailed in Chapter 2.

4.5 Sample descriptions and major element compositions

A total of eleven samples were analysed (Table 6). Samples with five digit numbers (e.g. 17702) have been previously described (Schertl and Schreyer, 2008; Xiong et al., 2022), whereas other samples are new (DMxx). Sample locations (Figure 14) follow the numbering of Schertl and Schreyer, 2008. A description of each lithology is provided below. Detailed mineralogy of each sample is provided in Table 6, major element compositions are presented in Appendix A.2, and selected photomicrographs of the samples are shown in Figure 16.

Sample	Lithology	Locality name	Locality number	Mineralogy
17702	Metagranite	Brossasco	10	Qz, Kfs, Pl, Phe, Bt, Grt, Zo, Jd, Ky
20178	Orthogneiss	Tapina	5	Qz, Ab, Bt, Phe, Grt, Ep, Rt, Ttn
DM1.1	Pyrope megablast	Case Ramello	1	Prp, Chl, Ell, Phl, Ky, Tlc
DM5.2	Whiteschist	Case Ramello	1	Phe, Prp, Qz, Ky, Tlc, Rt
DM6	Whiteschist	Case Ramello	1	Phe, Prp, Qz, Coe, Ky, Tlc, Rt, Ell
15597	Whiteschist	Case Ramello	1	Phe, Prp, Qz, Ky, Tlc, Rt, Tur, Jd
DM1b	Whiteschist	Tapina	5	Phe, Prp, Qz, Ky, Tlc
17478	Retrogressed whiteschist	Case Ramello	1	Qz, Chl, Ms, Phe, Tlc, Ky, Tur
21437	Phengite schist	Case Ramello	1	Phe, Qz, Tur, Chl, Grt
26405	Phengite schist	San Bernardo	near 5	Phe, Qz, Phl, Tur, Grt, Ky, Rt
17618	Phengite schist	Masueria	6	Phe, Ms, Pg, Phl, Chl, Tlc, Tur, Grt, Rt

Table 6: Summary of sample information. Locality numbers and names follow Schertl and Schreyer, 2008.

The whiteschist and phengite schist protoliths are represented by the metagranite (sample 17702) and orthogneiss (sample 20178). In the metagranite, randomly oriented K-feldspar occurs as large grains up to 2 cm in length. Quartz occurs in patches up to 1 cm, which are composed of granoblastic, polygonal grains about 0.2 mm in diameter. This texture has previously been interpreted to reflect the former presence of coesite (Biino and Compagnoni, 1992). Biotite (6.01 Si pfu [22 O pfu], X_{Mg}=0.40) is present, but is partially replaced by Ti-rich phengite (TiO_2 > 1.5 wt%), which was interpreted as forming during prograde HP metamorphism (Bruno et al., 2001). Rectangular plagioclase laths

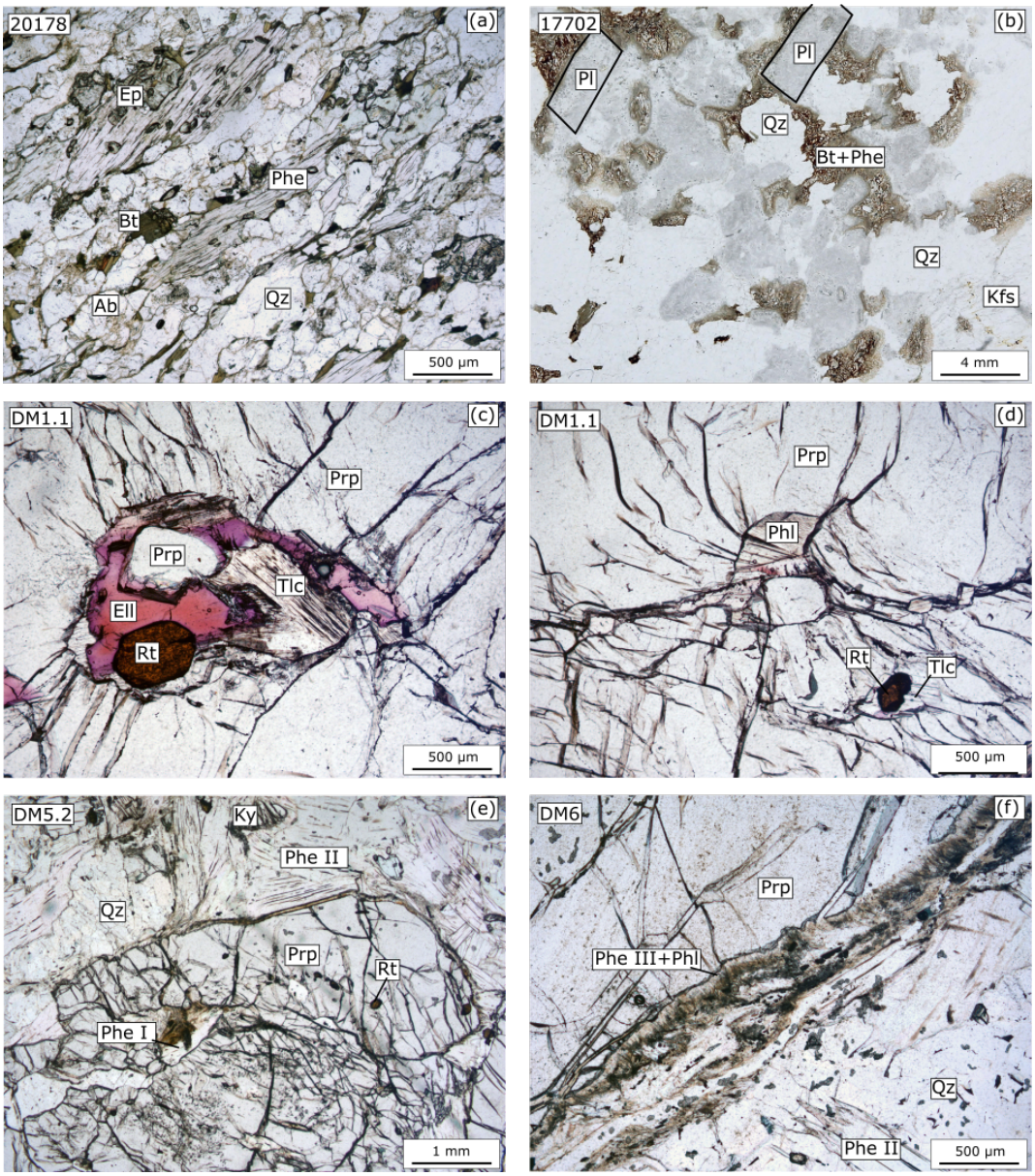


Figure 16: Thin section photomicrographs of metagranite, orthogneiss and whiteschist. All images are in plane polarized light. (a) Orthgneiss sample 20178, showing the amphibolite facies assemblage epidote, biotite, albite, phengite and quartz. (b) Metagranite sample 17702. Igneous K-feldspar is largely unaffected by high pressure metamorphism. Quartz is also largely unreacted, but is recrystallized into granoblastic, polygonal grains. Red-brown igneous biotite is partially replaced by colourless phengite. Plagioclase laths are pseudomorphed by a fine-grained aggregate of zoisite, jadeite, quartz and phengite. (c) Whiteschist sample DM1.1, showing a composite inclusion of ellenbergerite, talc and rutile in a pyrope megablast (Prp I). (d) Whiteschist sample DM1.1, showing inclusions of phlogopite, talc and rutile in a pyrope megablast (Prp I). (e) Whiteschist sample DM5.2, showing a small pyrope (Prp II) with inclusions of phengite (Phe I) and rutile. (f) Whiteschist sample DM6, showing Phe III + phlogopite forming at the expense of pyrope on the rim of pyrope megablasts.

are pseudomorphically replaced by a fine grained aggregate containing zoisite, jadeite, quartz and a Ti-poor phengite ($TiO_2 < 0.4$ wt%).

In the orthogneiss, phengite occurs as large, oriented grains up to 1 mm in length and also as a separate generation of smaller flakes, which along with biotite define the foliation. Epidote, albite and titanite are also weakly aligned in the direction of the foliation. The biotite-epidote-phengite-albite-titanite assemblage was previously interpreted to have crystallized at amphibolite facies ($\sim$ 1.0–1.5 GPa, 600–650 °C) on the retrograde path (Groppo et al., 2005). Garnet occurs as anhedral grains with a black oxide rim, suggesting that it is out of equilibrium with other minerals. Sharp et al., 1993 calculated temperatures of 700–750 °C from oxygen isotope thermometry of garnet–quartz–rutile in orthogneiss samples, similar to the peak temperatures recorded in whiteschists, suggesting that garnet and rutile represent relict UHP phases. No oxygen isotope data were available for phengite, but the cores of large phengites preserve high Si contents (6.97 $\pm$ 0.04 Si pfu), which are suggestive of HP metamorphism. Biotite was out of oxygen isotopic equilibrium with the garnet-quartz-rutile assemblage, which is consistent with it forming during retrogression (Sharp et al., 1993).

Whiteschists consist of a matrix containing quartz, phengite, kyanite and rutile $\pm$ jadeite $\pm$ tourmaline $\pm$ monazite $\pm$ zircon. Within the matrix there are large pyrope megablasts (up to 10 cm diameter) and small pyrope porphyroblasts (0.5–1 cm). Pyrope megablasts in my samples display two zones with differing garnet composition and inclusion assemblages. The cores (Prp I, $Prp_{92-97}Alm_{2-6}Grs_{1-2}$) contain inclusions of kyanite, talc, rutile, ellenbergerite, phlogopite and sometimes Mg-chlorite (sample DM1.1). The phlogopite is K-deficient and similar to that identified by Schertl et al., 1991. Ellenbergerite shows large compositional variation (0–4.3 wt% TiO_2, 0–2.2 wt% ZrO_2, 0–12.6 wt% P_2O_5) associated with the substitutions Si + Al $\rightarrow$ P + Mg and (Ti,Zr) + Mg $\rightarrow$ 2Al (Chopin et al., 1986). The megablast rims (Prp II) are almost entirely free of Ca and contain inclusions of phengite, coesite, quartz (after coesite), kyanite, talc, rutile and occasionally tourmaline (sample 15597). Small pyropes (Prp II, $Prp_{87-93}Alm_{6-12}Grs_1$) contain the same inclusion assemblage as the pyrope megablast rims. The outermost rim of the pyrope megablasts is replaced by fibrous phengite and phlogopite. Three generations of phengite are recognisable in the whiteschist: inclusions in Prp II (phengite I), matrix phengite (phengite II), breakdown products on pyrope rims (phengite III). Mean Si contents are very similar in Phe I (7.15 $\pm$ 0.06 pfu [22 O pfu]) and II

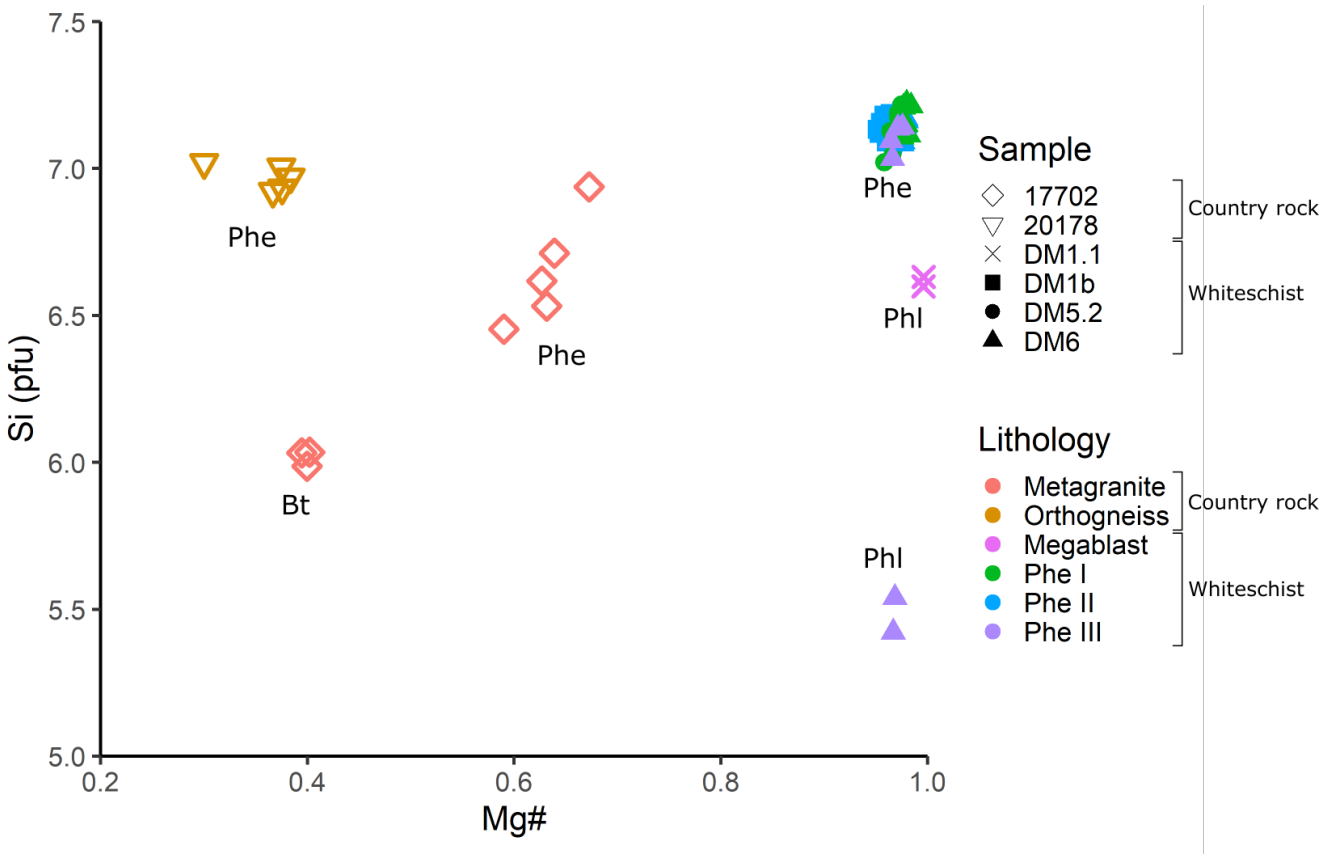


Figure 17: Si (pfu) and Mg number ($Mg/(Mg+Fe^{2+})$) in white mica and biotite. Colours represent the textural affinity of each analysis. For example, Phe III includes phengite as well as the associated phlogopite (see text for details, [Sample descriptions and major element compositions]

(7.14 ± 0.04 pfu) and slightly lower in Phe III (7.10 ± 0.05 pfu) but all three populations overlap significantly (Figure 17). $Mg/(Mg+Fe^{2+})$ is >0.85 in all whiteschist minerals, consistent with the high bulk rock value. My petrographic observations fit with the previously described phase evolution of the whiteschists (e.g. Ferrando et al., 2009; Schertl et al., 1991). Tourmaline occurs only in rare samples (Table 6), which were described in detail by Xiong et al., 2022. Tourmaline in these samples occurs only in the matrix and as inclusions in Prp II, alongside coesite/quartz, phengite, talc and kyanite.

Phengite schists are mineralogically variable but all contain significant amounts of phengite and quartz. Samples in this study also contain tourmaline and were described by Xiong et al., 2022. Other minerals present in the matrix include chlorite, phlogopite, muscovite, paragonite, garnet, kyanite and talc.

Sample	Textural position	Mineral	n	N	Li	B	Be	Rb	Sr	Cs	F	Cl	H_2O (wt%)
17702	Replacing Bt	Phe	5	72	547	64	16	1291	8.5	67	2909		3.7
	Replacing Pl	Phe	2		404	205	5.7	431	28	10	2017		4.2
	Igneous	Kfs	4		6.1	6.1	1.4	384	231	6.9	8.1		
	Igneous	Bt	4		914	2.5	7.3	1278	2.2	99	6199		
20178	Matrix	Phe	14	41*	160	277	17	586	9.9	9.2	1683	80	3.9
		Bt	2		646	1.2	4.6	1005	25	52	4600	1163	
		Ep	1	5	0.20	2.6	3.6	0.58	757	1	184		
		Ab	1	0.7	0.04	3.6	3.2	0.8	17	0.8	2.8		
DM1.1	Megablast core	Phl	2		11	50	2.9	172	15	19	5695	352	4.8
		Tlc	2		0.17	8.0	0.07	0.1	0.15	0.01	1316	601	3.8
		Ell	9		0.38	21	6.1	0.04	0.07	0.16	262	138	6.9
DM6	Megablast core	Ell	2		0.04	8.4	7.1	<0.01	0.11	2.2	130	84	6.1
	Megablast mantle	Ell	2		0.34	6.7	4.2	0.03	0.10	0.38	290	384	6.1
		Tlc	1	3.4	1.4	0.92	0.02	0.32	0.07	<0.01	3597	82	3.6
		Grt											
	Matrix pyrope	Grt	1.0	1.2	11	0.24					34		
	Megablast rim/ matrix pyrope	Phe I	5	39	71	272*	11	414	21	4.2	1389*	21	4.0
	Matrix	Phe II	9	29	68	188	11	390	17	3.5	2178	82	3.8
	Retrograded megablast rim	Phe III	5	208	53	196	11	409	20	3.8	1407	120	3.6
		Phl	1		65	33	3.0	67	1.7	0.81	8360		4.1
		Grt											
DM5.2	Matrix pyrope	Grt	2		9.9	0.27	<0.01	0.17	0.02	0.06	55		
		Phe I	10		54	231	11	388	19	3.7	1658		3.9
		Tlc	1		0.25	6.2	0.08	0.24	0.23	0.01	2905		3.4
	Matrix	Phe II	12		68*	193*	11	372	19	3.4	2296		3.9
DM1b	Matrix pyrope	Grt	1	0.61	14	1.1					41		
	Matrix	Phe II	16	17	45	358	9.7	339	12	5.5	2411	54	
	Retrograde pyrope rim	Phl	2		28	17					12542	118	

Table 7: SIMS trace element and H_2O data for selected minerals in whiteschist and country rocks. Concentrations in µg/g. n represents number of repeats. * denotes the mean exluding outlier data points. See text for discussion.

4.6 Mineral trace element and isotope compositions

4.6.1 Trace elements and H_2O

In the metagranite the Ti-rich phengites are enriched in B, Be and Sr compared to their parent biotites, and depleted in Li, Cs and F. Rb is very similar (Figure 18, Table 7). The Ti-poor phengites have lower Be, Rb, Cs, F, Li but higher B and Sr compared to Ti-rich phengites. K-feldspar contains large amounts of Sr and minor Rb but is otherwise not a significant host of trace elements. In the orthogneiss, phengite is rich in B, having similar contents to the Ti-poor phengite in the metagranite. Phengite is also the main host of Be and a significant host of Rb, Li and F. Biotite is the main host of Rb, Li, Cs, F and Cl, and epidote dominates the budget of Sr.

In the bulk rock, whiteschists are enriched in Mg, and depleted in Na, Ca, Fe, Sr, Rb and Li compared to the metagranite and orthogneiss (Schertl and Schreyer, 2008). Of the prograde minerals present as inclusions in Prp I, phlogopite has the highest concentrations of Li, B, Rb, Cs, Sr and F of all the minerals measured (sample DM1.1). Ellenbergerite is a significant host of Be, which correlates positively with Mg content, and a minor host of B, F and Cl. Ellenbergerite also contains large amounts of H_2O (6.0–8.8 wt%) compared to other minerals (Tlc: 3.5 wt%, Phl: 4.5–5.1 wt%). The K-deficient phlogopite present as inclusions in Prp I contains higher H_2O contents than "normal" phlogopite coexisting with Phe III (4.1 wt%). All other trace elements are present in negligible amounts. Talc hosts only Cl, and minor F and B. Kyanite is not a significant host of any of the measured trace elements. No N data were collected for these phases.

Compared to phlogopite, ellenbergerite and talc, whiteschist phengite in the matrix and as inclusions in Prp II is strongly enriched (>3x) in Li, B and Rb, and slightly enriched (1–3x) in Be and Sr (Figure 18). F contents are lower than phlogopite but similar to talc, and Cl is much lower in phengite than any of the earlier prograde minerals. Whiteschist DM6 contains all three phengite generations and has the most complete record of their trace element evolution. Li, Be, Rb, Sr, Cs and Cl contents are similar in all phengite generations. B contents are similar in Phe II and III (172–202 µg/g) but higher in Phe I (240–292 µg/g, one outlier grain with 189 µg/g). F is high in Phe II (2047–2253 µg/g) and lower in Phe I and III (1195–2066 µg/g). N contents in Phe I range from 37–41 µg/g, whereas N contents in Phe II range from 14–53 µg/g. Phengite III has elevated N

contents (64–530 µg/g, n=5) compared to other phengites. Phengite in other whiteschists contains mostly similar trace element concentrations to DM6, although B is notably higher in DM1b (342–402 µg/g), and Sr and Rb are slightly lower. Whiteschist phengite is depleted in N, Be, Li, Rb and Cs compared to metagranite phengite, and enriched in B and Sr. Whiteschist phengite has similar B contents to orthogneiss phengite, but Li, Be, Rb and Cs are lower in whiteschists, and Sr and Be are higher.

4.6.2 Boron isotopes

Boron isotope data is presented in Figure 19. In the metagranite, δ^{11}B values for Ti-rich phengite are -11.9 to -7.9 ‰ (n=5). Ti-poor phengite has lower, but overlapping values (-13.0 to -9.2, n=2). Orthogneiss has a larger range of δ^{11}B values (-15.4 to -5.7 ‰, n=8).

Phengite δ^{11}B in tourmaline-absent whiteschists ranges from -15.4 to -3.5 ‰ and therefore overlaps with both of the protolith lithologies. Both samples from Case Ramello have similar values (DM6 -15.3 to -8.0 ‰, DM5.2 -13.0 to -5.4 ‰), whereas the sample from Tapina has heavier values (-8.0 to -3.5 ‰). There is no significant difference between the mean δ^{11}B values of different phengite generations from the same sample, but Phe I has a wider range of δ^{11}B values than Phe II or III. There are no correlations between B concentrations and δ^{11}B of phengite in any of the samples that I analysed.

Tourmaline-bearing whiteschists and phengite schists were also analysed for B isotopes in tourmaline and phengite (Phe II). There are significant systematic differences in B concentration and isotopic composition of phengite in samples with and without tourmaline, even if both are from the same locality (Case Ramello). Here, Phe II in tourmaline-bearing samples has a mean B isotope composition of -6.0 ± 1.0 ‰ (n=26) with 198 ± 20 µg/g B. Phe II in tourmaline-absent samples has a consistently lighter B isotope composition (-10.6 ± 1.2‰, n=25) and contains less B (171 ± 14 µg/g). Phe I in these samples has a larger range of B isotope values (-10.3 ± 2.6‰, n=16) and B concentrations (196 ± 34 µg/g). Tourmaline from these samples has δ^{11}B values ranging from -10.7 to -1.4 ‰ (mean = -5.1±1.8 ‰ (n=56)). Phengite in phengite schist from other localities (samples 26405, 17618) has heavier δ^{11}B than Case Ramello for both phengite (26405 -4.5 to -0.7 ‰, 17618 -6.7 to -4.9 ‰) and tourmaline (26405: -1.8 to +0.3 ‰, 17618: -1.5 to +0.5 ‰ [one outlier -6.5

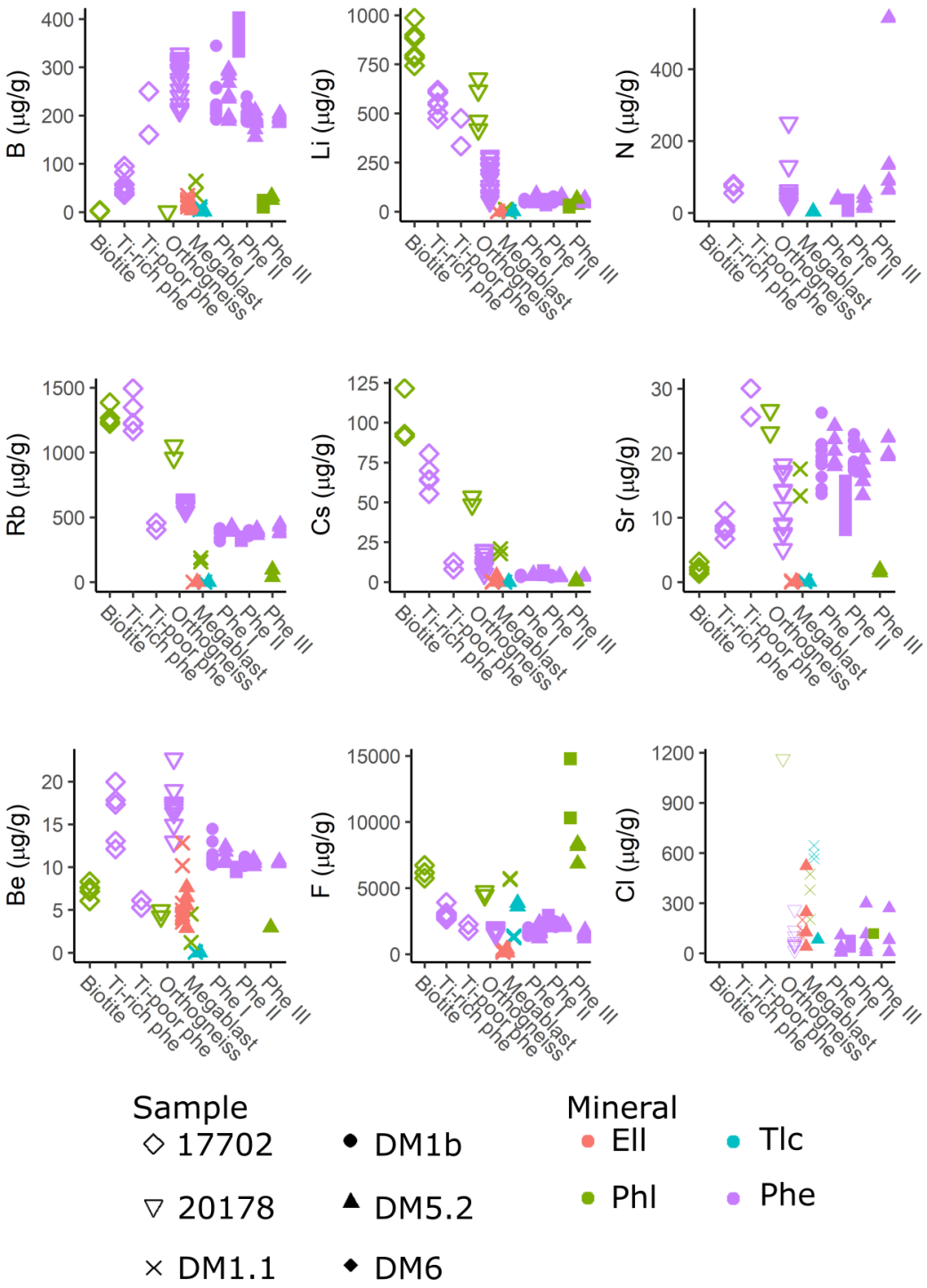


Figure 18: SIMS trace element concentrations for white micas, biotite, ellenbergerite and talc in metagranite (sample 17702), orthogneiss (sample 20178) and whiteschist (DM samples). Metagranite minerals are separated into texturally distinct categories (biotite, Ti-rich phengite, Ti-poor phengite , see 'Sample descriptions and major element compositions' section for details). Orthogneiss minerals are texturally related and so are plotted under one category. Whiteschist minerals are also separated into texturally distinct categories. Megablast consists of inclusions in pyrope megablast cores (Prp I). Phe I, II and III are different textural generations of phengite. Phe III is texturally associated with phlogopite, which is plotted under the same category in a different colour (see legend).

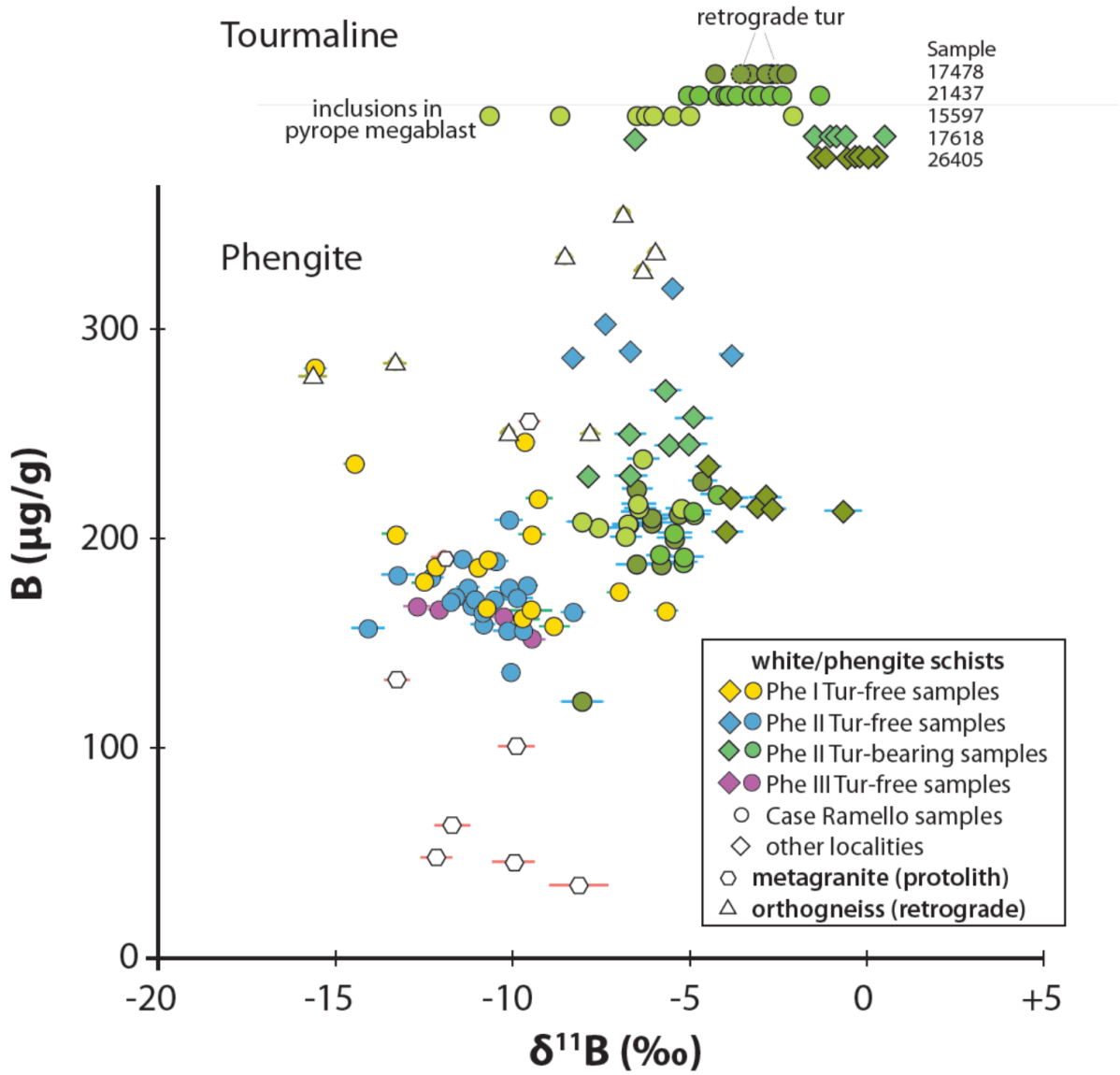


Figure 19: *Top panel:* δ^{11}B values in tourmaline from whiteschist and phengite schist. Uncertainties are smaller than symbol size. *Bottom panel:* δ^{11}B versus B concentration plot for phengite with 1s error bars. δ^{11}B is variable between different grains within the same sample but there are no strong correlations between δ^{11}B and B concentrations. Whiteschist and phengite schist divided into samples from Case Ramello (circles) and samples from other localities (diamonds). Case Ramello samples have heavier δ^{11}B and higher B contents in samples which contain tourmaline compared to those without (see text for discussion). Also shown are phengites from the metagranite and orthogneiss.

‰]). Some tourmaline grains have a narrow rim of ca. 50–150 µm which is around 1 ‰ lighter than the core of the grain. In samples where both tourmaline and phengite are present, the difference in boron isotope composition between coexisting matrix phengite (Phe II) and tourmaline is small but somewhat variable, with mean $\Delta^{11}B_{Phe-Tur}$ of -1.6, -2.6 and -5.0 ‰ in three separate samples. The difference between tourmaline rims and immediately adjacent phengite grains ranges from -3.7 to -1.1 ‰ (one outlier at +4.3 ‰).

4.7 Discussion

4.7.1 Element mobility during whiteschist prograde metamorphism: implications for fluid sources

The whiteschists underwent several major mineralogical changes during their metamorphic evolution, which are critical to understanding the fluid-mobile element evolution, and are divided into six stages (A-F; Figure 20). In this section I review the key reactions which lead to the formation of different mineral assemblages, and discuss the budget of major and trace elements associated with these reactions, to gain insight into element mobility.

4.7.1.1 Key prograde mineral reactions

Prp I (garnet megablast cores) formed by the reaction kyanite + Mg-chlorite + talc → pyrope + H_2O (Ferrando et al., 2009; Schertl et al., 1991). It is Mg-rich, and contains Mg-rich inclusions, which implies that Mg-metasomatism took place before the onset of garnet growth. The earliest prograde assemblage is preserved as inclusions in some pyrope megablast cores and consists of Mg-chlorite, kyanite, talc and rare muscovite (stage A, Figure 20). Crystallization pressure for this assemblage has been constrained to ∼ 1.7–2.1 GPa based on the Si content of muscovite (6.36 Si pfu Ferrando et al., 2009; Hermann, 2003). Therefore Mg-metasomatism took place during the early part of the subduction history, or prior to subduction altogether. Based on the most recent prograde P-T path published for the BIU (Groppo et al., 2019), a temperature estimate of 520–540 °C can be obtained from these pressures. Most pyrope megablasts also contain the inclusion assemblage ellenbergerite, talc, phlogopite, kyanite and rutile (stage B). This assemblage formed on the prograde path by the

reactions Mg-chlorite + kyanite + talc + rutile → ellenbergerite, and Mg-chlorite + muscovite → kyanite + phlogopite + talc + H_2O (Ferrando et al., 2009; Schertl et al., 1991). During the later prograde evolution, the reaction phlogopite + kyanite + talc → pyrope + phengite + H_2O replaces phlogopite with phengite (Hermann, 2003; Schertl et al., 1991), and grows additional Prp I (stage C). All the mentioned reactions also create fluid. Talc is found as inclusions in pyrope megablasts and small pyropes but not in the matrix so talc-out occurred later on the prograde path compared to ellenbergerite or phlogopite. Phase equilibrium modelling suggests that talc breakdown occurs gradually, over a wide P-T range, but that a final phase of fluid release occurs at ∼ 700–710 °C at >3.8 GPa (stage D), close to the metamorphic peak, by the reaction talc + kyanite → pyrope + coesite + H_2O (Gauthiez-Putallaz et al., 2016). This reaction grew Prp II (megablast rims and matrix garnet) which contains the inclusion assemblage kyanite + talc + coesite (Ferrando et al., 2009; Hermann, 2003; Schertl et al., 1991).

4.7.1.2 Element mobility during prograde reactions

The phlogopite breakdown reaction (phlogopite + kyanite + talc → pyrope + phengite + H_2O) is of particular interest in assessing the trace element mobility during prograde metamorphism, since both the products and reactants are significant hosts of fluid-mobile elements. Using the measured compositions of prograde phlogopite, phengite, pyrope and talc, and assuming pure kyanite, I calculated the stoichiometry of the phlogopite breakdown reaction by mass balancing K_2O, MgO, Al_2O_3, SiO_2 for the products and reactants. Then, using the measured H_2O contents of the products and reactants, I calculated the mass of H_2O released. The calculated stoichiometry (by mass) is 1.72 phlogopite + 0.55 talc + 0.84 kyanite → 1 phengite + 2.03 pyrope + 0.07 H_2O. By volume the stoichiometry is 1.79 phlogopite + 0.58 talc + 0.68 kyanite → 1 phengite + 1.57 pyrope + 0.15 H_2O. More phlogopite is consumed than phengite is produced because the measured phlogopite composition is deficient in K_2O. In order to balance the MgO contents, this leads to a large production of pyrope. This is problematic because if all the phengite in the whiteschists (∼ 25–50 vol%) was produced by this reaction, then the total product volume would be close to or greater than 100%. Since there are no other K-bearing phases which could break down to form phengite during prograde metamorphism, this suggests that phengite was in fact present throughout the prograde evolution,

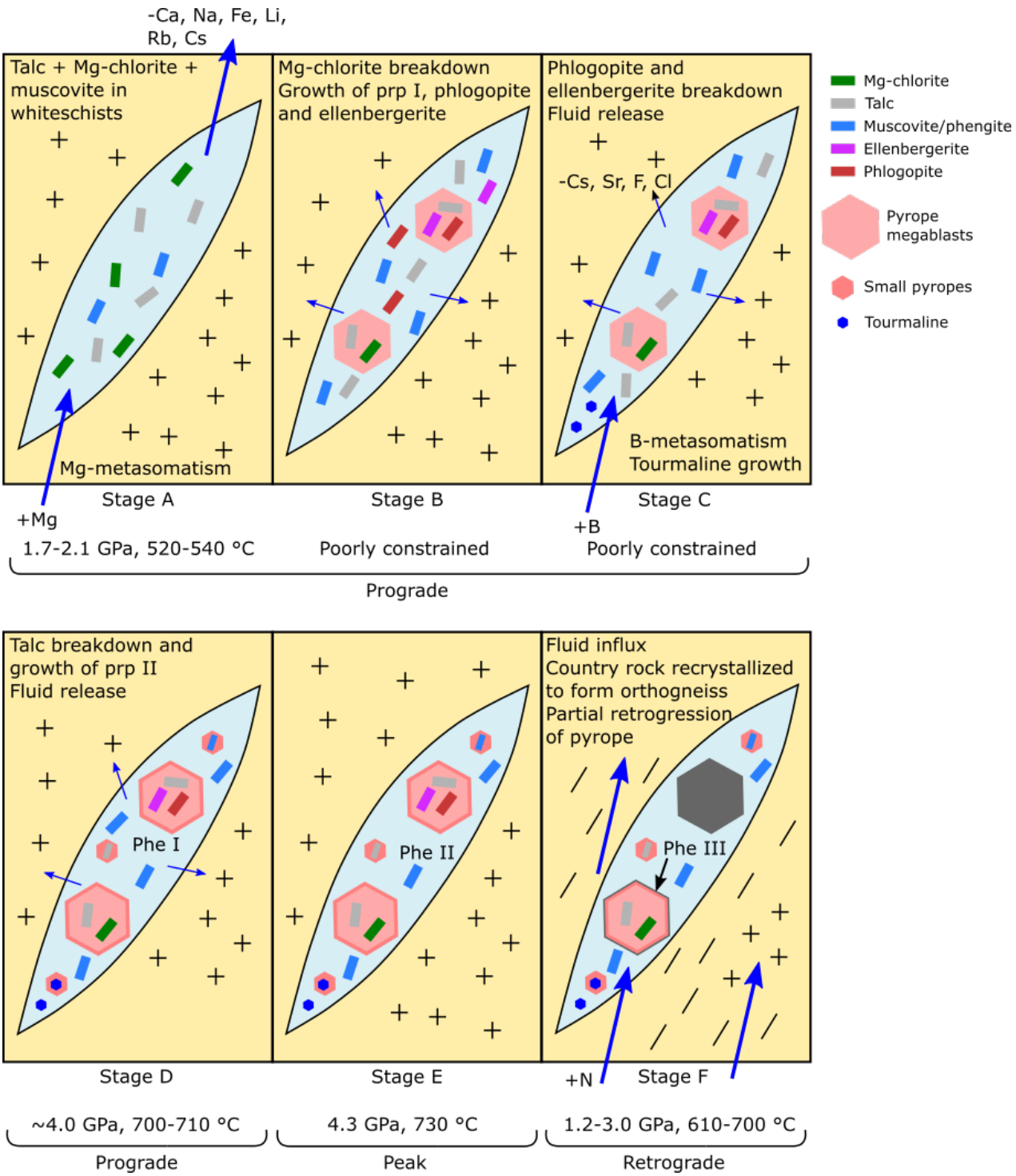


Figure 20: Metasomatic and metamorphic evolution of the whiteschists. P-T conditions for prograde stages B and C are poorly constrained because this part of the prograde path is largely constrained from other lithologies which are difficult to correlate with the whiteschist mineralogy. Large blue arrows indicate external fluid fluxes, whereas small blue arrows indicate internally derived fluids.

which is consistent with the thermodynamic modelling of Gauthiez-Putallaz et al., 2016. Schertl et al., 1991 found a single prograde phengite as an inclusion within a kyanite inclusion in Prp I, which is consistent with my conclusion. The reason why phengite inclusions are so rare in Prp I may relate to compositional heterogeneity in the whiteschist (Hermann, 2003). Phlogopite formed via reaction of Mg-chlorite and muscovite and therefore, in chlorite-rich domains, muscovite could be largely consumed during the formation of phlogopite. Since the first pyrope-forming reaction also involves Mg-chlorite as a reactant, these Mg-chlorite-rich domains also likely gave rise to the pyrope megablasts, which preserve the prograde inclusion assemblages. Prograde phengite would have been stable in the chlorite-poor matrix (see Figure 20) but it re-equilibrated at peak conditions and is not preserved. This is consistent with the experimental phase equilibria of Hermann, 2003, which show that phengite is stable under SiO_2-saturated conditions (matrix), whereas phlogopite is stable under SiO_2-undersaturated conditions (megablasts).

Of the reactant phases in the phlogopite breakdown reaction, kyanite is not a significant host of any trace elements that I measured, talc contains only F and minor B, and phlogopite is a significant host for multiple trace elements. Of the product phases, phengite hosts multiple trace elements, whilst garnet only contains significant amounts of Li. Compared to the later forming phengite, phlogopite contains less Li, B, Be and Rb, slightly less Sr, and substantially higher Cs and F. Ellenbergerite is also a significant host of B and Be. Using the reaction stoichiometry calculated for phlogopite breakdown and the phlogopite and talc trace element compositions measured from DM1.1, the trace element budget of the reactants can be calculated (Table 8). Comparing this budget to the measured compositions of Phe I and Prp II, there is not enough Li, B, Be and Rb in the phlogopite + talc assemblage to account for the measured phengite composition, if all of the trace elements in the products were sourced from phlogopite breakdown (i.e. there was no phengite/pyrope coexisting with phlogopite). For Sr, there is a slight excess in the reactant minerals compared to the products, and for Cs, F and Cl there are large excesses. The contribution of ellenbergerite cannot be assessed quantitatively using this method because the reaction through which it breaks down is not known, and likely does not involve phengite. However, the concentration of all these trace elements, except Cl, is lower in ellenbergerite than in phengite (by at least an order of magnitude for all elements except Be) so it would require large modal abundances of ellenbergerite relative to phengite in order

	Mineral	Li	B	Be	Rb	Sr	Cs	F	Cl
Avg. conc. (µg/g)	Ell	0.32	17	6.0	0.02	0.08	0.50	246	153
Avg. conc. (µg/g)	Tlc	0.59	5.7	0.05	0.07	0.12	<0.01	2076	471
Avg. conc. (µg/g)	Phl	11	50	2.9	172	15	19	5695	352
Avg. conc. (µg/g)	Phe I	58	237	11	395	20	3.9	1645	42
Avg. conc. (µg/g)	Prp II	22	<0.01					34	
	Stoichiometry	Li	B	Be	Rb	Sr	Cs	F	Cl
Phl budget (µg/g)	1.72	19	86	4.9	296	27	33	9821	607
Tlc budget (µg/g)	0.55	0.09	4.4	0.04	0.06	0.08	<0.01	729	333
Phe budget (µg/g)	1	58	237	11	395	20	3.9	1645	42
Prp budget (µg/g)	2.03	22	<0.01					69	
Reactants/products		24%	38%	44%	75%	137%	851%	616%	2215%

Table 8: Top panel: trace element concentrations in reactant and product phases involved in the phlogopite breakdown reaction. Ellenbergerite is also shown for comparison since it breaks down at similar conditions to phlogopite. Bottom panel: trace element budgets of the reactant and product phases involved in phlogopite breakdown. See text for calculation details and interpretation (Element mobility during whiteschist prograde metamorphism, and its implications for fluid sources).

to make up the missing concentrations of Li, Be, B and Rb. By comparing the measured Zr, P and Ti contents of ellenbergerite to average bulk contents reported in Schertl and Schreyer, 2008, I calculate that the ellenbergerite mode is unlikely to have exceeded 5% (Appendix B.1), and cannot therefore account for the missing trace elements. These missing concentrations suggest that either there was addition of these elements to the whiteschist during prograde metamorphism, or there is a missing reservoir of these elements which I have not measured. This missing reservoir could be prograde phengite, as there are not any other obvious candidate minerals which are rich in Li, B, Be and Rb. This matches my earlier conclusion from the major element mass balance of phlogopite breakdown. Alternatively, or perhaps additionally, external fluids rich in B, Li, Rb and Be infiltrated the whiteschist during prograde metamorphism and resulted in addition of these elements around stage C (Figure 7). Whiteschist phengites are significantly enriched in B compared to those in the metagranite ($\sim$ 4x enrichment) and coupled with the higher phengite mode in whiteschist, this leads to 10–20x bulk enrichment of B in the whiteschist compared to metagranite, supporting the conclusion that a substantial amount of B was added to the whiteschist during metasomatism.

For Cs, Sr, F and Cl, the excess of these elements in the reactants of phlogopite breakdown compared to the solid products suggests that these elements were liberated into prograde fluids and lost from the bulk rock. High Cl contents in phlogopite (203–474 µg/g), ellenbergerite (41–

522 µg/g) and talc (565–645 µg/g) compared to the measured phengite (5.3–299 µg/g, mean=43 µg/g, excluding 3 outliers with Cl> µg/g) are consistent with the presence of brines during early prograde metasomatism, and the subsequent evolution of the fluid-phase towards a Cl-poor fluid (Ferrando et al., 2009). Phengite-fluid ($D_{Cl}^{Phe-Fl} = 0.001$) and biotite-fluid ($D_{Cl}^{Bt-Fl} = 0.008$) partition coefficients for Cl in UHP eclogites can be calculated from the data in Svensen et al., 2001. Using these values, the Cl content in the fluid coexisting with prograde phlogopite is estimated at 2.5–6 wt%. This is comparable to the values of 3.6–17 wt% calculated by Ferrando et al., 2009 from microthermometry of fluid inclusions in prograde kyanite.

The trace element data therefore suggest that the external fluid composition evolved from Cl-rich during early prograde metamorphism (stage B) to Cl-poor and B, Be, Rb, Li-rich later on the prograde path (stage C). Most previous studies considered only a single major external fluid influx event (Mg metasomatism) followed by predominantly internally-derived fluids (e.g. Chen et al., 2023a; Chen et al., 2019b, 2016; Ferrando et al., 2009; Gauthiez-Putallaz et al., 2016; Schertl and Schreyer, 2008; Sharp et al., 1993; Tian et al., 2019; Xiong et al., 2022). I suggest that later B, Be, Rb, Li-rich fluids were derived from a distinct external source. This is supported by the composition of the orthogneiss: B contents are much higher in orthogneiss phengite than in Ti-rich phengite in metagranite by about a factor of 3. There are no additional B-rich phases in the metagranite which could break down to release B during recrystallization so this suggests that B was added to the orthogneiss during its metamorphic history. Thus, the orthogneiss has experienced B-metasomatism but not Mg-metasomatism. The occurrence of two separate metasomatic event in the whiteschists raises the possibility that different external fluid sources may explain different aspects of the whiteschist geochemistry (e.g. later B-rich vs earlier Mg, Cl-rich fluids), especially if the later event only partially overprinted the first event.

4.7.2 Effects of retrograde fluid addition

In the whiteschists, the retrograde stage is represented by Phe III, which occurs as fibrous phengite + phlogopite coronae on pyrope rims (stage F). These record the reaction pyrope + phengite + H_2O → phlogopite + kyanite + talc, which occurred during retrogression at ∼ 2.5–3.0 GPa, 670–700 °C (Hermann, 2003). This reaction requires fluid input so Phe III and the associated phlogopite record

the composition of retrograde fluids interacting with the whiteschist. There is little difference in B concentrations between Phe II and Phe III. Phe III has highly variable N contents (64–543 µg/g) but all grains are enriched in N compared to other phengite generations (14–41 µg/g), suggesting that N was added during retrogression. Two points measured on the rims of Phe II grains also have elevated N compared to other Phe II analyses and therefore seem to record the same retrograde signal as Phe III. The strong N enrichment in Phe III suggests an interaction with sediment-derived fluids, since sediments are the only common lithology which contains high N contents (100s–1000s µg/g, Johnson and Goldblatt, 2015 and references therein). Phe III contains less F than Phe II, and slightly less Li, but other trace elements are similar. Coexisting phlogopite has slightly higher Li contents than Phe III (65 µg/g vs. 42–61 µg/g), but contains much lower concentrations of all other trace elements, except F. The Li and F depletion in Phe III compared to Phe II may therefore be due to incorporation of Li and F into phlogopite.

4.7.3 Boron isotope constraints on metasomatic fluid compositions

Apart from some rare tourmaline-bearing samples, phengite is the major host for B in the metagranite and whiteschists and records information about B contents and isotopic composition of the metasomatic fluid. I will first discuss the record that phengite provides of the metasomatic fluid composition, and then compare this to the record in tourmaline.

At the conditions of B metasomatism ($\sim$ 600–700 °C), the B isotope fractionation between phengite and fluid is $\Delta^{11}B_{Phe-Fluid}$ = -11.2 to -9.3 ‰, for fluids that are neutral to acidic (Kowalski et al., 2013). Acidic fluids have been assumed in previous B isotope studies in order to explain the marked decrease in B isotope composition of the subducted slab with increasing depth (e.g. Konrad-Schmolke et al., 2016; Peacock and Hervig, 1999). Recent modelling work has suggested that fluids in equilibrium with crustal lithologies at subduction zone conditions should be moderately alkaline (pH 1.5–3 units above neutrality Galvez et al., 2016), which would result in a much smaller phengite-fluid B isotope fractionation (-3.2 to -2.6 ‰ at 600–700 °C, Kowalski et al., 2013). However, tourmaline is only stable in acidic fluids (Marschall et al., 2006b; Morgan and London, 1989) so the growth of tourmaline in my samples suggests that the fluids were in fact acidic. Whiteschist phengite B isotope compositions range from -15.6 to -3.8 ‰ (mean = -10.1 $\pm$ 2.3 ‰), suggesting a fluid composition

between ∼ -6 and +7 ‰, assuming high fluid-rock ratios that completely overprinted the B isotope signature of the protolith (δ^{11}B = -8 to -13 ‰), or somewhat higher δ^{11}B if fluid-rock ratios were low. In any case, independent of the composition of the fluid, and as long as temperature is comparable, the source lithology of the fluid will have had a δ^{11}B value comparable to phengite in my samples (ca. -10 ‰), as in most subducting lithologies, B will be hosted in minerals with similar B coordination as phengite, which is what controls B fractionation. There is some heterogeneity in phengite B isotope compositions within samples and particularly between different localities, suggesting that the fluid composition may have been variable or multiple episodes of fluids of different compositions were recorded. Phengite B contents in whiteschist range from 155–344 µg/g. Reported phengite-fluid partition coefficients for B in HP rocks range from 0.2–0.7 (Adam et al., 2014; Brenan et al., 1998; Marschall et al., 2006a), which suggests that B concentrations in the metasomatic fluid were in the range of 220–1720 µg/g, assuming element concentrations in phengite were not affected by changes in mineral modal abundance subsequent to fluid-rock interaction. As K_2O appears to have behaved conservatively during metasomatism (Schertl and Schreyer, 2008) and phlogopite, the only other K-bearing phase, was only stable during a short section of the prograde path, I conclude B in phengite reflects equilibrium with the B-rich fluid. This is supported by limited variation of B in different phengite generations and between samples. Thus, the B-rich fluid contained ca. 500 µg/g with a δ^{11}B of 0 ± 6 ‰.

Previously proposed sources for an Alpine metasomatic fluid include slab serpentinite (Ferrando et al., 2009; Sharp and Barnes, 2004), mantle wedge serpentinite (Chen et al., 2016; Tian et al., 2019) and altered oceanic crust (AOC) (Demény et al., 1997; Sharp et al., 1993). Fresh MORB contains 1.2 µg/g B and depleted mantle contains 0.08 µg/g B so these cannot be sources of B-rich fluids during subduction (Marschall et al., 2017). AOC has variable B isotope values from -4 ‰ to +25 ‰, with an average of +3.4 ‰ (Smith et al., 1995), and B contents of up to 100 µg/g, but averaging to values <10 µg/g since the B content depends strongly on the degree of alteration (Marschall, 2018; Smith et al., 1995; Yamaoka et al., 2012). AOC itself is therefore unlikely to be a source of B-rich, isotopically light fluids. Lighter isotope signatures can be generated by slab dehydration during subduction (Marschall et al., 2007) but this also depletes B, so deep AOC-derived fluids which are both B-rich and isotopically light are therefore highly unlikely. Slab-hosted serpentinites have

δ^{11}B $> +10$ ‰ (Clarke et al., 2020; De Hoog and Savov, 2018; Martin et al., 2020), so my isotopic composition for the metasomatic fluid is not consistent with a pure slab serpentinite source.

Mantle wedge serpentinites form by hydration of the dry mantle wedge by fluids derived from the subducting slab. Shallow (forearc) mantle wedge serpentinites can have high B contents (up to 80 µg/g) and heavy B isotope compositions (+15 to +25 ‰) (De Hoog and Savov, 2018 and references therein), whereas deep mantle wedge serpentinites have a range of B isotope values from +3 ‰ down to around -14 ‰, averaging to ca. -5 ‰ (De Hoog and Savov, 2018; Martin et al., 2020). The latter would be consistent with my suggested isotopic composition of the metasomatic fluid. However, these deep antigorite serpentinites contain <60 µg/g B, averaging to ca. 20 µg/g (De Hoog and Savov, 2018; Martin et al., 2020; Yamada et al., 2019). Major fluid release from serpentinites occurs mainly during antigorite breakdown at ca. 650°C. The amount of fluid released is 6–13 wt%, depending on the serpentinite composition (Padrón-Navarta et al., 2013; Ulmer and Trommsdorff, 1995), with B contents in the fluid (150–330 µg/g, based on 20 µg/g bulk B and 6-13 wt% fluid release) in the lower end of the range calculated for the metasomatic fluid (220-1720 µg/g, see above). However, up to 30 µg/g B can be retained in metamorphic olivine formed during antigorite breakdown (Clarke et al., 2020; De Hoog et al., 2014), which would reduce the amount of B released in the fluid. Fluid transport modelling suggests that B contents in fluids released from mantle wedge serpentinites could reach up to ca. 200 µg/g (Konrad-Schmolke et al., 2016), similar to my simple estimate, although fluid inclusions in HP antigorite serpentinites measured by Scambelluri et al., 2004 had lower B contents (1–50 µg/g, but mostly <20 µg/g, for bulk rock B contents ∼10 µg/g). Overall, fluids generated purely from dehydration of mantle wedge serpentinite are unlikely to explain the high B contents in the metasomatic fluid as recorded by phengite. Earlier fluids that caused Mg metasomatism likely contained B, and these may indeed have been derived from serpentine dehydration, but the majority of B in the rocks appears to be have been derived from other sources. The B isotope composition of the Mg-rich fluids is not preserved in phengite, since it was overprinted by the later B-rich fluids.

Sediments are another potential source of B-bearing fluids in subduction zones. Carbonate sediments have very heavy B isotope compositions (>20 ‰), but other oceanic sediments (e.g. pelagic clays, siliceous ooze, turbidites) can have negative B isotope values down to -13 ‰, with most values falling between -10 to 0 ‰ (Ishikawa and Nakamura, 1993; Marschall, 2018; Tonarini et al., 2011).

Boron contents are mostly in the range 50–150 µg/g. Fluids sourced from subducted sediments are consistent with the negative B isotope values of whiteschist phengite and and can also explain the high B contents calculated for the metasomatic fluid. White mica hosts >80% of the B in most meta-sedimentary rocks (Bebout et al., 2007; Marschall et al., 2006a). The average K_2O content of subducted sediments (excluding carbonates) is $\sim$ 2.5 wt% (Plank, 2014), which results in $\sim$ 25% white mica mode in the meta-sediment. Therefore whole rock B concentrations of 50–150 µg/g translate to white mica B concentrations of 120–360 µg/g, which is similar to the range in whiteschist phengite, and therefore whiteschists could be in equilibrium with a sediment-derived fluid.

4.7.4 Comparison with previous evidence for fluid compositions

Whiteschist trace elements do not present a clear argument in favour of either serpentinite or sediment-derived fluids. There is no enrichment in Ni and Cr in the whiteschists compared to their protoliths (Schertl and Schreyer, 2008). These elements are commonly enriched in serpentinite-derived fluids (e.g. Angiboust et al., 2014; Penniston-Dorland et al., 2010), including in mantle-wedge serpentinites (Martin et al., 2020), and the lack of enrichments in these were used to argue against serpentinite-derived fluids in the metasomatism of Monte Rosa whiteschists (Luisier et al., 2021). On the other hand, the whiteschists are depleted in many large ion lithophile elements (Na, Rb, Ba, Sr) compared to their protoliths, and these elements are commonly enriched in sediment-derived fluids (e.g. Sievers et al., 2017a; Sorensen et al., 1997). K is a major exception to this, behaving rather conservatively in the whiteschists despite its high solubility in HP fluids (Connolly and Galvez, 2018), which suggests metasomatic fluids were probably K-rich, or else K would have been leached from the rocks (Luisier et al., 2021).

Previous studies discounted sediments as a source for the metasomatic fluid on two main grounds. The whiteschists have light oxygen isotopes (whole rock $\delta^{18}O$=7.4–8.4 ‰, Gauthiez-Putallaz et al., 2016, Sharp et al., 1993, Chen et al., 2016), which are much lower than values for sediments. Additionally, fluids derived from sediment dehydration have low Mg contents (Herviou et al., 2021; Manning, 2004), which does not explain the Mg enrichment in whiteschists. Magnesium isotope data are also consistent with a talc-bearing serpentinite source for the fluid (Chen et al., 2016). Due to the high oxygen concentrations of rocks, resetting of whole rock O isotope signatures requires large

fluid-rock ratios. If the amount of B-rich fluid was small compared to the earlier Mg-metasomatism then O isotopes would likely still reflect the Mg-rich fluid source. *In situ* O isotopes have been measured in garnet, zircon, quartz, kyanite and phengite (Chen et al., 2017; Gauthiez-Putallaz et al., 2016; Sharp et al., 1993). The extent of zircon O isotope resetting during fluid-rock interaction is known to be variable (Rubatto, 2017). Other anhydrous minerals (garnet, quartz, kyanite) may also be expected to respond slowly to fluid-rock interaction. For phengite, there was a difference between the measured O isotope composition and the value predicted by closed-system fractionation, which was attributed to issues with fractionation factors and inter-sample comparison (Gauthiez-Putallaz et al., 2016), but could alternatively reflect a partial resetting of hydrous mineral O isotopes by B-rich fluids. As B metasomatism was separate from Mg metasomatism, neither the Mg-rich nature of the whiteschists, nor the Mg isotope data present a difficulty for my model, as Mg is a structural component of the main rock-forming minerals in whiteschists, and therefore requires large fluid-rock ratios to reset. In contrast, Li is a much more fluid-mobile element and is therefore likely to have been affected by fluid influx during B metasomatism. This may explain the lack of correlation between bulk Li concentrations, Li isotopes, and other isotope systems, as reported by Tian et al., 2019. Furthermore, significant kinetic isotope fractionation of Li can occur during garnet growth at HP conditions (Bebout et al., 2022). This could be significant in the whiteschists due to the large modal abundance of garnet, and adds to the complexity of interpreting the Li isotope data. Finally, recently published Ba isotope data (Chen et al., 2023a) are consistent with either a sediment-derived fluid or a mantle wedge serpentinite-derived fluid, since the Ba isotope signature of mantle wedge serpentinites is inherited from the slab-derived crustal fluids that formed them. Thus, a two stage model where the second stage involves a dominantly sediment-derived fluid is consistent with my own as well as previous isotope data.

Although the majority of B appears to have been sourced from sediments, it is possible that the B metasomatic fluid also contained a serpentinite-derived component, but this would have contributed little B due to the lower concentration of B in serpentinites. Several studies of serpentinite dehydration have observed open system behaviour, where dehydrating serpentinite is fluxed by B-rich, isotopically light, sediment derived fluids (Clarke et al., 2020; Harvey et al., 2014). The sediment-derived component can comprise at least 15-45% of the total fluid budget leaving the serpentinite,

and the resulting fluid would conceivably have mixed characteristics in terms of B contents and isotopes as well as other elements. This represents an alternative scenario of generating a mixture of sediment and serpentinite-derived geochemical signatures in the whiteschist. It would be difficult to distinguish such fluids from fluids derived from mantle-wedge serpentinites, which themselves formed by metasomatism of mantle peridotite by slab-derived crustal fluids.

Finally, it is worth noting that the whiteschists and associated metasomatic rocks constitute a volumetrically minor part of the entire Brossasco-Isasca UHP Unit. External fluids which affected the whiteschists therefore must have traversed a significant portion of the rest of the unit to reach the whiteschists, including metasediments. So it is possible that the sedimentary B isotope signature of the metasomatic fluids was acquired locally during transport and that the original source of the fluids has been obscured. Nevertheless, this would not explain Mg metasomatism, so does not affect my interpretation that these were distinct fluid infiltration events.

4.7.5 The differing records of tourmaline and phengite boron isotopes

Rare tourmaline-bearing samples (<1% of all samples) of metagranite, orthogneiss, whiteschist and phengite schist provide an additional window into B behaviour during metasomatism. My own B isotope data for tourmaline in these rocks matches data presented by Xiong et al., 2022. They explained the compositions of metasomatic whiteschist tourmaline by reaction of isotopically light tourmaline in the metagranite (-13.3 to -5.5 ‰) with isotopically heavier fluid (>+2.4 ‰: the fluid in equilibrium with the heaviest measured tourmaline) derived from dehydration of mantle wedge serpentinite (Mg metasomatism). If tourmaline grew during Mg metasomatism, then its B isotope composition should be unrelated to that of phengite, which I have argued was acquired during later B-metasomatism. Figure 21 shows the B isotope composition of a hypothetical phengite in equilibrium with tourmaline at prograde to peak conditions. This overlaps with the range of phengite B isotope compositions observed in tourmaline-absent samples, suggesting that tourmaline and phengite could therefore have equilibrated with the same B-rich fluid during B-metasomatism. High B concentrations in the fluid would explain the crystallization of tourmaline at this stage (stage C, Figure 20). This timing of tourmaline growth is supported by the observation than most tourmaline occurs in the matrix or as inclusions in prp II. Tourmaline inclusions in prp I are very rare (none were observed in

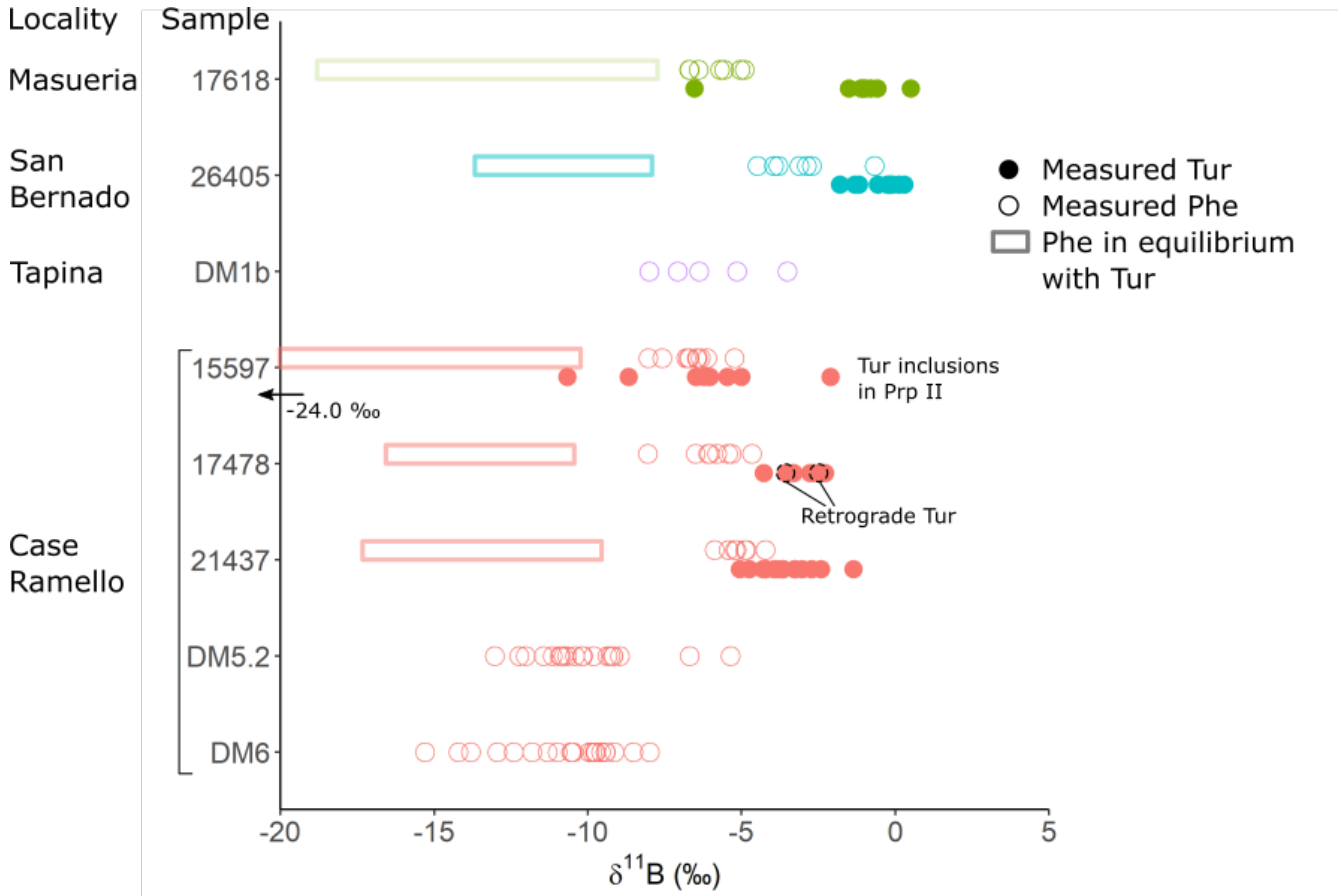


Figure 21: δ^{11}B values in tourmaline and phengite from whiteschist and phengite schist. 1s uncertainties for tourmaline are smaller than symbol size. Also shown is the range of δ^{11}B values which would represent phengite in isotopic equilibrium with tourmaline (see text for discussion). Phengite and tourmaline are therefore not in isotopic equilibrium in samples where both are present. Where tourmaline-bearing and tourmaline-absent samples are available for the same locality (Case Ramello), phengite in tourmaline-bearing samples has heavier δ^{11}B and higher B contents than in tourmaline absent samples (see text for discussion).

this study but they were documented in at least one sample by Schertl et al., 1991). Inclusions in prp I may reflect igneous tourmaline from the protolith that was recrystallized during Mg-metasomatism as suggested by Xiong et al., 2022 for sample 15597. The large variation of tourmaline B isotope values in this sample reflects incomplete re-equilibration with external fluid, whereas the relatively small range of tourmaline B isotope compositions in other samples suggest complete (re-)crystallization with a fluid, likely during B metasomatism.

In samples where both tourmaline and phengite are present, the boron isotope fractionation between coexisting matrix phengite (Phe II) differs significantly from predicted equilibrium fractionation between tourmaline and mica (observed $\Delta^{11}B_{Phe-Tur}$ = -1.6 to -5.0 ‰, predicted $\Delta^{11}B_{Phe-Tur}$

= -12.3 ‰ at 530 °C (early prograde conditions) and -8.2 ‰ at 730 °C (peak conditions), Figure 21, Klemme et al., 2011; Kowalski et al., 2013; Wunder et al., 2005). Furthermore, Phe II in tourmaline-bearing samples contains more B and has a heavier B isotope composition than Phe II in tourmaline-absent samples from the same locality (Case Ramello). Phe II in tourmaline-bearing samples could have interacted with a separate, isotopically heavier fluid to Phe II in tourmaline-absent samples, and to tourmaline itself. Tourmaline was not affected by this fluid due to a kinetic control, as B diffusion in tourmaline is slow as it is a structural component. Thus, isotopic disequilibrium could be preserved. As B isotope fractionation is strongly pH dependent, a change in fluid pH from tourmaline to phengite crystallisation may also have played a role. Alternatively, the fact that the anomalous B isotope composition of phengite only occurs in samples which contain tourmaline, which is a B-rich mineral, suggests that tourmaline may be involved in generating the anomalous composition. This would require some process to occur after B metasomatism which drove the phengite and tourmaline B isotope compositions away from equilibrium, and could explain the presence of thin rims on some tourmaline grains which have a B isotope composition ca. 1 ‰ lighter than the rest of the grain.

It is unclear which of these scenarios best explains the anomalous composition of phengite in tourmaline-bearing samples, but my data indicates that caution should be applied interpreting phengite from tourmaline-bearing samples as representing equilibrium B isotope fractionation. It is important to note that tourmaline occurs only very rarely in whiteschists (<1% of whiteschists and other related metasomatic rocks contain tourmaline), and that phengite from tourmaline-absent samples dominates the whiteschist B budget at the outcrop scale. Therefore, my interpretation of the fluid sources recorded by B isotopes are unaffected by these anomalous tourmaline-bearing phengites.

4.8 Wider implications

The occurrence of whiteschists and similar Mg-rich rocks hosted within metagranitoids has been documented in multiple locations across the Alps (Ferrando, 2012 and references therein). They occur in units that reached a range of peak P-T condition from greenschist facies right up to UHP eclogite facies. My study shows that the Dora-Maira whiteschists record multiple periods of fluid influx, which occurred over a range of P-T conditions experienced during subduction, suggesting that

they may represent a long-lived fluid pathway. Such pathways may transport multiple generations of fluids, not just those which led to their initial formation, and thus subduction-zone related rocks likely exhibit polymetasomatism. This may help to explain the conflicting interpretations put forward for the formation of different whiteschist bodies (e.g. Dora-Maira (my work and references herein) versus Monte Rosa (e.g. Marger et al., 2019; Pawlig and Baumgartner, 2001)).

4.9 Conclusions

Dora-Maira whiteschist are strongly enriched in Mg and B compared to their granite protolith. Multiple lines of evidence point to the conclusion that the majority of B was added to the whiteschist at a later stage to the Mg-metasomatism, which produced the unusual major element composition. Firstly, mass balance analysis of the metamorphic reactions which occurred during prograde metamorphism allows us to trace the gain or loss of different elements. My calculations suggest that there is an excess of B, Li, Rb and Be in the phases present during peak metamorphism compared to prograde phases and therefore that these elements were added by external fluids during prograde metamorphism. Secondly, high B concentrations and light δ^{11}B values in whiteschist phengite point to sediments as the main source of B-rich fluids. In some samples, tourmaline also grew during this stage and recorded B isotope compositions in equilibrium with the same fluid. Whiteschist phengite is more useful than tourmaline for recording the B concentration in the metasomatic fluid, since B behaves as a trace element in micas, and fluid compositions can be directly calculated using partitioning data. Finally, the protolith orthogneiss records similarly high B concentrations in phengite but has not undergone Mg metasomatism, which further supports the separation of B and Mg metasomatic events. These conclusions fit with the previously proposed idea that fluid evolved from Mg-Cl brines to Cl-poor, aluminosilicate-rich fluids during prograde metamorphism (Ferrando et al., 2009), and they further constrain the trace element contents of these fluids. The B data imply that multiple external fluid inputs were present throughout prograde metamorphism, suggesting that the whiteschists may record a long-lived fluid pathway. This study demonstrates the utility of *in situ* analyses in unravelling complex fluid-rock interaction histories, where whole rock analyses make it difficult to distinguish between different stages of fluid-rock interaction. Polymetasomatism of subduction-related rocks may result in decoupling of isotopic signatures for different elements.

Acknowledgements

I thank C. Hayward for help with EPMA analyses. This work was supported by a UK Natural Environment Research Council Doctoral Training Partnership grant (NE/ S007407/1) and UK Natural Environment Research Council Ion Microprobe Facility grants IMF 699/1119 and IMF 740/0522. Comments by three anonymous reviewers and editor Daniella Rubatto greatly improved the manuscript.

4.10 Post-script

In this chapter I presented a detailed case study of using B isotopes, and other FME concentrations in white micas to identify fluid sources and trace element redistribution processes in subduction-related metasomatic rocks (question 3). I argued that negative B isotopes associated with high B concentrations in white mica are a strong indicator of metasomatism by sediment-derived fluids, and that white micas are more useful for identifying such a signature compared to tourmaline because B concentrations in white mica are more directly related to the B concentration in the fluid which they interacted with. I focused less on N concentrations in this chapter because they were generally low and rather homogeneous in the prograde and peak generations of phengite (phe I, II). However, I did observe N-enrichment in early retrograde micas (phe III) compared to those which formed at UHP conditions, similar to, but of even greater magnitude than, the retrograde N-enrichments observed in UHP rocks from Lago di Cignana in Chapter 3.

5 Chapter 5: Partitioning, distribution and sources of nitrogen in subducted oceanic crust

5.1 Preface

In this final research chapter, I analyse the behaviour of N in a larger set of samples representing subducted oceanic crust from a range of localities around the world. I expand upon the work begun in Chapter 3 to thoroughly investigate the relative importance of white micas, other minerals, and non-mineral phases such as fluid inclusions or grain boundaries in contributing to the N budget of subducted metabasic rocks (question 1). I do this by combining N concentrations in minerals and mineral modal abundances to reconstruct the proportion of N hosted in each mineral, and comparing this with measured whole rock N concentrations to assess the proportion of N hosted in mineral and non-mineral sites. I also conduct a more detailed examination of the inter-mineral partitioning of N, B and Li and investigate possible differences in partitioning at different P-T conditions (question 2b).

The samples that I investigated have a range of major element compositions that encompass some of the important styles of hydrothermal alteration in oceanic crust. I compare the composition of HP rocks to those found on the seafloor to show how the seafloor alteration style affects the modal abundance and composition of white micas present at HP conditions, and I discuss the implications of different alteration styles for the N budget of subducted crust. Finally, I use a range of FME, alongside B isotopes to constrain the sources of N in HP metabasic rocks (question 3) and, in particular, to assess whether they preserve N that was acquired during seafloor alteration, or whether N was primarily added during subduction or exhumation, and if so from which lithologies in the slab it originated (question 4).

5.2 Introduction

Oceanic crust is a major and compositionally diverse reservoir of fluids, trace elements and volatiles in subduction zones. The bulk composition of oceanic crust is significantly altered by hydrothermal

activity on the ocean floor. Alteration can be locally highly variable, due to differences in protolith composition, hydrothermal fluid chemistry, alteration temperature and fluid-rock ratio, but several major alteration styles have been recognised through the study of drill cores in modern oceanic crust, and of ophiolites representing sections through old crust (Bach et al., 2013; Staudigel, 2014). Chloritization involves replacement of olivine and clinopyroxene by chlorite and clays, leading to bulk rock Mg-enrichment and Ca-depletion. Epidotization involves replacement of clinopyroxene and plagioclase by epidote, chlorite and quartz, leading to Ca-enrichment and Na-depletion. Spilitization involves replacement of plagioclase by albite, leading to Na-enrichment and Ca-depletion. Potassium-enrichment occurs via precipitation of the clay mineral celadonite, and tends to be concentrated in the upper ~500 m of the oceanic crust, with little K-enrichment below that depth, and potentially K-depletion instead (Bach et al., 2003; Schramm et al., 2005; Staudigel, 2014). Several studies have investigated the effect of oceanic alteration on the mineralogical evolution of metabasalts during subduction, and the effect this has on their ability to transport and release water (e.g. Hacker, 2008; Hernández-Uribe et al., 2020; Kerrick and Connolly, 2001) and carbon (e.g. Collins et al., 2015), but less attention has been given to the effect of alteration on the N cycle in subduction zones. The importance of K-enrichment in stabilizing phengite, an important N host, has widely been recognized, but less attention has been given to other phases such as paragonite, amphiboles, clinopyroxene and chlorite, which are also potential hosts for N.

Hydrothermal alteration of oceanic crust produces enrichment in N (up to 75 μg/g, Bebout et al., 2018; Busigny et al., 2019, 2005; Li and Li, 2022, 2023a,b; Li et al., 2007) compared to fresh MORB (1.5 μg/g, Li et al., 2007). Nitrogen enrichment does not show systematic trends with increasing depth across any studied core sections and consequently appears to be decoupled from K-enrichment (Busigny et al., 2019; Li and Li, 2022, 2023a,b; Li et al., 2007). Nitrogen-enrichment also does not correlate with changes in Na, Ca or Mg concentrations, demonstrating that the process of N-enrichment in AOC is not related to any common form of major element metasomatism. The heavier δ^{15}N values of most AOC (up to +8.3 ‰) compared to MORB (-5.0 ‰) have been used to argue that the N in AOC is sourced from organic matter and seafloor sediments, which have δ^{15}N of ~0 to +10 ‰ (Bebout et al., 2018; Busigny et al., 2019, 2005; Li and Li, 2022, 2023a; Li et al., 2007). Li and Li, 2023b showed that the average N concentration in the basaltic section of ocean drill cores

correlates positively with the average N concentration in the overlying sediments from that core, supporting this conclusion.

High pressure metabasalts (greenschists, blueschists, eclogites) represent the subducted equivalents of AOC. The N concentrations reported from HP metabasalts overlap significantly with those reported from AOC, but N concentrations greater than 10 μg/g are more common in HP metabasalts than in AOC. Concentrations up to 147 μg/g have been reported in HP samples that interacted with sediment-derived fluids during subduction (Halama et al., 2010, 2017; Li et al., 2021a; Mallik et al., 2023). Nitrogen concentrations less than 10 μg/g with δ^{15}N $<$ -1 ‰ (i.e. MORB-like compositions) have not been reported from HP metabasalts but form a significant population in AOC, suggesting that N addition to HP rocks during subduction (or exhumation) is a common process. The extent of, and controlling factors for, N addition to or loss from AOC during subduction have not been thoroughly investigated.

Most N concentration and isotope data for AOC and HP rocks have been acquired on bulk rock samples, or less commonly on mineral separates. Nitrogen is thought to be primarily speciated as NH_4^+, which could substitute for K^+, Na^+ or Ca^{2+}. In AOC, secondary minerals such as albite, amphibole, celadonite and other phyllosilicates are the most likely hosts of NH_4^+ (Busigny et al., 2005; Li and Li, 2022, 2023a; Li et al., 2007), but the lack of strong correlations between bulk N and K, Na or Ca, and lack of mineral N analyses, makes it hard to assess the relative importance of different minerals. Yu et al., 2023 recently showed that NH_4^+ can be effectively adsorbed onto the surface of a variety of clay minerals, which are common alteration products in AOC, providing an alternative mechanism of N incorporation into AOC. Correlation of bulk N concentrations with other elements such as K, Rb, Ba (Bebout and Fogel, 1992; Busigny et al., 2003a; Halama et al., 2010, 2017) or Na + Ca (Busigny et al., 2011) in HP rocks have been used to argue that N is primarily hosted in micas, or Na, Ca-bearing phases such as clinopyroxene, amphibole and feldspar. However, only two studies have analysed the N concentrations of minerals directly and compared them to bulk rock concentrations to assess the relative importance of different minerals, or other phases such as fluid inclusions, as hosts of N (Pitcairn et al., 2005, Chapter 3 [Harris et al., 2022]). The most common method of bulk analysis is to combust powders at high temperature (~900–1200 °C) under vacuum and measure the liberated N by mass spectrometry. It is known that different temperatures

result in different N yields (Bebout et al., 2018; Busigny et al., 2019; Li et al., 2021b), which could be explained by N fractions that are hosted in different phases, but no studies have investigated this hypothesis and the relative contribution of different phases to the N budget of subducted AOC remains unknown.

Since most previous work on N has been based on whole rock analyses, there is little available data on the partitioning of N between different minerals (Boocock et al., 2023b; Busigny et al., 2004; Duit et al., 1986; Honma and Itihara, 1981; Sadofsky and Bebout, 2000), and almost none from HP rocks (Chapter 3). No studies have investigated the variability of partitioning in different lithologies or at different P-T conditions. This prevents the development of quantitative models of N recycling in subduction zones that combine predicted phase relationships in subducted lithologies with inter-mineral and mineral-fluid-melt coefficients to model the transfer of N between the subducted slab and mantle wedge. These models have proved useful in exploring the relationship between slab metamorphic reactions, fluid release, and the compositions of igneous rocks produced at arcs, for other fluid-mobile elements such as B (e.g. Konrad-Schmolke and Halama, 2014; Konrad-Schmolke et al., 2016; Marschall et al., 2007), and for H_2O recycling into the mantle (e.g. Hacker, 2008; van Keken et al., 2011).

In this chapter I combine *in situ* SIMS analyses of N and other fluid-mobile trace element concentrations in HP minerals, with bulk analyses of N, N isotopes, trace elements and mineral modal abundances in a suite of HP metabasalts. I address four main research aims:

1) Assess the relative importance of micas, other minerals, and non-minerals in hosting N in subducted AOC by comparing mineral N concentrations determined by SIMS, mineral modal abundances, and bulk rock N concentrations determined by sealed tube combustion.

2) Investigate the variability of N partitioning in metabasalts with different peak P-T conditions with a view to expanding my dataset of inter-mineral N partition coefficients.

3) Explore how the compositional variability of AOC affects the stability of N-bearing minerals and the ability of the rock to transport N in subduction zones.

4) Explore the sources of N in subducted AOC.

5.3 Samples

Summary information concerning the location and lithology of each sample as well as peak P-T conditions previously determined for that locality are given in Table 9. A description of the geological background of each locality is not given here but can be found in the references cited in Table 9. All the localities have previously been suggested to represent fragments of oceanic crust that were subducted and exhumed back to the surface. The samples in this study were selected to represent a range of compositions of altered oceanic crust subducted to a range of peak P-T conditions in the greenschist, blueschist and eclogite facies. Representative BSE images are shown in Figure 22. Greenschists contain the typical assemblage actinolite + chlorite + albite + epidote + phengite ± quartz ± titanite. Blueschists have more variable mineralogy but all contain Na-rich amphibole (glaucophane *sensu lato*) and most contain phengite and/or paragonite. Other phases include epidote, garnet, albite, chlorite, and more rarely quartz, actinolite, titanite, rutile, talc, chloritoid, lawsonite, omphacite and carbonates. Eclogites are defined by the appearance of substantial amounts of omphacite, typically alongside garnet, phengite and/or paragonite. Other phases include quartz, epidote, lawsonite, glaucophane, rutile, actinolite, chlorite, albite and carbonates.

5.4 Analytical methods

The analytical methods are detailed in Chapter 2. No SIMS analyses were done on samples EXT00007N, EXT00007Q, DC26A and ZS0713 because they contained significant amounts of mineral alteration. In DC31C, there were unexplained drops in N count rate during most of the analyses, so all analyses from this sample were discarded. This did not appear to affect any of the other samples. Sample 0321 was not analysed by SIMS because it contained biotite. I tried analysing a biotite standard but the N concentrations measured by SIMS (31 ± 6 μg/g, n=7) were far from those previously measured using FT-IR (502 ± 15 μg/g, n=3, Busigny et al., 2004). Analyses of biotite were therefore considered to be unreliable. It is unclear whether this discrepancy results from issues with the SIMS analyses, or with the FT-IR analyses, but further development of SIMS N standards would be a useful direction of future research.

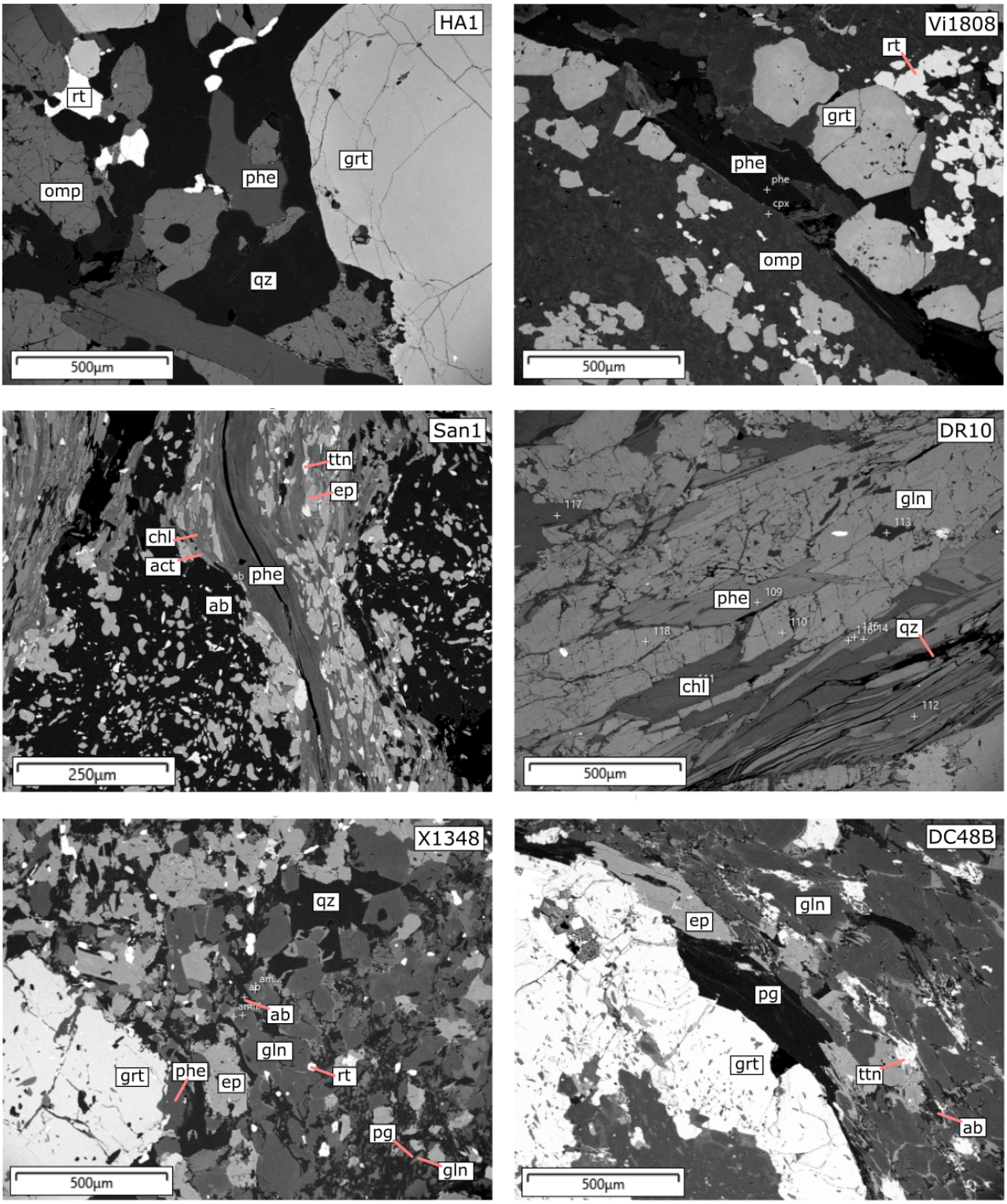


Figure 22: Representative back-scattered electron (BSE) images of samples in this study.

Sample	Locality	Location	Lithology	Pressure (GPa)	Temperature (°C)	Reference
EXT00007N	Chenaillet Massif, France	N 44.89516 E 6.7287	Mg gabbro	1.0 – 1.1	340 – 360	Corno et al., 2023
EXT00007Q	Chenaillet Massif, France	N 44.90209 E 6.74086	Pillow basalt	1.0 – 1.1	340 – 360	Corno et al., 2023
0321	Glockner Nappe, Austria	~N 47.166 E 12.727	Greenschist	0.75 ± 0.2	525 ± 25	Dachs, 1990
San2	Sanbagawa Belt, Japan	Higashi Aiachi area	Greenschist	0.7 – 0.85	440 ± 15	Enami et al., 1994 Otsuki and Banno, 1990
San1	Sanbagawa Belt, Japan	Higashi Aiachi area	Greenschist	0.7 – 0.85	440 ± 15	Enami et al., 1994 Otsuki and Banno, 1990
122	Inzecca Formation, Corsica, France	N 42.39098 E 9.28406	Blueschist	0.8 ± 0.2	350 ± 10	Vitale Brovarone et al., 2013
DR10	Punta Balandra, Dominican Republic	N 19.18270 W 69.22415	Blueschist	1.3 ± 0.2	450 ± 70	Goncalves et al., 2000
X1348	Cycladic Blueschist Unit, Syros, Greece	Syros	Blueschist	1.5 – 2.3	500 – 550	Gyomlai et al., 2021 and refs therein
X1008	Cycladic Blueschist Unit, Syros, Greece	W of Kambos, Syros	Blueschist	1.5 – 2.3	500 – 550	Gyomlai et al., 2021 and refs therein
DC26A	Zermatt-Saas Unit, Western Alps	N 46.04907 E 7.82492	Blueschist	2.3 ± 0.1	540 ± 20	Angiboust et al., 2009
DC48B	San Marcel Valley, Italy	N 45.70806 E 7.45389	Blueschist	2.1 ± 0.3	550 ± 60	Martin et al., 2008
DC46A	San Marcel Valley, Italy	N 45.70167 E 7.45556	Blueschist	2.1 ± 0.3	550 ± 60	Martin et al., 2008
DC31C	Zermatt-Saas Unit, Western Alps	N 46.03464 E 7.83645	Blueschist	2.3 ± 0.1	540 ± 20	Angiboust et al., 2009
DC46B	San Marcel Valley, Italy	N 45.70167 E 7.45556	Blueschist	2.1 ± 0.3	550 ± 60	Martin et al., 2008
C13	Lawsonite-eclogite Unit, Corsica, France	Summit of Mt. San Petrone	Eclogite	2.2 – 2.4	500 – 535	Vitale Brovarone et al., 2011
DR9	Punta Balandra, Dominican Republic	N 19.18270 W 69.22415	Eclogite	1.3 ± 0.2	450 ± 70	Goncalves et al., 2000
HA2	Sanbagawa Belt, Japan	Higashi Aiachi area	Eclogite	2.3 – 2.4	675 – 740	Miyamoto et al., 2007
HA1	Sanbagawa Belt, Japan	Higashi Aiachi area	Eclogite	2.3 – 2.4	675 – 740	Miyamoto et al., 2007
Vi1808	Lago Superiore Unit, Western Alps	N 44.70194 E 7.08528	Eclogite	2.6 – 2.75	530 – 550	Angiboust et al., 2012
ZS0713	Zermatt-Saas Unit, Western Alps	N 45.83722 E 7.61250	Eclogite	2.3 ± 0.1	540 ± 20	Angiboust et al., 2009
0275	Lago del Mucrone, Italy	~N 45.628 E 7.942	Eclogite	1.3 – 1.5	500 – 600	Zucali et al., 2002
ZS15	Zermatt-Saas Unit, Western Alps	N 46.01615 E 7.83461	Eclogite	2.3 – 2.5	530 – 550	Angiboust et al., 2009

Table 9: Location, lithology and peak P-T conditions of the samples used in this study. The references are for P-T conditions of samples from the same unit, not specifically the samples in this study.

5.5 Results

5.5.1 Bulk rock major and trace elements

Bulk rock major element and N data for all samples are shown in Table 10. Selected trace element data are shown in Figures 23, 29 and 31 and full data are listed in Appendix A.3. All the sample localities in this study were selected because they have previously been documented to host rocks with oceanic basalt protoliths. All samples except two (HA1, HA2) contain 45–53 wt% SiO_2 (Table 10), which is consistent with a basaltic protolith. Variation of fluid-immobile trace elements such as Ti, Nb, Y, Ce and Zr is a common tool for discriminating basalts from different tectonic settings (e.g. Pearce, 1996). A Nb/Ce–Ce/Y plot (Figure 23) shows that samples are distinct from the ocean island basalt (OIB) composition of Sun and McDonough, 1989, whereas Nb/Ce–Y distinguishes samples from arc basalts (Turner and Langmuir, 2022). On both plots samples scatter roughly around the mean composition of ALL MORB (Gale et al., 2013), consistent with previous work that

suggested these sample localities represent fragments of subducted oceanic crust. K_2O and Na_2O concentrations, which are important markers of oceanic alteration, range from 0.02–1.8 wt% and 0.24–5.9 wt% respectively in samples, compared to 0.16 wt% K_2O, 2.79 wt% Na_2O for MORB (Gale et al., 2013) and 0.01–8.10 wt% K_2O, 0.12–6.73 wt% Na_2O for AOC (Bach et al., 2003; Belgrano and Diamond, 2019; Coogan et al., 2017; Heft et al., 2008; Kelley et al., 2003).

Sample	Lithology	SiO_2	Al_2O_3	Fe_2O_3	MgO	CaO	Na_2O	K_2O	TiO_2	MnO	P_2O_5	LOI	N (μg/g)	δ^{15}N (‰)
EXT00007N	Mg gabbro	49.7	22.5	3.8	7.2	9.3	3.9	0.06	0.21	0.08		3.1	26.6	0.9
EXT00007Q	Pillow basalt	47.9	14.5	9.9	5.6	11.7	3.5	0.02	1.6	0.15	0.21	4.8	18.6	-10.1
0321	Greenschist	48.1	17.2	10.5	10.7	4.2	3.9	0.77	1.5	0.12	0.14	2.5	22.1	7.8
San2	Greenschist	47.3	14.2	11.0	7.3	11.4	2.5	0.26	1.2	0.16	0.11	4.2	22.1	5.0
San1	Greenschist	48.0	15.5	10.8	7.6	8.4	3.3	0.46	1.4	0.20	0.14	3.9	14.0	4.6
122	Blueschist	47.6	15.7	10.5	7.9	6.9	4.4	0.12	2.0	0.17	0.14	4.5	99.9	-4.3
DR10	Blueschist	46.5	10.3	7.6	14.7	7.5	2.2	1.8	0.55	0.15	0.11	8.4	245	5.0
X1348	Blueschist	52.3	16.4	9.8	4.4	8.3	4.4	0.37	1.8	0.21	0.29	1.5	31.5	4.2
X1008	Blueschist	52.9	15.2	11.5	6.1	6.1	3.5	0.95	2.2	0.16	0.33	1.1	61.0	4.6
DC26A	Blueschist	52.0	15.1	9.1	7.7	7.2	4.6	0.25	1.6	0.13	0.22	2.1	30.1	1.1
DC48B	Blueschist	51.2	15.2	9.4	6.5	8.4	5.0	0.03	1.9	0.15	0.27	1.8	22.3	-3.6
DC46A	Blueschist	47.7	14.4	10.6	6.0	10.9	2.7	0.28	1.5	0.16	0.09	5.4	13.4	3.1
DC31C	Blueschist	51.4	16.8	8.6	7.8	5.8	4.9	0.33	1.8	0.14	0.27	1.9	9.8	0.6
DC46B	Blueschist	52.7	15.2	9.2	10.0	3.3	4.8	0.03	1.7	0.07	0.22	2.8	11.2	-7.5
C13	Eclogite	46.2	16.4	8.8	4.7	14.1	3.0	0.47	1.6	0.24	0.20	4.2	31.3	0.4
DR9	Eclogite	46.2	16.0	11.1	6.2	12.1	2.9	1.3	1.5	0.12	0.08	2.5	88.9	-0.1
HA2	Eclogite	40.5	17.6	17.3	9.0	13.9	0.24	0.02	0.70	0.30		0.13	12.8	3.5
HA1	Eclogite	63.4	12.4	11.5	4.9	4.9	1.6	0.44	0.64	0.20	0.12	-0.45	17.6	-0.3
Vi1808	Eclogite	49.8	12.6	13.9	6.1	9.7	4.0	0.57	2.9	0.18	0.12	-0.13	36.0	-1.7
ZS0715	Eclogite	49.6	17.0	10.1	3.7	10.8	5.3	0.08	1.9	0.13	0.34	0.65	19.8	2.2
0275	Eclogite	48.5	15.5	12.6	6.1	9.5	4.1	1.6	1.9	0.19	0.18	-0.52	15.4	3.5
ZS15	Eclogite	49.4	17.7	8.4	5.1	10.9	5.9	0.05	1.7	0.13	0.20	0.43	13.8	1.3

Table 10: Whole rock major element concentrations (wt%), N concentration (μg/g) and δ^{15}N (‰).

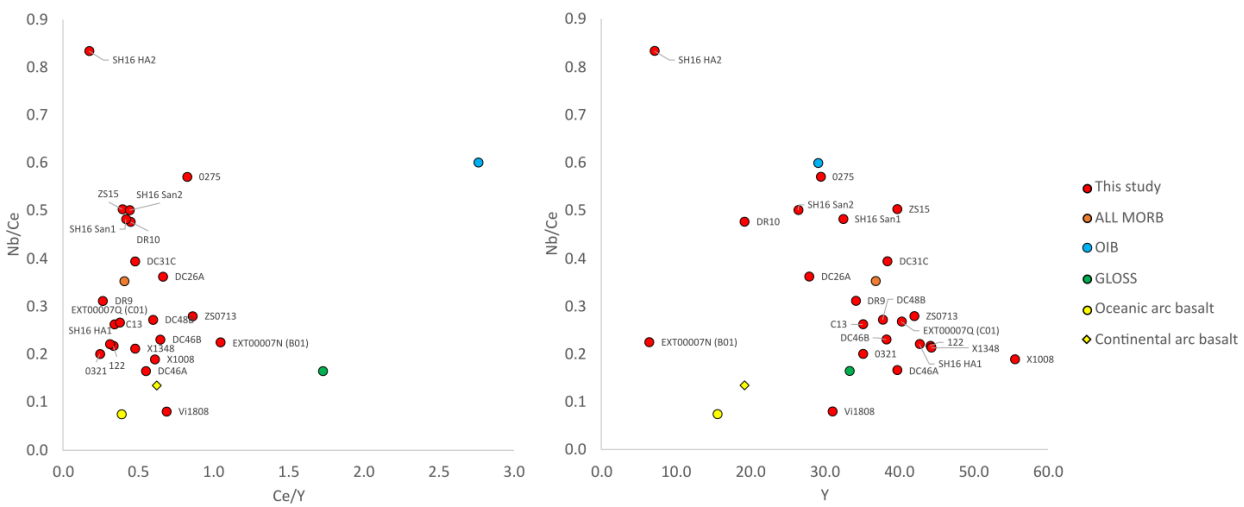


Figure 23: Nb–Ce–Y plots show that my samples are distinct from both OIB and arc basalt compositions. ALL MORB (Gale et al., 2013). OIB (Sun and McDonough, 1989). GLOSS (Plank, 2014). Arc basalt averages from data compiled by Turner and Langmuir, 2022.

Bulk N concentrations measured by sealed tube combustion range from 9.8–245 μg/g with δ^{15}N values from -10.1 to +7.8 ‰ (Table 10). To my knowledge, 245 μg/g N is the highest N concentration reported from a metabasalt to date. Nitrogen concentrations are largely within the range of HP

metabasalts reported in the literature (2.1–147 μg/g, Figure 24, Halama et al., 2010, 2017; Li et al., 2021a; Mallik et al., 2023), but low N concentrations ($<$ 10 μg/g) that are reported in some literature data are not observed in my samples. The range of δ^{15}N values is similar to previously studied HP metabasalts (-10.9 to + 10.0 ‰). There is no correlation between N and δ^{15}N.

A brief note on comparison with literature data: my N concentrations may be slightly underestimated due to the lower combustion temperature compared to other studies, but as noted above, my samples are already more N-rich than many literature data so this does not significantly affect my conclusions. More importantly, Li et al., 2021b showed that pre-heating samples at 400 °C during overnight evacuation results in 40-80 % lower N yields compared to pre-heating at $<$ 200 °C. For this reason, I do not plot any data from Busigny et al., 2019, 2011, 2005 in Figures 24 and 25 since they were obtained using pre-heating at 300-450 °C and are therefore not comparable to my data. The effects of pre-heating are discussed further in section 5.6.4.

5.5.2 Mineral major and trace elements

White mica major element compositions are classified using four end members: muscovite ($K_2Al_6Si_6O_{20}(OH)_4$), celadonite ($K_2(Mg,Fe^{2+})_2Al_2Si_8O_{20}(OH)_4$), paragonite ($Na_2Al_6Si_6O_{20}(OH)_4$) and margarite ($Ca_2Al_8Si_4O_{20}(OH)_4$). Phengites contain a substantial celadonite component (6.54–7.47 Si atoms per formula unit, 22 O pfu), minor paragonite component (Na/(K+Na+Ca) = 0.00–0.15) and negligible margarite component (Ca/(K+Na+Ca) $<$ 0.01). Paragonites contain very little celadonite (5.88–6.09 Si pfu) and minor muscovite and margarite (K/(K+Na+Ca) = 0.00–0.13 and Ca/(K+Na+Ca) = 0.00–0.03). Pyroxenes are all omphacite (0.28–0.63 Na pfu, 6 O pfu) with the exception of one sample (HA2), which contains diopside (0.05–0.07 Na pfu, 0.06–0.09 Al pfu, Mg/Mg+Fe^{2+} = 0.88–0.92) due to its unusually low bulk Na content. Amphiboles in samples San1, San2, DR9, DR10, and ZS15 broadly all have $<$ 1 Al pfu (23 O) and $<$ 1 Na pfu, placing them in the field of actinolite-winchite solid solution. Amphiboles from other samples have 1–2 Al pfu and, in most cases, 1–2 Na pfu, placing them in the winchite-glaucophane solid solution. Feldspars are all highly albitic ($X_{ab} = 0.94 - 1.00$) and have neglible K-feldspar component ($X_{kfs} < 0.02$). Epidotes are predominantly clinozoisite-epidote solid solutions (0.27–1.87 Fe^{3+} pfu, 25 O pfu) with minor piedmontite and allanite components in some samples. Chlorites have a range of Mg – Fe^{2+} substitution

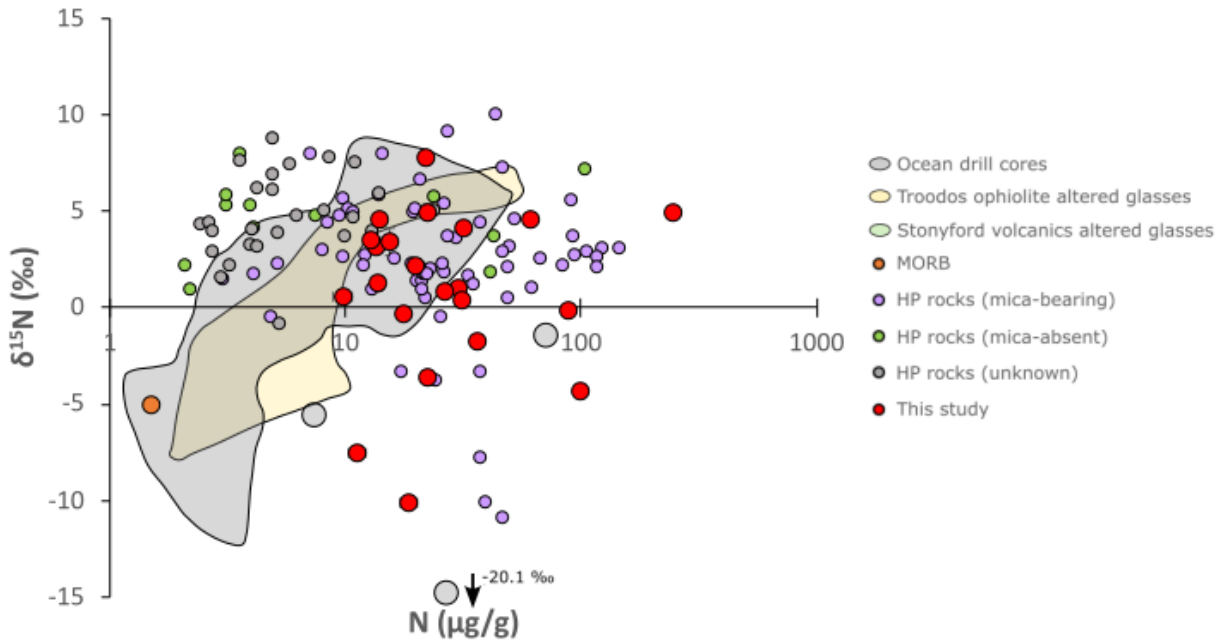


Figure 24: Bulk N–δ^{15}N plot showing my samples and literature data for ocean drill cores, ophiolites and HP rocks. 1s error bars are shown for my own samples, but for most samples the errors are smaller than the size of the markers. HP rocks are categorized by whether they contain mica, according to the petrographic descriptions provided by the authors. Ocean drill cores (Bebout et al., 2018; Li and Li, 2022, 2023a,b; Li et al., 2007). Palagonitized basaltic glasses from the Troodos ophiolite and Stonyford volcanics (Bebout et al., 2018). MORB (Li et al., 2007). Eclogites and blueschists from the Raspas Complex, Lago di Cignana, Cabo Ortegal and Zambezi Belt (Halama et al., 2010). Blueschists from the Heilongjiang Complex (Li et al., 2021a). Blueschists and amphibolites from the Qiangtang Metamorphic Belt (Mallik et al., 2023). Eclogites and blueschists from the Tian Shan orogen (Halama et al., 2017). Data from Busigny et al., 2019, 2011, 2005 are excluded because they followed different analytical protocols which mean their data are not necessarily comparable to the rest of the data plotted here (see Section 2.2).

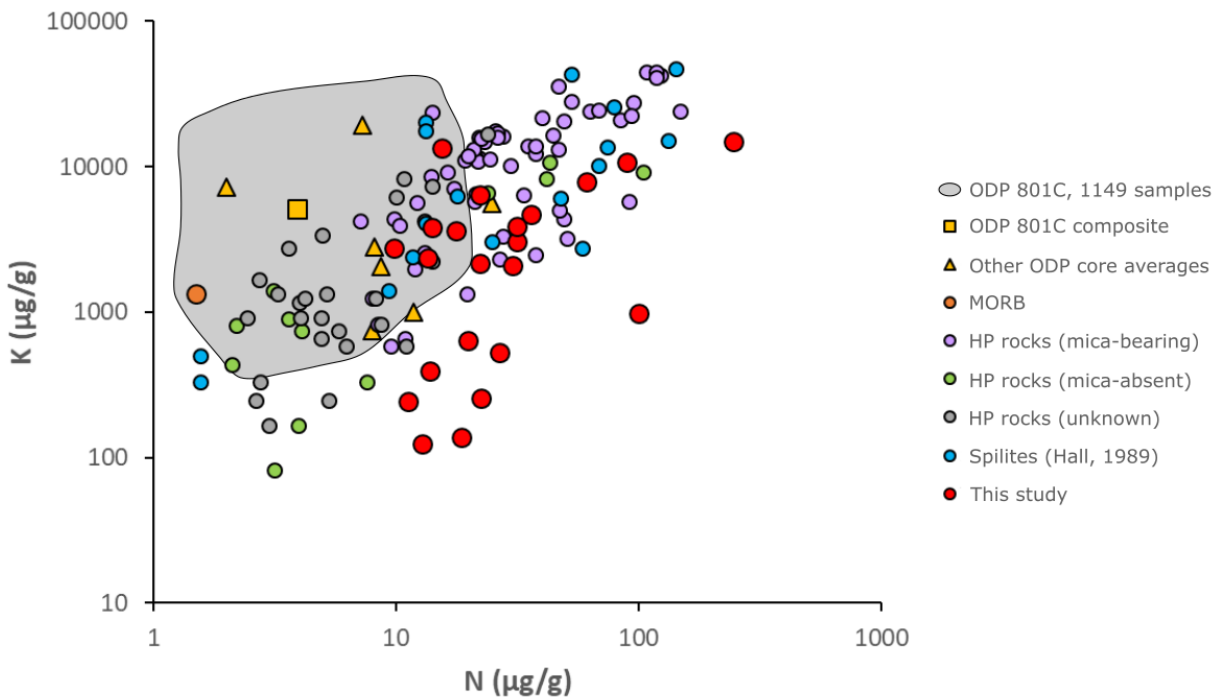


Figure 25: Bulk N–K in my samples, along with literature data on HP rocks and AOC. 1s error bars for my samples are smaller than the size of the markers. HP rocks are categorized by whether they contain mica, according to the petrographic descriptions provided by the authors. The AOC data are rather limited since only the data of Li et al., 2007 (ODP 801C, 1149) have major element data that can be correlated with the N analyses. ODP 801C composite is an average composition of the whole core section weighted by the proportion of different lithologies (Kelley et al., 2003; Li et al., 2007). Average compositions of other ODP cores were compiled by Li and Li, 2023b and are unweighted averages based on analyses of N and K in separate samples from the same core (hence only averages can be plotted rather than a field of individual data points). MORB N concentration from Li et al., 2007 and K from Gale et al., 2013. Eclogites and blueschists from the Raspas Complex, Lago di Cignana, Cabo Ortegal and Zambezi Belt (Halama et al., 2010). Blueschists from the Heilongjiang Complex (Li et al., 2021a). Blueschists and amphibolites from the Qiangtang Metamorphic Belt (Mallik et al., 2023). Eclogites and bluechists from the Tian Shan orogen (Halama et al., 2017). Spilites from SW England (Hall, 1989). Data from Busigny et al., 2019, 2011, 2005 are excluded because they followed different analytical protocols which mean their data are not necessarily comparable to the rest of the data plotted here (see Section 2.2).

($Mg/(Mg+Fe^{2+}$ = 0.51–0.81) and Al contents ranging from 2.25–2.58 pfu (14 O pfu). A detailed investigation of the compositional variation in each sample is outwith the scope of this study but suffice to say that these are typical compositions for these minerals in subducted metabasalts. A list of EDS analyses is given in Appendix Tables 35, 36 and 37.

Phengite is the most N-rich phase measured (7–1034 μg/g N, Figure 26, Table 11), followed by paragonite (2–89 μg/g N). Amphiboles (1–19 μg/g N), omphacite (1–15 μg/g N) and chlorite (1–36 μg/g N) have similar ranges of N concentrations. Epidote contains <1–14 μg/g N, and albite and lawsonite contain <3 μg/g N. Phengite also contains the highest concentrations of Rb and Cs, followed by paragonite and then other minerals. B concentrations decrease in the order paragonite > phengite >> amphibole ≈ omphacite ≈ chlorite > albite ≈ epidote ≈ lawsonite. Li displays more variable behaviour but is generally highest in chlorite, followed by omphacite, then phengite ≈ paragonite > amphibole > epidote > albite. Full SIMS trace element data are listed in Appendix A.3.

5.5.3 Mineral boron isotopes

δ^{11}B values of micas, amphiboles, omphacite and chlorite span a wide range from -23.9 to +16.9 ‰ (Figure 27). Within each sample, δ^{11}B values for each mineral typically vary by 2–5 ‰. Only two samples (Vi1808 and DR9) show strong correlations of B concentration and δ^{11}B. Most samples have a mica-amphibole δ^{11}B fractionation ($\Delta^{11}B_{mica-amph}$) around 0 ± 2 ‰, which is broadly consistent with previous work on B isotopes in blueschist minerals (Pabst et al., 2012). $\Delta^{11}B_{mica-chl}$ is around -5 ± 2 ‰, which is again broadly consistent with previous data. $\Delta^{11}B_{mica-omp}$ is around +5.5 ± 1.5 ‰, which is different to that observed by Pabst et al., 2012, but they only reported two pyroxene analyses in their study, compared to over twenty each for mica, amphibole and chlorite, so it is hard to assess the significance of this discrepancy. Given the lack of significant fractionation between micas and amphiboles, and the fact that all my mica-free samples contain amphibole, I assume that mica and amphibole δ^{11}B values are comparable when discussing the implications of my B isotope data.

5.5.4 Mineral modes

Weight percent mineral modal abundances are shown in Table 12 and Figure 36.

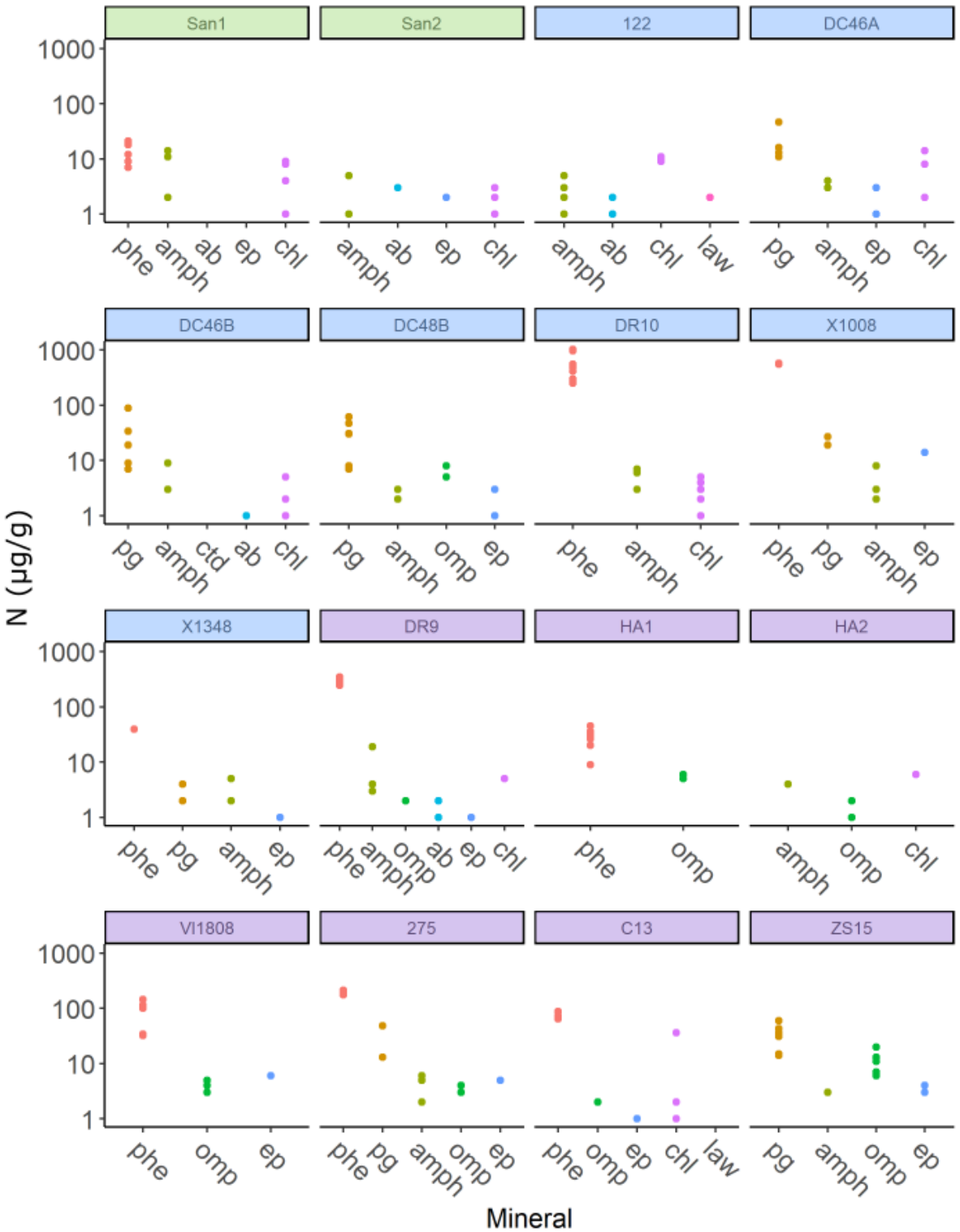


Figure 26: Mineral N concentrations measured by SIMS. Only minerals where SIMS measurements were made are listed. The complete mineralogy of each sample is shown in Figure 36. Samples are coloured by lithology: greenschist (green), blueschist (blue), eclogite (purple).

Sample		Mineral N concentration (μg/g)									
		phe	pg	act	gln	omp	chl	ep	ab	lws	ctd
San1	Mean	14		9.0			5.7	0.5	0.1		
	St dev	5		6.1			4.0				
	n	5		3			4	1	2		
San2	Mean	n.d.		3.1			1.7	1.0	1.8		
	St dev			2.4			0.8				
	n			2			6	2	2		
122	Mean			2.2	2.4		10.1		1.3	2.0	
	St dev			2.0			0.9		0.8		
	n			4	1		3		3	1	
DC46A	Mean		21		3.2		8	1.9			
	St dev		16				6.2				
	n		4		2		3	2			
DC46B	Mean		28		4.3		2.3		1.3		0.4
	St dev		31		2.8		1.7				
	n		6		4		4		2		2
DC48B	Mean		31		2.8	6.5		2.2	2.4		
	St dev		21								
	n		6		1	2		2	1		
DR10	Mean	483			5.6		3.0				
	St dev	294			1.4		1.3				
	n	10			4		5				
X1008	Mean	566	23		4.7			14			
	St dev	173			2.9						
	n	5	2		3			1			
X1348	Mean	39	2.9		3.3			0.8	6.3		
	St dev				1.8						
	n	1	2		3			1	1		
DR9	Mean	281			8.6	5.1	3.8	0.7	1.5		
	St dev	34			9.2	5.3					
	n	8			3	3	2	1	2		
HA1	Mean	28				4.9					
	St dev	12				0.7					
	n	7				6					
HA2	Mean			4.4		1.7	6.1				
	St dev					0.3					
	n			1		4	1				
Vi1808	Mean	85				3.7		5.9			
	St dev	50				0.9					
	n	5				4		1			
0275	Mean	199	31		4.4	3.3		5.0			
	St dev	13			2.4						
	n	9	2		3	2		1			
C13	Mean	76				2	13	0.7		0.4	
	St dev	12					20				
	n	3				1	3	1		1	
ZS15	Mean		33		3.4	12		3.4			
	St dev		17			6		0.5			
	n		6		1	5		3			

Table 11: Mean mineral N concentrations, standard deviations and number of analyses (n) for each sample. Phengite exists in San2 but its N concentration was not determined (n.d.) because the grains were too small to measure.

	Lithology	phe	pg	bt	gln	act	di	omp	grt	ep	ab	qz	rt	ttn	carb	chl	ctd	lws	tlc
San1	Greenschist	4.3				33				19	21	6.0		3.0		14			
San2	Greenschist	2.5				35				31	21					11			
122	Blueschist				7.0	22					35					24		12	
DR10	Blueschist	17			50							5.9			4.2	19			3.8
DC46B	Blueschist		13		44				3.1	11	6.9					11	6.0		6.0
DC46A	Blueschist		2.8		34					41	5.1	8.1	1.4			7.7			
DC48B	Blueschist		10		26	16		3.6	9.1	18	13			3.2		1.4			
X1008	Blueschist	9.0			46				11	16		13		4.9		0.9			
X1348	Blueschist	3.0	4.6		23				17	26	20	4.5	1.1			1.2			
Vi1808	Eclogite	5.0			3.7			53	15	3.5	5.3	7.5	2.8			4.5			
ZS15	Eclogite		13		18			33	8.5	15	8.9	0.7	1.7			1.8			
0275	Eclogite	10	3.0		13			55	14		4.5		1.2			0.8			
DR9	Eclogite	12			8.0			17	17	17	11				6.5	12			
HA1	Eclogite	4.5				3.0		25	21			46	0.6						
HA2	Eclogite					4.2	15		80				0.7			1.4			
C13	Eclogite	4.5			5.0			47								6.4		37	

Table 12: Estimated weight% mineral modal abundances of minerals.

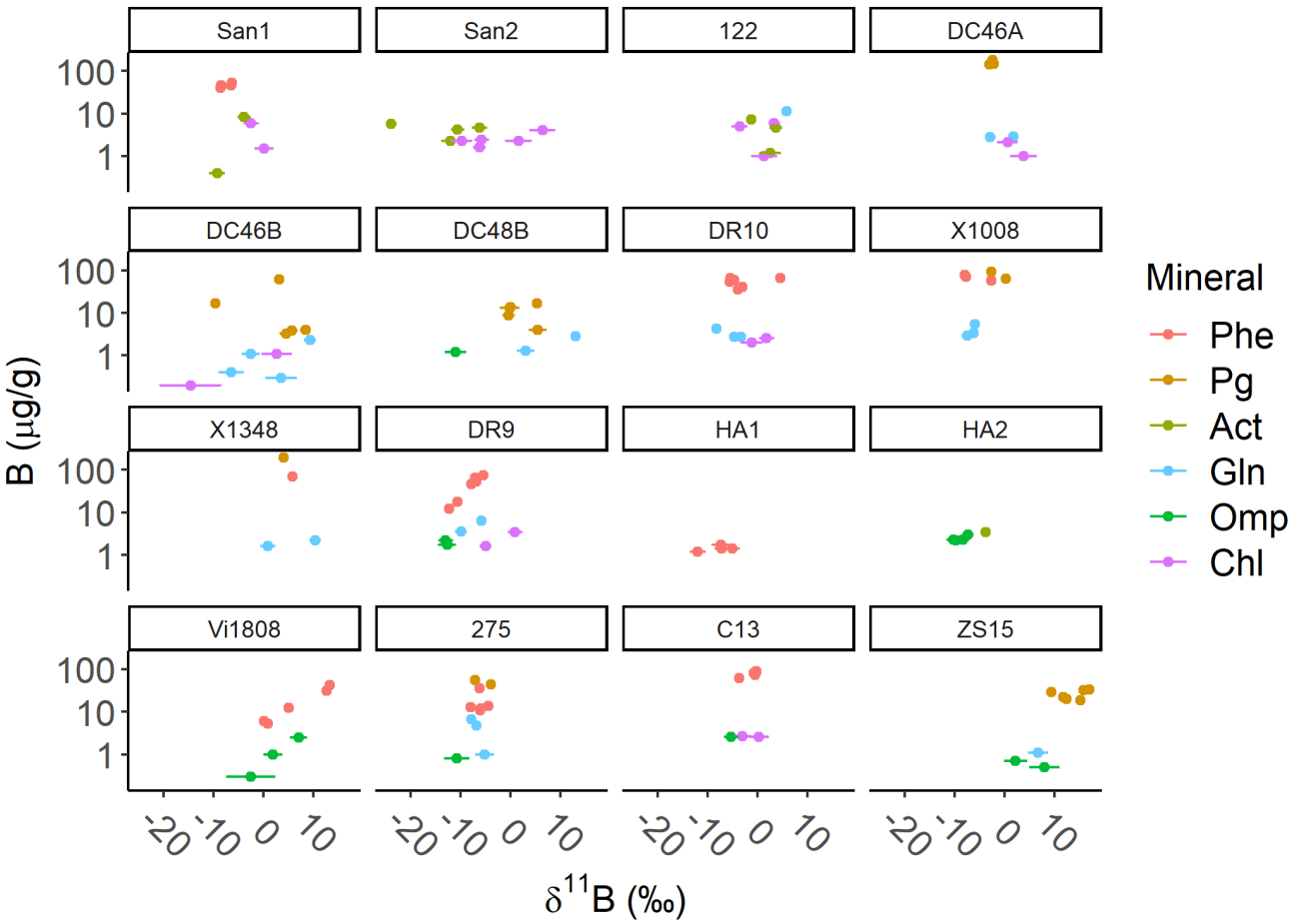


Figure 27: Boron isotope data for micas, amphibole, omphacite and chlorite. 1sd analytical uncertainties for δ^{11}B are shown where they are larger than the size of the points.

5.6 Discussion

5.6.1 Effects of seafloor and subduction-related alteration

5.6.1.1 Major elements and mineralogy

The major oceanic alteration styles of chloritization, spilitization and epidotization can be distinguished on CaO–Na_2O–MgO ternary plots (e.g. Hernández-Uribe et al., 2020). My samples fall within the range of compositions observed in ocean drill cores, but tend to be more Na-rich than the majority of these compositions (Figure 28a), suggesting that their protoliths may have undergone spilitization. This is particularly true of samples from Syros and the Alps/Corsica. Spilitization has not been observed in drill cores from modern oceanic crust, but is common in ophiolites, which may reflect the fact that drill cores have not sampled old or structurally deep oceanic crust where

spilitization is most likely to occur (Staudigel, 2014). A number of spilitized compositions from ophiolites are shown in Figure 28a, which encompasses the variation in my samples. Spilitization is not generally associated with K-enrichment (Figure 28b, Belgrano and Diamond, 2019; Cann, 1969; Gillis and Robinson, 1990; Hall, 1989; Nehlig et al., 1994). An exception is the spilites from SW England, which are plotted because they have bulk N data, which is referred to later. These are hosted within a sedimentary sequence and have likely gained K from interaction with sediment-derived fluids rather than from the spilitization process itself. Na-rich samples in my study overlap closely with the composition of spilites in a K_2O–Na_2O plot, having high Na and low K. K-rich samples have intermediate Na-contents and are more similar to compositions observed in ocean drill cores, and to basalts which have been metasomatised by sediment-derived fluids during subduction (Li et al., 2021a; Sorensen et al., 1997). None of my samples show strong Ca-enrichment, but three samples show moderate degrees of Mg-enrichment (DR10, DC46B, 0321).

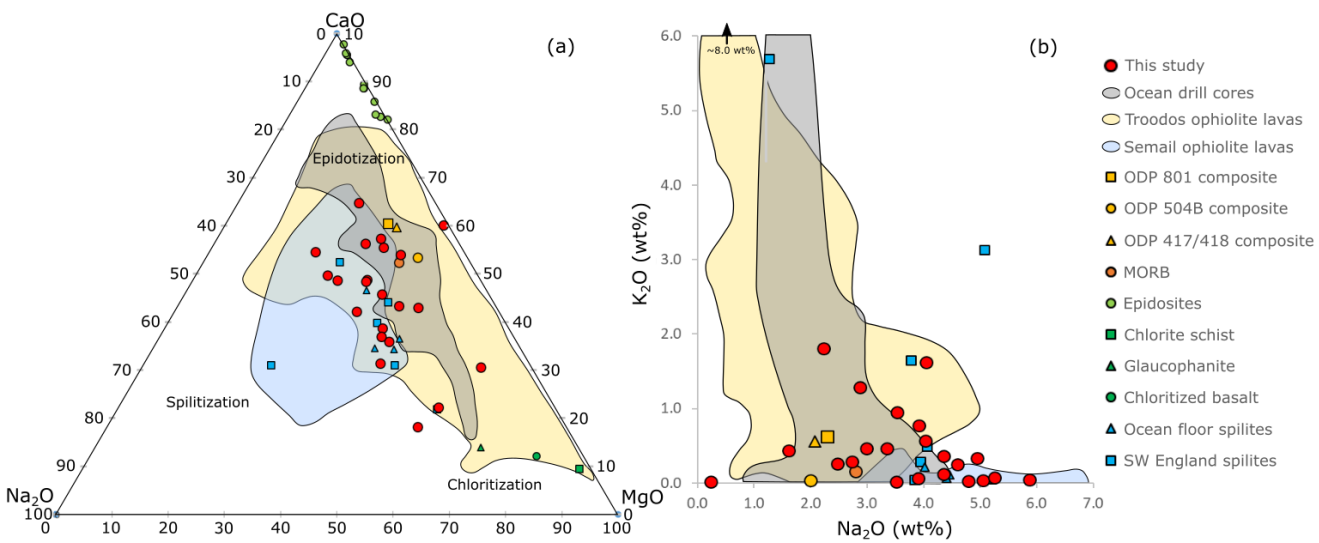


Figure 28: Bulk CaO–Na_2O–MgO-K_2O plots showing my samples and a range of compositions for hydrothermally altered oceanic crust. Ocean drill cores from ODP 801, 1149 (Kelley et al., 2003), ODP 504B (Bach et al., 2003), ODP 417/417 (composite value only, Staudigel et al., 1996) and Pito Deep (Heft et al., 2008). Alkali basalts from ODP 801 are excluded. Lavas from the Semail ophiolite (Belgrano and Diamond, 2019) and Troodos ophiolite (Coogan et al., 2017). ALL MORB (Gale et al., 2013). Ocean floor spilites, Carlsberg Ridge, Indian Ocean (Cann, 1969). SW England spilites (Hall, 1989) are pillow basalts and dykes hosted within a sedimentary sequence and have associated N concentration data (Figure 25). Epidosites from the Semail ophiolite (Weber et al., 2021). Chloritized basalt, Flin Flon, Canada (Starr and Pattison, 2019). Chlorite schist and glaucophanite, St Marcel Valley, Western Alps (Martin et al., 2008).

The amount of K versus Na in my samples correlates with the mica mineralogy. K-rich samples

(> 2500 μg/gK or 0.3 wt.% K_2O) contain phengite (or biotite in sample 0321), whereas K-poor (< 2500 μg/g K) samples either contain paragonite, or no micas (Figure 29). Most of the paragonite-bearing samples are also Na-rich (> 4.6 wt% Na_2O), with the exception of one, which has MORB-like Na contents (2.7 wt% Na_2O). Samples with intermediate composition can contain either phengite, paragonite or both. Paragonite has been observed in many low temperature metabasites (Massonne and Sobiech, 2007 and references therein), and is common in my Na-rich samples. The peak P-T conditions reached by my paragonite-bearing samples all fall within the stability field of paragonite (Figure 30), which at high pressures (> 2.25–2.5 GPa) dehydrates to form jadeite + kyanite + H_2O (Massonne and Sobiech, 2007), which is consistent with the petrographic observation that paragonite forms part of the peak metamorphic assemblage in these samples. In contrast, thermodynamic models of subducted oceanic crust do not predict paragonite to be stable in most altered MORB compositions, including spilites, and instead favour phengite/biotite, even at very low bulk K concentrations (Hacker, 2008; Hernández-Uribe and Palin, 2019; Hernández-Uribe et al., 2020; Poli and Schmidt, 2002). This suggests a discrepancy between the modelled and observed mica mineralogy in the subducted oceanic crust, where models underestimate the stability of paragonite and any addition of K to the modelled bulk composition results in the appearance of phengite. Instead, my samples suggest that, at sufficiently low bulk K concentrations (<2000 μg/g K or 0.25 wt% K_2O, i.e., including fresh MORB), paragonite should form instead of phengite, with a higher modal abundance due to its lower K content. This could have important implications for trace element budgets in subducted oceanic crust. For elements which partition into white mica relative to other minerals (e.g. B, N, Rb, Cs, Ba, Be) the flux of these elements transported in the subducting slab could be larger than previously thought since there will be more white mica present than models predict, and in a wider range of lithologies. This underestimate will be particularly significant for elements that specifically partition into paragonite in preference to phengite (e.g. B, Be, Marschall et al., 2006a).

5.6.1.2 Trace elements

Relationships between K-Ba-Rb-Nb-Ni-Cr have been used to distinguish seafloor alteration from subduction-related metasomatism in mafic rocks (e.g. Bebout, 2007; van der Straaten et al., 2012). K/Nb–Ba/Nb plots demonstrate that ocean drill cores show K enrichment compared to fresh MORB

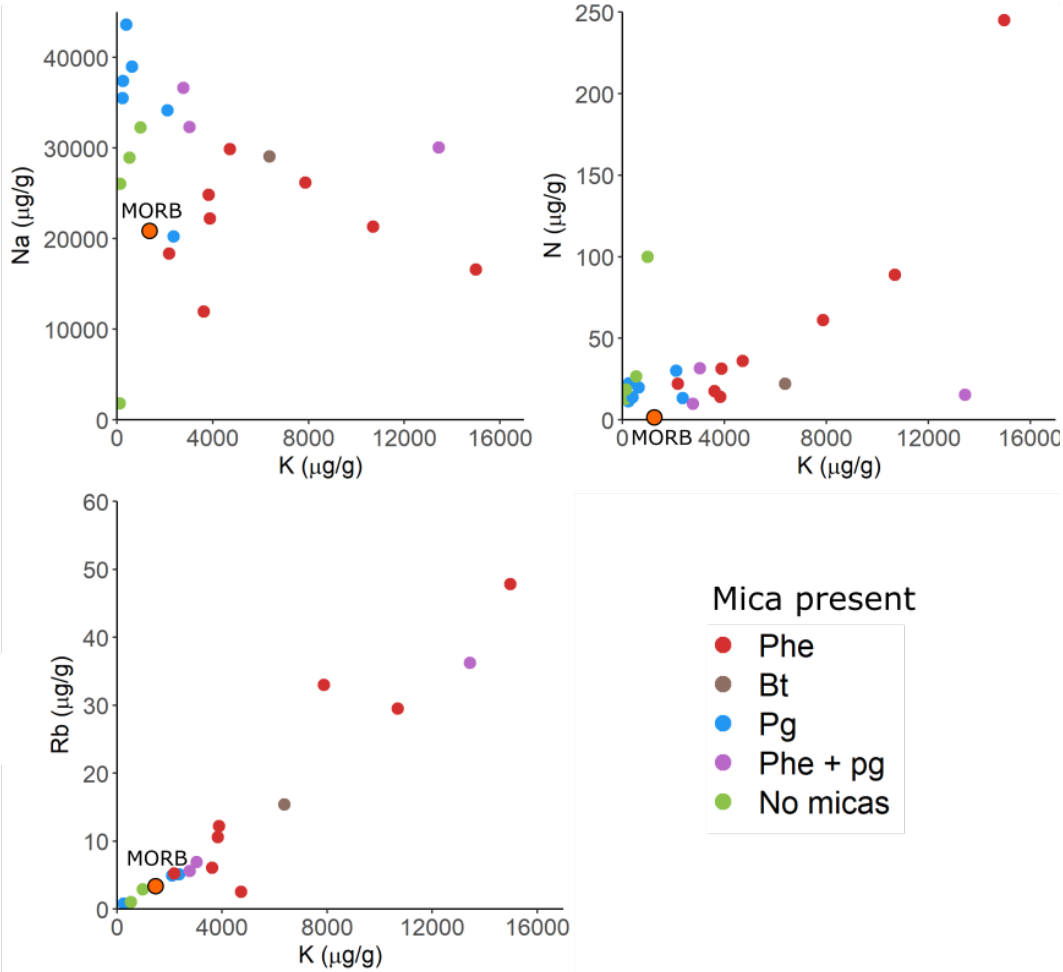


Figure 29: Bulk K–Na–N–Rb plots of my samples. The type of mica present in my samples varies with the bulk K and Na concentration. K correlates strongly with Rb, but less strongly with N, particularly at low N concentrations. The composition of ALL MORB (Gale et al., 2013; Li et al., 2007) is shown for comparison.

but Ba enrichment is less significant, and many samples instead show Ba depletion (Figure 31). Simultaneous enrichment of Ba and K is observed in a few spilitized lavas from the Semail ophiolite, but the majority of these samples show trends similar to ocean drill cores. Some HP rocks show significant simultaneous enrichment of K and Ba, which has been attributed to metasomatism by sediment-derived fluids (e.g. Li et al., 2021a; Sorensen et al., 1997; van der Straaten et al., 2012). Simultaneous depletion of K and Ba is also observed but is less common and may be related to LILE loss during devolatilization (Bebout, 2007). Ba/Rb–K_2O plots show similar trends, where AOC shows K enrichment with decreasing Ba/Rb whereas some HP rocks show K enrichment with approximately constant Ba/Rb (i.e. simultaneous enrichment of all three elements). Spilites are

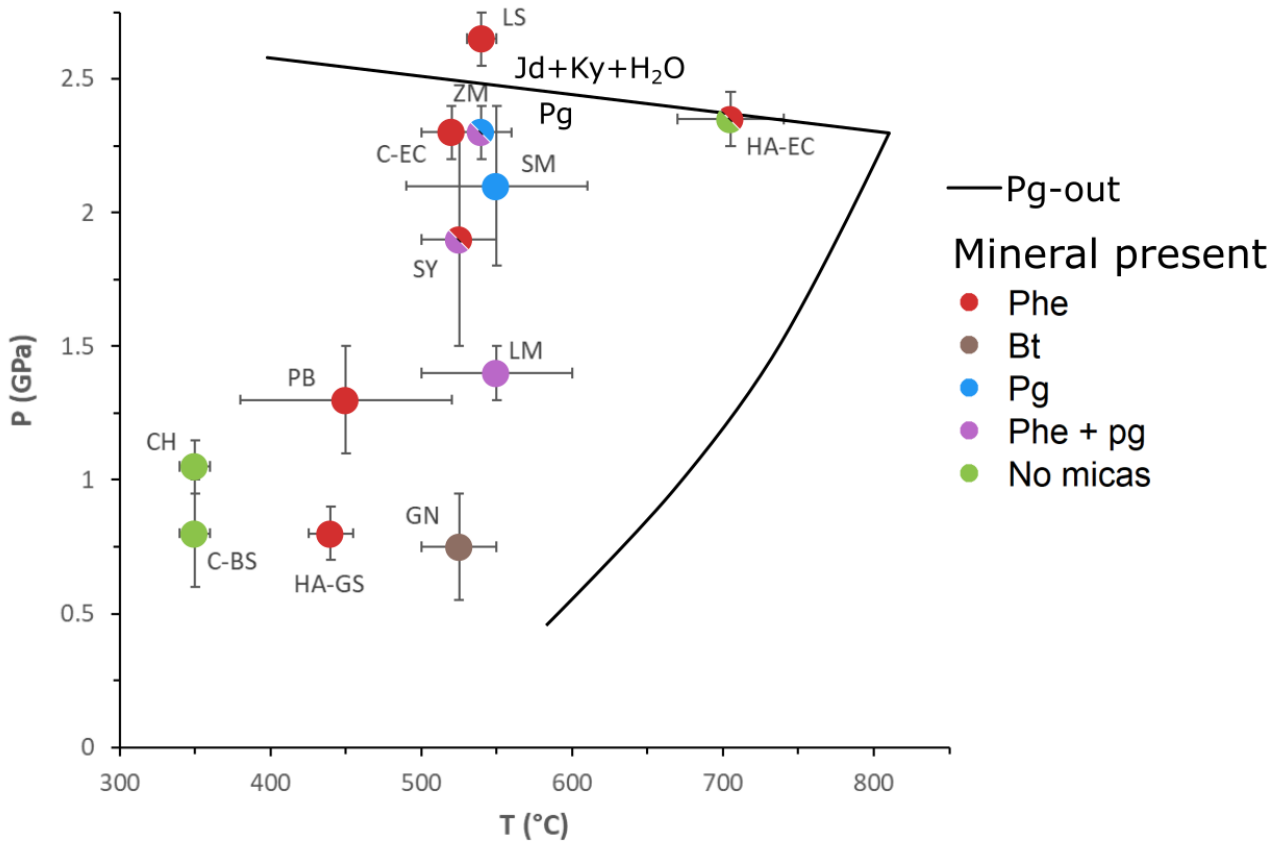


Figure 30: P-T conditions recorded by samples from different localities in this study (see Table 9 for details). CH = Chenaillet, C-BS = Corsica blueschist, C-EC = Corsica eclogite, HA-GS = Higashi Aiachi greenschist, HA-EC = Higashi Aiachi eclogite, GN = Glockner Nappe, PB = Punta Balandra, LM = Lago del Mucrone, SY = Syros, SM = San Marcel Valley, ZM = Zermatt-Sass, LS = Lago Superiore. Each locality is coloured by the mica mineralogy present in samples from that locality. Also shown is the paragonite breakdown reaction from Massonne and Sobiech, 2007.

similar to K-depleted AOC and not to most HP rocks. Samples DR10, DR9, X1008 and 0275 all plot outside of the field of AOC/spilites and show K-Ba-Rb enrichment indicating interaction with sediment-derived fluids during subduction.

Nickel and Cr are enriched in serpentinites due to their high compatibility in olivine and can be mobilised during serpentinite-dehydration in subduction zones, resulting in Ni–Cr enrichment in rocks that are metasomatised by serpentinite-derived fluids (Angiboust et al., 2014; Marschall, 2005). AOC generally shows Ni–Cr depletion relative to unaltered MORB, which is especially pronounced in some spilitized lavas (Figure 31). Only sample DR10 shows a clear Ni-Cr enrichment above the range of AOC compositions, suggesting that it interacted with serpentinite-derived fluids during

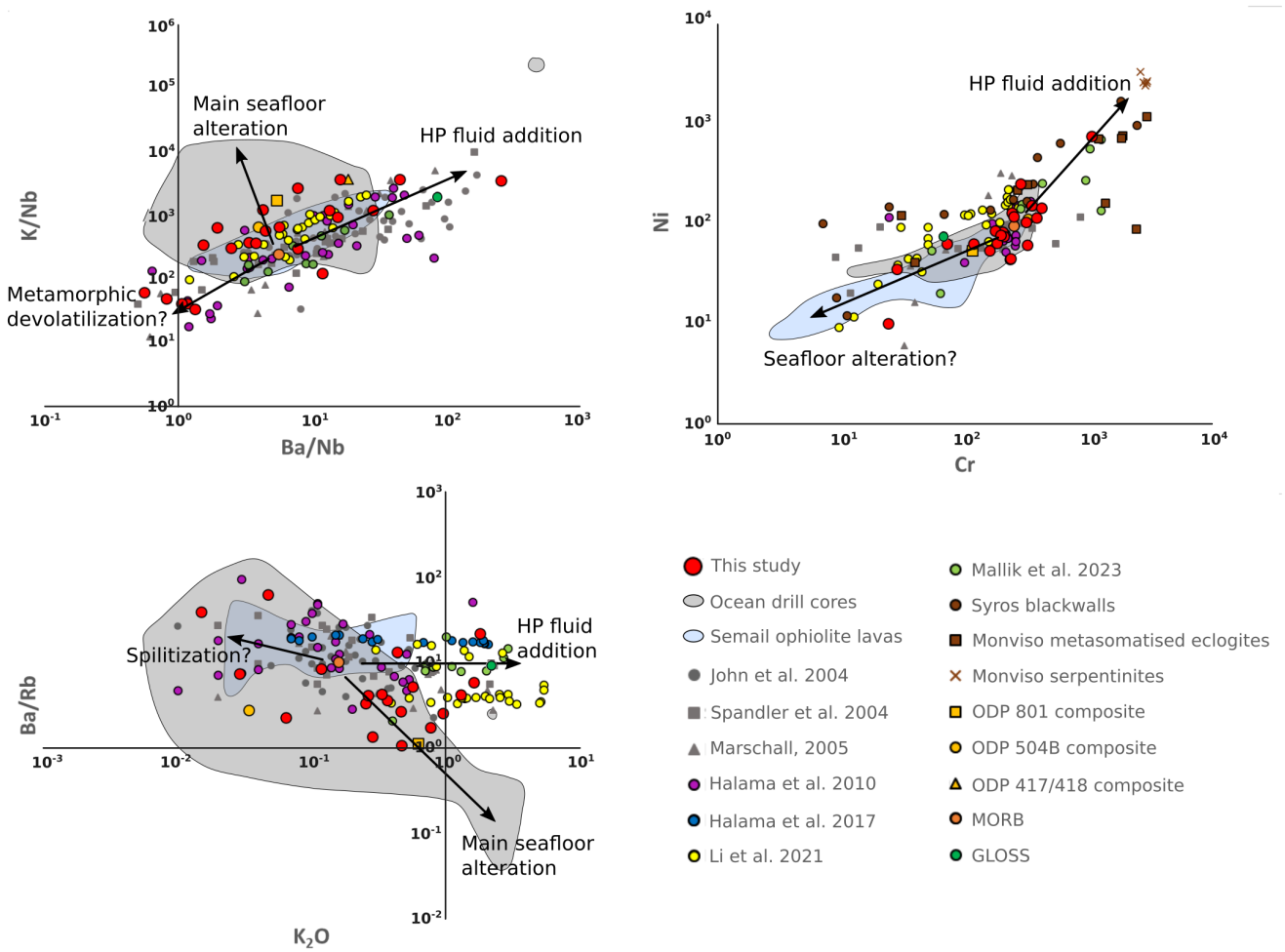


Figure 31: Whole rock trace element plots showing distinct trends for seafloor hydrothermal alteration and subducted-related metasomatism based on Bebout, 2007 and van der Straaten et al., 2012. AOC data are plotted for ODP 801 (excluding alkali basalts), ODP 1149 (Kelley et al., 2003), ODP 504B (Bach et al., 2003), ODP 417/418 (composite only, Staudigel et al., 1996) and Semail ophiolite lavas (Belgrano and Diamond, 2019). ALL MORB (Gale et al., 2013). GLOSS (Plank, 2014). HP rocks with MORB-like major and immobile element compositions are plotted to illustrate subduction-related metasomatic trends (John et al., 2004; Marschall, 2005; Spandler et al., 2004). HP mafic rocks which have been analysed for bulk N are also plotted (Halama et al., 2010, 2017; Li et al., 2021a; Mallik et al., 2023). For Ni–Cr trends, there are additional samples which have been metasomatised by serpentinite-derived fluids during subduction (Angiboust et al., 2014; Marschall, 2005).

subduction. Some other samples show elevated Ni-Cr compositions compared to average MORB but still fall within the range of AOC so there is no definitive evidence of a serpentinite-derived fluid component.

With the exception of the samples highlighted above, the rest of my samples show no significant deviations from AOC in either K-Ba-Rb-Nb or Ni-Cr systematics, suggesting that they do not preserve clear evidence of fluid-rock interaction during subduction.

5.6.2 Nitrogen partitioning between HP minerals

Phengite and paragonite contain the highest N concentrations of the analysed minerals (> 10 μg/g in all samples where they are present and > 1000 μg/g in some phengites, Figure 26, Table 11), consistent with previous suggestions that NH_4^+ easily substitutes for K^+ and Na^+ in micas (Honma and Itihara, 1981, Chapter 3), due to their similar ionic radii (NH_4^+: 1.67 Å, K^+: 1.64 Å, Na^+: 1.39 Å, Shannon, 1976; Sidey, 2016). Na-Ca amphiboles and omphacite contain $1 - 15$ μg/g N, which is presumed to be hosted as NH_4^+ substituting for Na^+ and Ca^{2+}. Albite contains surprisingly low N contents (< 5 μg/g N in all but one sample), despite being a Na-bearing mineral. Epidote contains (< 5 μg/g N) in all but one sample, suggesting that it too does not incorporate significant N. Chlorite contains $1 - 15$ μg/g N, confirming the suggestion in Chapter 3 that chlorite can host appreciable amounts of N. The mechanism of N incorporation in chlorite is still unclear.

The mean N, B and Li concentrations in each mineral in each sample were used to investigate the partitioning of N, B and Li between HP minerals. A plot of mean mineral N, B and Li concentrations in phengite, paragonite, amphibole and omphacite for all samples from this chapter and chapter 3 is shown in Figure 33. Marschall et al., 2006a previously reported inter-mineral partitioning data for B and Li in a range of subduction-related lithologies from Syros, Greece, and their data are also plotted for comparison. Samples were then excluded from further calculations on the following basis. DR10, DR9, Vi1808 and SEC16-1 were excluded because they have large correlated variations in N, B and Li in phengite (Figure 32), which are interpreted to reflect variable re-equilibration with an externally-derived fluid, similar to that observed in Chapter 3. These phengites therefore do not represent a single population that can be considered to be in equilibrium with the other minerals in the sample. Paragonite in X1008 was removed because it occurs as inclusions in an Fe-oxide phase

and so may not be in equilibrium with the matrix minerals. The remaining data are plotted in Figure 34. Variability in B and Li partition coefficients is generally lower in the filtered dataset, although some N partition coefficients still show large variability that is discussed below.

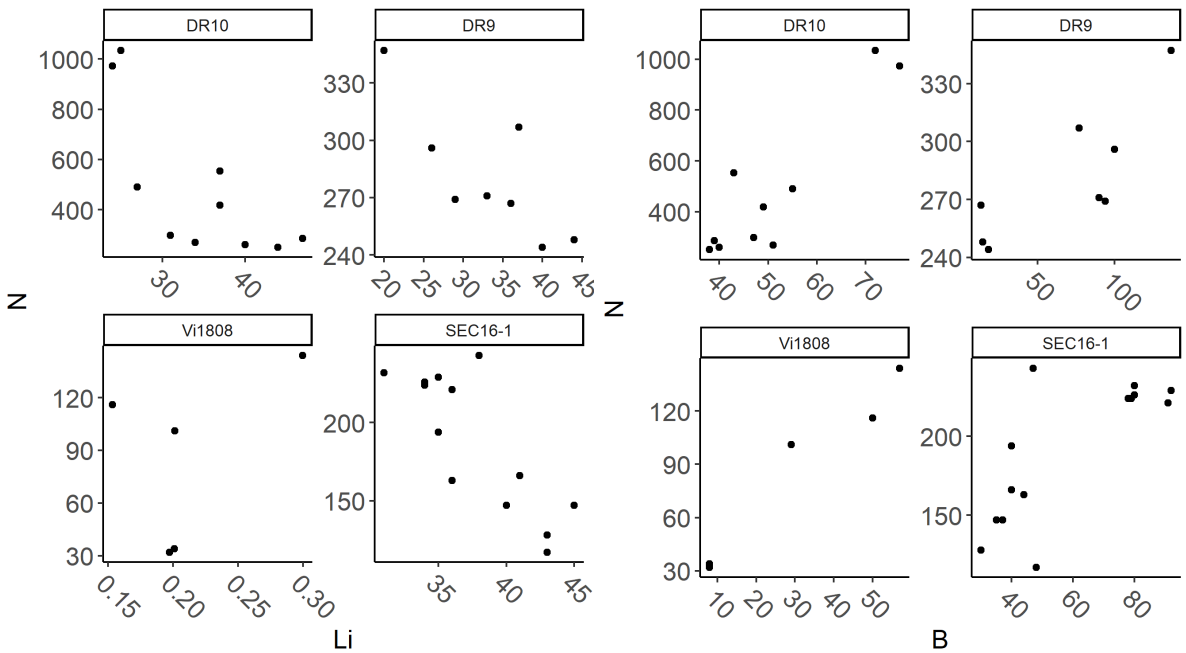


Figure 32: N–B–Li correlations in phengite from selected samples. Sample SEC16-1 is from Chapter 3.

Partition coefficients for B and Li mostly fall within or close to the range reported by Marschall et al., 2006a (Figure 34, Table 13), supporting the assertion that my samples record equilibrium partitioning for B and Li. A few exceptions exist, such as $D^{B}_{pg/amph}$ in sample DC48B and $D^{B}_{phe/amph}$ in sample 0275. These could indicate that equilibrium partitioning is not recorded in these samples or they could simply indicate that the variation in partition coefficients is larger than that reported by Marschall et al., 2006a. The samples from Marschall et al., 2006a all formed at similar P-T conditions in a small number of localities (1.3–2.0 GPa, 470–520 °C, whereas my samples span a wider range of P-T conditions (0.8–2.4 GPa, 430–700 °C and are from a wider range of localities, which could partly explain the greater variation in partition coefficients that I observe. Nitrogen partition coefficients are more variable than those for B or Li, especially for phengite-amphibole and phengite-omphacite partitioning. Fluid-mineral N partitioning has been experimentally shown to vary significantly with P, T and fO_2 (Bos et al., 1988; Förster et al., 2019; Jackson et al., 2021; Kupriyanov et al., 2023; Li et al., 2015; Pöter et al., 2004), which is likely a result of the dependence of N speciation in the

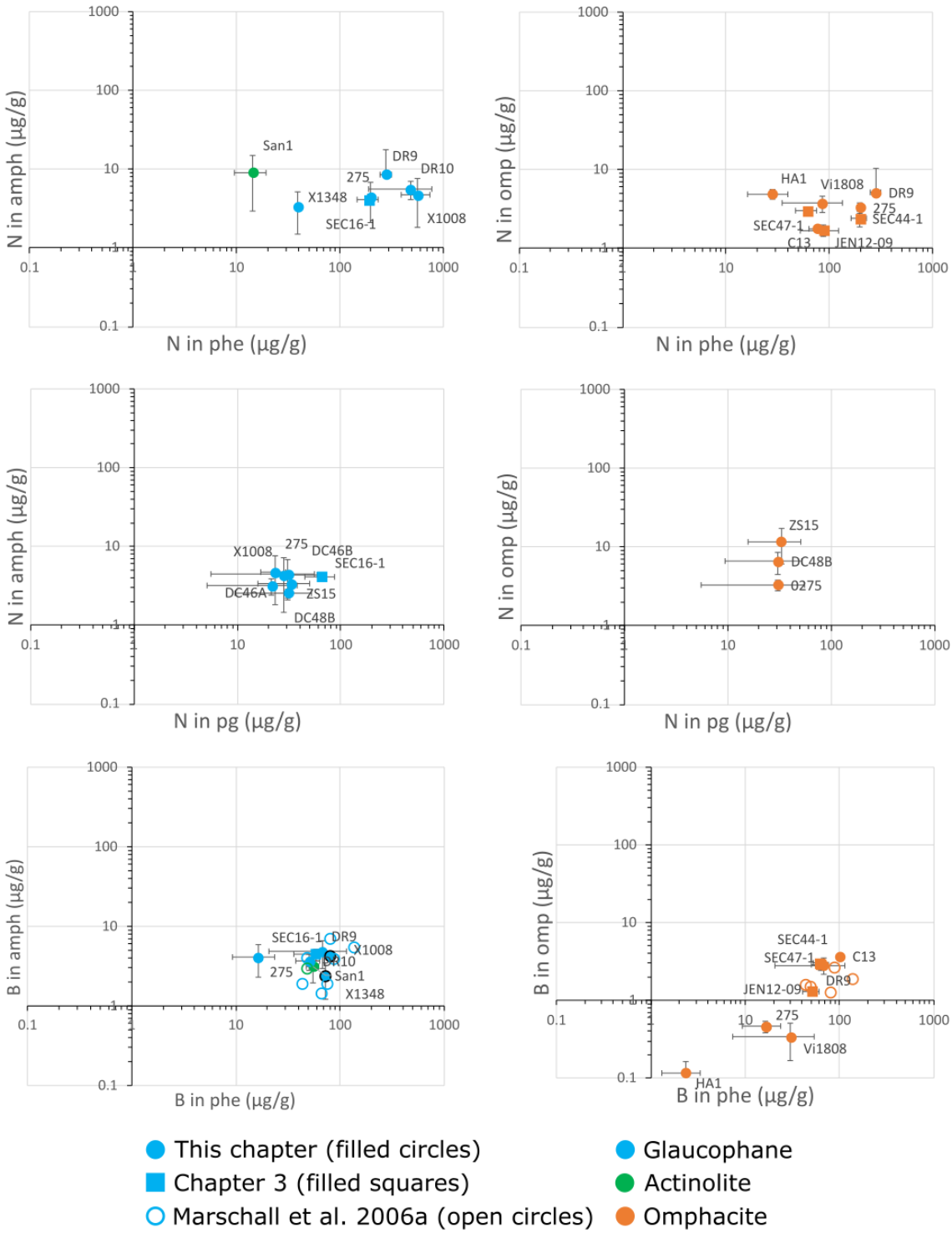


Figure 33: Mean concentrations of N, B and Li in phengite, paragonite, amphibole and omphacite for all samples, including those from Chapter 3. Not all samples appear on every plot since they contain different combinations of these minerals. Error bars are 1 standard deviation on the mean. Boron and Li concentrations reported by Marschall et al., 2006a are also plotted for comparison. Two of my samples from the same area as the Marschall data (Syros) are highlighted with black outlines. Figure continued overleaf.

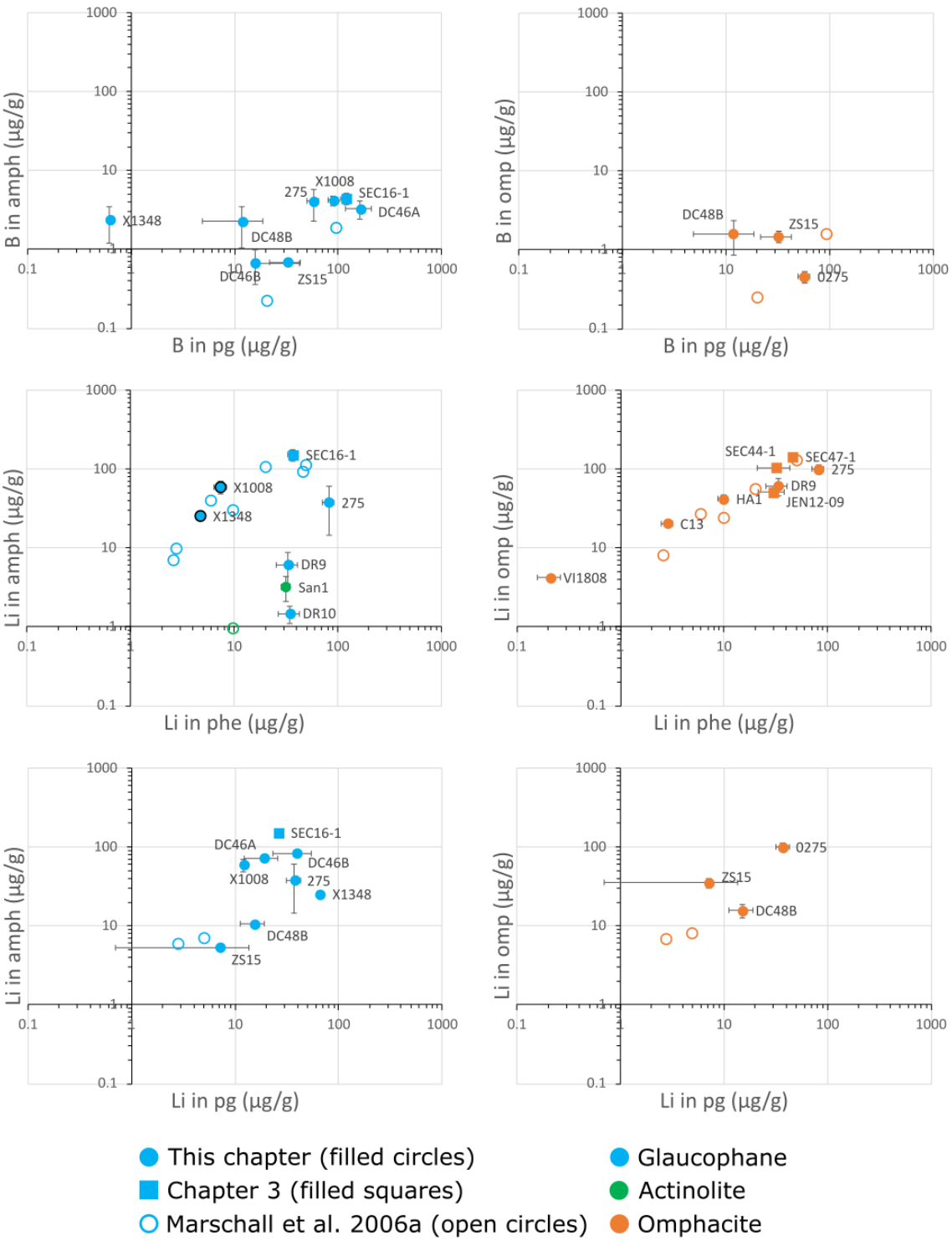


Figure 33: Continued from previous page.

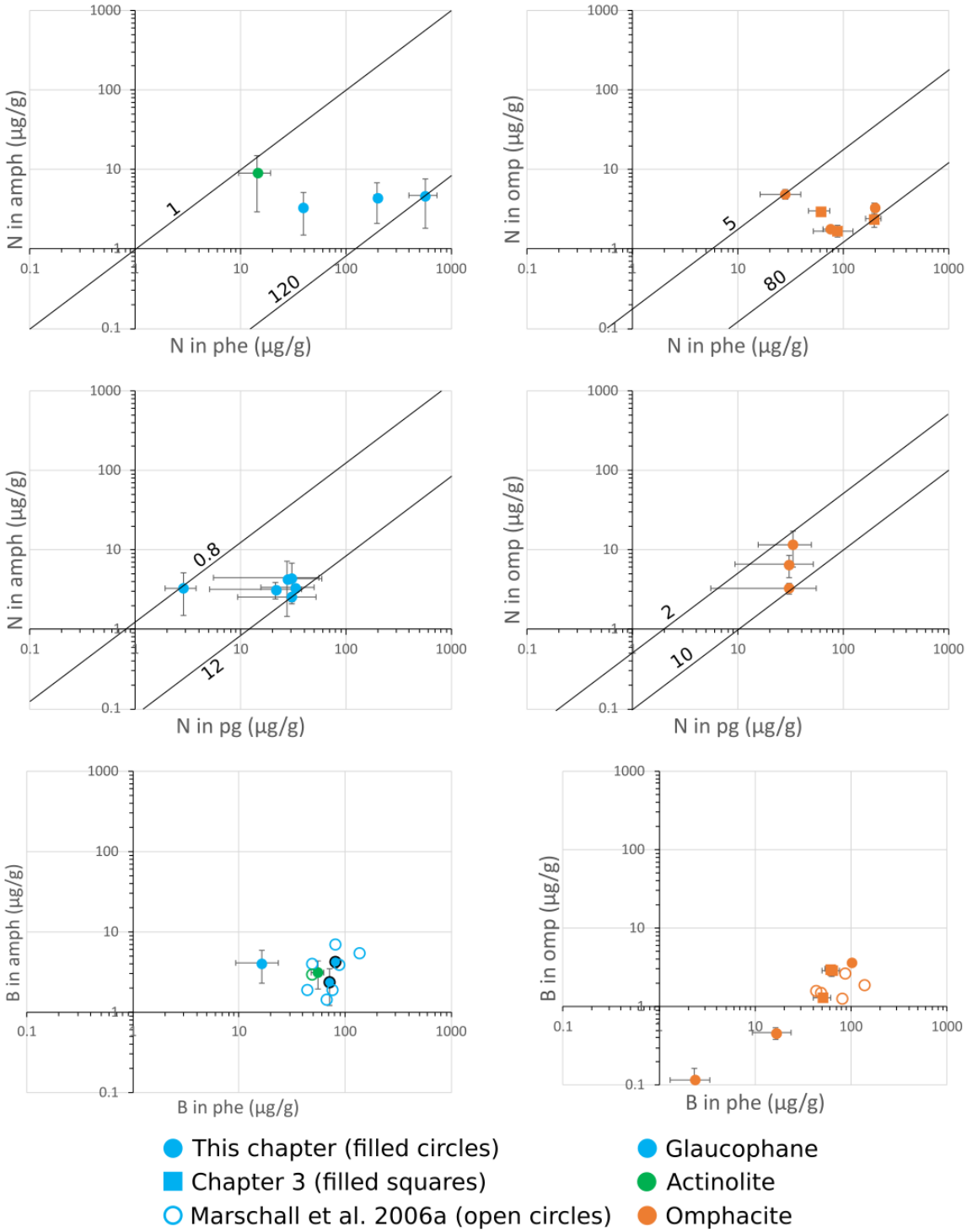


Figure 34: Mean concentrations of N, B and Li in phengite, paragonite, amphibole and omphacite for selected samples (see text for discussion). Error bars are 1 standard deviation on the mean. Lines of constant partitioning are shown for N, where the values given are $D^{N}_{\text{min x/min y}}$.Boron and Li concentrations reported by Marschall et al., 2006a are also plotted for comparison. Two of my samples from the same area as the Marschall data (Syros) are highlighted with black outlines. Figure continued overleaf.

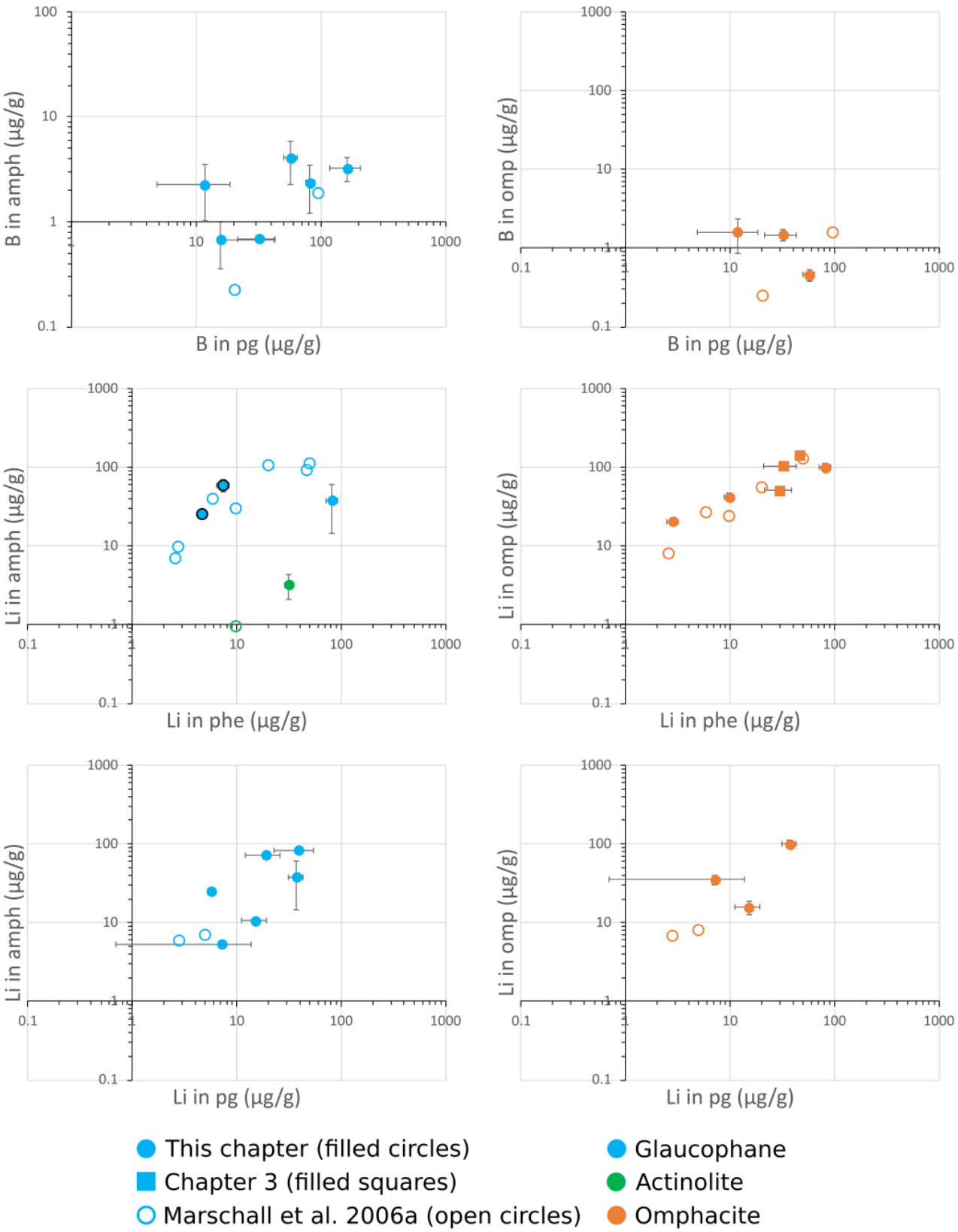


Figure 34: Continued from previous page.

fluid on these parameters (and also pH, which has not been experimentally investigated, but has been theoretically predicted to be important (Mikhail et al., 2017; Mikhail and Sverjensky, 2014)). However, N speciation seems less likely to have an effect on inter-mineral partitioning since N in these minerals is assumed to be present only as NH_4^+. Nevertheless, it may be that inter-mineral N partitioning is more strongly dependent on P, T, and potentially other thermodynamic parameters, compared to B and Li, which could explain the greater variability. Another possibility is that the behaviour of N is decoupled from that of B and Li, such that B and Li might record equilibrium partitioning, whilst N does not. Kinetic effects may play a larger role in the behaviour of N compared to B and Li, because the NH_4^+ ion is much larger than B or Li, or indeed many other fluid-mobile trace elements. NH_4^+ diffusion is therefore expected to be slow and so equilibrium will be harder to achieve.

There are weak correlations between N partition coefficients and peak pressure and temperature, although the range of pressures represented is quite small (Figure 35). In particular, $D^N_{phe-omp}$ may be negatively correlated with both temperature and pressure, and D^N_{pg-omp} may be negatively correlated with pressure. Incorporation of up to 1000 μg/g NH_4^+ in diopside has been experimentally demonstrated at 9.5–12.8 GPa (Watenphul et al., 2010), which supports the suggestion that N could partition more strongly into pyroxenes at high pressure. The K-bearing site in micas is significantly more compressible than in pyroxenes. Since the NH_4^+ ion is slightly larger than K^+ at ambient pressure (NH_4^+: 1.67 Å, K^+: 1.64 Å, Shannon, 1976; Sidey, 2016), and also significantly less compressible, high pressure should have a greater effect on NH_4^+ compatibility in micas than in pyroxenes, providing an explanation for the observed variation in partitioning behaviour. Mineral major element compositions could also affect partitioning behaviour, but there are no strong correlations between major element variations and N partition coefficients. Given the small number of samples, and significant variability between samples it is hard to make definitive conclusions and combined effects of P, T and crystallographic controls could be hard to disentangle. These data provide a useful first order constraint on the partitioning behaviour of N between micas, Na-Ca amphiboles, omphacite and chlorite, which appear to be the main mineral hosts for N in metabasic rocks. If $D^N_{mica-omp}$ is inversely correlated with pressure, then increasing amounts of N would partition into omphacite as the slab is subducted. This may help to retain N within the subducting slab and return it to the

mantle, since omphacite is less easily dissolved by HP fluids than micas (Connolly and Galvez, 2018) and therefore could persist to greater depths in the subducting slab.

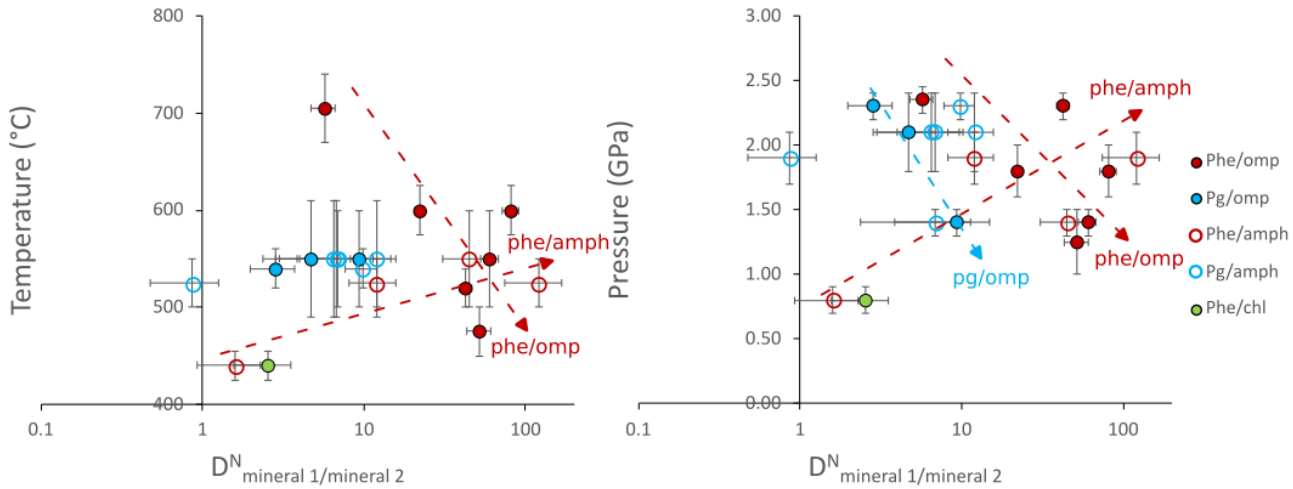


Figure 35: Variation of inter-mineral N partition coefficients with pressure and temperature in selected samples (see text for discussion). P-T conditions are from the literature for these localities (Table 9). Uncertainties on partition coefficients are propagated from the standard error ($1sd/\sqrt{n}$) on the mean mineral N concentrations presented in Table 11. Indicative trends are shown with arrows (see text for discussion).

5.6.3 Mineral contributions to reconstructed bulk nitrogen concentrations

Combining mineral modes and mineral N concentrations allows reconstruction of mineral-hosted bulk rock N concentrations. In this section I discuss the contribution of different minerals to the reconstructed bulk N. In eclogites that did not interact with HP, sediment-derived fluids (see Section 5.6.1.2) the mica contribution to the reconstructed bulk is 37–69%, with the rest being mostly in omphacite with minor contributions from glaucophane, epidote or retrograde chlorite (Figure 36). Even though micas have the highest N concentration of the measured minerals, their low modal abundance means that other minerals also host a substantial portion of the N budget. Phengite typically has higher N concentrations than paragonite, but this is balanced by the fact that paragonite typically has a higher modal abundance, so the total N hosted in micas is similar in both phengite and paragonite-bearing eclogites. In blueschists that did not interact with HP, sediment-derived fluids the mica contribution is 37–65% (excluding DC46A where 20% of the N is hosted in retrograde chlorite), with the rest being in glaucophane and epidote. Other phases besides micas can therefore play a

	D_N	D_B	D_{Li}	D_N	D_B	D_{Li}	D_N	D_B	D_{Li}
	phe/omp			phe/gln			phe/act		
Marschall et al., 2006a		27–71	0.22–0.34		11–46	0.14–0.49		16	10
HA1	5.7 ± 0.9	20	0.23						
X1008				121 ± 46	19	0.13			
0275	60 ± 10	36	0.81	45 ± 24	4.0	2.2			
San1							1.6 ± 0.7	18	9.8
C13	43 ± 4	27	0.14						
SEC44-1	81 ± 9	21							
SEC47-1	22 ± 2	20							
JEN12-09	52 ± 9	39							
X1348				12 ± 4	31	0.19			
	pg/omp			pg/gln			phe/chl		
Marschall et al., 2006a		59–81	0.41–0.61		50–90	0.47–0.69		32–92	0.17–0.23
0275	9.3 ± 5.5	125	0.37	6.9 ± 4.5	14	0.98			
DC46B				6.5 ± 3.6	23	0.47			
DC46A				6.8 ± 2.8	50	0.26			
ZS15	2.8 ± 0.9	22	0.20	9.8 ± 5.4	47	1.3			
DC48B	4.7 ± 1.7	7.4	0.97	12 ± 8	8.5	1.4			
San1							2.5 ± 1.0	22	0.34
X1348				0.86 ± 0.55	0.26	2.6			

Table 13: Inter-mineral partition coefficients for N, B and Li in selected samples (see text for discussion). Coefficients are calculated from the mean element concentrations in each mineral and uncertainties are propagated from the standard error on the mean concentrations.

significant role in hosting N. In the greenschist San1, only 14% of the N is hosted in phengite due to its low modal abundance. 66% of the N is hosted in actinolite and the rest mostly in chlorite, which have slightly lower N concentrations than phengite but higher modal abundances, particularly in the case of actinolite. I were unable to estimate the partitioning in San2 because the phengite grains were too small to be analysed by SIMS without overlapping adjacent grains. The low proportion of N hosted in micas in the San1 greenschist compared to higher grade samples could reflect changes in the equilibrium partition coefficient for N between micas and other minerals as a function of pressure and temperature. Alternatively, the low peak temperature reached by greenschists may prevent equilibrium N partitioning from being achieved between minerals. More work is required to investigate the P-T dependence of N partitioning and in particular its behaviour in low grade samples.

In samples which did interact with HP, sediment-derived fluids (simultaneous enrichment of K-Ba-Rb, see Section 5.6.1.2), the proportion of reconstructed bulk N hosted in phengite is very high (92–96%), since coupled K-N enrichment leads to high phengite modes and N-rich phengite. This emphasises the importance of mica stability in controlling the ability of oceanic crust to sequester N during HP fluid-rock interaction (e.g. Halama et al., 2017; Li et al., 2021a).

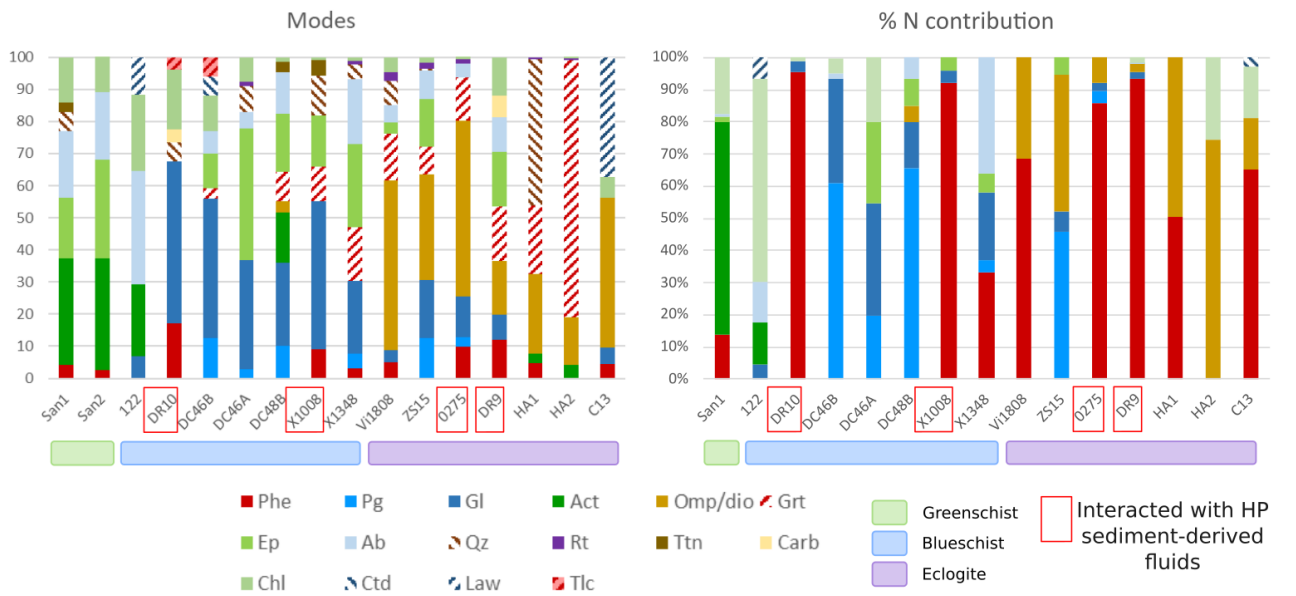


Figure 36: *Left:* Mineral modal abundances (wt%). *Right:* % contribution of each phase to the total reconstructed bulk N, calculated by combinining mineral mdoes with average N concentrations in each mineral as measured by SIMS. Sample San2 is excluded from the N contribution plot because although phengite is present, and N-bearing, the grains were too small to accurately measure the N concentration by SIMS.

5.6.4 Comparison of measured and reconstructed bulk nitrogen

In this section I now compare the total reconstructed bulk N to measured N concentrations in whole rock powders. Previous studies have used correlations of bulk N with K and Rb to suggest that N is primarily hosted in micas (e.g. Bebout and Fogel, 1992; Busigny et al., 2003a; Halama et al., 2010). In my samples, bulk rock Rb correlates strongly with bulk rock K, which is consistent with both Rb and K being primarily hosted in white micas (Figure 29). Samples with $< 40 \mu g/g$ N show no correlation of N with K at all. Some N-rich samples are also enriched in K, but there is also one sample which is K-enriched but N-poor, and one sample which is N-rich but K-poor. The overall lack of correlation of bulk N and K, especially compared to Rb and K, suggests that N is additionally hosted in phases other than white mica, consistent with the results discussed in the previous section. Lack of N-K-Rb correlations was also observed for most of the metabasic rocks in Halama et al., 2010.

In most samples, reconstructed bulk concentrations for K and Rb are close to the measured values, but reconstructed bulk N is often significantly lower than the measured value (Figure 37).

Even though phengite has the highest N concentration of the measured minerals, its low modal abundance means that only ~5–15% of the measured bulk N could be hosted in phengite. Even in the very K-rich samples DR9 and DR10, where phengite mode is >10%, the bulk N is so high that phengite still only accounts for ~35–40% of the measured bulk N. The only two samples where phengite accounts for >80% of the measured bulk N are 0275 and X1008, which are K-rich but comparatively N-poor. Paragonite also contributes <35% of the measured bulk N in samples where it is present. Thus, in many samples measured N in minerals does not add up to the total amount of N measured in the bulk rock, so either there are additional N reservoirs, or there is a problem with either bulk N or SIMS N measurements. These options are discussed below.

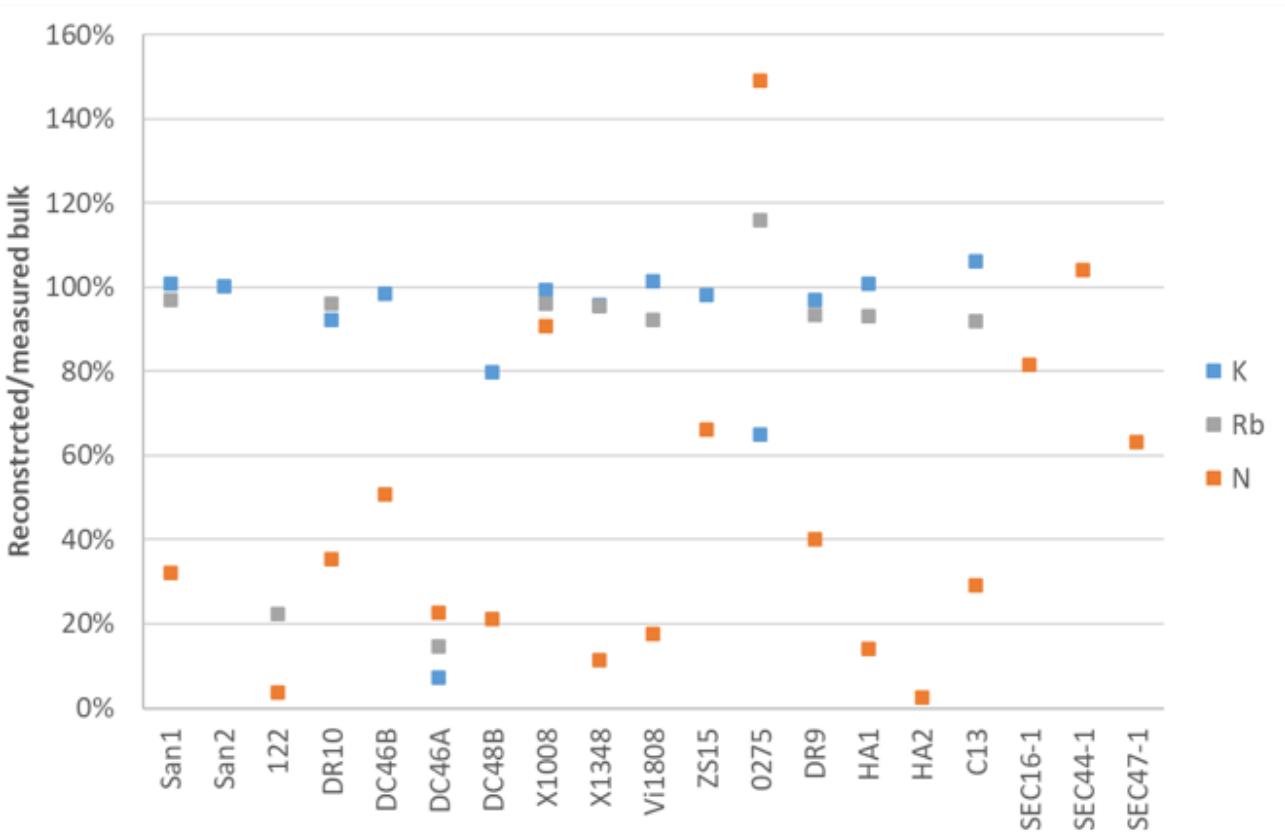


Figure 37: Reconstructed/measured bulk concentrations for K, Rb and N in each sample. Most samples have R/M close to 1 for K and Rb, but N is highly variable. Where reconstructions are not shown for some elements, this is because these elements were below detection limit. Samples SEC16-1, SEC44-1 and SEC47-1 are from Chapter 3 but the mineral modes were updated from the previous chapter by using bulk K_2O and K_2O in micas to better constrain mica mode, resulting in slightly different reconstructed bulk N concentrations to the previous study.

Since I do not have reference materials for measuring N concentrations in phases other than white

mica, it is possible that my N concentrations for other phases are too low, which could account for the low reconstructed bulk N contents. If N in phase X was systematically too low then I would expect to see larger discrepancies between measured and reconstructed bulks (lower reconstructed/measured bulk ratio) in samples where phase X has higher modal abundance. However, there are no clear correlations between reconstructed/measured bulk ratios and modal abundances of potential N-bearing minerals (Figure 38), which suggests that analytical error is not a significant cause of low reconstructed bulk N contents. Furthermore, N concentrations in non-mica minerals would have to be one or two orders of magnitude higher than my values for the reconstructed and measured bulks to match. This would mean that N concentrations in other minerals were the same or higher than in micas, which seems highly unlikely, so I suggest that matrix effects between white mica and other minerals cannot account for the discrepancy in measured versus reconstructed bulks.

A different possibility is that the N calibration for white mica is systematically off and therefore N concentrations of all minerals are too low. The N concentrations of the mica standards used for calibration were determined by bulk combustion by Busigny et al., 2003b using a pre-heating treatment, where the sample powders were heated at 450 °C during evacuation, prior to being combusted at higher temperature to liberate N for analysis (see Section 2.2 for full method description). The rationale for pre-heating was that it should remove organic contamination and adsorbed air from the samples. Different laboratories have used lower temperatures and shorter durations of pre-heating. Li et al., 2021b showed that pre-heating phengite grains at 400 °C can result in 40% lower measured N concentrations compared to no pre-heating, whereas pre-heating at 100 and 200 °C (as in my analyses, and those reported from the laboratories of L. Li and G. Bebout) results in only 5% N loss. An important question, therefore, is where the fraction of N that is lost at 400 °C is hosted within the phengite grains, and whether this N is measured during SIMS analysis. If the latter is true, then my N calibration will be systematically low. If it is not true, then this source of calibration error cannot explain the discrepancy between measured and reconstructed bulk N concentrations. If this N is hosted within the crystal lattice then it should be measured during SIMS analyses, whereas if it is hosted in defect-rich regions near the grain boundaries, or within micro-fractures or fluid inclusions, or adsorbed onto the surface of the grain, then it would likely be missed by SIMS analyses. Two possible pieces of evidence are available from my data which could shed light on this question. Firstly, if N

concentrations are assumed to be systematically 40% too low in all minerals, then reconstructed bulk N concentrations would increase by 66%. Since some of my samples do have reconstructed/measured bulk N concentrations close to 100%, these samples would then have the opposite problem of having significantly more N in the reconstructed compared to the measured bulk. This is rather harder to explain than having too little N, since one cannot simply invoke additional unmeasured sources of N. The most obvious explanation would seem to be that the thin sections used for SIMS analyses of these samples are unrepresentative of the whole rock and have unusually high N concentrations. However, this seems unlikely since reconstructed concentrations of K and Rb agree with measured concentrations. The second piece of evidence is that some SIMS analyses of fine grained samples resulted in spots that overlapped cracks in the target grains, or overlapped grain boundaries. A number of these analyses appear to have elevated N counts compared to analyses which did not overlap such features, which suggests that there could be N-rich material hosted at grain boundaries. This could be the origin of N that is lost during pre-heating, and would confirm that this N is not measured during normal SIMS analyses (i.e. not analyses which overlapped cracks). The mechanisms of N incorporation into minerals require further investigation to understand the origin and significance of low temperature N loss, but I provisionally suggest that this does not significantly affect my SIMS calibration.

This suggests that a significant proportion (10–85%) of the N measured by bulk rock methods is not hosted in the analysed silicate minerals in some samples. My observations are similar to those of Urann et al., 2020, who measured Cl in eclogites in bulk powders (by pyrohydrolysis) and in minerals (by SIMS) and performed a similar reconstruction analysis to my study. They observed that reconstructed bulk Cl concentrations are 59–88% lower than measured bulk Cl concentrations and suggested three possible explanations: retrograde alteration, grain boundary-hosted Cl and Cl-bearing fluid inclusions. I discuss these explanations in the context of N below.

Retrograde minerals could be an additional source of N. My samples were selected because they contain fresh HP phases that could be measured by SIMS, so the amount of retrogression is generally low. A few samples contain localised domains of chlorite, which is likely retrograde after amphibole or clinopyroxene. Retrograde chlorite also occurs as rims on garnet. Chlorite in these samples was analysed by SIMS and its N concentrations are included in the bulk reconstructions so it cannot be

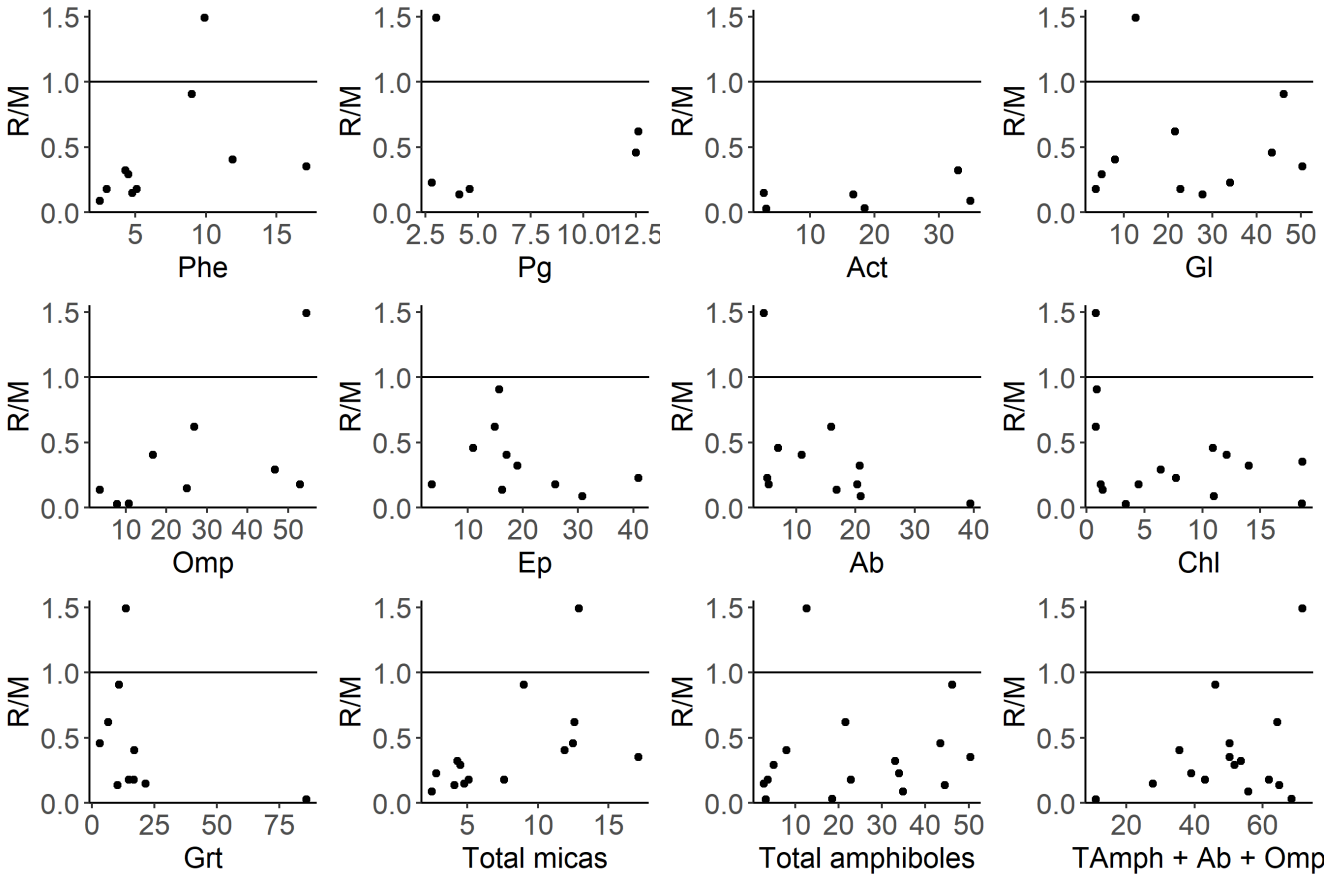


Figure 38: Plots showing the relationship of the ratio of the reconstructed/measured bulk N contents against modal abundance of different phases. R/M is <1 for most samples, meaning that the bulk N concentration reconstructed from combining mineral N concentrations with mineral modes is less than that measured by bulk combustion. R/M does not show correlations with modal abundances of potential N-bearing phases (see text for discussion).

the source of the discrepancy. Some samples also contain retrograde albite after amphibole, clinopyroxene or paragonite but again this was analysed by SIMS and contained very low N concentrations (< 7 μg/g). If the missing N is hosted in other minor alteration phases that were not measured by SIMS then their modal abundance is at most 1%, based on optical microscopy and back scattered electron imaging. To add 10–100 μg/g N, which would reconcile my measured and reconstructed bulk N concentrations, would require 0.1–1 wt% N in the alteration phases. N concentrations of this magnitude have been observed in clays from associated with sedimentary diagenesis and hydrothermal alteration (e.g. Bobos and Williams, 2017; Schroeder and Ingall, 1994) so, in principle, low temperature alteration to clays could be a possible source of N. However, no clay minerals were observed in my samples, either by BSE-EDS imaging, or during XRD mineral mode quantification, although the

detection limit on the latter technique is ~1%, so small modes of retrograde minerals could be missed. Therefore, whilst I cannot completely exclude the possibility, it appears that retrograde minerals are unlikely to explain the discrepancy between measured and reconstructed bulk N concentrations.

Grain boundaries are another potential site where N could be hosted. The hosting of LILE and other trace elements at grain boundaries has been recognised as an important process in mantle peridotites, where up to 90% of the whole rock budget of elements such as Rb, Ba, Nb and Ta may be hosted in grain boundaries (Alard et al., 2022 and references therein). Elements can be hosted either within tiny (< 10 μm) trace element-rich phases formed in the interstices between major rock-forming minerals, or within the crystal lattice of the rock forming minerals themselves, which is altered at grain boundaries (e.g. there is a high density of cation vacancies). As mentioned earlier, some of my SIMS analyses which overlapped cracks or grain boundaries had elevated N and Cl counts. Similar elevated SIMS counts were observed for Cl at grain boundaries in eclogites by Urann et al., 2020. BSE and EDS imaging of the SIMS spots with elevated N counts did not reveal any additional minerals at the grain boundaries, which suggests that the former mechanism is not relevant for N in my samples, although the imaging of grain boundaries is not trivial so this possibility cannot be entirely discounted. To assess the possible contribution of lattice hosted N at grain boundaries, I followed the method employed by Urann et al., 2020. The analyses which show elevated N counts at grain boundaries correspond to a N concentration of up to 91 μg/g. This should be taken as approximate since there are likely unknown matrix effects involved with analysing over a grain boundary, but it gives an order of magnitude estimate of the N concentration that might be hosted in grain boundaries. However, since the grain boundary is much smaller than the analysis spot (ca. 10 μm diameter for these fine grained samples), the N concentration in the grain boundary would be much higher. I then use Equation 9.6 of Turcotte and Schubert, 2002, which models the grain boundary porosity as circular tubes bordering cubic grains (Appendix B.2), to estimate the grain boundary porosity values over a range of grain boundary widths (1–1000 nm) and grain sizes (1–1000 μm). The contribution of grain boundary N to the total bulk increases with increasing grain boundary width and decreases with increasing grain size. For grain sizes of 100 μm, which are typical for many of my samples, the N contribution from grain boundaries is < 1 μg/g for grain boundary widths up to 1 μm and therefore it appears that grain boundaries cannot make a significant

contribution to the bulk N concentration. At 10 μm grain size, which is typical of my fine grained samples (e.g. 122, San1, San2), N contribution would be 2 μg/g for a 100 nm grain boundary, and 21 μg/g for a 1 μm grain boundary. Recent studies have documented grain boundary widths up to ca. 500 μm in a range of igneous and metamorphic rocks (Kruhl et al., 2024, 2013; Nagurney et al., 2021; Wirth et al., 2022). Such large grain boundaries are interpreted to form due to grain volume changes during exhumation and are commonly partially or completely filled by secondary minerals. Nitrogen hosted in such wide grain boundaries would therefore likely be an exhumation-related feature. At a 1 μm grain size the grain boundary contribution reaches significant amounts (2.1, 21 μg/g) even for narrow grain boundaries (1, 10 nm), but these grain sizes are not observed in my samples. The potential grain boundary contribution to bulk N concentrations is therefore strongly dependent on grain size. My calculations suggest that it is unlikely to be significant for my samples, except for a few finer grained samples, although it deserves further investigation. In particular, a more accurate determination of the total grain boundary porosity, and of the N concentrations in grain boundaries, would allow more confidence to be placed in these calculations.

Compared to peridotites for which grain-boundary hosting has been recognised to be significant, the bulk N concentration in my samples is several orders of magnitude higher than the bulk concentrations of trace elements considered there. Since the total contribution of grain boundaries to bulk element concentrations is limited by grain geometry, which is similar in both rock types, this conceptually explains why grain boundaries are less likely to make an important contribution to bulk N in my samples (even if they may still be comparatively N-rich, as evidenced by the SIMS analyses).

Fluid inclusions can host significant concentrations of fluid-mobile trace elements (e.g. Ferrando et al., 2009; Philippot and Selverstone, 1991; Scambelluri et al., 2015) and are therefore another potential host of N. To add 10–100 μg/g N, which would reconcile my measured and reconstructed bulk N concentrations, would require 1–10 wt% N in fluid inclusions with a modal abundance of 0.1 vol%. The N contents of fluid inclusions in HP metabasalts are highly variable, and their interpretation as primary/secondary features is complex (Frezzotti and Ferrando, 2015), but N concentrations of this magnitude have been observed in a number of studies of eclogites (e.g. Andersen et al., 1991, 1989; Fu et al., 2003; Sprán itz et al., 2022). Sprán itz et al., 2022 recently suggested that passive N-enrichment in fluid inclusions may occur in eclogites during exhumation below 300–400 °C, due to

crystallization of hydrous and C-bearing phases from the fluid inclusion, leaving the remaining fluid with N concentrations up to 75 wt% N_2. From a mass balance perspective it is therefore possible for fluid inclusions to account for the missing N in my samples. However, fluid inclusions are typically 1–10 μm in diameter, and the grain size of the powders prepared for bulk combustion is likely < 10 μm so it is unclear whether they could be preserved during sample preparation. Some authors have suggested that they would not be preserved (Busigny et al., 2011), but to my knowledge this has never been explicitly tested.

A significant number of minerals across multiple samples show moderate to strong positive correlations between Cl and N concentrations (Figure 39). Combined with the observation of elevated N and Cl contents at grain boundaries, there appears to be some relationship between the behaviour of Cl and N. If N and Cl are enriched at grain boundaries due to the high density of lattice defects then the broader correlation of N and Cl could indicate the N and Cl incorporation into minerals is in general sensitive to lattice defects across the whole grain. More work is required to investigate this hypothesis. Urann et al., 2020 suggested that fluid inclusions in eclogites are a significant host of Cl, but it is unclear whether the correlation of N and Cl could be related to fluid inclusions in my samples.

In summary, a mass balance analysis shows that grain boundaries alone probably cannot account for the observed discrepancy in N concentrations in most samples, even though there is some evidence that they may be more N-rich than the bulk minerals. Retrograde minerals and fluid inclusions are both possible explanations from a mass balance perspective but they each present problems of their own. Based on the lack of observed N-rich retrograde minerals, I tentatively suggest that fluid inclusions are the main explanation for the discrepancy in N concentrations. My data suggest that care should be taken in interpreting bulk rock analyses of metabasalts (and potentially other lithologies) as representing mineral-hosted N.

5.6.4.1 Literature data on reconstructed versus bulk nitrogen concentrations

To further investigate the comparison between mineral and bulk rock N concentrations I analysed data from three previous studies which have bulk rock concentrations for N and K_2O alongside N concentrations of mica separates in the same samples (Busigny et al., 2003a; Jia, 2006; Pitcairn et al.,

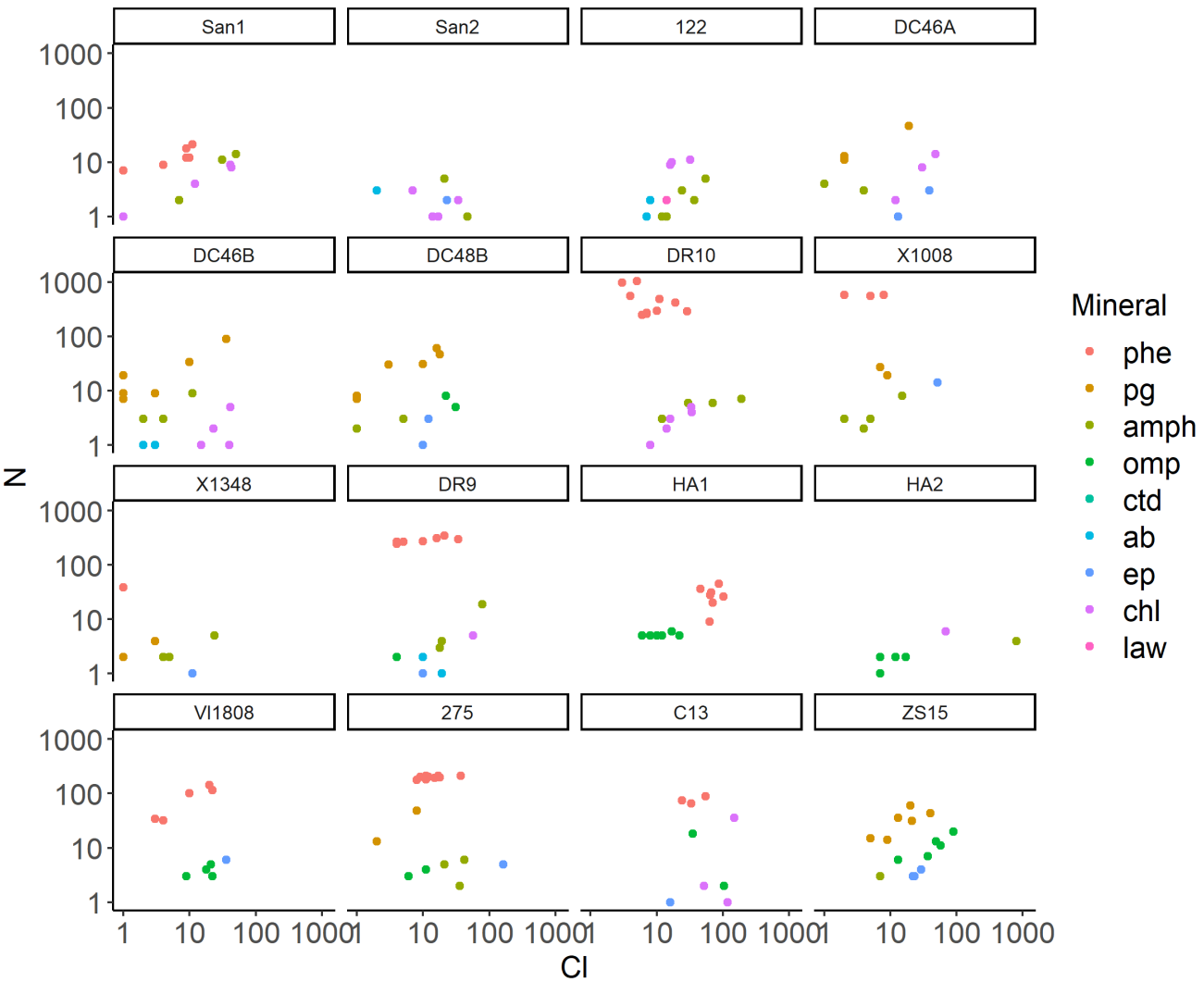


Figure 39: N versus Cl concentrations in different minerals measured by SIMS.

2005). These samples are all metasediments and span a wide range of metamorphic facies. Assuming that all K is hosted by micas (either muscovite or biotite) I can estimate the modal abundance of mica in these samples based on the bulk K_2O content, and then calculate the proportion of the bulk N that is hosted in micas (Table 14). This is necessarily a maximum proportion since the presence of other K-bearing phases such as feldspars (e.g. higher grade samples from Jia, 2006 contain K-feldspar) would cause mica mode to be overestimated in this calculation (unless micas contain a significant paragonite component in which case mica mode could be underestimated). My calculations show that the proportion of N hosted in micas is variable, but is less than 85% in three quarters of samples and less than 50% in a fifth of samples, which is generally higher than in my metabasalts but is still significantly less than 100%. Pitcairn et al., 2005 suggested that N might additionally be hosted in poorly-matured carbonaceous matter (kerogen), particularly in the lowest grade samples. In the samples from Jia, 2006, almost all N is hosted in micas in lower grade samples, whereas the lower amount of mica hosted N in sillimanite and migmatite grade samples may be at least partially accounted for by the presence of K-feldspar at these grades. The samples from Busigny et al., 2003a are perhaps the most interesting, since 10-45% of the N is not hosted in micas, but there are no other obvious candidate phases for N. Of the phases reported by the authors, only chlorite is a potential N host, but modes are <15% in all samples and do not correlate with the proportion of non-mica hosted N. Grain boundary-hosted N or fluid inclusions may therefore also play a role in some samples from previous studies, emphasizing that care needs to be taken in interpreting bulk N analyses as representing mineral-hosted N. The analytical protocols (pre-heating and other protocols) are all internally consistent within each of these three studies so this is not a factor to consider here.

5.6.4.2 N concentrations obtained using different analytical protocols

I will briefly return to the possible effects of pre-heating protocols in more detail and compare the measured and reconstructed bulk N data to those reported in the literature for AOC and HP metabasalts, both with and without pre-heating. In addition to the effect on phengite that was already discussed, Li et al., 2021b showed that pre-heating altered basalts at 400 °C during overnight evacuation (prior to combustion at ca. 1000 °C) results in 40-80 % lower N yields compared to pre-heating at < 200 °C. They suggest that the amount and isotopic signature of this lost N is

Source	Sample	Facies	Bulk K_2O	Bulk N	Phe N	Pg N	Bt N	Estimated mica mode	% of bulk N in micas
Pitcairn et al. 2005	Metapelite	Low grade	2.56	138	245			23%	41%
	Metapelite	Chl-grade	4.21	279	163			38%	22%
	Qz-fsp schist	Chl-grade	3.05	128	206			28%	45%
	Metapelite	Chl-grade	3.6	387	971			33%	82%
	Metapelite	Chl-grade	3.29	249	278			30%	33%
	Qz-fsp schist	Bt-grade	5.95	459			421	60%	55%
	Qz-fsp schist	Gt-grade	4.47	119			459	45%	172%
	Qz-fsp schist	Gt-olig grade	3.99	23			88	40%	153%
Busigny et al. 2003	Metapelite	Blueschist	2.48	560	1600			23%	64%
	Calc-silicate	Blueschist	0.88	232	2021			8%	70%
	Phe schist	Blueschist	7.96	1637	1700			72%	75%
	Metapelite	Blueschist	3.52	621	1300			32%	67%
	Calc-silicate	Blueschist	2.94	523	1150			27%	59%
	Calc-silicate	Eclogite	1.59	195	1200			14%	89%
	Calc-silicate	Eclogite	2.23	446	1200			20%	55%
Jia, 2006	Metapelite	Low grade	5.61	120	232			51%	99%
	Metapelite	Chl-grade	5.14	110	228			47%	97%
	Metapelite	Bt-grade	4.49	86	153			41%	73%
	Metapelite	And-grade	4.29	81			156	43%	83%
	Metapelite	Sil-grade	2.88	43			76	29%	51%
	Metapelite	Migmatite	2.77	41			72	28%	49%
This study	San1	Greenschist	0.44	14	14			4%	4%
	DR10	Blueschist	0.03	245	483			17%	34%
	DC46B	Blueschist	0.28	11		28		13%	31%
	DC46A	Blueschist	0.05	13		21		3%	4%
	DC48B	Blueschist	0.95	22		31		10%	14%
	X1008	Blueschist	0.57	61	566	23		9%	84%
	X1348	Blueschist	1.29	32	39	3		8%	4%
	Vi1808	Eclogite	0.02	36	85			5%	12%
	ZS15	Eclogite	0.03	14		33		13%	30%
	0275	Eclogite	0.46	15	199	31		13%	134%
	DR9	Eclogite	0.26	89	281			12%	38%
	HA1	Eclogite	0.47	18	28			5%	7%
	C13	Eclogite	0.37	31	76			5%	11%

Table 14: Literature data for samples that have bulk N, bulk K_2O and N concentrations in mica separates from the same sample. Bulk K_2O is used to estimate the white mica mode assuming 11% K_2O in white mica and 10% K_2O in biotite. This modal abundance is then used to calculate the proportion of the bulk N that is hosted in micas. *Mixed ms and bt separates (ms>bt). **Mixed ms and bt separates (bt>ms). Mica-bearing samples from this study are also shown for comparison but their mica modes were calculated using a different method (Section 2.6).

similar to that which is added to fresh basalts during seafloor alteration, and therefore that the N added during seafloor alteration is rather labile. They attribute this to the fact that the N is likely hosted in low temperature alteration phases such as clays. Likewise, Busigny et al., 2005 and Bebout et al., 2018 both analysed altered basalts from the same ODP core (although not specifically the same powders), with pre-heating at 450 °C and 100 °C respectively, and the latter study reported N concentrations that were 2–4 times higher. To my knowledge, similar comparative tests have not yet been performed on fresh HP rocks, so it is unknown whether labile N would also be present in rocks that do not contain low temperature alteration phases. However, the fact that pre-heating also results in N loss from pure phengite suggests that labile N could still be present in fresh rocks. It seems plausible that the N fraction which is released during pre-heating could correspond to, or at least overlap with, the fraction that I identified as not being hosted in silicate minerals from comparison of measured and reconstructed N concentrations (Section 5.6.4). All three possibilities that I discussed

for this non-mineral-hosted N (retrograde minerals, grain boundaries, and fluid inclusions) would likely be more susceptible to N loss at low temperatures.

Currently there is only one study that reports N concentrations obtained from HP rocks using preheating (Busigny et al., 2011). The N–δ^{15}N systematics of these samples fully overlap with data obtained from similar HP rocks by other studies which did not use pre-heating so it is hard to draw any conclusions about the relationship beween pre-heating and different N fractions from comparing either my reconstructed or measured data to these samples.

A useful avenue of future research would be to measure bulk N by combustion using a range of different pre-heating temperatures up to at least 500 °C in the same sample, then also measure N concentrations in mineral separates with varying pre-heating, and finally measure N concentrations in minerals by SIMS to calculate reconstructed N concentrations. This will establish a more quantitative relationship between non-mineral-hosted N and labile N lost during pre-heating, and could inform when or whether pre-heating should be used in bulk combustion studies. For example, if one wishes to only study mineral-hosted N then it might be useful to employ a pre-heating stage to remove labile N, whereas if total N from all sources is of interest then pre-heating may give inaccurate results.

5.6.5 Boron isotope constraints on the origin of nitrogen enrichment

In this section I discuss the origin of N enrichment in my samples. All samples are enriched in N compared to fresh MORB, and I propose three possible scenarios in which N enrichment could take place: seafloor alteration, N addition during prograde subduction, N addition during exhumation from the subduction zone. It is also possible that multiple of these processes occur in the same sample and, in particular, that the mineral-hosted fraction and non-mineral-hosted fractions of N may have been added at different times. In addition to the trace element and N signatures that I have already discussed, I discuss B isotope compositions of micas and other minerals to provide additional constraints on the geochemical evolution on these samples. Seafloor alteration produces heavy B isotope compositions (δ^{11}B = -4.3 to +24.9 ‰, De Hoog and Savov, 2018; Marschall, 2018 and references therein), whereas sediments have lighter B isotope compositions (-13.1 to +2.8 ‰). I also discuss bulk N isotope compositions, although these will reflect a mixture of mineral and non-mineral-hosted N fractions and are less easy to interpret. No studies have investigated covariation of

δ^{15}N and δ^{11}B but the range of reported compositions for each isotope system is plotted in Figure 40.

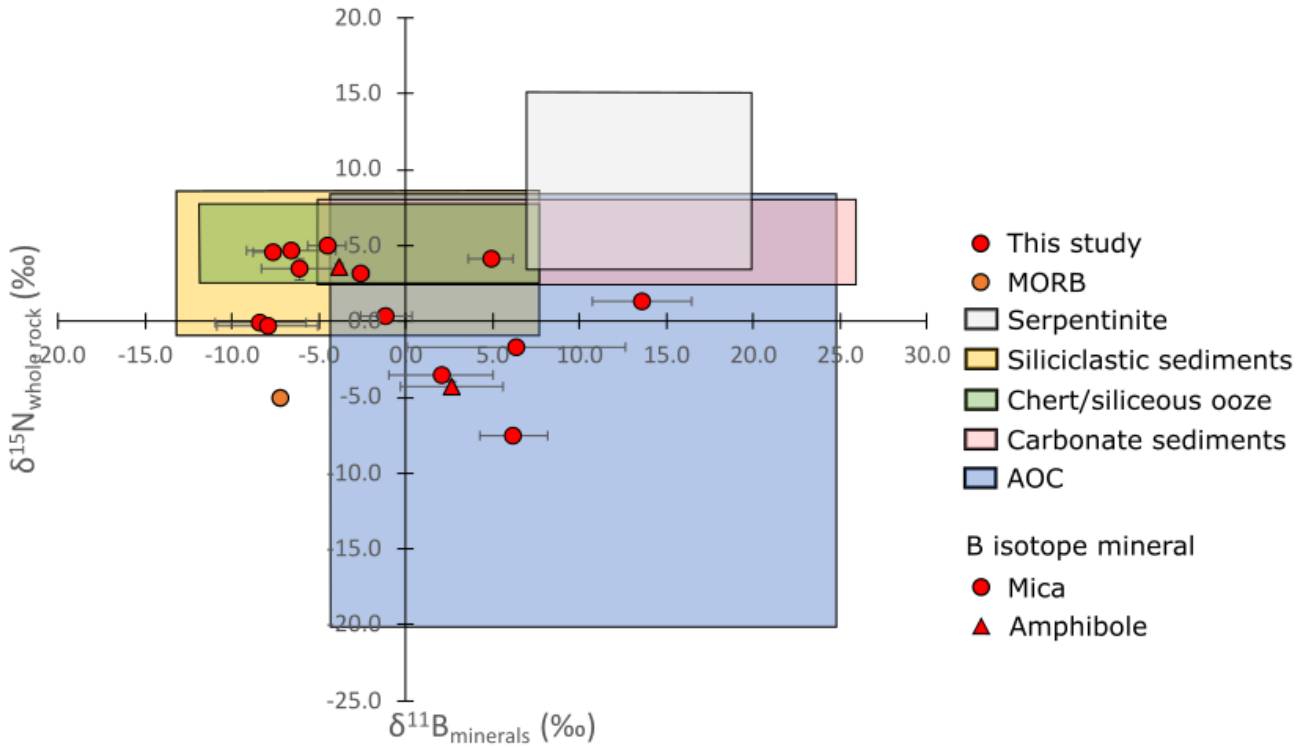


Figure 40: Covariation of whole rock δ^{15}N and mineral δ^{11}B compositions. B isotopes from amphibole are shown for mica-absent samples but there is minimal B isotope fractionation between mica and amphibole (Section 5.5.3) so these values are comparable.

Several lines of evidence show that the mineral-hosted fraction of N was either acquired during subduction or seafloor alteration. Most of this N is hosted in fresh HP phases which preserve HP major element compositions that appear relatively unaffected by retrogression. Where retrograde minerals (chlorite, albite in some samples) were observed, their N concentrations were not elevated compared to the peak HP phases. Mineral-hosted N was therefore either acquired during subduction, or was already present on the seafloor and was incorporated into HP minerals during prograde metamorphism. It is much harder to determine whether the non-mineral-hosted fraction of N is related to seafloor, subduction or exhumation processes.

Prograde devolatilization during subduction is expected to result in loss of B and other FME such as N, Ba and Rb from the rock (e.g. Bebout and Fogel, 1992; Busigny et al., 2003a), and a shift to lighter δ^{11}B values, since ^{11}B preferentially partitions into the fluid (Marschall et al., 2007;

Peacock and Hervig, 1999). Since B partitions strongly into mica compared to other minerals, the modal abundance of mica is predicted to exert a strong control on the amount of B loss during devolatilization and the associated shift in δ^{11}B. I observe no correlation between mica modal abundance and δ^{11}B, either as a whole or when the data are separated by mica composition. Whilst it is hard to make conclusions about individual samples that are not genetically related, since there could be variation in protolith composition, this suggests that devolatilization may not be a primary factor affecting the B systematics of these samples. Furthermore, K, Ba, Rb contents of my samples overlap with the field of AOC and show no strong signatures of devolatilization (Figure 31, Section 5.6.1.2). There are also weak negative correlations of δ^{11}B with Ba/Nb and bulk K_2O across the whole sample set (Figure 41). Devolatilization would be expected to result in a positive correlation of these variables (more devolatilized rocks have lower δ^{11}B, lower K and lower Ba), and therefore devolatilization is unlikely to be major process affecting these samples.

Four samples (DR9, DR10, X1008, 0275) show K-Ba-Rb enrichment (Section 5.6.1.2), $\delta^{11}B_{phe}$ ranging from -12.3 to -2.7 ‰ (Figure 41), and δ^{15}N ranging from -0.1 to + 5.0 ‰, all of which are consistent with interaction with HP sediment-derived fluids. Mineral-hosted N in these samples is also elevated compared to other samples, suggesting that a significant proportion of this N was added to the rock by sediment-derived fluids during subduction. Similar conclusions have been reached for some other HP metabasalts based on simultaneous enrichment of K, Ba, Rb and N (Li et al., 2021a; Mallik et al., 2023).

Another subset of six samples (Vi1808, DC46B, ZS15, DC48B, 122, X1348) have δ^{11}B values ranging from -1.3 to +16.9 ‰. These samples all show no trace element evidence of HP fluid-rock interaction (Section 5.6.1.2), and have high bulk Na contents ($>$ 4 wt% Na_2O, Figure 41) which likely reflect spilitization of the samples during seafloor alteration (Section 5.6.1.1). Heavy δ^{11}B is also consistent with seafloor alteration, suggesting that these samples preserve a seafloor alteration signature that was minimally affected by subduction-related processes. Preservation of seafloor δ^{11}B signatures at eclogite facies has recently been suggested in metagabbros from the Western Alps (Cannaò et al., 2023). As such, mineral-hosted N in these samples, which ranges from 3.6–9.1 μg/g, could also be suggested to derive from seafloor alteration.

The remaining five samples for which I have B isotope data (DC46A, C13, X1348, HA1, HA2) all

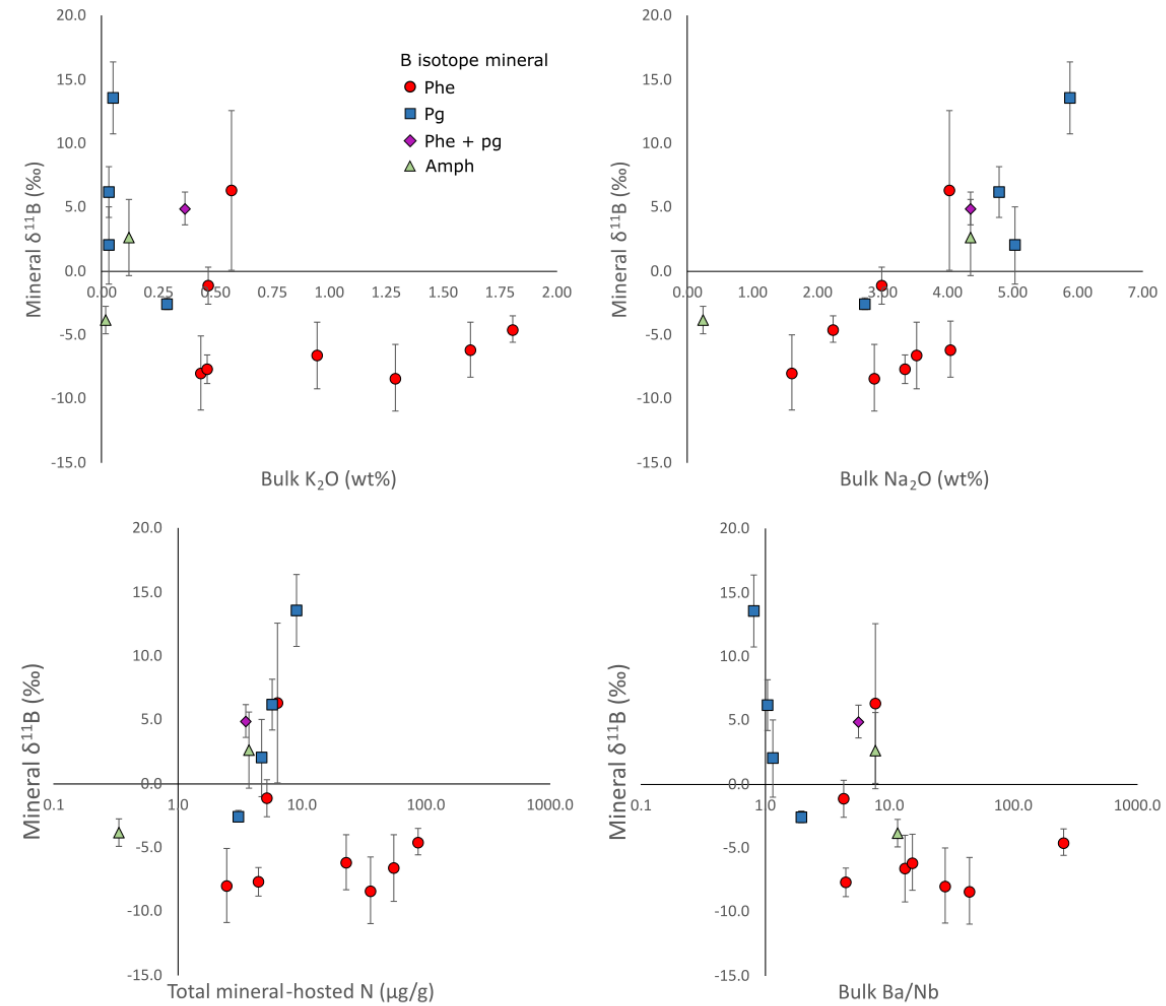


Figure 41: Covariation of mineral δ^{11}B compositions with whole rock K_2O, Na_2O, mineral-hosted N and bulk Ba/Nb. B isotopes from amphibole are shown for mica-absent samples but there is minimal B isotope fractionation between mica and amphibole (Section 5.5.3) so these values are comparable.

have negative δ^{11}B ranging from -0.3 to -12 ‰. Despite having negative δ^{11}B, they do not show clear evidence of K-Ba-Rb enrichment compared to AOC (Section 5.6.1.2), and δ^{11}B does not correlate with mineral-hosted N, which makes it unclear whether this N could have been sourced from sediment-derived fluids.

In summary, two distinct subsets of my samples record evidence of N addition from sediment-derived fluids during subduction, and N inherited from seafloor alteration respectively, and the remaining samples show conflicting evidence which makes it difficult to interpret the sources of N.

Whether the non-mineral-hosted fraction of N has the same origin as the mineral-hosted fraction is unclear. Samples with δ^{15}N < -1 ‰ all have positive δ^{11}B and are enriched in Na, which I interpreted to represent a preserved seafloor alteration signature (see above). Negative δ^{15}N values, associated with N concentrations that are significantly elevated above MORB, have previously been interpreted to record abiotic reduction of N_2 to NH_4^+ (Li et al., 2021a; Li et al., 2007, 2014). The measured bulk N concentrations and δ^{15}N values of these samples overlap with AOC samples that have previously been interpreted in this way. Combined with the δ^{11}B and Na data, this suggests that not only the mineral-hosted fraction, but the majority of N in these samples could be inherited from seafloor alteration. δ^{15}N in other samples in harder to interpret, since positive δ^{15}N values are common in both AOC and in other lithologies such as sediments, which could be potential sources of N during subduction, and δ^{15}N does not correlate strongly with mineral chemistry.

5.7 Implications for nitrogen recycling

The recognition that a significant fraction of mineral-hosted N may reside in minerals other than micas, even in mica-bearing samples has significant implications for our understanding of N within subducting slabs. Phengite is stable beyond sub-arc depths (i.e. >80–100 km, 2.4–3 GPa, Schmidt and Poli, 2014; Schmidt and Poli, 1998; Schmidt et al., 2004). Paragonite is not stable above 2.2–2.5 GPa (Massonne and Sobiech, 2007), which corresponds to 70–80 km depth. Amphibole and chlorite stabilities have a greater dependence on temperature and bulk composition, so the depth at which they break down will depend on the subduction zone geothermal gradient and the degree of alteration of the downgoing slab. However, the majority of chlorite in most slabs will have broken down by 50 km depth, and amphibole by 80 km depth (Hernández-Uribe and Palin, 2019; Hernández-

Uribe et al., 2020; Schmidt and Poli, 2014; Schmidt and Poli, 1998). Hernández-Uribe et al., 2020 modelled the mineralogical evolution of three representative compositions for chloritized, spilitized and epidotized AOC along typical subduction geotherms. Epidosites *sensu stricto* consist almost entirely of epidote and quartz across the entire P-T range. Given that I observe epidote to contain little N (and quartz to be essentially N-free), epidotization should not increase the ability of AOC to retain N during subduction. Chloritized AOC stabilises large amounts of chlorite at low pressure, which dehydrates to form garnet between 1.7–2.2 GPa. Since chlorite is a significant N-bearing phase but garnet is essentially N-free, chloritized rocks could host significant N at shallower depths but may undergo significant N loss during prograde devolatilization. Spilitized AOC stabilises large amounts of amphibole, which dehydrates to form omphacite between 1.8–2.4 GPa. Nitrogen loss during amphibole dehydration may be less significant than during chlorite dehydration since the product omphacite can host similar N concentrations to the reactant amphibole, although some N will still be partitioned into the fluid and lost from the rock. The other main style of alteration which will affect the ability of subducted AOC to retain N will be potassic alteration. I have shown that the mica mineralogy of HP metabasalts depends on bulk K_2O, and possibly also Na_2O, concentrations, and identified a threshold of around 0.3 wt% K_2O, above which phengite occurs as the main mica phase in HP metabasalts. Below this threshold, either paragonite or no micas occur. The presence of paragonite versus phengite is significant because whilst phengite is stable beyond the arc, paragonite will break down at depths approaching that of the arc front in most subduction zones. Paragonite breakdown in subducted AOC could potentially be a source of N at sub-arc depths. Potassium-enrichment is therefore the most important alteration style that affects the ability of AOC to subduct mineral-hosted N beyond the arc. Spilitization may also increase N transport capacity by stabilising omphacite, but this may be offset if spilitization is associated with K-depletion, as observed in some ophiolitic spilites (Belgrano and Diamond, 2019). The impact of the non-mineral-hosted fraction of N on the ability of AOC to retain N is harder to assess. If a significant portion is hosted in fluid inclusions then these could provide an alternative mechanism to subduct N beyond the arc that is likely less dependent on bulk rock composition. On the other hand, N hosted in wide grain boundaries is likely an exhumation-related feature and is therefore unrelated to prograde subduction processes.

Although I did not study the behaviour of N in sediments in this chapter, it is worth considering

the implications of paragonite-hosted N for the dehydration behaviour of sediments. Paragonite is predicted to be present in most metapelites up to its maximum pressure stability, with a modal abundance of up to ca. 10 vol% (Kouketsu and Enami, 2011; Massonne and Sobiech, 2007). Paragonite breakdown in metapelites could therefore be a source on N at depths approaching that of the arc, and since sediments can contain large amounts of N, this could represent a significant N release in subducting slabs. Likewise, B could also be released since it is strongly enriched in paragonite compared to other phases.

In common with some previous studies (Li et al., 2021a; Mallik et al., 2023), I find evidence that metabasalts can acquire large amounts of N (potentially > 100 μg/g) during interaction with sediment-derived fluids inside subduction zones. Mafic crust could therefore act as a trap for sedimentary N which would otherwise be directly transferred to the mantle wedge. Several factors are likely to affect the efficiency of this process. The degree of seafloor alteration in the mafic crust will control how much N it is able to take up, with K and Na-enrichment being particularly important in determining the N storage capacity. The lithostratigraphy of the subducting slab also likely exerts a strong control on the extent of sediment-mafic crust interaction. If the slab is composed of a coherent layer of sediments overlying a coherent mafic crust layer, as is typical of crust formed at fast-spreading mid-ocean ridges (e.g. Moores et al., 1997), then sediment-derived fluid input into the mafic crust is likely to be limited, since fluids from dehydrating sediments should migrate upwards into the overlying mantle wedge. On the other hand, if sediments and mafic crust are tectonically intercalated, as is typical of slow-spreading crust (e.g. Agard, 2021; Manatschal and Müntener, 2009), then there would be much greater potential for transfer of N and other FME from sediments into the mafic crust. The extent to which fluid flow through the slab is channelized will also control the extent of sediment-crust interaction but this is presently poorly constrained (e.g. Konrad-Schmolke et al., 2011; Piccoli et al., 2021; Plümper et al., 2017). Whether this N trapped in mafic lithologies is released at greater depth or subducted beyond the arc will depend on the factors discussed above.

5.8 Conclusions

This study presents N concentrations in minerals from subduction-related greenschists, blueschists and eclogites. The data confirm that micas have the highest N concentrations of typical metabasalt

minerals. Omphacite, Na-Ca amphiboles and chlorite can also host moderate levels of N, but epidote, albite and other minerals are not significant N hosts. When the modal abundance of these minerals is accounted for, micas typically host around half of the total mineral-hosted N, since their high N concentrations are offset by low modal abundance. Metabasalts that have been metasomatised by sediment-derived fluids during subduction can have very high fractions ($> 90\%$) of mineral-hosted N hosted in mica, since metasomatic K-enrichment leads to elevated mica modes. Greenschists appear to have relatively low N concentrations in mica compared to blueschists and eclogites and therefore have a lower proportion of N hosted in micas.

Amongst micas, paragonite appears to be an equally important host of N as phengite since its lower N concentration is offset by higher modal abundance. Paragonite occurs in a number of my samples with bulk compositions representing spilitized oceanic crust, which conflicts with previous models of the phase petrology of subducted crust. Its importance for the cycling of N and other FME may therefore be underestimated in previous studies. Spilitization and K-enrichment are the two styles of oceanic alteration which could increase the capacity of AOC to subduct N to, and beyond, sub-arc depths.

Nitrogen concentration data were used to calculate inter-mineral partition coefficients. I suggest that mica-omphacite partitioning may be P-T-dependent, with more N going into phengite at lower pressures and lower temperatures, but no P-T effect is observed for mica-amphibole partitioning. The behaviour of N may be decoupled from other FME such as B and Li.

Total mineral-hosted N, based on mineral N concentrations and modal abundances, is significantly lower than measured bulk N for many samples, whereas mineral-hosted K and Rb agree with bulk values, suggesting that significant N may be hosted in phases other than the measured silicate minerals. I tentatively suggest that fluid inclusions are the mostly likely site for non-mineral-hosted N, but more work is required to investigate this hypothesis. Nitrogen hosted in grain boundaries could also be important for some samples but this contribution depends strongly on grain size and grain boundary width. Caution should be exercised in interpreting bulk analyses of N in metabasalts as representing mineral-hosted N.

Comparison of N concentrations, other FME concentrations, B isotopes and N isotopes suggests that N concentrations in HP metabasalts could increase by an order of magnitude if they interact

with N-rich fluids during subduction, which could be easily produced from dehydrating sediments. In other cases, HP metabasalts can retain N that was acquired during seafloor alteration throughout the subduction and exhumation cycle, emphasising the variety of outcomes that can occur when N-bearing crust is subducted.

Acknowledgements

Alberto Vitale-Brovarone (University of Bologna), Samuel Angiboust (École normale supérieure de Lyon), Simon Harley (University of Edinburgh), Ray Burgess (University of Manchester), the EFIRE collection (Pennsylvania State University) and the John Dixon collection (University of Edinburgh) are thanked for their contribution of samples to this study, alongside those collected by the authors.

5.9 Post-script

In this chapter I expanded upon work in Chapter 3 to determine the relative importance of different minerals and non-mineral phases as hosts for N in HP metabasalts (question 1). In common with that previous chapter I showed that white micas contain the highest N concentrations of any common mineral, but that the total contribution of micas to the bulk N is limited by their low modal abundance, and that omphacite, amphiboles and chlorite can be equally important N hosts. I discussed the implications of this for the retention of N within the subducted crust which has undergone different degrees and styles of seafloor alteration, leading to the appearance of different HP mineral assemblages. I also refined estimates for inter-mineral N partition coefficients (question 2b). In contrast with the preliminary conclusion in Chapter 3, investigation of a larger suite of samples showed that non-mineral N hosts can be very significant in some samples and I suggest that this should be a priority for further investigation. By combining B isotopes, N concentrations, N isotopes and other FME concentrations I identified two separate origins for N hosted in HP metabasalts (question 3). One group of samples retains N that was acquired during seafloor alteration, whereas another group of samples has acquired significant amounts of additional N from interaction with HP sediment-derived fluids. In common with Chapter 4 I demonstrate that B isotopes are a useful tool to identify such HP sediment-derived fluids.

6 Chapter 6: Conclusions and further work

Here I integrate the conclusions of each research chapter to answer the questions set out in the introduction to this thesis. Finally, I suggest some directions for future research.

1. What is the significance of white mica as a host for N and other FME in subducted oceanic crust compared to other HP minerals, and to non-mineral hosts? How does the mineralogy of subducted rocks affect their ability to retain FME during subduction?

In Chapters 3 and 5 I showed that N concentrations in HP metabasic minerals decrease in the order phengite > paragonite > Na-Ca amphibole ≈ chlorite ≈ omphacite > epidote ≈ albite ≈ lawsonite. However, the total amount of N stored in each mineral depends not only on its N concentration but also on its modal abundance. When this is taken into account, the total N storage capacity of phengite, paragonite, Na-Ca amphiboles, omphacite and chlorite can be similar in typical metabasalt phase assemblages. The major element composition of the rock therefore becomes a significant factor in controlling where N is hosted due to its effect on the modal abundances of different minerals. In Chapter 5 I showed that significant amounts of N can also be hosted in non-mineral sites in HP metabasalts. Fluid inclusions are the most likely source of this non-mineral-hosted N fraction, although grain boundaries could also be significant in some samples.

I investigated the role of phengite versus paragonite as a host for N in two different contexts. In Chapter 3 I showed that the growth of paragonite at the expense of amphibole, resulting from the addition of carbonate-bearing fluids to HP metabasalts, sequestered N from coexisting phengite and resulted in minimal N loss from the bulk rock during fluid-rock interaction. In Chapter 5 I showed that the stability of phengite versus paragonite in HP metabasalts depends on the bulk K_2O, and possibly also bulk Na_2O, content of the rock, and that paragonite can be an important host of N in K-poor (MORB-like) metabasalts. Paragonite breaks down at depths approaching that of the arc front, whereas phengite is typically stable beyond the arc. Therefore paragonite may be more important for recycling volatiles back to the surface, whereas phengite is more important for subduction of volatiles into the deep mantle.

In Chapter 4 I investigated the redistribution of FME during a dehydration reaction where phlogopite is replaced by phengite. In this case, the product phengite has a significantly higher capacity

to host B compared to the reactant phlogopite which allowed the rock to sequester B from an incoming B-rich fluid. The opposite was true for elements such as Cs, Cl and F, which were lost during this dehydration reaction.

A common theme is that the loss of FME during metamorphic dehydration reactions depends strongly on whether those elements are more compatible in the product phases, or in the fluid. Not all dehydration reactions will result in the same degree of FME loss from the rock, even if the amount of fluid released is the same.

2. How does N partition between different minerals at HP and can we place constraints on a) fluid-mineral, and b) inter-mineral partition coefficients for N in natural samples and compare these with experimental data?

In Chapter 3 I estimated the phengite-fluid partition coefficient for N (D_N^{phe-fl}) to be 0.1–1.5 in a sample that experienced fluid-rock interaction at ~600 °C and 2.7–3.2 GPa. This is towards the lower end of the range of experimentally determined values, and is lower than the value for Rb^+, which some previous studies have assumed behaves similarly to NH_4^+.

In Chapters 3 and 5 I estimated white mica-amphibole ($D_N^{phe-amph}$=2.8–121), white mica-omphacite ($D_N^{phe-omp}$= 5.7–81) and white mica-chlorite ($D_N^{phe-chl}$=2.5) partition coefficients for N in HP rocks, which provides a starting point for modelling the redistribution of N between minerals during subduction and devolatilization. I suggested that mica-omphacite partitioning may be P-T dependent, with more N going into omphacite at higher pressures and temperatures.

3. Can we use coupled analyses of B isotopes, N and other FME to trace the fluid sources within subducted crust, and disentangle processes such as seafloor alteration, devolatilization and HP fluid-rock interaction?

In all three chapters I demonstrated that N concentrations can be successfully analysed in micas and other HP minerals using SIMS. Other FME concentrations can be analysed in the same spots, allowing N behaviour to be compared to that of more commonly studied elements.

I showed that B isotopes and concentrations in micas are a useful tool to investigate fluid processes in subducted crust. Boron isotopes are particularly useful for distinguishing between processes that occurred on the seafloor, which have a heavy B isotope signature, and processes involving mobilization of sediment or continental crust-derived B during subduction, which has a light B isotope signature.

Metasomatism by sediment-derived fluids was recorded in both subducted continental (Chapter 4) and oceanic crust (Chapter 5) by negative δ^{11}B values associated with high B concentrations. White mica is a particularly useful recorder of information about fluid processes compared to the more commonly studied tourmaline because it records information about the B concentration in the fluid as well as its isotope composition.

The combination of B and N isotopes could be useful for some applications but more work is required to explore the covariation of these two isotope systems in seafloor and HP rocks. For example, in Chapter 5 I used B isotopes to show that abiotic N reduction, which is recorded by strongly negative δ^{15}N values, occurred on the seafloor and this signature was preserved during subduction and exhumation. Another difficulty is that, at present, it is only possible to measured N isotopes with sufficient precision to be useful using bulk combustion methods. In Chapter 5 I showed that significant fractions of N can reside in different hosts within a bulk sample and therefore bulk isotope analyses could represent a mixture of N from different sources, hampering their interpretation.

4. How are N and other mica-hosted FME redistributed between different lithologies in the subducting slab, and what are the implications of this for the recycling of these elements into the mantle?

In all three research chapters I found varying degrees of evidence for addition of N to white mica-bearing rocks by the infiltration of N-rich fluids at high pressures. In Chapter 3, high N concentrations which correlate positively with B, and negatively with Li, occur in metabasite-hosted white micas from a melange setting (Jenner). Such correlations were also observed in melange samples from a different locality (Punta Balandra) in Chapter 5. P-T conditions recorded at these localities are quite similar (Jenner: 1.0–1.5 GPa, 450–500 °C; Punta Balandra 1.3 ± 0.2 GPa, 450 ± 70 °C), but studies of more localities would be required to determine whether this is a coincidence or whether such fluid compositions are common at these P-T conditions. Separately, in Chapters 3 and 4 I observed higher N concentrations in white micas that formed during early retrograde metamorphism compared to micas that formed at peak UHP conditions at both Lago di Cignana and Dora-Maira. In Chapter 5 I observed high bulk and mica-hosted N concentrations in several metabasalts that also displayed FME and B isotope signatures consistent with interaction with sediment-derived fluids. Redistribution of N and B from sediments into the mafic crust therefore appears to be a common process, which has

also been observed in a few other studies (Li et al., 2021a; Mallik et al., 2023). Any model of N or B in the subducting slab should therefore consider that a portion of these elements lost from dehydrating sediments may be sequestered into the mafic crust rather than transferred directly into the mantle wedge. Whether this is a particular feature of exhumed high-pressure rocks, which are perhaps more likely to be exposed to sediment-derived fluids, or whether it occurs during steady state subduction remains an open question.

6.1 Recommendations for further work

1. Development of a wider range of mineral standards for N to include pyroxenes, amphiboles and chlorite would improve the accuracy of SIMS measurements in these minerals and remove any question of whether matrix effects are partly responsible for some of the discrepancies I observed between measured and reconstructed bulk compositions, or variations in inter-mineral partition coefficients.

2. The suggestion from Chapter 5 that a significant fraction of N could be hosted in fluid inclusions or along grain boundaries should be explicitly tested by measuring N concentrations in these sites, although this could be analytically challenging, especially for grain boundaries. One option that may provide indirect insight into this question would be comparison of the reconstructed mineral-hosted N with bulk N concentrations determined using different pre-heating temperatures or step heating protocols similar to those used for Ar-Ar dating. Fractions of N that are lost at low temperatures are more likely to be hosted in fluid inclusions or other labile sites compared to in mineral lattices. This hypothesis is important to address, since non-mineral hosted fractions of N could behave very differently to mineral-hosted N during subduction and therefore could have a significant impact on the amount of N recycled into the mantle. Models which only consider mineral-hosted N might lead to erroneous results.

3. A comparison should be done between SIMS N analyses of individual minerals and combustion analyses of mineral separates from the same sample, using different pre-heating conditions. This would investigate why a significant fraction of N is lost from micas (and possibly other minerals as well) at 400 °C, how this fraction of N is hosted within the mineral separate, and whether

SIMS N concentrations measure the full N concentration of the mineral separate, or only some fraction of it. The latter seems unlikely since SIMS is insensitive to how N is bound in the mineral, but if N is concentrated in small regions such as near grain boundaries then it might easily be missed by SIMS analyses. This may include investigating whether all N in minerals is hosted as NH_4^+. For example, I showed that chlorite can contain moderate amounts of N, as measured by SIMS, and yet it does not contain significant amounts of K^+ or Na^+ which NH_4^+ could most easily substitute for and therefore the mechanism of N incorporation into chlorite is unclear.

4. Better mineral standards for non-mica minerals would improve upon the inter-mineral partition coefficients determined in this thesis. The apparent difference in partitioning behaviour between greenschist facies and blueschist/eclogite facies samples should be also investigated to see whether there is a true difference in the equilibrium partition coefficients, or whether disequilibrium processes are important at the low temperatures and pressures of the greenschist facies. This may be analytically challenging due to the small grain size of many greenschist facies samples. A more systematic analysis of the effects of mineral major element composition (particularly amphiboles and pyroxenes) on partition coefficients would be useful to try to explain more of the variability in N partition coefficients. This would require specifically selecting samples with differing bulk compositions, which therefore cover a range of mineral compositions at similar P-T conditions.

5. Our current quantitative understanding of the N recycling efficiency is primarily based on comparisons between input and output fluxes at modern subduction zones but this is hampered by poor constraints on several of these fluxes, particularly on the output side. Now that we have some first order constraints on the importance of different minerals to the N budget of HP metabasalts, and the partition coefficients between these minerals, an attempt can be made at modelling the dehydration behaviour of subducted metabasalts as a function of pressure and temperature (e.g. Konrad-Schmolke and Halama, 2014; Marschall et al., 2007), which would provide an alternative way to estimate the N recycling efficiency and the overall magnitude of the flux into the deep mantle. Such a model would also provide a quantitative basis to make

inferences about the relative importance of factors such as subduction zone geothermal gradient, seafloor alteration, and transfer of N between sediments and mafic crust, in determining the N recycling efficiency. It could also provide a basis to quantitatively investigate how recycling efficiency has changed over geological time in response to secular changes in these parameters. Since the N-bearing minerals in metasediments are largely the same as those in metabasalts, but with different modal abundances, a model using my data could also include sediments in the subducting slab. Serpentinites have very different mineralogy and the mineral hosts of N in serpentinites are poorly understood so would be much harder to incorporate into such a model at present. The mechanisms of N incorporation into HP serpentinites are therefore also a useful target for future study.

The overall conclusion of this thesis is that white micas are an excellent tracer of fluid processes in subducting crust due to their incorporation of multiple FME, including N, and the useful B stable isotope system. Seafloor alteration of oceanic crust can increase the stability of both phengite and paragonite during subduction and therefore increase ability of the crust to transport N, B and other volatiles to sub-arc depths. However, other mineral and non-mineral hosts besides white micas also play an important role for transporting N and potentially other volatiles in the subducting crust. This is a major area where future work should be focused. As such white mica alone cannot be used to infer N recycling in subduction zones. Having said that, eclogite facies phengite can still host significant amounts of N and, alongside omphacite, will be the main mineral that transports N in both oceanic crust and sediments beyond the arc and into the deep mantle. Complete loss of N from the subducting slab is unlikely and some N will be subducted into the mantle in all but the warmest subduction zones, where phengite melting might occur. A significant ingassing of N into the Earth's mantle through subduction zones therefore appears to be a likely scenario.

A Appendix A: Data

A.1 Data for Chapter 3

Tables 15, 16, 17: This is a complete list of all EPMA major element data collected for these samples. The laboratory where the data were collected is listed as either Kiel or Cambridge.

Tables 18, 19: This is a complete list of all SIMS N, B, Li, F and Cl data collected for these samples.

Tables 20, 21, 22, 23: This is a complete list of all standards analysed during the SIMS sessions. Reference values for concentrations are from: Phe80-3 (Busigny et al., 2003b), LMMN (Busigny et al., 2004), ms98973 (Dyar et al., 2001), GSD1-G and BCR2-G (Jochum et al., 2005), Fba5 (Guggino and Hervig, 2011), JJE01-X-3_mica and MVE02-8-5_mica (Martin et al., 2015), St8.1.A9 (Lesne et al., 2011).

Table 24: This table details the modal abundances of phengite, paragonite and chlorite determined by point counting, and bulk concentrations calculated by combining mineral modes and concentrations.

Sample	Grain	Mineral	Data source	Si (p.f.u.)	Ti	Al	Fe^{2+}	Mn	Mg	Ca	Na	K	O	SiO_2 (wt%)	TiO_2	Al_2O_3	FeO	MnO	MgO	CaO	Na_2O	K_2O
LC-1b	m1	pa	Kiel	6.06	0.01	5.86	0.02	0.00	0.03	0.03	1.94	0.07	22	47.12	0.06	38.67	0.23	0.01	0.16	0.21	7.79	0.43
Cignana	m2	pa	Kiel	6.10	0.01	5.76	0.04	0.00	0.06	0.02	1.92	0.12	22	47.60	0.09	38.09	0.33	0.00	0.32	0.18	7.74	0.73
Eclogite	m3	pa	Kiel	6.07	0.01	5.80	0.04	0.00	0.05	0.02	1.96	0.09	22	47.53	0.06	38.56	0.34	0.02	0.27	0.15	7.91	0.55
	m4	pa	Kiel	6.06	0.00	5.85	0.02	0.00	0.03	0.03	2.00	0.07	22	47.54	0.00	38.96	0.22	0.00	0.16	0.19	8.11	0.40
	m5	pa	Kiel	6.08	0.00	5.78	0.04	0.00	0.05	0.03	1.97	0.09	22	47.40	0.04	38.26	0.40	0.03	0.26	0.21	7.93	0.55
	m7	pa	Kiel	6.09	0.01	5.73	0.03	0.00	0.10	0.02	1.96	0.13	22	47.76	0.06	38.13	0.32	0.00	0.54	0.17	7.93	0.78
LC-2a	m1	phe	Kiel	6.77	0.01	4.33	0.18	0.01	0.68	0.00	0.21	1.80	22	50.58	0.13	27.45	1.63	0.05	3.39	0.00	0.82	10.52
Cignana	m3	phe	Kiel	6.69	0.03	4.42	0.18	0.00	0.66	0.00	0.23	1.75	22	50.37	0.32	28.20	1.59	0.01	3.35	0.00	0.89	10.32
Metagabbro	m4	phe	Kiel	6.67	0.01	4.49	0.18	0.00	0.63	0.00	0.24	1.79	22	49.78	0.15	28.45	1.65	0.00	3.14	0.00	0.92	10.50
	m5	phe	Kiel	6.74	0.02	4.36	0.20	0.00	0.66	0.00	0.21	1.76	22	50.35	0.25	27.60	1.79	0.00	3.29	0.02	0.79	10.33
	m6	phe	Kiel	6.84	0.02	4.23	0.14	0.00	0.72	0.00	0.18	1.81	22	51.55	0.22	27.00	1.26	0.02	3.65	0.00	0.70	10.71
	m7	phe	Kiel	6.75	0.01	4.36	0.19	0.00	0.67	0.00	0.21	1.78	22	50.63	0.08	27.78	1.68	0.02	3.37	0.00	0.83	10.49
	m8	phe	Kiel	7.03	0.00	3.82	0.10	0.00	0.95	0.00	0.07	1.93	22	52.68	0.00	24.33	0.93	0.03	4.80	0.00	0.28	11.34
	m9	phe	Kiel	6.77	0.02	4.30	0.15	0.00	0.70	0.00	0.21	1.79	22	50.85	0.18	27.41	1.34	0.03	3.53	0.00	0.83	10.53
LC-3	m1	phe	Kiel	6.91	0.02	3.98	0.45	0.01	0.69	0.00	0.12	1.89	22	51.16	0.22	25.01	4.01	0.07	3.42	0.02	0.45	10.98
Cignana	m2	phe	Kiel	6.97	0.02	3.85	0.46	0.01	0.79	0.00	0.06	1.94	22	51.33	0.17	24.06	4.04	0.08	3.90	0.00	0.22	11.19
Gt-phe-	m3	phe	Kiel	6.89	0.01	4.02	0.46	0.01	0.68	0.00	0.09	1.91	22	50.72	0.15	25.12	4.06	0.06	3.34	0.00	0.35	11.01
quartzite	m4	phe	Kiel	7.00	0.02	3.82	0.47	0.00	0.75	0.00	0.05	1.96	22	51.18	0.15	23.70	4.11	0.04	3.70	0.00	0.19	11.22
	m5	phe	Kiel	6.94	0.03	3.91	0.47	0.01	0.72	0.00	0.09	1.94	22	51.13	0.27	24.44	4.15	0.07	3.55	0.00	0.33	11.20
	m6	phe	Kiel	7.01	0.02	3.83	0.46	0.00	0.74	0.01	0.06	1.93	22	51.18	0.15	23.75	4.04	0.03	3.62	0.08	0.23	11.04
	m7	phe	Kiel	6.94	0.01	3.97	0.44	0.01	0.70	0.00	0.10	1.89	22	51.06	0.12	24.79	3.89	0.07	3.48	0.00	0.36	10.90
	m8	phe	Kiel	6.97	0.03	3.85	0.46	0.00	0.74	0.00	0.06	1.96	22	51.46	0.29	24.08	4.10	0.04	3.66	0.00	0.21	11.31
	wm1	phe	Kiel	6.85	0.03	4.05	0.48	0.01	0.66	0.00	0.10	1.92	22	50.43	0.28	25.29	4.27	0.13	3.28	0.00	0.38	11.08
	wm10r	phe	Kiel	6.87	0.03	4.02	0.48	0.01	0.67	0.00	0.12	1.89	22	50.68	0.26	25.17	4.26	0.05	3.33	0.00	0.47	10.91
	wm11	phe	Kiel	6.97	0.02	3.84	0.49	0.01	0.74	0.00	0.05	1.95	22	51.24	0.23	23.96	4.31	0.06	3.67	0.00	0.18	11.24
	wm12	phe	Kiel	6.85	0.02	4.03	0.52	0.02	0.67	0.00	0.12	1.89	22	50.22	0.24	25.06	4.52	0.13	3.28	0.02	0.44	10.88
	wm5r	phe	Kiel	6.93	0.02	3.95	0.46	0.00	0.70	0.00	0.09	1.94	22	51.06	0.15	24.66	4.07	0.03	3.47	0.00	0.34	11.18
	wm7r	phe	Kiel	6.85	0.01	4.10	0.45	0.01	0.65	0.00	0.12	1.90	22	50.08	0.14	25.44	3.93	0.08	3.17	0.01	0.46	10.91
SEC16-1	chlA	chl	Cambridge	2.79	0.00	2.42	2.20	0.03	2.55	0.00	0.00	0.00	14	26.49	0.03	19.52	25.06	0.29	16.29	0.02	0.02	-0.01
Raspas	chlB	chl	Cambridge	2.78	0.00	2.47	1.91	0.01	2.79	0.00	0.00	0.00	14	27.17	0.06	19.48	22.89	0.20	17.28	0.07	0.01	0.10
Blueschist	chlC	chl	Cambridge	2.84	0.00	2.40	2.00	0.02	2.69	0.01	0.00	0.01	14	26.89	0.04	20.25	22.04	0.16	18.10	0.02	-0.02	-0.01
	paC	pa	Cambridge	6.11	0.00	5.59	0.21	0.00	0.21	0.02	1.43	0.46	22	47.01	0.02	36.47	1.94	0.01	1.09	0.12	5.66	2.74
	paD	pa	Cambridge	6.01	0.01	5.94	0.09	0.00	0.03	0.02	1.79	0.08	22	47.07	0.05	39.50	0.81	0.00	0.14	0.12	7.24	0.50
	paE	pa	Cambridge	5.98	0.01	5.96	0.07	0.00	0.03	0.02	1.77	0.15	22	46.77	0.08	39.53	0.62	0.01	0.13	0.16	7.15	0.92
	paF	pa	Cambridge	6.01	0.00	5.95	0.08	0.00	0.03	0.01	1.74	0.10	22	46.72	0.03	39.24	0.77	0.00	0.16	0.11	6.97	0.59
	m1	phe	Kiel	6.68	0.04	4.50	0.34	0.00	0.55	0.00	0.24	1.63	22	49.17	0.36	28.09	2.98	0.02	2.72	0.01	0.91	9.41
	m10	phe	Kiel	6.76	0.02	4.37	0.34	0.01	0.59	0.01	0.16	1.73	22	49.49	0.15	27.19	3.02	0.06	2.91	0.04	0.59	9.91
	m11	phe	Kiel	6.64	0.05	4.53	0.33	0.00	0.53	0.00	0.27	1.64	22	48.61	0.52	28.09	2.91	0.00	2.59	0.00	1.02	9.43
	m3	phe	Kiel	6.79	0.02	4.32	0.34	0.00	0.63	0.00	0.12	1.73	22	49.99	0.18	26.96	3.01	0.04	3.09	0.03	0.45	9.97
	m5	phe	Kiel	6.65	0.04	4.51	0.34	0.00	0.56	0.00	0.24	1.68	22	48.38	0.42	27.83	2.98	0.04	2.72	0.00	0.91	9.56
	m6	phe	Kiel	6.68	0.04	4.46	0.34	0.00	0.57	0.00	0.23	1.67	22	49.32	0.41	27.93	3.01	0.01	2.82	0.01	0.89	9.66
	m7	phe	Kiel	6.80	0.01	4.32	0.33	0.00	0.62	0.00	0.14	1.74	22	49.87	0.08	26.87	2.87	0.02	3.07	0.00	0.54	10.03
	m8	phe	Kiel	6.73	0.04	4.41	0.34	0.00	0.58	0.00	0.19	1.68	22	49.29	0.34	27.41	3.01	0.00	2.83	0.00	0.73	9.64
	m9	phe	Kiel	6.71	0.04	4.40	0.35	0.01	0.61	0.00	0.22	1.66	22	49.46	0.38	27.49	3.04	0.06	2.99	0.00	0.82	9.58
	pheD	phe	Cambridge	6.69	0.00	4.47	0.34	0.00	0.59	0.00	0.15	1.81	22	48.98	-0.04	27.76	2.97	0.01	2.92	0.00	0.57	10.36
	pheF	phe	Cambridge	6.71	-0.01	4.45	0.36	0.00	0.59	0.01	0.13	1.78	22	48.69	-0.11	27.42	3.10	0.02	2.89	0.04	0.48	10.13
	pheA	phe	Cambridge	6.67	0.01	4.53	0.33	0.00	0.55	0.00	0.22	1.68	22	48.92	0.14	28.23	2.87	0.01	2.71	0.00	0.82	9.65
SEC44-1	cpxA	cpx	Cambridge	1.99	0.00	0.42	0.15	0.00	0.47	0.56	0.43	0.00	6	55.36	0.09	9.82	4.88	0.02	8.69	14.52	6.24	0.00
Raspas	cpxB	cpx	Cambridge	1.98	0.00	0.46	0.15	0.00	0.43	0.54	0.44	0.00	6	55.34	0.17	10.84	5.00	0.02	8.12	14.21	6.33	-0.01
Eclogite	cpxC	cpx	Cambridge	1.99	0.00	0.46	0.16	0.00	0.42	0.52	0.47	0.00	6	55.49	0.10	10.93	5.22	0.02	7.91	13.44	6.78	-0.01
	cpxD	cpx	Cambridge	1.99	0.00	0.44	0.16	0.00	0.43	0.53	0.46	0.00	6	55.40	0.11	10.39	5.48	0.03	8.00	13.76	6.54	-0.01
	glA	gl	Cambridge	6.61	0.06	2.52	1.42	0.00	2.45	1.38	1.14	0.12	23	45.21	0.52	14.62	11.63	0.03	11.22	8.78	4.04	0.67
	glB	gl	Cambridge	6.59	0.07	2.58	1.27	0.00	2.49	1.37	1.19	0.14	23	45.38	0.63	15.08	10.47	0.01	11.48	8.82	4.22	0.74
	m1	phe	Kiel	6.59	0.09	4.56	0.22	0.00	0.59	0.00	0.26	1.71	22	49.29	0.89	28.94	2.00	0.03	2.98	0.00	1.01	10.06
	m2	phe	Kiel	6.71	0.07	4.38	0.20	0.00	0.67	0.00	0.25	1.72	22	50.26	0.70	27.80	1.81	0.00	3.38	0.00	0.98	10.07
	m3	phe	Kiel	6.60	0.09	4.56	0.21	0.00	0.58	0.00	0.27	1.70	22	49.54	0.86	29.05	1.90	0.02	2.93	0.01	1.04	9.98
	m4	phe	Kiel	6.61	0.09	4.53	0.20	0.00	0.60	0.00	0.28	1.73	22	49.12	0.86	28.59	1.82	0.00	2.99	0.00	1.07	10.08
	m5	phe	Kiel	6.66	0.06	4.50	0.23	0.00	0.61	0.00	0.26	1.67	22	49.53	0.60	28.38	2.04	0.01	3.03	0.00	0.99	9.76
	m6	phe	Kiel	6.79	0.08	4.24	0.22	0.00	0.69	0.00	0.25	1.72	22	50.81	0.83	26.92	1.98	0.00	3.44	0.00	0.98	10.08
	m7	phe	Kiel	6.67	0.07	4.45	0.22	0.00	0.62	0.00	0.28	1.72	22	49.58	0.70	28.06	1.99	0.02	3.11	0.00	1.08	10.05
	m8	phe	Kiel	6.70	0.06	4.41	0.24	0.00	0.65	0.00	0.22	1.75	22	50.25	0.57	28.11	2.19	0.00	3.25	0.00	0.84	10.27
	pheA	phe	Cambridge	6.54	0.08	4.60	0.21	0.00	0.64	0.00	0.24	1.77	22	49.35	0.77	29.46	1.90	0.00	3.22	0.00	0.93	10.45
	pheB	phe	Cambridge	6.49	0.10	4.69	0.21	0.00	0.57	0.00	0.26	1.71	22	49.06	1.04	30.08	1.92	0.01	2.87	0.00	1.02	10.10

Table 15: EPMA major element data for Chapter 3.

Sample	Grain	Mineral	Data source	Si (p.f.u.)	Ti	Al	Fe^{2+}	Mn	Mg	Ca	Na	K	O	SiO_2 (wt%)	TiO_2	Al_2O_3	FeO	MnO	MgO	CaO	Na_2O	K_2O
SEC47-1	cpxA	cpx	Cambridge	1.99	0.00	0.40	0.19	0.00	0.46	0.55	0.43	0.00	6	54.99	0.12	9.30	6.41	0.02	8.46	14.22	6.12	-0.01
Raspas	glA	gl	Cambridge	6.62	0.06	2.47	1.50	0.01	2.42	1.36	1.19	0.13	23	45.08	0.59	14.26	12.20	0.04	11.04	8.62	4.20	0.70
Eclogite	B1	phe	Kiel	6.58	0.06	4.58	0.26	0.00	0.60	0.00	0.27	1.68	22	49.48	0.59	29.25	2.36	0.01	3.03	0.00	1.06	9.87
	B1b	phe	Kiel	6.60	0.06	4.54	0.25	0.00	0.62	0.00	0.28	1.69	22	49.45	0.64	28.89	2.26	0.00	3.12	0.00	1.07	9.91
	B2	phe	Kiel	6.57	0.07	4.57	0.28	0.00	0.59	0.00	0.27	1.70	22	48.96	0.68	28.88	2.50	0.00	2.95	0.00	1.05	9.95
	B2b	phe	Kiel	6.56	0.07	4.60	0.26	0.00	0.58	0.00	0.29	1.68	22	48.96	0.68	29.09	2.36	0.02	2.91	0.00	1.10	9.82
	B3	phe	Kiel	6.54	0.07	4.62	0.27	0.00	0.58	0.00	0.30	1.67	22	49.13	0.68	29.41	2.46	0.00	2.93	0.00	1.18	9.82
	B4	phe	Kiel	6.57	0.07	4.58	0.27	0.00	0.59	0.00	0.29	1.67	22	49.32	0.68	29.13	2.44	0.01	2.98	0.00	1.11	9.81
	B5	phe	Kiel	6.51	0.08	4.68	0.28	0.00	0.56	0.00	0.28	1.64	22	48.96	0.77	29.90	2.49	0.00	2.83	0.00	1.08	9.68
	B6	phe	Kiel	6.54	0.07	4.63	0.28	0.00	0.57	0.00	0.28	1.66	22	49.02	0.74	29.47	2.50	0.00	2.86	0.00	1.07	9.73
	B7	phe	Kiel	6.53	0.08	4.65	0.28	0.00	0.56	0.00	0.28	1.67	22	48.80	0.77	29.48	2.48	0.01	2.81	0.00	1.07	9.79
	B8	phe	Kiel	6.59	0.06	4.53	0.27	0.00	0.64	0.00	0.26	1.70	22	49.27	0.56	28.75	2.40	0.03	3.23	0.00	1.01	9.93
	pheA	phe	Cambridge	6.55	0.07	4.60	0.27	0.00	0.60	0.00	0.24	1.77	22	48.74	0.64	29.01	2.36	0.00	3.01	-0.01	0.91	10.30
JEN12-03	chlA	chl	Cambridge	2.90	0.00	2.36	1.54	0.05	2.27	0.00	0.01	0.02	14	27.50	0.02	19.05	26.26	0.56	14.49	0.03	0.05	0.14
Jenner	chlB	chl	Cambridge	2.88	0.00	2.36	1.55	0.05	2.29	0.00	0.00	0.02	14	27.38	0.03	19.02	26.41	0.59	14.57	0.02	0.02	0.17
Blueschist	chlC	chl	Cambridge	2.88	0.00	2.38	1.53	0.06	2.31	0.00	0.00	0.01	14	27.38	0.01	19.16	26.07	0.68	14.73	-0.01	0.02	0.06
	chlD	chl	Cambridge	2.84	0.00	2.40	1.54	0.06	2.35	0.00	0.00	0.01	14	26.79	0.01	19.20	26.13	0.67	14.86	0.02	0.00	0.07
	chlE	chl	Cambridge	2.85	0.00	2.33	1.57	0.06	2.38	0.00	0.01	0.00	14	26.78	0.01	18.59	26.55	0.69	15.04	0.02	0.02	0.04
	chlF	chl	Cambridge	2.97	0.00	2.34	1.53	0.06	2.14	0.01	0.04	0.04	14	28.31	0.01	18.95	26.14	0.71	13.67	0.05	0.18	0.26
	chlG	chl	Cambridge	2.83	0.00	2.31	1.71	0.07	2.20	0.01	0.02	0.05	14	26.56	0.01	18.37	28.68	0.74	13.80	0.06	0.09	0.39
	B11	phe	Cambridge	6.81	-0.03	4.18	0.52	0.01	0.68	0.00	0.04	1.86	22	48.76	-0.31	25.41	4.46	0.05	3.25	0.01	0.16	10.44
	B12	phe	Cambridge	6.82	-0.03	4.18	0.53	0.01	0.67	0.00	0.04	1.84	22	48.78	-0.30	25.40	4.58	0.05	3.23	0.00	0.13	10.32
	B15	phe	Cambridge	6.92	-0.03	4.03	0.53	0.01	0.66	0.00	0.05	1.88	22	48.87	-0.30	24.72	4.89	0.06	3.20	0.00	0.14	10.67
	B19	phe	Cambridge	6.90	-0.03	4.05	0.53	0.01	0.69	0.00	0.04	1.89	22	48.80	-0.31	24.29	4.51	0.05	3.26	-0.01	0.13	10.45
	B2	phe	Kiel	6.73	0.01	4.21	0.52	0.00	0.62	0.00	0.04	1.88	22	48.87	0.13	25.95	4.51	0.03	3.04	0.00	0.17	10.71
	B20	phe	Cambridge	6.88	-0.01	4.11	0.40	0.00	0.76	0.00	0.05	1.80	22	50.73	-0.10	25.71	3.48	0.04	3.77	0.00	0.18	10.41
	B21	phe	Cambridge	7.00	-0.01	3.89	0.45	0.00	0.76	0.00	0.05	1.88	22	50.60	-0.10	23.86	3.91	0.04	3.67	0.01	0.17	10.65
	B22	phe	Cambridge	6.69	0.01	4.48	0.35	0.00	0.57	0.00	0.17	1.76	22	49.94	0.10	28.38	3.10	0.01	2.87	0.02	0.64	10.28
	B26	phe	Cambridge	6.91	-0.02	4.08	0.40	0.00	0.72	0.00	0.04	1.86	22	51.01	-0.15	25.56	3.55	0.04	3.55	0.03	0.16	10.73
	B28	phe	Cambridge	6.82	-0.02	4.17	0.47	0.01	0.72	0.00	0.03	1.89	22	49.10	-0.31	25.21	4.34	0.06	3.34	-0.01	0.15	10.82
	B30	phe	Cambridge	6.97	-0.02	4.02	0.41	0.00	0.69	0.00	0.05	1.88	22	50.70	-0.16	24.82	3.53	0.04	3.36	0.00	0.18	10.73
	B4	phe	Cambridge	6.83	-0.03	4.06	0.59	0.01	0.73	0.00	0.04	1.89	22	48.82	-0.24	24.58	5.04	0.07	3.52	0.01	0.16	10.57
	B5	phe	Cambridge	6.89	-0.04	4.06	0.53	0.01	0.69	0.00	0.03	1.91	22	48.75	-0.42	24.40	4.52	0.06	3.30	0.00	0.10	10.59
	B6	phe	Kiel	6.83	0.01	4.13	0.47	0.00	0.67	0.00	0.05	1.81	22	49.98	0.09	25.65	4.15	0.04	3.27	0.00	0.18	10.40
	B8	phe	Cambridge	6.82	-0.04	4.18	0.54	0.01	0.67	0.00	0.03	1.85	22	49.20	-0.35	25.57	4.69	0.06	3.22	0.02	0.13	10.47
	B9	phe	Kiel	6.78	0.01	4.17	0.50	0.01	0.64	0.00	0.03	1.81	22	49.31	0.10	25.70	4.39	0.05	3.14	0.00	0.13	10.33
	pheA_c	phe	Cambridge	6.67	0.02	4.50	0.34	0.00	0.56	0.00	0.19	1.73	22	49.31	0.21	28.24	2.99	0.01	2.77	0.00	0.73	10.05
	pheA_r	phe	Cambridge	6.80	-0.03	4.19	0.56	0.01	0.65	0.00	0.05	1.92	22	48.03	-0.31	25.11	4.70	0.04	3.07	0.00	0.19	10.61
	pheB_c	phe	Cambridge	6.61	0.01	4.58	0.35	0.00	0.54	0.00	0.22	1.78	22	48.35	0.10	28.43	3.04	0.00	2.66	0.02	0.82	10.20
	pheB_r	phe	Cambridge	6.87	-0.03	4.15	0.50	0.00	0.67	0.00	0.04	1.84	22	48.07	-0.30	24.62	4.16	0.04	3.12	0.01	0.13	10.11
	pheC_c	phe	Cambridge	6.84	-0.04	4.13	0.58	0.01	0.66	0.00	0.04	1.86	22	48.63	-0.34	24.94	4.91	0.06	3.13	0.00	0.14	10.38
	pheC_r	phe	Cambridge	6.93	-0.02	4.00	0.51	0.01	0.71	0.00	0.04	1.86	22	49.76	-0.18	24.39	4.41	0.06	3.42	-0.02	0.13	10.48
	pheD	phe	Cambridge	6.82	-0.04	4.16	0.55	0.01	0.67	0.00	0.03	1.87	22	48.73	-0.36	25.21	4.73	0.06	3.22	0.00	0.13	10.47
	pheE	phe	Cambridge	6.81	-0.03	4.17	0.55	0.01	0.69	0.00	0.03	1.86	22	48.99	-0.33	25.46	4.71	0.07	3.35	0.01	0.12	10.47
	pheF	phe	Cambridge	6.88	-0.02	4.10	0.45	0.00	0.73	0.00	0.04	1.83	22	50.64	-0.16	25.60	3.95	0.04	3.59	0.00	0.14	10.54
	B18	phe	Cambridge	6.91	-0.03	4.06	0.50	0.01	0.69	0.00	0.03	1.88	22	49.51	-0.29	24.66	4.28	0.06	3.34	0.01	0.12	10.56
JEN12-07	m1	phe	Kiel	6.98	0.01	3.97	0.43	0.01	0.67	0.00	0.04	1.89	22	51.71	0.084	24.95	3.8	0.046	3.35	0.009	0.151	10.96
Jenner	m2	phe	Kiel	6.99	0.02	3.85	0.41	0.00	0.82	0.00	0.08	1.85	22	51.61	0.211	24.11	3.61	0.009	4.07	0	0.293	10.68
Blueschist	m3	phe	Kiel	7.06	0.00	3.86	0.42	0.00	0.72	0.00	0.03	1.88	22	52.87	0	24.55	3.73	0.032	3.61	0.009	0.127	11.03
	m4	phe	Kiel	6.97	0.01	3.95	0.44	0.00	0.72	0.00	0.05	1.86	22	51.35	0.086	24.67	3.92	0.012	3.56	0	0.195	10.77
	m5	phe	Kiel	6.83	0.03	4.16	0.41	0.00	0.66	0.00	0.13	1.80	22	50.49	0.275	26.08	3.65	0.021	3.29	0	0.501	10.42
	m6	phe	Kiel	7.00	0.00	3.92	0.41	0.00	0.74	0.00	0.04	1.89	22	51.39	0.038	24.4	3.58	0	3.64	0	0.142	10.85
	m7	phe	Kiel	6.76	0.03	4.33	0.35	0.00	0.59	0.00	0.18	1.79	22	49.96	0.297	27.16	3.12	0.016	2.95	0	0.678	10.36
	m8	phe	Kiel	6.98	0.03	3.88	0.40	0.00	0.78	0.00	0.08	1.87	22	51.23	0.319	24.17	3.55	0.029	3.83	0.013	0.288	10.75
	pheA	phe	Cambridge	6.92	0.02	3.99	0.36	0.00	0.79	0.00	0.08	1.88	22	50.47	0.21	24.69	3.15	0.02	3.88	0.01	0.29	10.74
	pheB	phe	Cambridge	6.66	0.02	4.42	0.41	0.00	0.63	0.00	0.15	1.82	22	48.44	0.15	27.27	3.53	0.02	3.08	0.01	0.58	10.40
	pheC	phe	Cambridge	6.86	0.03	4.06	0.38	0.00	0.77	0.00	0.09	1.88	22	50.05	0.26	25.14	3.36	0.00	3.79	0.00	0.34	10.77
	pheD	phe	Cambridge	6.95	0.01	3.94	0.39	0.00	0.80	0.00	0.06	1.89	22	50.70	0.10	24.40	3.39	0.01	3.93	0.01	0.24	10.84
	pheE	phe	Cambridge	6.87	-0.02	4.14	0.40	0.00	0.70	0.00	0.03	1.93	22	50.20	-0.17	25.64	3.47	0.03	3.42	0.01	0.12	11.04
	pheF	phe	Cambridge	6.88	0.02	4.01	0.39	0.00	0.82	0.00	0.06	1.87	22	50.50	0.23	24.93	3.43	0.01	4.01	-0.01	0.24	10.75
	pheG	phe	Cambridge	6.78	0.02	4.23	0.37	0.00	0.70	0.00	0.13	1.85	22	49.21	0.19	26.07	3.19	0.00	3.39	0.02	0.48	10.54

Table 16: EPMA major element data for Chapter 3.

Sample	Grain	Mineral	Data source	Si (p.f.u.)	Ti	Al	Fe^{2+}	Mn	Mg	Ca	Na	K	O	SiO_2 (wt%)	TiO_2	Al_2O_3	FeO	MnO	MgO	CaO	Na_2O	K_2O
JEN12-09	chlA	chl	Cambridge	2.81	0.00	2.40	2.43	0.03	2.29	0.00	0.00	0.00	14	26.55	0.01	19.25	27.47	0.38	14.51	0.01	0.00	0.01
Jenner	chlB	chl	Cambridge	2.83	0.00	2.40	2.49	0.04	2.21	0.00	0.00	0.00	14	26.61	0.02	19.19	28.01	0.43	13.96	0.00	0.00	0.03
Eclogite	chlC	chl	Cambridge	2.82	0.00	2.38	2.43	0.03	2.33	0.00	0.00	0.00	14	26.58	0.02	19.06	27.36	0.35	14.74	0.02	-0.02	0.00
	chlD	chl	Cambridge	2.81	0.00	2.40	2.38	0.03	2.35	0.00	0.00	0.00	14	26.59	0.01	19.28	26.95	0.35	14.90	0.00	0.00	0.00
	cpxA	cpx	Cambridge	2.01	0.00	0.33	0.27	0.00	0.43	0.53	0.47	0.00	6	54.60	0.06	7.60	8.73	0.01	7.90	13.47	6.62	-0.01
	cpxB	cpx	Cambridge	2.01	0.00	0.40	0.25	0.00	0.38	0.48	0.53	0.00	6	55.19	0.05	8.73	7.81	0.00	7.62	13.15	7.05	-0.01
	B1	phe	Kiel	6.71	0.03	4.35	0.33	0.00	0.66	0.00	0.14	1.86	22	49.45	0.28	27.18	2.93	0.02	3.25	0.00	0.52	10.76
	B2	phe	Kiel	6.55	0.02	4.60	0.36	0.00	0.57	0.00	0.16	1.85	22	47.85	0.23	28.49	3.15	0.00	2.78	0.00	0.61	10.62
	B3	phe	Kiel	6.70	0.03	4.33	0.35	0.00	0.69	0.00	0.12	1.88	22	49.33	0.27	27.07	3.10	0.01	3.43	0.00	0.47	10.84
	B4	phe	Kiel	6.82	0.00	4.20	0.38	0.00	0.66	0.00	0.06	1.93	22	49.96	0.04	26.07	3.29	0.02	3.24	0.00	0.21	11.10
	B5	phe	Kiel	6.66	0.03	4.40	0.32	0.00	0.68	0.00	0.15	1.87	22	49.08	0.30	27.49	2.84	0.00	3.38	0.00	0.57	10.78
	B6	phe	Kiel	6.78	0.03	4.24	0.29	0.00	0.72	0.00	0.13	1.86	22	49.98	0.25	26.57	2.59	0.00	3.58	0.00	0.48	10.77
	B7	phe	Kiel	6.76	0.03	4.28	0.31	0.00	0.70	0.00	0.11	1.85	22	49.73	0.29	26.74	2.71	0.00	3.45	0.00	0.43	10.70
	B8	phe	Kiel	6.50	0.02	4.72	0.31	0.00	0.54	0.00	0.22	1.75	22	47.59	0.24	29.33	2.74	0.00	2.65	0.00	0.83	10.05
	pheA	phe	Cambridge	6.74	0.03	4.25	0.38	0.00	0.68	0.00	0.15	1.92	22	49.69	0.28	26.60	3.39	0.00	3.35	0.01	0.58	11.08
	pheB	phe	Cambridge	6.88	0.02	4.14	0.32	0.00	0.68	0.00	0.12	1.84	22	51.97	0.16	26.56	2.88	0.01	3.46	0.01	0.45	10.88
	pheC	phe	Cambridge	6.79	0.03	4.19	0.34	0.00	0.72	0.00	0.13	1.91	22	49.95	0.26	26.17	2.98	0.01	3.55	0.00	0.49	11.04
	pheD	phe	Cambridge	6.79	0.02	4.24	0.32	0.00	0.70	0.00	0.13	1.85	22	50.39	0.19	26.71	2.87	0.00	3.48	0.00	0.51	10.79

Table 17: EPMA major element data for Chapter 3.

Sample	Grain	Mineral	Li (µg/g)	1s	B (µg/g)	1s	N (µg/g)	1s	F (µg/g)	1s	Cl (µg/g)	1s	MgO (wt%)	1s
LC-1b	cpxA	cpx	59	0.5	2	0.1	3	0.8	23	23	63	6.6	8.16	0.05
Cignana	epA	ep	0	0.0	0	0.0	1	0.3	47	47	45	3.8	0.14	0.01
Eclogite	m1	pa	9	0.1	18	0.1	21	3.3	327	327	32	5.0	0.32	0.13
	m2	pa	10	0.1	19	0.3	47	7.7	74	74	25	3.5	0.21	0.02
	m2_2	pa	9	0.1	24	0.3	28	4.4	74	74	20	3.9	0.26	0.08
	m3	pa	10	0.1	15	0.2	27	4.5	56	56	9	1.7	0.17	0.02
	m4	pa	11	0.1	13	0.1	15	0.9	61	61	9	1.1	0.27	0.03
	m5	pa	6	0.1	14	0.1	16	1.8	38	38	8	1.6	0.22	0.03
	m7	pa	5	0.1	21	0.3	43	7.0	63	63	19	4.6	0.29	0.11
	m8	pa	5	0.1	67	0.3	36	4.5	46	46	13	2.7	0.13	0.01
	paA	pa	5	0.0	69	0.4	5	0.5	52	52	3	1.2	0.15	0.01
	paC	pa	9	0.1	14	0.1	13	1.5	55	55	8	2.2	0.14	0.01
	paD	pa	6	0.1	22	0.2	14	2.9	74	74	10	3.8	0.20	0.05
	paF	pa	9	0.1	19	0.2	22	1.4	68	68	8	1.2	0.23	0.06
LC-2a	chlA	chl	81	0.7	11	0.3	5	0.4	245	4.8	28	5.7	27.52	0.12
Cignana	chlB	chl	79	0.7	2	0.1	1	0.4	233	5.1	13	3.0	26.74	0.11
Metagabbro	chlC	chl	90	0.8	3	0.2	5	0.9	249	7.6	18	5.7	28.94	0.12
	m1	phe	62	0.5	36	0.2	75	3.2	83	2.3	13	5.7	2.98	0.02
	m3	phe	64	0.5	33	0.2	66	2.9	88	1.8	5	2.4	2.88	0.03
	m4	phe	61	0.5	26	0.2	67	1.5	82	1.9	9	4.3	2.88	0.04
	m5	phe	61	0.5	30	0.4	123	6.3	108	4.3	20	5.5	3.11	0.01
	m6	phe	41	0.4	49	0.2	20	2.3	116	2.8	38	7.0	4.31	0.03
	m7	phe	57	0.5	28	0.2	92	4.2	86	2.5	15	4.3	3.01	0.02
	m8	phe	47	0.4	48	0.2	24	2.1	127	3.9	34	1.1	4.31	0.02
	m9	phe	55	0.4	25	0.1	107	4.6	85	2.7	28	4.4	3.11	0.02
	pheA	phe	41	0.3	18	0.1	96	2.5	76	2.2	8	1.7	2.74	0.02
	pheB	phe	34	0.3	47	0.2	39	5.4	98	2.3	14	3.0	3.61	0.02
	pheC	phe	47	0.4	14	0.1	88	3.4	78	2.5	20	3.4	2.87	0.01
LC-3	gt1	g	3	0.0	0	0.0	1	0.2	25	2.0			5.61	0.03
Cignana	m1	phe	55	0.5	108	0.5	19	2.1	866	16	11	3.0	3.22	0.02
Gt-phe-	m2	phe	43	0.4	259	0.7	10	1.2	903	13	19	2.4	3.48	0.03
quartzite	m3	phe	50	0.4	320	0.8	20	2.1	835	13	8	4.2	3.13	0.02
	m4	phe	39	0.3	218	0.5	15	1.7	885	14	16	2.4	3.41	0.02
	m5	phe	46	0.4	188	0.6	11	0.6	852	15	6	2.4	3.30	0.03
	m6	phe	50	0.4	329	0.8	18	1.4	820	15	6	1.9	3.18	0.02
	m7	phe	59	0.5	107	0.5	15	1.9	837	13	12	2.6	3.25	0.02
	m8	phe	41	0.3	252	0.7	13	0.9	866	15	20	3.6	3.46	0.03
	mA	phe	50	0.4	98	0.2	12	1.2	837	16	7	2.4	3.17	0.03
	mB	phe	55	0.5	96	0.4	16	1.4	812	13	14	3.7	3.10	0.02
	wm1	phe	43	0.3	253	0.6	14	1.5	832	12	13	3.2	3.35	0.03
	wm10r	phe	48	0.4	295	0.7	14	0.8	829	13	7	1.5	3.11	0.02
	wm11	phe	44	0.4	188	1.0	14	1.4	893	14	14	3.1	3.43	0.02
	wm12	phe	62	0.5	85	0.6	21	1.0	788	13	6	2.2	2.96	0.02
	wm5r	phe	50	0.4	170	0.5	19	1.3	842	14	21	1.8	3.21	0.02
	wm7r	phe	49	0.4	142	0.5	17	2.4	841	13	13	2.9	2.99	0.02
SEC16-1	chlA	chl	140	1.2	2	0.0	3	0.3	216	6.2	105	9.7	17.39	0.08
Raspas	chlB	chl	132	1.2	1	0.1	1	0.3	276	7.2	135	11	18.60	0.08
Blueschist	chlC	chl	124	1.0	3	0.4	2	1.0	348	7.0	109	14	19.16	0.09
	glA	gl	169	1.4	4	0.0	4	0.5	385	7.7	22	6.5	8.85	0.05
	glB	gl	132	1.5	5	0.1	4	0.8	936	20	54	9.2	10.07	0.05
	paC	pa	28	0.2	136	0.8	41	2.8	124	2.1	4	1.8	0.37	0.40
	paD	pa	26	0.2	139	0.6	78	2.7	114	3.6	154	16	0.22	0.06
	paE	pa	24	0.2	112	0.8	31	1.8	95	2.1	10	2.9	0.13	0.02
	paF	pa	27	0.2	113	0.4	64	2.2	125	4.5	27	8.1	0.19	0.02
	m1	phe	41	0.3	40	0.1	166	6.5	386	5.8	7	1.1	2.57	0.02
	m10	phe	34	0.3	78	0.3	224	6.8	396	6.2	7	2.0	2.74	0.03
	m11	phe	43	0.4	48	0.3	117	3.8	379	8.7	27	3.9	2.60	0.01
	m3	phe	35	0.3	92	0.3	229	5.1	378	7.3	10	4.4	2.78	0.02
	m5	phe	43	0.4	30	0.1	128	3.7	429	7.3	13	2.1	3.66	0.02
	m6	phe	40	0.3	37	0.2	147	3.9	346	6.2	29	6.7	2.59	0.02
	m7	phe	31	0.3	80	1.0	232	7.0	401	7.9	5	1.8	2.74	0.04
	m8	phe	35	0.3	40	0.2	194	5.4	430	8.5	11	2.0	2.65	0.01
	m9	phe	34	0.3	79	0.3	224	6.7	481	7.0	13	2.4	2.73	0.02
	pheC	phe	45	0.4	35	0.2	147	5.3	426	9.7	43	6.8	2.55	0.01
	pheD	phe	36	0.3	91	0.4	221	5.3	396	6.6	1	0.8	2.76	0.01
	pheE	phe	34	0.3	80	0.2	226	7.6	376	7.6	13	9.8	2.75	0.02
	pheF	phe	38	0.3	47	0.3	243	5.2	379	7.8	72	4.6	2.66	0.02
	pheA	phe	36	0.3	44	0.3	163	6.4	360	5.7			2.57	0.02
SEC44-1	cpxA	cpx	94	0.8	3	0.0	2	0.7	38	2.3	31	4.9	8.09	0.04
Raspas	cpxB	cpx	105	0.8	3	0.0	2	0.3	53	1.4	39	4.7	7.81	0.05
Eclogite	cpxC	cpx	107	0.9	3	0.1	3	0.6	37	1.5	29	5.5	7.80	0.06
	cpxD	cpx	110	0.9	2	0.0	2	0.8	36	1.4	29	5.3	7.82	0.05
	glA	gl	7	0.1	18	0.1	5	0.6	2942	51	32	5.2	11.50	0.05
	glB	gl	6	0.1	19	0.1	3	0.4	3381	54			11.44	0.06
	m1	phe	24	0.2	38	0.2	147	5.5	632	11	19	3.7	2.79	0.02
	m2	phe	32	0.3	63	0.2	172	8.6	638	11	7	2.0	2.89	0.02
	m3	phe	48	0.4	81	0.3	237	8.4	771	14	2	1.6	3.38	0.03
	m4	phe	28	0.2	81	0.2	233	5.5	772	12	4	1.4	3.27	0.02
	m5	phe	20	0.2	71	0.2	244	6.2	660	11	9	1.7	2.88	0.02
	m6	phe	34	0.3	53	0.2	171	4.5	661	13	4	1.8	2.73	0.03
	m7	phe	46	0.4	61	0.3	193	4.8	572	10	9	2.6	2.84	0.03
	m8	phe	24	0.2	63	0.3	165	5.6	691	12			2.96	0.02
	pheA	phe	19	0.2	56	0.2	193	6.9	750	12	5	2.6	3.00	0.02
	pheB	phe	42	0.3	60	0.2	216	5.5	654	10	8	2.6	2.65	0.02

Table 18: SIMS trace element data for Chapter 3.

Sample	Grain	Mineral	Li (µg/g)	1s	B (µg/g)	1s	N (µg/g)	1s	F (µg/g)	1s	Cl (µg/g)	1s	MgO (wt%)	1s
SEC47-1	cpxA	cpx	142	1.2	3	0.0	3	0.3	28	0.7	28	6.8	8.21	0.04
Raspas	epA	ep	0	0.0	0	0.0	1	0.3	30	0.8	44	11	0.15	0.01
Eclogite	epB	ep	0	0.0	0	0.0	1	0.4	29	1.4	42	8.0	0.08	0.01
	glA	gl	7	0.1	18	0.1	3	0.7	1430	21	42	4.1	10.81	0.20
	B1	phe	39	0.3	51	0.2	50	2.2	329	6.5	7	2.7	2.76	0.03
	B1b	phe	38	0.3	58	0.2	69	3.0	314	5.5	13	4.7	2.68	0.02
	B2	phe	39	0.3	56	0.2	71	3.3	313	7.3	14	2.7	2.71	0.03
	B2b	phe	39	0.3	55	0.2	83	3.1	296	6.1	21	4.9	2.56	0.03
	B3	phe	43	0.4	50	0.2	42	1.9	305	5.0	11	3.2	2.66	0.02
	B4	phe	47	0.4	77	0.2	50	3.4	296	4.7	8	2.7	2.65	0.03
	B5	phe	40	0.3	62	0.2	56	2.2	274	5.5	11	3.2	2.58	0.02
	B6	phe	44	0.4	52	0.2	44	1.4	287	5.3	8	3.1	2.62	0.03
	B7	phe	49	0.4	52	0.2	37	2.2	309	4.9	7	3.4	2.64	0.03
	B8	phe	43	0.4	52	0.3	62	1.5	309	7.6	17	4.4	2.87	0.02
	pheA	phe	46	0.4	60	0.2	54	3.2	319	6.3	7	3.0	2.71	0.03
JEN12-03	chlA	chl	32	0.3	1	0.1	83	11	34	1.3	207	14	16.17	0.09
Jenner	chlB	chl	32	0.3	2	0.1	75	4	46	1.1	36	3.6	15.57	0.07
Blueschist	chlC	chl	34	0.3	2	0.1	43	2	36	1.3	135	8.0	16.68	0.07
	chlD	chl	32	0.3	2	0.1	10	1	52	3.2	157	6.1	16.44	0.08
	chlE	chl	29	0.2	2	0.1	18	1	37	0.8	86	11	16.72	0.08
	chlF	chl	44	0.6	2	0.1	24	2	34	1.4	90	11	15.69	0.09
	chlG	chl	31	0.3	3	0.2	59	3	43	1.9	80	15	15.26	0.06
	cpxA	cpx	71	0.6	1	0.0	2	1	9	0.6			7.43	0.04
	cpxB	cpx	19	0.2	4	0.1	19	1	28	1.3	28	3.9	7.50	0.04
	B11	phe	23	0.2	68	0.2	179	5.6	46	1.3	17	2.5	3.08	0.02
	B12	phe	19	0.2	63	0.3	182	4.7	53	1.4	32	5.4	3.07	0.03
	B15	phe	22	0.2	76	0.2	187	5.2	45	1.5	10	3.3	3.09	0.01
	B19	phe	22	0.2	67	0.2	208	7.8	47	2.0	39	8.0	3.06	0.02
	B2	phe	17	0.2	87	0.2	206	4.9	42	1.7	7	2.2	3.12	0.02
	B20	phe	29	0.3	73	0.3	270	7.0	39	1.3	25	3.5	3.03	0.02
	B21	phe	20	0.2	59	0.3	239	5.5	40	2.6	21	4.3	3.28	0.02
	B22	phe	18	0.2	63	0.3	212	5.6	54	2.2	47	4.6	3.17	0.02
	B26	phe	14	0.1	64	0.3	189	6.0	41	1.0	33	5.6	3.02	0.03
	B28	phe	30	0.3	48	0.1	108	2.9	38	1.8	214	18	2.68	0.01
	B30	phe	33	0.3	43	0.2	158	4.8	57	2.1	32	7.5	2.82	0.02
	B4	phe	31	0.5	74	0.3	233	7.3	41	1.0	33	8.0	3.15	0.02
	B5	phe	19	0.7	96	1.0	251	9.0	65	3.5	16	2.5	3.24	0.03
	B6	phe	16	0.1	66	0.2	190	7.1	48	1.1	19	4.1	3.03	0.02
	B8	phe	26	0.2	73	0.3	175	4.4	46	2.6	40	6.1	3.16	0.02
	B9	phe	26	0.2	67	0.3	174	4.3	41	1.9	31	7.8	3.20	0.02
	pheA_c	phe	14	0.2	51	0.1	197	5.1	47	1.4	30	6.2	3.09	0.03
	pheA_r	phe	21	0.2	59	0.2	191	6.6	47	1.0	16	1.7	3.00	0.02
	pheB_c	phe	27	0.2	42	0.3	121	3.0	52	1.2	23	5.3	2.54	0.03
	pheB_r	phe	17	0.2	65	0.3	179	5.3	43	2.9	29	2.8	2.98	0.02
	pheC_c	phe	16	0.1	67	0.2	162	4.0	49	1.6	13	2.8	2.93	0.03
	pheC_r	phe	13	0.1	74	0.2	177	5.1	47	0.9	11	3.6	3.01	0.02
	pheD	phe	18	0.2	72	0.2	209	4.6	50	1.6	9	2.1	3.55	0.02
	pheE	phe	27	0.2	70	0.3	176	5.9	48	1.6	5	1.8	3.03	0.02
	pheF	phe	14	0.1	67	0.2	206	4.6	50	1.9	27	3.8	3.27	0.02
	B18	phe	15	0.5	64	0.5	202	16	42	3.3	17	20	2.82	0.14
	ttnA	ttn	0	0.0	0	0.0	3	0.7	833	19.1	43	7.8	0.18	0.02
JEN12-07	m1	phe	13	0.1	61	0.3	247	7.5	74	1.8	16	4.5	3.03	0.02
Jenner	m2	phe	25	0.2	44	0.2	237	6.0	89	1.6	38	5.7	3.40	0.03
Blueschist	m3	phe	25	0.2	40	0.2	170	5.3	86	3.8	41	6.5	2.59	0.03
	m4	phe	13	0.1	53	0.2	249	6.1	85	1.5	28	1.7	3.11	0.02
	m5	phe	26	0.2	48	0.2	266	5.9	83	1.8	31	3.3	3.46	0.02
	m6	phe	29	0.2	47	0.2	174	4.3	86	3.0	50	8.8	2.81	0.01
	m7	phe	30	0.2	46	0.1	169	4.0	80	3.2	11	3.9	2.88	0.02
	m8	phe	18	0.1	51	0.3	249	6.0	85	2.7	17	2.5	3.49	0.02
	pheA	phe	35	0.3	44	0.2	161	4.6	77	2.3	15	3.3	2.69	0.01
	pheB	phe	38	0.3	35	0.2	155	4.7	67	1.5	11	2.0	2.57	0.02
	pheC	phe	17	0.1	58	0.2	317	8.2	90	2.1	16	3.6	3.54	0.04
	pheD	phe	15	0.1	60	0.3	320	7.7	96	1.5	15	4.4	3.57	0.02
	pheE	phe	6	0.1	58	0.2	244	6.5	85	3.5	10	1.8	3.06	0.01
	pheF	phe	21	0.2	60	0.2	302	7.6	85	2.9	12	2.8	3.50	0.02
	pheG	phe	23	0.2	33	0.2	177	5.5	97	1.6	37	4.1	3.29	0.02
JEN12-09	chlA	chl	34	0.3	0	0.0	0	0.2	43	1.1	48	9.8	16.66	0.07
Jenner	chlB	chl	32	0.3	1	0.1	9	0.9	57	1.9	72	7.7	16.41	0.07
Eclogite	chlC	chl	37	0.3	0	0.0	2	0.4	47	1.5	12	2.1	16.57	0.08
	chlD	chl	33	0.3	0	0.0	0	0.2	44	1.6	10	2.7	16.73	0.09
	cpxA	cpx	46	0.4	1	0.0	2	0.4	7	0.4	28	4.7	7.99	0.04
	cpxB	cpx	55	0.5	1	0.0	1	0.6	7	0.6	41	3.1	7.95	0.04
	B1	phe	23	0.2	52	0.3	116	6.0	74	2.6	6	2.4	3.03	0.03
	B2	phe	17	0.1	63	0.3	110	4.0	61	2.0	7	2.7	2.90	0.03
	B3	phe	42	0.3	51	0.1	42	3.6	74	3.6	26	3.3	2.98	0.02
	B4	phe	16	0.1	64	0.3	103	5.2	68	2.1	9	2.2	2.88	0.02
	B5	phe	38	0.3	29	0.2	56	4.5	76	3.2	31	4.7	3.03	0.02
	B6	phe	28	0.3	56	0.3	112	3.7	75	1.8	19	5.0	3.19	0.03
	B7	phe	37	0.3	53	0.2	110	2.5	67	2.1	8	1.3	3.27	0.03
	B8	phe	27	0.2	54	0.3	117	4.2	97	5.8	66	8.8	3.22	0.02
	pheA	phe	36	0.3	53	0.3	22	1.6	68	1.9	9	3.9	3.07	0.03
	pheB	phe	27	0.2	37	0.1	99	3.8	77	3.1	34	3.8	3.05	0.02
	pheC	phe	37	0.3	43	0.3	43	4.6	87	3.7	39	9.5	3.28	0.02
	pheD	phe	32	0.3	57	0.1	127	3.7	71	2.6	8	3.5	3.15	0.03

Table 19: SIMS trace element data for Chapter 3.

Standard	Li (µg/g)	1s	B (µg/g)	1s	N (µg/g)	1s	F (µg/g)	1s	MgO (wt%)	1s	Cl (µg/g)	1s
Phe80-3	36.5	0.2	30.8	0.2	69	3	603	5	3.54	0.05	n.a.	
Phe80-3	45.0	0.1	32.4	0.1	91	2	645	7	3.70	0.02	n.a.	
Phe80-3	39.7	0.1	39.4	0.1	89	3	627	8	3.68	0.01	n.a.	
Phe80-3	42.0	0.1	33.9	0.2	79	2	647	7	3.66	0.02	n.a.	
Phe80-3	41.0	0.2	35.8	0.2	99	2	640	7	3.71	0.02	n.a.	
Phe80-3	38.2	0.1	33.3	0.1	84	4	595	3	3.38	0.02	n.a.	
Phe80-3	41.7	0.1	38.6	0.1	95	3	652	3	3.71	0.03	n.a.	
Phe80-3	38.9	0.4	48.3	0.4	55	2	587	7	3.18	0.02	n.a.	
Phe80-3	41.1	0.2	39.4	0.2	73	4	637	9	3.42	0.01	n.a.	
Phe80-3	43.3	0.1	35.6	0.1	98	2	643	9	3.68	0.02	n.a.	
Phe80-3	37.4	0.1	39.0	0.3	72	2	622	6	3.73	0.07	n.a.	
Phe80-3	36.4	0.2	33.8	0.2	86	1	643	6	3.83	0.01	n.a.	
Phe80-3	46.1	0.1	36.3	0.1	100	1	635	12	3.82	0.01	n.a.	
Phe80-3	39.9	0.1	35.2	0.2	85	2	647	9	3.80	0.02	n.a.	
Phe80-3	41.2	0.1	36.1	0.1	72	2	593	3	3.58	0.03	n.a.	
Phe80-3	44.8	0.1	37.6	0.1	95	2	639	10	3.70	0.02	n.a.	
Phe80-3	40.3	0.2	37.0	0.2	90	2	628	6	3.50	0.02	n.a.	
Phe80-3	46.8	0.2	37.4	0.1	87	2	667	6	3.66	0.02	n.a.	
Phe80-3	50.2	0.1	37.4	0.1	90	2	667	9	3.72	0.02	n.a.	
Phe80-3	49.4	0.2	34.8	0.2	79	3	673	8	3.65	0.03	n.a.	
Phe80-3	36.9	0.1	34.7	0.2	88	2	639	8	3.79	0.02	n.a.	
Phe80-3	45.0	0.1	35.5	0.2	97	2	653	4	3.84	0.02	n.a.	
Phe80-3	41.2	0.1	36.3	0.1	100	4	618	9	3.73	0.03	n.a.	
Phe80-3	43.3	0.2	37.4	0.2	96	3	639	5	3.72	0.02	n.a.	
Phe80-3	36.2	0.1	43.0	0.6	74	3	589	11	3.66	0.02	n.a.	
Phe80-3	40.4	0.1	35.9	0.2	84	2	648	8	3.90	0.01	n.a.	
Phe80-3	40.6	0.1	39.3	0.4	61	2	615	8	3.45	0.02	n.a.	
Phe80-3	39.8	0.1	38.6	0.2	74	4	623	3	3.60	0.05	n.a.	
Phe80-3	43.7	0.1	50.2	0.2	80	3	597	8	3.55	0.02	n.a.	
Phe80-3	32.6	0.0	36.4	0.2	88	2	648	9	3.91	0.02	n.a.	
Phe80-3	44.0	0.1	33.8	0.1	94	1	636	4	3.76	0.01	n.a.	
Phe80-3	40.8	0.1	36.3	0.3	86	4	642	8	3.76	0.03	n.a.	
Phe80-3	39.2	0.1	33.7	0.2	86	2	614	5	3.68	0.02	n.a.	
Phe80-3	40.5	0.1	36.3	0.2	76	2	627	4	4.10	0.01	n.a.	
Phe80-3	48.5	0.1	38.8	0.2	105	3	647	9	3.66	0.01	n.a.	
Phe80-3	40.0	0.1	37.7	0.1	75	4	614	10	3.73	0.02	n.a.	
Phe80-3	53.0	0.1	37.8	0.1	98	3	634	7	3.85	0.03	n.a.	
Phe80-3	39.6	0.2	36.2	0.1	91	4	658	8	3.89	0.02	n.a.	
Phe80-3	46.6	0.1	38.2	0.2	96	3	650	6	3.76	0.04	n.a.	
Phe80-3	44.5	0.1	36.3	0.1	87	1	626	8	3.73	0.02	n.a.	
Phe80-3	40.3	0.5	38.8	0.2	61	1	598	10	3.33	0.05	n.a.	
Phe80-3	48.1	0.1	36.2	0.2	95	2	677	5	3.81	0.03	n.a.	
Phe80-3	44.4	0.2	48.7	0.1	86	3	653	7	3.64	0.01	n.a.	
Phe80-3	40.3	0.5	37.2	0.1	76	4	612	9	3.54	0.03	n.a.	
Phe80-3	41.9	0.2	38.7	0.2	82	2	619	5	3.67	0.01	n.a.	
Phe80-3	43.2	0.2	34.8	0.2	91	2	706	7	3.85	0.03	n.a.	
Phe80-3	39.0	0.1	41.0	0.5	79	3	626	9	3.53	0.04	n.a.	
Phe80-3	37.6	0.1	37.6	0.1	93	5	633	7	3.63	0.01	n.a.	
Phe80-3	46.9	0.2	35.6	0.1	99	4	652	7	3.81	0.02	n.a.	
Phe80-3	37.2	0.1	38.0	0.2	84	2	637	14	3.84	0.03	n.a.	
Phe80-3	44.6	0.2	54.1	0.2	92	3	602	10	3.57	0.03	n.a.	
Phe80-3	46.8	0.2	36.2	0.2	89	2	647	4	3.85	0.04	n.a.	
Phe80-3	43.6	0.2	39.6	0.2	81	2	609	8	3.63	0.01	n.a.	
Average	42.1		37.8		86		634		3.69			
rsd%	9.6%		11.3%		12.7%		3.8%		4.3%			
Reference value					71							
LMMN#1	1674	3	64.7	0.7	205	8	5620	55	0.78	0.03	n.a.	
LMMN#1	1483	2	99.6	1.3	210	11	6658	60	0.76	0.03	n.a.	
LMMN#1	1885	1	72.6	0.9	178	4	6740	55	0.83	0.02	n.a.	
LMMN#1	1735	3	69.5	1.1	206	14	6156	55	0.78	0.01	n.a.	
LMMN#1	1460	2	77.1	1.2	244	13	4719	33	0.77	0.02	n.a.	
LMMN#1	1362	3	67.4	0.4	200	11	6124	53	0.68	0.03	n.a.	
LMMN#1	1548	1	92.5	0.4	180	6	6530	62	0.78	0.01	n.a.	
LMMN#1	1852	3	126.5	0.5	185	7	6385	84	0.90	0.01	n.a.	
LMMN#1	1424	2	48.2	0.6	170	11	6311	37	0.70	0.02	n.a.	
LMMN#1	1310	1	63.4	0.3	183	4	6177	51	0.80	0.03	n.a.	
LMMN#1	1575	1	63.2	0.1	158	4	6483	47	0.72	0.03	n.a.	
LMMN#1	1723	2	73.4	0.2	172	6	7060	46	0.79	0.03	n.a.	
LMMN#1	1575	2	59.2	0.4	169	6	6488	58	0.74	0.02	n.a.	
LMMN#1	1729	2	62.6	0.7	186	10	6910	57	0.72	0.04	n.a.	
LMMN#1	1708	1	61.2	1.0	213	13	6637	63	0.76	0.02	n.a.	
LMMN#1	1232	1	64.2	1.0	210	9	6395	44	0.63	0.05	n.a.	
LMMN#1	1432	2	56.4	0.4	169	3	6434	62	0.63	0.04	n.a.	
LMMN#1	1322	2	47.4	0.6	185	13	6330	51	0.62	0.03	n.a.	
LMMN#1	1887	5	83.4	0.2	162	4	7069	39	0.81	0.03	n.a.	
LMMN#1	1695	2	89.3	0.3	162	4	7247	54	0.90	0.03	n.a.	
Average	1581		72.1		187		6424		0.76			
rsd%	12.5%		26.0%		11.7%		8.6%		10.4%			
Reference value					186							

Table 20: SIMS standards for Chapter 3.

Standard	Li (µg/g)	1s	B (µg/g)	1s	N (µg/g)	1s	F (µg/g)	1s	MgO (wt%)	1s	Cl (µg/g)	1s
LMMN#2	1590	1	44.2	0.1	146	2	6577	59	0.79	0.03	n.a.	
LMMN#2	1587	4	60.2	0.8	162	3	4553	55	0.86	0.03	n.a.	
LMMN#2	1874	1	57.4	0.3	151	2	6999	66	0.83	0.02	n.a.	
LMMN#2	1955	2	70.4	0.3	147	3	5877	65	0.95	0.01	n.a.	
LMMN#2	1674	1	67.8	0.3	156	5	6590	62	0.86	0.02	n.a.	
LMMN#2	1223	2	36.2	0.4	163	3	5689	42	0.63	0.01	n.a.	
LMMN#2	1100	3	46.2	0.2	148	4	5882	52	0.71	0.04	n.a.	
LMMN#2	1053	1	47.3	0.2	140	3	6567	46	0.72	0.03	n.a.	
LMMN#2	1283	1	42.7	0.1	152	3	6362	59	0.62	0.03	n.a.	
LMMN#2	1613	1	49.7	0.3	154	3	6481	56	0.73	0.03	n.a.	
LMMN#2	1464	2	55.1	0.4	162	4	6278	47	0.73	0.02	n.a.	
LMMN#2	1582	1	44.4	0.3	156	3	6435	76	0.82	0.01	n.a.	
LMMN#2	1601	2	70.1	0.4	150	5	5721	53	0.92	0.02	n.a.	
LMMN#2	1316	4	40.5	0.2	156	3	6002	48	0.71	0.04	n.a.	
LMMN#2	1452	3	42.0	0.2	150	4	6077	35	0.71	0.03	n.a.	
LMMN#2	1598	2	54.0	0.1	161	4	6371	53	0.76	0.04	n.a.	
Average	1498		51.8		153		6154		0.77			
rsd%	16.8%		21.0%		4.3%		9.1%		12.4%			
Reference value					186							
GSD1-G	44.70	0.11	65.0	0.2	2.4	0.7	23.2	0.7	3.60	0.01	n.a.	
GSD1-G	43.20	0.08	64.6	0.3	1.2	0.3	21.9	0.6	3.60	0.02	n.a.	
GSD1-G	41.97	0.03	65.6	0.2	1.4	0.4	19.3	1.2	3.61	0.02	n.a.	
GSD1-G	41.34	0.04	65.0	0.4	0.8	0.4	17.3	0.4	3.51	0.02	n.a.	
GSD1-G	41.79	0.09	65.3	0.1	2.0	0.6	20.2	0.3	3.64	0.01	n.a.	
GSD1-G	42.00	0.09	65.6	0.3	1.7	0.6	21.5	0.9	3.63	0.02	n.a.	
GSD1-G	41.71	0.10	65.1	0.3	1.1	0.4	21.6	1.3	3.65	0.01	n.a.	
GSD1-G	41.90	0.10	65.3	0.4	0.8	0.3	20.2	0.7	3.64	0.02	n.a.	
GSD1-G	41.86	0.06	65.7	0.2	1.3	0.4	17.7	0.7	3.65	0.02	n.a.	
Average	42.27		65.2		1.4		20.3		3.61			
rsd%	2.5%	0.8%	0.5%	0.2%	37%		9.6%		1.2%	0.4%		
Reference value	44.7		65		n.a.		19		3.6			
BCR2G	8.50	0.07	5.13	0.04	1.0	0.3	260	2	3.58	0.01	n.a.	
BCR2G	8.47	0.03	4.93	0.09	1.0	0.4	247	3	3.55	0.02	n.a.	
BCR2G	9.10	0.03	6.85	0.03	0.4	0.2	261	4	3.63	0.03	n.a.	
BCR2G	8.60	0.03	5.06	0.05	1.6	0.3	264	5	3.51	0.02	n.a.	
Average	8.67		5.5		1.0		258.2		3.56			
rsd%	3.4%		16.5%		52.8%		3.1%		1.4%			
Reference value	9.36		5		n.a.		359		3.56			
JJE01-X-3_mica	22.85	0.12	235.5	0.8	574	7	47.6	1.5	3.67	0.02	n.a.	
JJE01-X-3_mica	20.75	0.09	246.3	0.4	750	8	47.5	1.2	3.57	0.03	n.a.	
JJE01-X-3_mica	29.97	0.09	355.0	0.3	737	5	46.3	2.0	3.77	0.03	n.a.	
Average	24.52		278.9		687.3		47.1		3.67			
rsd%	19.7%		23.7%		14.3%		1.5%		2.7%			
mve02-8-5_mica	380.9	0.3	104.6	0.5	170	5	20.6	1.3	3.59	0.03	n.a.	
mve02-8-5_mica	330.9	1.0	97.3	0.4	257	5	22.3	0.7	3.67	0.03	n.a.	
mve02-8-5_mica	291.0	0.6	99.6	0.7	316	15	23.2	1.6	3.54	0.05	n.a.	
Average	334.25		100.5		247.8		22.0		3.60			
rsd%	13.5%		3.7%		29.6%		5.8%		1.8%			
Fba5	4.25	0.01	1.49	0.01	3.6	1.0	22400	318	7.38	0.01	n.a.	
Reference value							22400					
ms98973	2061	5	23.1	0.2	17.3	1.6	12785	136	n.a.	n.a.	n.a.	
ms98973	2636	5	34.9	0.1	16.8	1.1	12897	132	n.a.	n.a.	n.a.	
Reference value	2500		180		n.a.		16800		0.02			
SE-Qz	0.33	0.01	0.078	0.003	0.32	0.15	1.36	0.12	1.0E-05	2.8E-06		

Table 21: SIMS standards for Chapter 3.

Standard	Li (µg/g)	1s	B (µg/g)	1s	N (µg/g)	1s	F (µg/g)	1s	MgO (wt%)	1s	Cl (µg/g)	1s
Phe80-3	n.a.		n.a.		n.a.		n.a.		4.161	0.012	48	6.8
Phe80-3	n.a.		n.a.		n.a.		n.a.		3.884	0.010	41	9.1
Phe80-3	n.a.		n.a.		n.a.		n.a.		3.988	0.007	42	5.2
Phe80-3	n.a.		n.a.		n.a.		n.a.		3.845	0.015	89	19.9
Phe80-3	n.a.		n.a.		n.a.		n.a.		3.454	0.011	51	7.9
Phe80-3	n.a.		n.a.		n.a.		n.a.		3.539	0.007	63	8.1
Phe80-3	n.a.		n.a.		n.a.		n.a.		3.805	0.011	74	6.4
Phe80-3	n.a.		n.a.		n.a.		n.a.		3.481	0.009	71	12.1
Phe80-3	n.a.		n.a.		n.a.		n.a.		3.850	0.005	47	9.2
Phe80-3	n.a.		n.a.		n.a.		n.a.		3.880	0.008	72	9.3
Phe80-3	n.a.		n.a.		n.a.		n.a.		3.439	0.009	57	7.6
Phe80-3	n.a.		n.a.		n.a.		n.a.		4.053	0.024	52	3.6
Phe80-3	n.a.		n.a.		n.a.		n.a.		3.383	0.018	65	9.8
Phe80-3	n.a.		n.a.		n.a.		n.a.		3.078	0.012	57	6.9
Phe80-3	n.a.		n.a.		n.a.		n.a.		3.832	0.011	75	7.3
Phe80-3	n.a.		n.a.		n.a.		n.a.		4.179	0.195	56	9.2
Phe80-3	n.a.		n.a.		n.a.		n.a.		3.841	0.017	43	4.0
Phe80-3	n.a.		n.a.		n.a.		n.a.		3.749	0.008	46	7.0
Phe80-3	n.a.		n.a.		n.a.		n.a.		3.998	0.030	48	4.0
Phe80-3	n.a.		n.a.		n.a.		n.a.		3.375	0.009	64	8.2
Phe80-3	n.a.		n.a.		n.a.		n.a.		3.534	0.009	69	13.1
Phe80-3	n.a.		n.a.		n.a.		n.a.		3.616	0.010	66	9.4
Phe80-3	n.a.		n.a.		n.a.		n.a.		4.366	0.012	129	17.3
Phe80-3	n.a.		n.a.		n.a.		n.a.		3.063	0.009	87	11.3
Phe80-3	n.a.		n.a.		n.a.		n.a.		3.348	0.007	29	5.0
Phe80-3	n.a.		n.a.		n.a.		n.a.		4.020	0.004	29	4.7
Phe80-3	n.a.		n.a.		n.a.		n.a.		3.737	0.005	27	8.4
phe80-3	n.a.		n.a.		n.a.		n.a.		4.725	0.301	34	7.4
phe80-3	n.a.		n.a.		n.a.		n.a.		3.371	0.005	30	6.3
phe80-3	n.a.		n.a.		n.a.		n.a.		3.376	0.006	82	10.3
phe80-3	n.a.		n.a.		n.a.		n.a.		3.615	0.013	29	6.1
phe80-3	n.a.		n.a.		n.a.		n.a.		3.798	0.031	28	7.2
phe80-3	n.a.		n.a.		n.a.		n.a.		3.774	0.019	44	4.3
phe80-3	n.a.		n.a.		n.a.		n.a.		3.407	0.007	30	2.7
Average									3.723		55	
rsd%									9.5%		40.4%	

Table 22: SIMS standards for Chapter 3.

Standard	Li (µg/g)	1s	B (µg/g)	1s	N (µg/g)	1s	F (µg/g)	1s	MgO (wt%)	1s	Cl (µg/g)	1s
ms98973	n.a.		n.a.		n.a.		n.a.		0.0203	0.0003	32	3
ms98973	n.a.		n.a.		n.a.		n.a.		0.0215	0.0003	32	5
ms98973	n.a.		n.a.		n.a.		n.a.		0.0204	0.0002	22	4
ms98973	n.a.		n.a.		n.a.		n.a.		0.0213	0.0003	32	6
ms98973	n.a.		n.a.		n.a.		n.a.		0.0208	0.0003	19	5
ms98973	n.a.		n.a.		n.a.		n.a.		0.0205	0.0002	30	5
ms98973	n.a.		n.a.		n.a.		n.a.		0.0212	0.0002	49	25
ms98973	n.a.		n.a.		n.a.		n.a.		0.0198	0.0002	18	2
ms98973	n.a.		n.a.		n.a.		n.a.		0.0206	0.0001	41	6
ms98973	n.a.		n.a.		n.a.		n.a.		0.0203	0.0003	32	9
ms98973	n.a.		n.a.		n.a.		n.a.		0.0201	0.0004	47	6
ms98973	n.a.		n.a.		n.a.		n.a.		0.0212	0.0002	27	3
ms98973	n.a.		n.a.		n.a.		n.a.		0.0198	0.0003	33	7
ms98973	n.a.		n.a.		n.a.		n.a.		0.0194	0.0002	37	3
ms98973	n.a.		n.a.		n.a.		n.a.		0.0199	0.0004	41	4
ms98973	n.a.		n.a.		n.a.		n.a.		0.0197	0.0002	36	10
ms98973	n.a.		n.a.		n.a.		n.a.		0.0225	0.0003	30	3
ms98973	n.a.		n.a.		n.a.		n.a.		0.0216	0.0003	39	3
ms98973	n.a.		n.a.		n.a.		n.a.		0.0230	0.0005	25	5
ms98973	n.a.		n.a.		n.a.		n.a.		0.0194	0.0002	34	8
ms98973	n.a.		n.a.		n.a.		n.a.		0.0203	0.0005	54	8
ms98973	n.a.		n.a.		n.a.		n.a.		0.0195	0.0006	51	8
ms98973	n.a.		n.a.		n.a.		n.a.		0.0207	0.0001	63	18
ms98973	n.a.		n.a.		n.a.		n.a.		0.0192	0.0004	12	3
ms98973	n.a.		n.a.		n.a.		n.a.		0.0203	0.0003	8	3
ms98973	n.a.		n.a.		n.a.		n.a.		0.0210	0.0002	14	3
ms98973	n.a.		n.a.		n.a.		n.a.		0.0203	0.0002	12	3
ms98973	n.a.		n.a.		n.a.		n.a.		0.0189	0.0004	23	11
ms98973	n.a.		n.a.		n.a.		n.a.		0.0191	0.0001	28	3
ms98973	n.a.		n.a.		n.a.		n.a.		0.0199	0.0003	27	7
ms98973	n.a.		n.a.		n.a.		n.a.		0.0207	0.0001	12	3
ms98973	n.a.		n.a.		n.a.		n.a.		0.0190	0.0002	15	2
Average									0.0204		31	
rsd%									4.7%		43.8%	
GSD	n.a.		n.a.		n.a.		n.a.		3.744	0.012	158	9
GSD	n.a.		n.a.		n.a.		n.a.		3.741	0.012	158	19
GSD	n.a.		n.a.		n.a.		n.a.		3.731	0.007	141	7
GSD	n.a.		n.a.		n.a.		n.a.		3.742	0.006	152	12
GSD	n.a.		n.a.		n.a.		n.a.		3.734	0.014	173	18
GSD	n.a.		n.a.		n.a.		n.a.		3.727	0.014	189	14
GSD	n.a.		n.a.		n.a.		n.a.		3.728	0.007	144	14
GSD	n.a.		n.a.		n.a.		n.a.		3.723	0.014	149	15
GSD	n.a.		n.a.		n.a.		n.a.		3.728	0.007	174	7
GSD	n.a.		n.a.		n.a.		n.a.		3.724	0.010	137	10
GSD	n.a.		n.a.		n.a.		n.a.		3.715	0.004	140	14
GSD	n.a.		n.a.		n.a.		n.a.		3.723	0.012	125	5
GSD	n.a.		n.a.		n.a.		n.a.		3.718	0.011	153	12
GSD	n.a.		n.a.		n.a.		n.a.		3.718	0.003	135	11
GSD	n.a.		n.a.		n.a.		n.a.		3.737	0.006	166	8
GSD	n.a.		n.a.		n.a.		n.a.		3.713	0.009	140	14
GSD	n.a.		n.a.		n.a.		n.a.		3.740	0.011	153	5
GSD	n.a.		n.a.		n.a.		n.a.		3.735	0.007	144	13
GSD	n.a.		n.a.		n.a.		n.a.		3.738	0.009	144	10
GSD	n.a.		n.a.		n.a.		n.a.		3.719	0.010	124	11
GSD	n.a.		n.a.		n.a.		n.a.		3.725	0.012	180	12
GSD	n.a.		n.a.		n.a.		n.a.		3.723	0.008	144	6
GSD	n.a.		n.a.		n.a.		n.a.		3.722	0.009	149	21
GSD	n.a.		n.a.		n.a.		n.a.		3.695	0.006	160	17
GSD	n.a.		n.a.		n.a.		n.a.		3.581	0.004	180	20
GSD	n.a.		n.a.		n.a.		n.a.		3.712	0.015	139	6
GSD	n.a.		n.a.		n.a.		n.a.		3.712	0.014	163	18
GSD	n.a.		n.a.		n.a.		n.a.		3.711	0.012	139	14
GSD	n.a.		n.a.		n.a.		n.a.		3.695	0.010	178	16
GSD	n.a.		n.a.		n.a.		n.a.		3.696	0.010	160	17
GSD	n.a.		n.a.		n.a.		n.a.		3.702	0.008	134	19
GSD	n.a.		n.a.		n.a.		n.a.		3.714	0.009	149	7
GSD	n.a.		n.a.		n.a.		n.a.		3.688	0.017	128	20
GSD	n.a.		n.a.		n.a.		n.a.		3.600	0.009	156	6
GSD	n.a.		n.a.		n.a.		n.a.		3.575	0.007	171	14
GSD	n.a.		n.a.		n.a.		n.a.		3.569	0.007	152	20
GSD	n.a.		n.a.		n.a.		n.a.		3.582	0.003	174	8
GSD	n.a.		n.a.		n.a.		n.a.		3.564	0.006	183	9
GSD	n.a.		n.a.		n.a.		n.a.		3.559	0.006	202	46
GSD	n.a.		n.a.		n.a.		n.a.		3.571	0.007	146	10
GSD	n.a.		n.a.		n.a.		n.a.		3.565	0.008	170	12
GSD	n.a.		n.a.		n.a.		n.a.		3.556	0.008	183	21
GSD	n.a.		n.a.		n.a.		n.a.		3.564	0.017	160	15
GSD	n.a.		n.a.		n.a.		n.a.		3.562	0.011	143	10
Average									3.68		156	
rsd%									1.9%		11.7%	
Reference value									3.60		145	
St81-A9	n.a.		n.a.		n.a.		n.a.		5.76	0.01	2000	27
St81-A9	n.a.		n.a.		n.a.		n.a.		5.33	0.01	2000	39
Reference value											2000	

Table 23: SIMS standards for Chapter 3.

Sample	Phe mode	Phe N (µg/g)	Phe K_2O (wt%)	Pg mode	Pg N (µg/g)	Pg K_2O (wt%)
SEC16-1	16	190	10.05	16	53	1.19
SEC44-1	8	203	10.28			
SEC47-1	10	55	10.30			
JEN12-03	30	193	10.48			
JEN12-07	25	229	10.73			
JEN12-09	15	88	10.95			
LC-3	33	15	11.08			
LC-2a	5	72	10.59			
LC-1b				5	24	0.57

	Chl mode	Chl N (µg/g)	Calculated bulk N (µg/g)	Measured bulk N (µg/g)	Calculated bulk K_2O (wt%)	Measured bulk K_2O (wt%)
SEC16-1		2.1	39	46	1.8	1.6
SEC44-1			16	10	0.82	0.48
SEC47-1			5.5	7.2	1.0	0.51
JEN12-03	30	44	71		3.1	
JEN12-07			57		2.7	
JEN12-09		2.9	13		1.6	
LC-3			5.1		3.7	
LC-2a		3.6	3.6		0.53	
LC-1b			1.2		0.03	

Table 24: Mineral modal abundances for Chapter 3.

A.2 Data for Chapter 4

Tables 25, 26: This is a complete list of all EPMA major element data collected for these samples.

Table 27: This is a complete list of all H_2O, Li, Be, B, F, Rb, Sr, Cs data collected from the first SIMS trace element session for these samples.

Table 28: This is a complete list of all Li, B, N, F data collected from the second SIMS trace element session for these samples.

Table 29: This is a complete list of all Cl data collected from the third SIMS trace element session for these samples.

Table 30: This is a complete list of all phengite B isotope data collected from the first SIMS B isotopes session for these samples.

Tables 31, 32: This is a complete list of all phengite and tourmaline B isotope data collected from the second SIMS B isotopes session for these samples.

Sample	Analysis	Mineral	Textural position	Si	Ti	Al	Fe^{2+}	Mn	Mg	Ca	Na	K	P	Zr
17702	17702_phe2	phe	Replacing pl	6.45	0.03	4.87	0.30	0.00	0.43	0.00	0.04	1.92	0.00	0.00
Metagranite	17702_phe3	phe	Replacing pl	6.53	0.03	4.79	0.26	0.00	0.44	0.00	0.06	1.92	0.00	0.00
	17702_phe1	phe	Replacing bt	6.71	0.23	4.10	0.36	0.00	0.63	0.00	0.03	1.91	0.00	0.00
	17702_phe4	phe	Replacing bt	6.94	0.31	3.66	0.35	0.00	0.72	0.00	0.02	1.87	0.00	0.00
	17702_fsp1	kfs		3.01	0.00	0.99	0.00	0.00	0.00	0.00	0.07	0.91		
	17702_fsp2	kfs		3.00	0.00	1.01	0.00	0.00	0.00	0.00	0.09	0.90		
	17702_fsp3	kfs		3.01	0.00	0.99	0.00	0.00	0.00	0.00	0.09	0.90		
	17702_fsp4	kfs		3.02	0.00	0.99	0.00	0.00	0.00	0.00	0.10	0.87		
	17702_biA	bt		5.99	0.57	2.70	2.90	0.01	1.93	0.00	0.01	1.96		
	17702_biB	bt		6.03	0.55	2.74	2.83	0.01	1.90	0.00	0.02	1.92		
	17702_biC	bt		6.03	0.54	2.73	2.89	0.01	1.88	0.00	0.02	1.92		
20178	20179_phe5	phe		7.02	0.04	3.86	0.76	0.01	0.32	0.00	0.00	2.00	0.00	0.00
Orthogneiss	20179_phe4	phe		7.00	0.04	3.85	0.71	0.01	0.42	0.00	0.01	1.99	0.00	0.00
	20179_phe1	phe		6.93	0.04	4.01	0.67	0.00	0.40	0.00	0.02	1.93	0.00	0.00
	20179_phe2	phe		6.97	0.04	3.90	0.71	0.01	0.44	0.00	0.01	1.91	0.00	0.00
	20179_phe3	phe		6.92	0.04	4.03	0.66	0.01	0.38	0.00	0.02	1.93	0.00	0.00
DM1.1	DM1.1_phe4_c	phl	Prp I inclusion	6.63	0.02	2.05	0.02	0.00	6.00	0.03	0.07	1.08	0.00	0.00
Whiteschist	DM1.1_phe4_r	phl	Prp I inclusion	6.60	0.02	2.09	0.02	0.00	5.98	0.02	0.08	1.14	0.00	0.00
	DM1.1_phe15	phl	Prp I inclusion	6.60	0.02	2.04	0.02	0.00	5.97	0.01	0.08	1.31	0.00	0.00
	DM1.1_ta3	chl	Prp I inclusion	6.17	0.00	4.27	0.04	0.00	9.21	0.00	0.00	0.00	0.00	0.00
	DM1.1_ell1	ell	Prp I inclusion	8.01	0.40	5.92	0.02	0.00	6.67	0.00	0.00	0.00	0.06	0.22
	DM1.1_ell2_c1	ell	Prp I inclusion	8.00	0.64	5.98	0.03	0.00	6.61	0.00	0.01	0.00	0.04	0.00
	DM1.1_ell2_c2	ell	Prp I inclusion	7.88	0.53	5.72	0.03	0.00	6.79	0.00	0.00	0.00	0.27	0.05
	DM1.1_ell2_r	ell	Prp I inclusion	7.95	0.62	5.93	0.03	0.00	6.71	0.00	0.00	0.00	0.08	0.00
	DM1.1_ell3	ell	Prp I inclusion	8.01	0.63	5.96	0.03	0.00	6.67	0.00	0.00	0.00	0.02	0.00
	DM1.1_ell3_r	ell	Prp I inclusion	8.07	0.62	5.94	0.03	0.00	6.60	0.00	0.00	0.00	0.02	0.01
	DM1.1_ell4	ell	Prp I inclusion	7.74	0.34	5.72	0.03	0.00	6.91	0.00	0.00	0.00	0.36	0.20
	DM1.1_ell5	ell	Prp I inclusion	6.31	0.05	4.60	0.02	0.00	8.18	0.01	0.00	0.00	1.91	0.20
	DM1.1_ell6	ell	Prp I inclusion	6.08	0.06	4.53	0.02	0.00	8.32	0.01	0.00	0.00	2.14	0.11
	DM1.1_ell2_g1	grt	Prp I	2.98	0.00	2.03	0.04	0.00	2.91	0.02	0.01	0.00	0.01	0.00
	DM1.1_ell2_g2	grt	Prp I	2.98	0.00	2.03	0.05	0.00	2.90	0.02	0.01	0.00	0.01	0.00
	DM1.1_ell3_gt	grt	Prp I	2.99	0.00	2.03	0.05	0.00	2.89	0.01	0.01	0.00	0.01	0.00
	DM1.1_ell4_gt	grt	Prp I	2.99	0.00	2.02	0.05	0.00	2.91	0.02	0.01	0.00	0.01	0.00
	DM1.1_phe4_gt	grt	Prp I	3.02	0.00	2.01	0.07	0.00	2.85	0.02	0.00	0.00	0.00	0.00
	DM1.1_phe15_gt	grt	Prp I	2.99	0.00	2.02	0.06	0.00	2.87	0.03	0.01	0.00	0.01	0.00
	DM1.1_ell6_gt	grt	Prp I	3.01	0.00	2.01	0.06	0.00	2.86	0.02	0.01	0.00	0.01	0.00
	DM1.1_ta5_gt	grt	Prp I	2.98	0.00	2.00	0.05	0.00	2.97	0.01	0.00	0.00	0.00	0.00
	DM1.1_gt2	grt	Prp I	3.01	0.00	2.02	0.05	0.00	2.89	0.01	0.00	0.00	0.00	0.00
	DM1.1_ta1	tlc	Prp I inclusion	7.54	0.00	0.62	0.02	0.00	5.98	0.00	0.00	0.00	0.00	0.00
	DM1.1_ta2	tlc	Prp I inclusion	7.95	0.00	0.17	0.02	0.00	5.82	0.00	0.00	0.00	0.00	0.00
	DM1.1_ta4	tlc	Prp I inclusion	7.91	0.00	0.21	0.01	0.00	5.86	0.00	0.00	0.00	0.00	0.00
	DM1.1_ta5	tlc	Prp I inclusion	7.88	0.00	0.15	0.01	0.00	5.99	0.00	0.00	0.00	0.00	0.00
	DM1.1_ta6	tlc	Prp I inclusion	7.97	0.00	0.18	0.01	0.00	5.77	0.00	0.00	0.00	0.00	0.00
DM1b	DM-1b wm9c m1	phe	Phe II	7.13		3.64	0.06		1.17		0.04	1.92		
Whiteschist	DM-1b wm9r m2	phe	Phe II	7.16		3.63	0.06		1.16		0.04	1.93		
	DM-1b wm10 m3	phe	Phe II	7.13		3.66	0.05		1.14		0.04	1.92		
	DM-1b wm11 m4	phe	Phe II	7.18		3.55	0.05		1.22		0.05	1.89		
	DM-1b wm7 m5	phe	Phe II	7.19		3.58	0.04		1.18		0.05	1.91		
	DM-1b wm4c m6	phe	Phe II	7.16		3.58	0.05		1.22		0.04	1.91		
	DM-1b wm4r m7	phe	Phe II	7.09		3.71	0.05		1.13		0.05	1.96		
	DM-1b wm5c m8	phe	Phe II	7.14		3.62	0.05		1.17		0.05	1.92		
	DM-1b wm5r m9	phe	Phe II	7.12		3.69	0.06		1.12		0.05	1.93		
	DM-1b wm3 m10	phe	Phe II	7.13		3.65	0.05		1.17		0.05	1.93		

Table 25: EMPA major element data for Chapter 4.

Sample	Analysis	Mineral	Textural position	Si	Ti	Al	Fe^{2+}	Mn	Mg	Ca	Na	K	P	Zr
DM5.2	DM5.2_phe6_gt	grt	Prp II	2.99	0.00	2.02	0.37	0.01	2.51	0.07	0.01	0.00	0.00	0.00
Whiteschist	DM5.2_phe7_gt	grt	Prp II	3.01	0.00	2.02	0.42	0.01	2.46	0.06	0.01	0.00	0.00	0.00
	DM5.2_phe2_gt	grt	Prp II	3.00	0.00	2.05	0.33	0.01	2.57	0.02	0.00	0.00	0.00	0.00
	DM5.2_phe1_gt	grt	Prp II	3.01	0.00	2.03	0.28	0.00	2.63	0.02	0.01	0.00	0.00	0.00
	DM5.2_phe3_gt	grt	Prp II	3.00	0.00	2.04	0.35	0.01	2.52	0.04	0.01	0.00	0.01	0.00
	DM5.2_phe15_gt	grt	Prp II	3.01	0.00	2.02	0.29	0.00	2.57	0.07	0.00	0.00	0.00	0.00
	DM5.2_ta1	tlc	Prp II inclusion	8.02	0.00	0.13	0.16	0.00	5.61	0.00	0.00	0.00	0.00	0.00
	DM5.2_phe9	phe	Phe II	7.13	0.03	3.70	0.03	0.00	1.12	0.00	0.04	1.89	0.00	0.00
	DM5.2_phe10	phe	Phe II	7.10	0.03	3.72	0.03	0.00	1.15	0.00	0.04	1.90	0.00	0.00
	DM5.2_phe11_c	phe	Phe II	7.15	0.03	3.64	0.03	0.00	1.19	0.00	0.04	1.87	0.00	0.00
	DM5.2_phe11_r	phe	Phe II	7.18	0.03	3.62	0.03	0.00	1.16	0.00	0.04	1.89	0.00	0.00
	DM5.2_phe8_c	phe	Phe II	7.12	0.03	3.66	0.04	0.00	1.21	0.00	0.04	1.88	0.00	0.00
	DM5.2_phe8_r	phe	Phe II	7.21	0.03	3.54	0.03	0.00	1.22	0.00	0.04	1.88	0.00	0.00
	DM5.2_phe12_c	phe	Phe II	7.14	0.03	3.60	0.03	0.00	1.26	0.00	0.04	1.87	0.00	0.00
	DM5.2_phe12_r	phe	Phe II	7.13	0.03	3.67	0.03	0.00	1.19	0.00	0.04	1.83	0.00	0.00
	DM5.2_phe13_c	phe	Phe II	7.21	0.03	3.53	0.03	0.00	1.25	0.00	0.03	1.85	0.00	0.00
	DM5.2_phe13.5	phe	Phe II	7.10	0.03	3.79	0.02	0.00	1.08	0.00	0.06	1.83	0.00	0.00
	DM5.2_phe14_c	phe	Phe II	7.09	0.03	3.74	0.04	0.00	1.13	0.00	0.04	1.89	0.00	0.00
	DM5.2_phe14_r	phe	Phe II	7.06	0.03	3.82	0.04	0.00	1.08	0.00	0.04	1.88	0.00	0.00
	DM5.2_phe6	phe	Phe I	7.04	0.02	3.80	0.04	0.00	1.16	0.00	0.05	1.88	0.00	0.00
	DM5.2_phe7	phe	Phe I	7.02	0.02	3.85	0.05	0.00	1.12	0.00	0.05	1.90	0.00	0.00
	DM5.2_phe2	phe	Phe I	7.19	0.03	3.58	0.03	0.00	1.18	0.00	0.05	1.91	0.00	0.00
	DM5.2_phe1	phe	Phe I	7.13	0.03	3.68	0.04	0.00	1.19	0.00	0.05	1.82	0.00	0.00
	DM5.2_phe3	phe	Phe I	7.17	0.03	3.56	0.04	0.00	1.24	0.00	0.07	1.89	0.00	0.00
	DM5.2_phe3_r	phe	Phe I	7.12	0.03	3.70	0.04	0.00	1.18	0.00	0.06	1.80	0.00	0.00
	DM5.2_phe4	phe	Phe I	7.14	0.02	3.77	0.02	0.00	1.04	0.00	0.05	1.85	0.00	0.00
	DM5.2_phe5	phe	Phe I	7.14	0.03	3.69	0.03	0.00	1.13	0.00	0.05	1.90	0.00	0.00
	DM5.2_phe15	phe	Phe I	7.22	0.03	3.55	0.03	0.00	1.18	0.00	0.05	1.89	0.00	0.00
DM6	DM6.1_ell1	ell	Prp I inclusion	7.91	0.30	5.90	0.10	0.00	6.68	0.00	0.00	0.00	0.15	0.29
Whiteschist	DM6.1_ell2	ell	Prp I inclusion	7.90	0.29	5.85	0.10	0.00	6.75	0.00	0.00	0.00	0.14	0.32
	DM6.1_phe5_gt	grt	Prp I	3.01	0.00	2.02	0.15	0.00	2.71	0.06	0.01	0.00	0.01	0.00
	DM6.1_phe2_gt	grt	Prp I	2.99	0.00	2.02	0.19	0.00	2.71	0.05	0.01	0.00	0.01	0.00
	DM6.1_phe1_ta	tlc	Prp I	8.01	0.00	0.07	0.04	0.00	5.84	0.00	0.00	0.00	0.00	0.00
	DM6.2_phe15	phl	Phe III	5.42	0.00	3.58	0.16	0.00	4.67	0.02	0.26	1.63	0.00	0.00
	DM6.2_phe25	phl	Phe III	5.54	0.00	3.36	0.16	0.00	4.81	0.00	0.19	1.64	0.00	0.00
	DM6.2_ell1	ell	Prp I inclusion	7.96	0.31	6.04	0.06	0.00	6.62	0.00	0.00	0.00	0.06	0.28
	DM6.2_ell2	ell	Prp I inclusion	8.06	0.33	5.96	0.07	0.00	6.59	0.00	0.00	0.00	0.04	0.26
	DM6.2_phe17_gt	grt	Prp II	3.00	0.00	2.01	0.27	0.00	2.69	0.02	0.00	0.00	0.00	0.00
	DM6.2_phe27_gt	grt	Prp II	3.00	0.00	2.01	0.28	0.00	2.63	0.07	0.00	0.00	0.00	0.00
	DM6.2_phe21_gt	grt	Prp II	2.98	0.00	2.01	0.23	0.00	2.77	0.01	0.01	0.00	0.00	0.00
	DM6.2_phe21_2_gt	grt	Prp II	2.99	0.00	2.01	0.18	0.00	2.79	0.01	0.01	0.00	0.01	0.00
	DM6.2_gt3	grt	Prp I	3.00	0.00	1.99	0.17	0.00	2.77	0.05	0.01	0.00	0.01	0.00
	DM6.2_gt4	grt	Prp I	2.98	0.00	2.01	0.17	0.00	2.77	0.05	0.01	0.00	0.01	0.00
	DM6.2_phe2_ta	tlc	Prp I inclusion	8.00	0.00	0.04	0.03	0.00	5.92	0.00	0.00	0.00	0.00	0.00
	DM6.2_phe3_ta	tlc	Prp I inclusion	8.02	0.00	0.06	0.03	0.00	5.84	0.00	0.00	0.00	0.00	0.00
	DM6.2_phe18_r	phe	Phe II	7.15	0.03	3.65	0.03	0.00	1.17	0.00	0.05	1.90	0.00	0.00
	DM6.2_phe18_c	phe	Phe II	7.16	0.03	3.59	0.03	0.00	1.26	0.00	0.04	1.87	0.00	0.00
	DM6.2_phe18_r2	phe	Phe II	7.09	0.03	3.71	0.03	0.00	1.20	0.00	0.04	1.88	0.00	0.00
	DM6.2_phe19_r	phe	Phe II	7.10	0.04	3.71	0.03	0.00	1.16	0.00	0.05	1.87	0.00	0.00
	DM6.2_phe19_c	phe	Phe II	7.17	0.03	3.59	0.03	0.00	1.25	0.00	0.05	1.83	0.00	0.00
	DM6.2_phe20	phe	Phe II	7.08	0.03	3.73	0.03	0.00	1.19	0.00	0.05	1.85	0.00	0.00
	DM6.2_phe26	phe	Phe II	7.16	0.03	3.58	0.03	0.00	1.27	0.00	0.05	1.85	0.00	0.00
	DM6.2_phe17_c	phe	Phe I	7.15	0.02	3.60	0.03	0.00	1.24	0.00	0.07	1.87	0.00	0.00
	DM6.2_phe17_r	phe	Phe I	7.11	0.03	3.70	0.03	0.00	1.19	0.00	0.05	1.87	0.00	0.00
	DM6.2_phe27	phe	Phe I	7.22	0.03	3.53	0.03	0.00	1.23	0.00	0.06	1.83	0.00	0.00
	DM6.2_phe27_r	phe	Phe I	7.21	0.03	3.55	0.03	0.00	1.23	0.00	0.06	1.84	0.00	0.00
	DM6.2_phe21	phe	Phe I	7.11	0.03	3.64	0.02	0.00	1.27	0.00	0.06	1.87	0.00	0.00
	DM6.2_phe21_2	phe	Phe I	7.21	0.03	3.54	0.02	0.00	1.23	0.00	0.06	1.85	0.00	0.00
	DM6.2_phe23	phe	Phe III	7.14	0.03	3.65	0.03	0.00	1.21	0.00	0.04	1.86	0.00	0.00
	DM6.2_phe14	phe	Phe III	7.14	0.03	3.65	0.04	0.00	1.20	0.00	0.05	1.85	0.00	0.00
	DM6.2_phe13	phe	Phe III	7.03	0.03	3.83	0.04	0.00	1.14	0.00	0.05	1.85	0.00	0.00
	DM6.2_phe24	phe	Phe III	7.09	0.03	3.72	0.04	0.00	1.18	0.00	0.06	1.84	0.00	0.00

Table 26: EMPA major element data for Chapter 4.

Sample	Analysis	Mineral	Textural position	H_2O (wt%)	Li (µg/g)	Be	B	F	Rb	Sr	Cs
17702	17702_phe2	phe	Replacing pl	4.20	475	6	161	2255	458	30	12
Metagranite	17702_phe1	phe	Replacing bt	3.78	616	13	37	2949	1495	9	81
	17702_phe4	phe	Replacing bt	3.58	608	17	48	3926	1348	11	70
	17702_phe6	phe	Replacing bt	3.82	606	18	95	3052	1165	7	64
	17702_phe7	phe	Replacing bt	3.72	552	20	56	2760	1222	8	55
	17702_phe8	phe	Replacing pl	4.30	334	5	250	1779	403	26	8
	17702_phe9	phe	Replacing bt	3.76	503	12	58	2817	1227	8	64
20178	20179_phe5	phe		3.81	71	18	328	1556	578	7	9
Orthogneiss	20179_phe5_r	phe		3.94	84	17	307	1583	585	9	11
	20179_phe4	phe		3.82	187	17	304	1927	585	9	10
	20179_phe4_r	phe		4.06	272	19	269	1633	579	8	5
	20179_phe1	phe		3.90	187	15	289	1890	599	17	10
	20179_phe2	phe		3.76	187	17	223	1863	593	5	10
	20179_phe3	phe		3.87	185	17	276	1761	583	14	9
DM1.1	DM1.1_phe4_c	phl	Prp I inclusion	5.14	12	5	64	5658	157	18	21
Whiteschist	DM1.1_phe15	phl	Prp I inclusion	4.49	10	1	36	5731	187	13	18
	DM1.1_ell1	ell	Prp I inclusion	6.39	0	5	11	375	0	0	0
	DM1.1_ell2_c1	ell	Prp I inclusion	6.51	0	4	17	252	0	0	0
	DM1.1_ell2_c2	ell	Prp I inclusion	6.30	0	4	21	273	0	0	0
	DM1.1_ell2_r	ell	Prp I inclusion	6.46	0	5	35	191	0	0	0
	DM1.1_ell3	ell	Prp I inclusion	6.48	0	4	18	151	0	0	0
	DM1.1_ell3_r	ell	Prp I inclusion	6.44	0	5	20	143	0	0	0
	DM1.1_ell4	ell	Prp I inclusion	6.30	0	6	26	165	0	0	0
	DM1.1_ell5	ell	Prp I inclusion	8.54	2	10	18	417	0	0	0
	DM1.1_ell6	ell	Prp I inclusion	8.76	1	13	21	394	0	0	0
	DM1.1_ta1	tlc	Prp I inclusion	3.71	0	0	5	1254	0	0	0
	DM1.1_ta2	tlc	Prp I inclusion	3.79	0	0	11	1378	0	0	0
DM5.2	DM5.2_phe2_gt	grt	Prp II	-0.01	11	0	0	60	0	0	0
Whiteschist	DM5.2_phe1_gt	grt	Prp II	-0.01	9	0	0	49	0	0	0
	DM5.2_ta1	tlc	Prp II inclusion	3.38	0	0	6	2905	0	0	0
	DM5.2_phe9	phe	Phe II	3.89	70	11	198	2379	384	18	3
	DM5.2_phe10	phe	Phe II	3.89	77	10	189	2262	389	18	4
	DM5.2_phe11_c	phe	Phe II	3.81	75	11	187	2454	380	18	4
	DM5.2_phe11_r	phe	Phe II	3.89	73	11	191	2414	377	18	4
	DM5.2_phe8_c	phe	Phe II	3.98	62	11	198	2321	354	19	3
	DM5.2_phe8_r	phe	Phe II	3.87	63	11	188	2280	364	23	3
	DM5.2_phe12_c	phe	Phe II	3.86	72	11	191	2302	362	18	3
	DM5.2_phe12_r	phe	Phe II	3.61	63	11	188	2393	398	18	4
	DM5.2_phe13_c	phe	Phe II	3.85	60	11	194	2358	365	17	3
	DM5.2_phe13.5	phe	Phe II	3.88	53	10	239	2056	356	21	3
	DM5.2_phe14_c	phe	Phe II	3.92	64	11	206	2203	369	18	3
	DM5.2_phe14_r	phe	Phe II	3.88	46	10	221	2124	362	22	3
	DM5.2_phe6	phe	Phe I	3.98	50	10	259	1593	315	26	3
	DM5.2_phe6_2	phe	Phe I	3.91	45	11	222	1664	338	21	4
	DM5.2_phe7	phe	Phe I	3.94	45	11	207	1604	381	19	4
	DM5.2_phe2	phe	Phe I	3.93	56	11	219	1519	413	14	3
	DM5.2_phe1	phe	Phe I	3.92	60	11	193	2005	412	14	4
	DM5.2_phe1_c	phe	Phe I	3.95	55	11	203	1975	411	19	4
	DM5.2_phe3	phe	Phe I	3.98	46	14	344	1662	406	21	4
	DM5.2_phe3_r	phe	Phe I	3.85	64	13	212	1707	414	20	5
	DM5.2_phe5	phe	Phe I	3.89	51	10	191	1467	383	18	3
	DM5.2_phe15	phe	Phe I	3.87	62	11	256	1381	410	16	3
DM6	DM6.1_ell1	ell	Prp I inclusion	6.10	0	8	8	132	0	0	0
Whiteschist	DM6.1_ell2	ell	Prp I inclusion	6.09	0	6	8	129	0	0	4
	DM6.2_phe15	phl	Phe III	4.08	43	3	31	6849	39	1	0
	DM6.2_phe25	phl	Phe III	4.10	34	3	25	8180	95	2	1
	DM6.2_ell1	ell	Prp I inclusion	6.31	1	5	10	196	0	0	0
	DM6.2_ell2	ell	Prp I inclusion	5.98	0	3	3	384	0	0	1
	DM6.2_phe2_ta	tlc	Prp I inclusion	3.57	1	0	1	3877	0	0	0
	DM6.2_phe18_r	phe	Phe II	3.77	62	10	196	2117	385	17	3
	DM6.2_phe18_c	phe	Phe II	3.84	80	10	193	2390	385	16	4
	DM6.2_phe18_r2	phe	Phe II	3.84	72	11	189	2301	362	21	3
	DM6.2_phe19_r	phe	Phe II	3.89	74	11	191	2221	411	19	3
	DM6.2_phe19_c	phe	Phe II	3.80	78	11	210	2390	408	13	4
	DM6.2_phe20	phe	Phe II	3.87	71	11	155	2127	394	17	4
	DM6.2_phe26	phe	Phe II	3.82	82	11	189	2343	383	17	3
	DM6.2_phe17_c	phe	Phe I	3.87	59	11	235	1921	426	24	4
	DM6.2_phe17_r	phe	Phe I	3.91	67	11	198	1665	431	22	4
	DM6.2_phe27	phe	Phe I	4.18	79	12	268	1542	402	18	4
	DM6.2_phe27_r	phe	Phe I	4.16	80	12	296	1239	396	19	4
	DM6.2_phe21	phe	Phe I	3.61	42	11	195	2274	394	20	5
	DM6.2_phe21_2	phe	Phe I	3.72	59	10	195	2390	387	18	4
	DM6.2_phe23	phe	Phe III	3.76	54	11	186	1693	376	20	3
	DM6.2_phe14	phe	Phe III	3.83	67	11	184	1813	387	19	4
	DM6.2_phe13	phe	Phe III	3.56	61	11	192	1551	426	22	4
	DM6.2_phe24	phe	Phe III	3.45	52	10	185	1653	446	20	4

Table 27: SIMS trace element data for Chapter 4 - session 1.

Sample	Lithology	Analysis	Mineral	Textural position	Li (µg/g)	B (µg/g)	N (µg/g)	F (µg/g)
17702	Metagranite	17702_fsp1	ksp		5	5	6	16
17702	Metagranite	17702_fsp2	ksp		5	6	6	6
17702	Metagranite	17702_fsp3	ksp		7	8	2	5
17702	Metagranite	17702_fsp4	ksp		7	6	3	5
17702	Metagranite	17702_biA	bt		899	2		6157
17702	Metagranite	17702_biB	bt		887	2		6173
17702	Metagranite	17702_biC	bt		883	3		5749
17702	Metagranite	17702_pheA	bt	Replacing bt	986	3		6715
20178	Orthogneiss	20179_pheA	phe		250	294	130	2028
20178	Orthogneiss	20179_fspA	ab		0	4	1	3
20178	Orthogneiss	20179_biA	bt		677	1		4455
20178	Orthogneiss	20179_epA_2	ep		0	3	5	184
20178	Orthogneiss	20179_biB	bt		615	1		4745
20178	Orthogneiss	20179_pheB	phe		222	314	251	1996
20178	Orthogneiss	20179_pheC	phe		217	253	29	1705
20178	Orthogneiss	20179_pheD	phe		113	209	22	1629
20178	Orthogneiss	20179_pheE	phe		130	309	54	1529
DM1b	Whiteschist	DM-1b wm9c m1	phe	Phe II	52	353	12	2560
DM1b	Whiteschist	DM-1b wm9r m2	phe	Phe II	45	358	19	2451
DM1b	Whiteschist	DM-1b wm10 m3	phe	Phe II	42	353	25	2246
DM1b	Whiteschist	DM-1b wm11 m4	phe	Phe II	37	377	13	2121
DM1b	Whiteschist	DM-1b wm7 m5	phe	Phe II	37	351	29	2125
DM1b	Whiteschist	DM-1b wm4c m6	phe	Phe II	55	346	6	2560
DM1b	Whiteschist	DM-1b wm4r m7	phe	Phe II	48	346	7	2386
DM1b	Whiteschist	DM-1b wm5c m8	phe	Phe II	38	345	14	2187
DM1b	Whiteschist	DM-1b wm5r m9	phe	Phe II	40	350	17	2264
DM1b	Whiteschist	DM-1b wm3 m10	phe	Phe II	40	402	11	2227
DM1b	Whiteschist	DM-1b m11	phe	Phe II	50	345	9	2539
DM1b	Whiteschist	DM-1b m12	phe	Phe II	46	342	9	2416
DM1b	Whiteschist	DM-1b m13	phl	Phe III	34	24		14780
DM1b	Whiteschist	DM-1b m14	phl	Phe III	23	10		10303
DM1b	Whiteschist	DM-1b gt1	grt	Prp II	14	1	1	48
DM1b	Whiteschist	DM-1b m17	phe	Phe II	41	355	18	2238
DM1b	Whiteschist	DM-1b m18	phe	Phe II	63	351	34	2947
DM1b	Whiteschist	DM-1b m15	phe	Phe II	35	396	36	2508
DM1b	Whiteschist	DM-1b m16	phe	Phe II	53	365	18	2805
DM6	Whiteschist	DM6.2_phe25	phl	Phe III	65	33		8360
DM6	Whiteschist	DM6.2_phe27_gt	grt	Prp II	11	0	1	34
DM6	Whiteschist	DM6.2_phe2_ta	tlc	Prp I inclusion	1	1	3	3597
DM6	Whiteschist	DM6.2_phe18_r	phe	Phe II	56	186	21	2159
DM6	Whiteschist	DM6.2_phe18_c	phe	Phe II	75	187	21	2224
DM6	Whiteschist	DM6.2_phe19_r	phe	Phe II	66	197	53	2174
DM6	Whiteschist	DM6.2_phe19_c	phe	Phe II	76	200	41	2254
DM6	Whiteschist	DM6.2_phe20	phe	Phe II	67	172	14	2047
DM6	Whiteschist	DM6.2_phe26	phe	Phe II	67	186	24	2210
DM6	Whiteschist	DM6.2_phe17_c	phe	Phe I	65	240	41	1754
DM6	Whiteschist	DM6.2_phe27	phe	Phe I	89	283	37	1201
DM6	Whiteschist	DM6.2_phe27_r	phe	Phe I	59	292	40	1212
DM6	Whiteschist	DM6.2_phe21	phe	Phe I	70	189	41	2283
DM6	Whiteschist	DM6.2_phe23	phe	Phe III	61	199	134	1581
DM6	Whiteschist	DM6.2_phe13	phe	Phe III	51	184	64	1415
DM6	Whiteschist	DM6.2_phe24	phe	Phe III	42	205	90	1195
DM6	Whiteschist	DM6.2_pheA	phe	Phe II	79	184	21	2253
DM6	Whiteschist	DM6.2_pheB	phe	Phe III	56	196	543	1437

Table 28: SIMS trace element data for Chapter 4 - session 2.

Sample	Lithology	Analysis	Mineral	Textural position	Cl (µg/g)
20178	Orthogneiss	20179_pheA	phe		138
20178	Orthogneiss	20179_biA	phl		1163
20178	Orthogneiss	20179_pheC	phe		18
20178	Orthogneiss	20179_pheD	phe		47
20178	Orthogneiss	20179_pheE	phe		48
DM1.1	Whiteschist	DM1.1_phe4_c	phl	Prp I inclusion	203
DM1.1	Whiteschist	DM1.1_phe4_r	phl	Prp I inclusion	474
DM1.1	Whiteschist	DM1.1_phe15	phl	Prp I inclusion	380
DM1.1	Whiteschist	DM1.1_ell1	ell	Prp I inclusion	138
DM1.1	Whiteschist	DM1.1_ell2_c1	ell	Prp I inclusion	133
DM1.1	Whiteschist	DM1.1_ell2_c2	ell	Prp I inclusion	105
DM1.1	Whiteschist	DM1.1_ell2_r	ell	Prp I inclusion	133
DM1.1	Whiteschist	DM1.1_ell3	ell	Prp I inclusion	197
DM1.1	Whiteschist	DM1.1_ell3_r	ell	Prp I inclusion	105
DM1.1	Whiteschist	DM1.1_ell4	ell	Prp I inclusion	204
DM1.1	Whiteschist	DM1.1_ell5	ell	Prp I inclusion	136
DM1.1	Whiteschist	DM1.1_ell6	ell	Prp I inclusion	91
DM1.1	Whiteschist	DM1.1_ta1	tlc	Prp I inclusion	645
DM1.1	Whiteschist	DM1.1_ta4	tlc	Prp I inclusion	565
DM1.1	Whiteschist	DM1.1_ta5	tlc	Prp I inclusion	593
DM1b	Whiteschist	DM-1b wm9c m1	phe	Phe II	56
DM1b	Whiteschist	DM-1b wm9r m2	phe	Phe II	62
DM1b	Whiteschist	DM-1b wm10 m3	phe	Phe II	35
DM1b	Whiteschist	DM-1b wm11 m4	phe	Phe II	50
DM1b	Whiteschist	DM-1b wm7 m5	phe	Phe II	79
DM1b	Whiteschist	DM-1b wm4c m6	phe	Phe II	40
DM1b	Whiteschist	DM-1b wm4r m7	phe	Phe II	58
DM1b	Whiteschist	DM-1b wm5c m8	phe	Phe II	52
DM1b	Whiteschist	DM-1b wm5r m9	phe	Phe II	53
DM1b	Whiteschist	DM-1b wm3 m10	phe	Phe II	49
DM1b	Whiteschist	DM-1b m11	phe	Phe II	61
DM1b	Whiteschist	DM-1b m12	phe	Phe II	44
DM1b	Whiteschist	DM-1b m13	phl	Phe III	118
DM1b	Whiteschist	DM-1b m17	phe	Phe II	44
DM1b	Whiteschist	DM-1b m18	phe	Phe II	51
DM1b	Whiteschist	DM-1b m15	phe	Phe II	79
DM1b	Whiteschist	DM-1b m16	phe	Phe II	53
DM6	Whiteschist	DM6.1_ell1	ell	Prp I inclusion	41
DM6	Whiteschist	DM6.1_ell2	ell	Prp I inclusion	126
DM6	Whiteschist	DM6.2_ell1	ell	Prp I inclusion	246
DM6	Whiteschist	DM6.2_ell2	ell	Prp I inclusion	522
DM6	Whiteschist	DM6.2_phe2_ta	tlc	Prp I inclusion	82
DM6	Whiteschist	DM6.2_phe18_r	phe	Phe II	48
DM6	Whiteschist	DM6.2_phe18_c	phe	Phe II	299
DM6	Whiteschist	DM6.2_phe19_r	phe	Phe II	114
DM6	Whiteschist	DM6.2_phe19_c	phe	Phe II	11
DM6	Whiteschist	DM6.2_phe20	phe	Phe II	8
DM6	Whiteschist	DM6.2_phe26	phe	Phe II	11
DM6	Whiteschist	DM6.2_phe17_c	phe	Phe I	41
DM6	Whiteschist	DM6.2_phe27	phe	Phe I	5
DM6	Whiteschist	DM6.2_phe27_r	phe	Phe I	16
DM6	Whiteschist	DM6.2_phe21	phe	Phe I	108
DM6	Whiteschist	DM6.2_phe23	phe	Phe III	8
DM6	Whiteschist	DM6.2_phe13	phe	Phe III	81
DM6	Whiteschist	DM6.2_phe24	phe	Phe III	270
DM6	Whiteschist	DM6.2_pheA	phe	Phe II	26

Table 29: SIMS trace element data for Chapter 4 - session 3.

Sample	Lithology	Analysis	Mineral	Textural position	B (µg/g)	δ^{11}B (‰)	1σ (‰)
17702	Metagranite	17702_phe2	phe	Ti-poor phe	133	-13.0	0.4
17702	Metagranite	17702_phe1	phe	Ti-rich phe	34	-7.8	0.8
17702	Metagranite	17702_phe4	phe	Ti-rich phe	45	-9.7	0.6
17702	Metagranite	17702_phe6	phe	Ti-rich phe	101	-9.6	0.5
17702	Metagranite	17702_phe7	phe	Ti-rich phe	48	-11.9	0.5
17702	Metagranite	17702_phe8	phe	Ti-poor phe	256	-9.2	0.3
17702	Metagranite	17702_phe9	phe	Ti-rich phe	63	-11.4	0.5
20178	Orthogneiss	20179_phe5	phe		328	-6.1	0.2
20178	Orthogneiss	20179_phe5_r	phe		337	-5.7	0.2
20178	Orthogneiss	20179_phe4	phe		334	-8.2	0.2
20178	Orthogneiss	20179_phe4_r	phe		277	-15.4	0.4
20178	Orthogneiss	20179_phe4_r2	phe		355	-6.6	0.2
20178	Orthogneiss	20179_phe1	phe		250	-7.5	0.3
20178	Orthogneiss	20179_phe2	phe		250	-9.8	0.2
20178	Orthogneiss	20179_phe3	phe		284	-13.1	0.3
DM1b	Whiteschist	DM-1b wm10 m3	phe	Phe II	288	-3.5	0.4
DM1b	Whiteschist	DM-1b wm11 m4	phe	Phe II	320	-5.2	0.3
DM1b	Whiteschist	DM-1b wm7 m5	phe	Phe II	287	-8.0	0.3
DM1b	Whiteschist	DM-1b wm4c m6	phe	Phe II	303	-7.1	0.3
DM1b	Whiteschist	DM-1b wm4r m7	phe	Phe II	290	-6.4	0.3
DM5.2	Whiteschist	DM5.2_phe9	phe	Phe II	171	-10.8	0.3
DM5.2	Whiteschist	DM5.2_phe10	phe	Phe II	169	-11.4	0.4
DM5.2	Whiteschist	DM5.2_phe11_c	phe	Phe II	168	-10.9	0.3
DM5.2	Whiteschist	DM5.2_phe11_r	phe	Phe II	170	-10.9	0.3
DM5.2	Whiteschist	DM5.2_phe8_c	phe	Phe II	181	-12.0	0.4
DM5.2	Whiteschist	DM5.2_phe8_r	phe	Phe II	166	-10.4	0.3
DM5.2	Whiteschist	DM5.2_phe12_c	phe	Phe II	176	-9.8	0.4
DM5.2	Whiteschist	DM5.2_phe12_r	phe	Phe II	171	-10.2	0.4
DM5.2	Whiteschist	DM5.2_phe13_c	phe	Phe II	189	-10.2	0.3
DM5.2	Whiteschist	DM5.2_phe13.5	phe	Phe II	209	-9.8	0.4
DM5.2	Whiteschist	DM5.2_phe14_c	phe	Phe II	177	-9.3	0.3
DM5.2	Whiteschist	DM5.2_phe14_r	phe	Phe II	191	-11.1	0.3
DM5.2	Whiteschist	DM5.2_phe6	phe	Phe I	190	-10.4	0.3
DM5.2	Whiteschist	DM5.2_phe6_2	phe	Phe I	202	-13.0	0.4
DM5.2	Whiteschist	DM5.2_phe7	phe	Phe I	219	-9.0	0.4
DM5.2	Whiteschist	DM5.2_phe2	phe	Phe I	187	-10.7	0.4
DM5.2	Whiteschist	DM5.2_phe1	phe	Phe I	166	-5.4	0.3
DM5.2	Whiteschist	DM5.2_phe1_c	phe	Phe I	179	-12.2	0.3
DM5.2	Whiteschist	DM5.2_phe3	phe	Phe I	246	-9.4	0.3
DM5.2	Whiteschist	DM5.2_phe3_r	phe	Phe I	174	-6.7	0.3
DM5.2	Whiteschist	DM5.2_phe5	phe	Phe I	166	-9.2	0.6
DM5.2	Whiteschist	DM5.2_phe15	phe	Phe I	202	-9.2	0.4
DM6	Whiteschist	DM6.2_phe18_r	phe	Phe II	177	-11.0	0.3
DM6	Whiteschist	DM6.2_phe18_c	phe	Phe II	156	-9.4	0.3
DM6	Whiteschist	DM6.2_phe18_r2	phe	Phe II	159	-10.5	0.3
DM6	Whiteschist	DM6.2_phe19_r4	phe	Phe II	165	-10.5	0.4
DM6	Whiteschist	DM6.2_phe19_r	phe	Phe II	165	-8.0	0.4
DM6	Whiteschist	DM6.2_phe19_m1	phe	Phe II	157	-13.8	0.5
DM6	Whiteschist	DM6.2_phe19_m2	phe	Phe II	183	-13.0	0.5
DM6	Whiteschist	DM6.2_phe19_m3	phe	Phe II	165	-10.5	0.4
DM6	Whiteschist	DM6.2_phe19_m4	phe	Phe II	175	-9.8	0.3
DM6	Whiteschist	DM6.2_phe19_m5	phe	Phe II	171	-9.6	0.4
DM6	Whiteschist	DM6.2_phe19_c	phe	Phe II	172	-11.3	0.3
DM6	Whiteschist	DM6.2_phe20	phe	Phe II	136	-9.8	0.2
DM6	Whiteschist	DM6.2_phe26	phe	Phe II	156	-9.8	0.4
DM6	Whiteschist	DM6.2_phe17_c	phe	Phe I	187	-11.8	0.3
DM6	Whiteschist	DM6.2_phe17_r	phe	Phe I	162	-9.4	0.5
DM6	Whiteschist	DM6.2_phe27	phe	Phe I	236	-14.2	0.3
DM6	Whiteschist	DM6.2_phe27_r	phe	Phe I	281	-15.3	0.3
DM6	Whiteschist	DM6.2_phe21	phe	Phe I	158	-8.5	0.4
DM6	Whiteschist	DM6.2_phe21_2	phe	Phe I	175	-9.8	0.3
DM6	Whiteschist	DM6.2_phe23	phe	Phe III	162	-10.0	0.5
DM6	Whiteschist	DM6.2_phe14	phe	Phe III	152	-9.1	0.4
DM6	Whiteschist	DM6.2_phe13	phe	Phe III	168	-12.4	0.4
DM6	Whiteschist	DM6.2_phe24	phe	Phe III	166	-11.8	0.3

Table 30: SIMS B isotope data for Chapter 4 - session 1.

Sample	Lithology	Analysis	Mineral	Textural position	B (µg/g)	δ^{11}B (‰)	1σ (‰)
26405	Phengite schist	1_tur1	tur	Matrix		-1.8	0.1
26405	Phengite schist	2_tur2	tur	Matrix		-1.2	0.1
26405	Phengite schist	3_tur3	tur	Matrix		-0.2	0.1
26405	Phengite schist	4_tur4	tur	Matrix		-0.1	0.1
26405	Phengite schist	5_tur5	tur	Matrix		-0.2	0.1
26405	Phengite schist	6_tur6	tur	Matrix		-0.3	0.1
26405	Phengite schist	7_tur7	tur	Matrix		0.3	0.1
26405	Phengite schist	9_tur9	tur	Matrix		-1.3	0.1
26405	Phengite schist	10_tur10	tur	Matrix		-0.6	0.1
26405	Phengite schist	11_tur11	tur	Matrix		-0.2	0.1
26405	Phengite schist	12_tur12	tur	Matrix		0.1	0.1
26405	Phengite schist	1_phe1	phe	Phe II	234	-4.5	0.4
26405	Phengite schist	2_phe2	phe	Phe II	203	-4.0	0.4
26405	Phengite schist	3_phe3	phe	Phe II	219	-3.8	0.5
26405	Phengite schist	5_phe5	phe	Phe II	213	-0.7	0.5
26405	Phengite schist	6_phe6	phe	Phe II	220	-2.9	0.5
26405	Phengite schist	7_phe7	phe	Phe II	214	-2.7	0.4
26405	Phengite schist	8_phe8	phe	Phe II	215	-3.1	0.5
17618	Phengite schist	1_tur1	tur	Matrix		-0.9	0.1
17618	Phengite schist	2_tur3	tur	Matrix		-0.6	0.1
17618	Phengite schist	3_tur2	tur	Matrix		0.5	0.1
17618	Phengite schist	4_tur4	tur	Matrix		-1.0	0.1
17618	Phengite schist	5_tur5	tur	Matrix		-0.8	0.1
17618	Phengite schist	6_tur6	tur	Matrix		-0.8	0.1
17618	Phengite schist	7_tur7	tur	Matrix		-1.0	0.1
17618	Phengite schist	8_tur8	tur	Matrix		-1.1	0.1
17618	Phengite schist	10_tur10	tur	Matrix		-6.5	0.1
17618	Phengite schist	11_tur11	tur	Matrix		-1.1	0.1
17618	Phengite schist	12_tur12	tur	Matrix		-1.5	0.1
17618	Phengite schist	1_phe1	phe	Phe II	250	-6.7	0.4
17618	Phengite schist	3_phe3	phe	Phe II	213	-6.4	0.6
17618	Phengite schist	4_phe4	phe	Phe II	244	-5.6	0.4
17618	Phengite schist	5_phe5	phe	Phe II	230	-6.7	0.5
17618	Phengite schist	6_phe6	phe	Phe II	245	-5.0	0.5
17618	Phengite schist	7_phe7	phe	Phe II	271	-5.7	0.4
17618	Phengite schist	8_phe8	phe	Phe II	258	-4.9	0.5
15597	Phengite schist	1_tur1	tur	Prp II inclusion		-6.0	0.1
15597	Phengite schist	2_tur2	tur	Prp II inclusion		-6.0	0.1
15597	Phengite schist	3_tur3	tur	Prp II inclusion		-5.0	0.1
15597	Phengite schist	4_tur4	tur	Prp II inclusion		-6.5	0.1
15597	Phengite schist	5_tur5	tur	Prp II inclusion		-5.5	0.1
15597	Phengite schist	6_tur6	tur	Prp II inclusion		-2.1	0.1
15597	Phengite schist	7_tur7	tur	Prp II inclusion		-6.2	0.1
15597	Phengite schist	8_tur8	tur	Prp II inclusion		-8.7	0.1
15597	Phengite schist	9_tur9	tur	Prp II inclusion		-10.7	0.1
15597	Phengite schist	5_phe5	phe	Phe II	207	-6.7	0.5
15597	Phengite schist	6_phe6	phe	Phe II	205	-7.6	0.6
15597	Phengite schist	1_phe7	phe	Phe II	208	-8.0	0.4
15597	Phengite schist	2_phe8	phe	Phe II	201	-6.8	0.4
15597	Phengite schist	3_phe9	phe	Phe II	209	-6.1	0.5
15597	Phengite schist	4_phe10	phe	Phe II	238	-6.3	0.5
15597	Phengite schist	5_phe11	phe	Phe II	214	-6.4	0.5
15597	Phengite schist	6_phe12	phe	Phe II	206	-6.7	0.5
15597	Phengite schist	7_phe13	phe	Phe II	217	-6.5	0.5
15597	Phengite schist	8_phe14	phe	Phe II	214	-5.2	0.5
21437	Phengite schist	1_tur1	tur	Matrix		-4.3	0.1
21437	Phengite schist	2_tur2	tur	Matrix		-5.0	0.1
21437	Phengite schist	3_tur3	tur	Matrix		-3.8	0.1
21437	Phengite schist	4_tur4	tur	Matrix		-3.3	0.1
21437	Phengite schist	5_tur5	tur	Matrix		-3.6	0.1
21437	Phengite schist	6_tur6	tur	Matrix		-3.0	0.1
21437	Phengite schist	7_tur7	tur	Matrix		-3.3	0.1
21437	Phengite schist	10_tur10	tur	Matrix		-1.4	0.1
21437	Phengite schist	11_tur11	tur	Matrix		-2.7	0.1
21437	Phengite schist	12_tur12	tur	Matrix		-2.4	0.1
21437	Phengite schist	13_tur13	tur	Matrix		-4.2	0.1
21437	Phengite schist	14_tur14	tur	Matrix		-4.7	0.1
21437	Phengite schist	15_tur16	tur	Matrix		-3.9	0.1
21437	Phengite schist	16_tur15	tur	Matrix		-3.7	0.1
21437	Phengite schist	1_phe1	phe	Phe II	192	-5.9	0.4
21437	Phengite schist	2_phe2	phe	Phe II	189	-5.2	0.4
21437	Phengite schist	6_phe6	phe	Phe II	221	-4.2	0.5
21437	Phengite schist	7_phe7	phe	Phe II	191	-5.2	0.5
21437	Phengite schist	8_phe8	phe	Phe II	212	-4.8	0.4
21437	Phengite schist	9_phe9	phe	Phe II	203	-5.4	0.5
21437	Phengite schist	10_phe10	phe	Phe II	213	-4.9	0.5

Table 31: SIMS B isotope data for Chapter 4 - session 2.

Sample	Lithology	Analysis	Mineral	Textural position	B (µg/g)	δ^{11}B (‰)	1σ (‰)
17478	Retrogressed whiteschist	1_tur1	tur	Retrograde		-2.5	0.1
17478	Retrogressed whiteschist	3_tur3	tur	Retrograde		-3.6	0.1
17478	Retrogressed whiteschist	4_tur4	tur	Inclusion in matrix kyanite		-2.8	0.1
17478	Retrogressed whiteschist	5_tur5	tur	Inclusion in matrix kyanite		-2.3	0.1
17478	Retrogressed whiteschist	6_tur6	tur	Inclusion in matrix kyanite		-2.7	0.2
17478	Retrogressed whiteschist	7_tur7	tur	Inclusion in matrix kyanite		-4.3	0.2
17478	Retrogressed whiteschist	8_tur8	tur	Inclusion in matrix kyanite		-3.3	0.1
17478	Retrogressed whiteschist	1_phe1	phe	Phe II	208	-6.0	0.5
17478	Retrogressed whiteschist	2_phe2	phe	Phe II	200	-5.5	0.5
17478	Retrogressed whiteschist	3_phe3	phe	Phe II	224	-6.5	0.4
17478	Retrogressed whiteschist	4_phe4	phe	Phe II	228	-4.7	0.4
17478	Retrogressed whiteschist	5_phe5	phe	Phe II	211	-5.3	0.5
17478	Retrogressed whiteschist	6_phe6	phe	Phe II	188	-5.8	0.5
17478	Retrogressed whiteschist	7_phe7	phe	Phe II	210	-6.1	0.5
17478	Retrogressed whiteschist	8_phe8	phe	Phe II	188	-6.5	0.6
17478	Retrogressed whiteschist	9_phe9	phe	Phe II	122	-8.0	0.6

Table 32: SIMS B isotope data for Chapter 4 - session 2.

Standard	δ^{11}B (‰)	$\delta^{11}B_{ref}$ (‰)	IMF (‰)	B (μg/g)	B_{ref} (μg/g)	Standard	δ^{11}B (‰)	$\delta^{11}B_{ref}$ (‰)
Session 1								
GSDG-1								
Mean	10.2	10.2		64	65			
2se	0.8							
n	8							
B6								
Mean	-1.6	-1.79						
2se	0.4							
n	8							
ARM-3								
Mean	-3.8	-3.78		473	463			
2se	0.4							
n	4							
GB4								
Mean	-13.5	-12.9		997	970			
2se	0.3							
n	8							
Phe 80-3								
Mean	-16.5	-13.5	-3.0	31	27			
2se	0.6							
n	28							
ms98973								
Mean	-23.2	-20.0	-3.2	33	44			
2se	0.7							
n	12							
Session 2								
GB4						Schorl 112566		
Mean	-15.0	-12.9		1021	970	*Mean*	-11.7	-12.5
2se	0.1					*2se*	0.2	0.1
n	17					*n*	8	
B6						Elbaite 98144		
Mean	-1.3	-1.79				*Mean*	-11.1	-10.5
2se						*2se*	0.3	0.4
n	2					*n*	8	
GSDG-1						Dravite 108796		
Mean	9.9	10.2		68	65	*Mean*	-6.7	-6.6
2se	0.9					*2se*	0.4	0.2
n	7					*n*	8	
Phe80-3								
Mean	-17.4	-13.5	-3.9	37	27			
2se	0.7							
n	25							
ms98973								
Mean	-23.9	-20.0	-3.9	35	44			
2se	0.9							
n	18							

Table 33: SIMS B isotope standards for Chapter 4.

A.3 Data for Chapter 5

Table 34: This is a complete list of all XRF bulk trace element data for these samples.

Tables 35, 36, 37: This is a complete list of EDS major element data for these samples.

Tables 38, 39, 40: This is a complete list of SIMS trace element data for these samples.

Table 41: This is a complete list of the SIMS trace element standards analysed for this chapter.

Table 42: This is a complete list of SIMS B isotope data for these samples.

Table 43: This is a complete list of SIMS B isotope standards analysed for this chapter.

Sample	Lithology	Ba (μg/g)	Ce	Cr	Cu	La	Nb	Nd	Ni	Pb	Rb	Sc	Sr	Th	U	V	Y	Zn	Zr
122	Blueschist	25	15	241	57	2.0	3.2	11	124	3.0	2.9	38	52	n.d.	0.5	320	44	83	142
DR10	Blueschist	1054	8.6	1057	31	4.4	4.1	5.3	710	15	48	24	159	1.1	2.3	157	19	152	69
X1348	Blueschist	25	21	158	31	2.2	4.5	16	53	3.4	6.9	33	146	n.d.	0.7	253	44	98	174
X1008	Blueschist	85	34	28	405	5.0	6.4	23	34	7.6	33	28	206	0.6	n.d.	248	56	96	248
DC26A	Blueschist	17	19	345	25	2.0	6.7	11	146	1.1	4.9	30	154	n.d.	2.3	198	28	69	141
DC48B	Blueschist	7.1	23	200	57	1.2	6.1	14	80	2.1		34	199	n.d.	0.8	273	38	65	181
DC46A	Blueschist	7.0	22	249	321	2.9	3.6	18	114	1.7	5.1	43	507	n.d.	0.7	304	40	106	145
DC31C	Blueschist	24	18	206	57	1.4	7.2	15	72	2.8	5.6	30	167	n.d.	2.6	226	38	63	184
DC46B	Blueschist	6.0	25	176	33	3.6	5.7	14	82	0.7	0.8	33	132	n.d.	2.3	247	38	80	159
C13	Eclogite	13	12	231	18	1.0	3.1	12	43	2.1	12	36	148	1.0	0.6	277	35	46	128
DR9	Eclogite	125	9.0	381	85	n.d.	2.8	8.0	111	0.5	30	51	134	n.d.	n.d.	322	34	97	101
HA2	Eclogite	12	1.2	233	24	n.d.	1.0	n.d.	44	n.d.	n.d.	78	39	n.d.	0.7	570	7.1	120	1.2
HA1	Eclogite	82	13	24	21	0.5	2.9	8.0	9.9	0.6	6.1	50	75	0.5	1.4	105	43	108	42
Vi1808	Eclogite	13	21	n.d.	52	n.d.	1.7	21	23	1.0	2.5	61	263	n.d.	0.6	747	31	128	99
ZS0715	Eclogite	5.6	36	118	26	6.5	10	21	61	3.0	n.d.	31	458	0.5	n.d.	250	42	82	238
0275	Eclogite	213	24	71	9.1	4.4	14	15	62	3.3	36	46	84	0.6	0.9	308	29	107	129
ZS15	Eclogite	6.3	16	181	15	n.d.	7.8	8.0	63	1.6	n.d.	31	467	n.d.	2.0	236	40	63	203
0321	Greenschist	27	8.5	414	120	n.d.	1.7	9.0	140	0.2	15	44	155	n.d.	2.4	312	35	83	99
San2	Greenschist	22	12	321	111	0.7	5.8	8.0	59	n.d.	5.2	47	173	0.2	n.d.	275	26	85	76
San1	Greenschist	29	14	311	103	0.5	6.5	11	100	0.1	11	44	103	n.d.	n.d.	268	32	98	95
EXT00007N	Mg gabbro	2.3	6.7	280	3.0	2.0	1.5	5.0	239	1.0	1.0	9.5	255	1.4	1.5	41	6.4	23	28
EXT00007Q	Pillow basalt	5.3	15	193	78	3.9	4.0	13	75	2.5	n.d.	32	83	n.d.	1.1	264	40	67	144

Table 34: XRF trace element data for Chapter 5.

Sample	Grain	Si	Ti	Al	Fe*	Mn*	Mg	Ca	Na	K	Ba	Ni	Cr	Total cations	Oxygens
HA1	01_phe1	6.65	0.05	4.43	0.33	0.00	0.67	0.00	0.24	1.69	0.00	0.00	0.00	14.05	22
	01_cpx1	2.01	0.00	0.44	0.23	0.00	0.39	0.43	0.56	0.00	0.00	0.00	0.00	4.05	6
	02_phe1	6.61	0.05	4.49	0.35	0.00	0.62	0.00	0.21	1.73	0.00	0.00	0.00	14.06	22
	04_phe1	6.56	0.07	4.59	0.33	0.00	0.56	0.00	0.22	1.72	0.00	0.00	0.00	14.05	22
	04_cpx1	1.98	0.00	0.44	0.25	0.00	0.41	0.48	0.49	0.00	0.00	0.00	0.00	4.04	6
	03_phe1	6.61	0.05	4.50	0.33	0.00	0.60	0.00	0.28	1.69	0.00	0.00	0.00	14.07	22
	03_cpx1	2.00	0.00	0.45	0.23	0.00	0.38	0.43	0.54	0.00	0.00	0.00	0.00	4.04	6
DR10	01_2_chl1	2.88	0.00	2.33	0.92	0.03	3.81	0.00	0.00	0.00	0.00	0.00	0.00	9.96	14
	01_2_amph1	7.80	0.00	0.60	0.89	0.00	3.82	1.48	0.59	0.00	0.00	0.00	0.00	15.19	23
	01_4_phe1	6.86	0.00	4.27	0.15	0.00	0.83	0.00	0.12	1.66	0.00	0.00	0.00	13.90	22
	01_4_phe2	6.68	0.04	4.36	0.29	0.00	0.75	0.00	0.17	1.72	0.06	0.00	0.00	14.05	22
	01_5_chl1	2.86	0.00	2.35	1.06	0.00	3.69	0.00	0.00	0.00	0.00	0.00	0.00	9.96	14
	02_2_phe1	6.69	0.00	4.43	0.26	0.00	0.71	0.00	0.14	1.72	0.08	0.00	0.00	14.02	22
	02_2_amph1	8.00	0.00	0.00	0.60	0.03	4.48	1.78	0.24	0.00	0.00	0.00	0.00	15.12	23
	02_3_chl	2.89	0.00	2.34	0.99	0.00	3.72	0.00	0.00	0.00	0.00	0.00	0.00	9.94	14
	02_5_phe1	6.84	0.00	4.20	0.23	0.00	0.81	0.00	0.10	1.75	0.06	0.00	0.00	13.99	22
	02_5_phe2	6.73	0.04	4.27	0.30	0.00	0.77	0.00	0.13	1.73	0.06	0.00	0.00	14.02	22
	03_2_amph	7.67	0.00	0.91	0.89	0.00	3.65	1.44	0.64	0.00	0.00	0.00	0.00	15.20	23
	03_3_phe	6.93	0.00	4.17	0.13	0.00	0.85	0.00	0.11	1.64	0.03	0.00	0.00	13.86	22
	03_4_chl	2.89	0.00	2.34	1.02	0.00	3.69	0.00	0.00	0.00	0.00	0.00	0.00	9.94	14
	05_2_amph	7.64	0.00	0.90	1.12	0.03	3.48	1.24	0.90	0.04	0.00	0.00	0.03	15.37	23
	05_2_chl	2.86	0.00	2.34	1.04	0.02	3.69	0.00	0.00	0.00	0.00	0.03	0.00	9.97	14
	05_4_phe1	6.75	0.00	4.38	0.13	0.00	0.74	0.00	0.21	1.64	0.03	0.00	0.07	13.95	22
	05_4_phe2	6.61	0.00	4.47	0.25	0.00	0.66	0.00	0.18	1.74	0.07	0.00	0.09	14.07	22
275	01_2_amph														
	01_3_phe	6.78	0.00	4.40	0.14	0.00	0.75	0.00	0.19	1.71	0.00	0.00	0.00	13.97	22
	01_3_amph	7.46	0.00	1.85	1.15	0.00	2.68	0.82	1.31	0.00	0.00	0.00	0.00	15.27	23
	01_4_phe	6.77	0.05	4.32	0.13	0.00	0.78	0.00	0.25	1.69	0.00	0.00	0.00	13.99	22
	01_4_ep	5.97	0.00	5.27	0.78	0.06	0.00	3.87	0.00	0.00	0.00	0.00	0.00	15.96	25
	02_3_pa	5.95	0.00	6.06	0.03	0.00	0.00	0.03	1.80	0.11	0.00	0.00	0.00	13.97	22
	02_3_phe	6.74	0.06	4.32	0.14	0.00	0.78	0.00	0.29	1.69	0.00	0.00	0.00	14.03	22
	02_3_amph	7.43	0.00	1.37	0.99	0.00	3.30	1.32	0.92	0.03	0.00	0.00	0.00	15.36	23
	02_4_phe	6.73	0.05	4.41	0.14	0.00	0.72	0.00	0.25	1.69	0.00	0.00	0.00	13.99	22
	02_4_pa	6.06	0.00	5.91	0.00	0.00	0.07	0.00	1.70	0.21	0.00	0.00	0.00	13.94	22
	03_2_cpx	1.99	0.00	0.52	0.08	0.00	0.45	0.47	0.50	0.00	0.00	0.00	0.00	4.00	6
	04_phe	6.69	0.05	4.43	0.12	0.00	0.77	0.00	0.25	1.73	0.00	0.00	0.00	14.04	22
	04_2_cpx	1.99	0.00	0.49	0.09	0.00	0.46	0.49	0.47	0.00	0.00	0.00	0.00	4.00	6
	04_phe2														
DC46B	05_chl2	2.84	0.00	2.39	1.26	0.00	3.48	0.00	0.00	0.00	0.00	0.00	0.00	9.97	14
	05_2_pa	5.98	0.00	6.08	0.00	0.00	0.00	0.00	1.84	0.00	0.00	0.00	0.00	13.90	22
	05_2_chl	2.81	0.00	2.46	1.27	0.00	3.43	0.00	0.00	0.00	0.00	0.00	0.00	9.96	14
	01_2_amph	7.90	0.00	1.76	0.83	0.00	2.61	0.25	1.72	0.00	0.00	0.00	0.00	15.08	23
	01_2_ctd	2.02	0.00	3.96	1.24	0.00	0.79	0.00	0.00	0.00	0.00	0.00	0.00	8.00	12
	01_3_amph	7.91	0.00	1.93	1.08	0.00	2.16	0.11	1.87	0.00	0.00	0.00	0.00	15.06	23
	01_3_ctd	2.03	0.00	3.95	1.23	0.00	0.79	0.00	0.00	0.00	0.00	0.00	0.00	8.00	12
	01_4_pa	5.89	0.00	6.11	0.04	0.00	0.00	0.03	1.91	0.04	0.00	0.00	0.00	14.03	22
	01_4_chl	2.81	0.00	2.46	1.38	0.00	3.32	0.00	0.00	0.00	0.00	0.00	0.00	9.96	14
	04_2_pa	5.94	0.00	6.09	0.00	0.00	0.00	0.04	1.88	0.03	0.00	0.00	0.00	13.97	22
	04_2_amph	2.07	0.00	0.49	0.18	0.00	0.67	0.02	0.48	0.00	0.00	0.00	0.00	3.92	6
	04_3_pa	5.90	0.00	6.10	0.04	0.00	0.00	0.05	1.86	0.06	0.00	0.00	0.00	14.02	22
	04_3_chl	2.81	0.00	2.47	1.07	0.00	3.60	0.00	0.00	0.00	0.00	0.00	0.00	9.95	14
	06_ab	2.95	0.00	1.05	0.00	0.00	0.00	0.03	0.95	0.01	0.00	0.00	0.00	5.00	8
	06_2_ab	2.95	0.00	1.06	0.00	0.00	0.00	0.03	0.95	0.00	0.00	0.00	0.00	5.00	8
DC46A	02_im26_amph	7.96	0.00	1.65	1.37	0.00	2.18	0.15	1.84	0.00	0.00	0.00	0.00	15.14	23
	02_im26_ep	5.94	0.00	4.91	1.20	0.08	0.00	3.83	0.00	0.00	0.00	0.00	0.00	15.96	25
	02_im26_pa1	6.03	0.00	5.95	0.05	0.00	0.00	0.00	1.87	0.08	0.00	0.00	0.00	13.97	22
	02_im26_pa2	6.07	0.00	5.84	0.06	0.00	0.08	0.00	1.83	0.09	0.00	0.00	0.00	13.97	22
	01_im21_amph	8.02	0.00	1.49	1.50	0.00	2.18	0.11	1.87	0.00	0.00	0.00	0.00	15.17	23
	03_im30_pa	6.09	0.00	5.81	0.08	0.00	0.05	0.00	1.68	0.24	0.00	0.00	0.00	13.96	22
	03_im30_chl	2.76	0.00	2.53	1.66	0.00	3.03	0.00	0.00	0.00	0.00	0.00	0.00	9.98	14
	03_im31_pa	6.06	0.00	5.86	0.08	0.00	0.06	0.00	1.72	0.20	0.00	0.00	0.00	13.97	22
	03_im31_chl	2.83	0.00	2.41	1.61	0.02	3.10	0.00	0.00	0.00	0.00	0.00	0.00	9.97	14
ZS15	02_2_pa	5.94	0.00	6.05	0.05	0.00	0.00	0.04	1.79	0.11	0.00	0.00	0.00	13.98	22
	02_2_ep	5.96	0.00	5.50	0.60	0.00	0.00	3.95	0.00	0.00	0.00	0.00	0.00	16.00	25
	02_3_cpx	2.01	0.00	0.55	0.15	0.00	0.34	0.37	0.60	0.00	0.00	0.00	0.00	4.02	6
	02_4_pa	6.02	0.00	5.95	0.03	0.00	0.04	0.00	1.84	0.06	0.00	0.00	0.00	13.95	22
	02_5_pa	5.96	0.00	6.07	0.04	0.00	0.00	0.00	1.81	0.06	0.00	0.00	0.00	13.94	22
	01_2_cpx	2.01	0.00	0.44	0.17	0.00	0.41	0.48	0.50	0.00	0.00	0.00	0.00	4.01	6
	01_3_amph	7.95	0.00	1.90	1.05	0.00	2.16	0.06	1.93	0.00	0.00	0.00	0.00	15.06	23
	01_3_ep	5.93	0.00	5.31	0.89	0.00	0.00	3.85	0.00	0.00	0.00	0.00	0.00	15.97	25
	03_2_pa	5.95	0.00	6.03	0.05	0.00	0.00	0.03	1.88	0.06	0.00	0.00	0.00	14.00	22
	03_3_cpx	2.01	0.00	0.53	0.20	0.00	0.31	0.35	0.64	0.00	0.00	0.00	0.00	4.04	6
	03_3_ep	6.00	0.00	5.08	1.01	0.00	0.00	3.86	0.00	0.00	0.00	0.00	0.00	15.95	25
	03_4_pa	6.02	0.00	5.98	0.03	0.00	0.00	0.00	1.88	0.04	0.00	0.00	0.00	13.95	22
	03_5_pa	5.99	0.00	6.02	0.03	0.00	0.00	0.00	1.86	0.04	0.00	0.00	0.00	13.94	22
	04_2_cpx	2.07	0.00	0.48	0.24	0.00	0.62	0.03	0.49	0.00	0.00	0.00	0.00	3.94	6

Table 35: EDS major element data for Chapter 5. *Fe and Mn are calculated as 2+ ions, except for epidote where they are calculated as 3+ ions.

Sample	Grain	Si	Ti	Al	Fe*	Mn*	Mg	Ca	Na	K	Ba	Ni	Cr	Total cations	Oxygens
X1008	03_gl	7.96	0.00	1.89	1.01	0.00	2.21	0.08	1.89	0.00	0.00	0.00	0.00	15.04	23
	04_phe	6.81	0.00	4.33	0.19	0.00	0.75	0.00	0.13	1.76	0.00	0.00	0.00	13.97	22
	05_gl	7.89	0.00	1.92	0.98	0.00	2.28	0.22	1.74	0.00	0.00	0.00	0.00	15.02	23
	05_phe	7.91	0.00	1.75	1.08	0.00	2.38	0.23	1.74	0.00	0.00	0.00	0.00	15.09	23
	06_phe2	6.84	0.00	4.31	0.19	0.00	0.72	0.00	0.12	1.79	0.00	0.00	0.00	13.97	22
	opq_pa	5.99	0.00	5.94	0.14	0.00	0.00	0.00	1.88	0.05	0.00	0.00	0.00	14.00	22
	opq_pa2	5.97	0.00	5.98	0.12	0.00	0.00	0.00	1.84	0.11	0.00	0.00	0.00	14.02	22
VI1808	01_3_phe	7.38	0.00	3.14	0.35	0.00	1.23	0.00	0.00	1.91	0.00	0.00	0.00	14.00	22
	01_3_cpx	2.03	0.00	0.33	0.24	0.00	0.46	0.50	0.50	0.00	0.00	0.00	0.00	4.06	6
	01_4_phe	7.47	0.00	3.02	0.35	0.00	1.23	0.00	0.00	1.92	0.00	0.00	0.00	13.99	22
	01_4_cpx	2.03	0.00	0.26	0.25	0.00	0.53	0.58	0.39	0.00	0.00	0.00	0.00	4.04	6
	02_3_phe	7.45	0.00	3.04	0.31	0.00	1.27	0.00	0.00	1.95	0.00	0.00	0.00	14.01	22
	02_3_cpx	2.03	0.00	0.36	0.30	0.00	0.38	0.44	0.56	0.00	0.00	0.00	0.00	4.07	6
	02_4_phe	7.41	0.00	3.17	0.28	0.00	1.20	0.00	0.00	1.92	0.00	0.00	0.00	13.97	22
	02_4_cpx	6.00	0.00	5.81	0.27	0.00	0.00	3.88	0.00	0.00	0.00	0.00	0.00	15.96	25
	04_phe	7.39	0.00	3.12	0.35	0.00	1.23	0.00	0.00	1.93	0.00	0.00	0.00	14.02	22
	04_cpx	2.02	0.00	0.33	0.21	0.00	0.49	0.53	0.46	0.00	0.00	0.00	0.00	4.05	6
DR9	01_2_phe	6.81	0.04	4.24	0.23	0.00	0.77	0.00	0.10	1.79	0.00	0.00	0.00	13.97	22
	01_2_chl	2.84	0.00	2.42	1.50	0.00	3.19	0.00	0.00	0.00	0.00	0.00	0.00	9.95	14
	01_3_phe	6.82	0.03	4.24	0.21	0.00	0.79	0.00	0.10	1.79	0.00	0.00	0.00	13.97	22
	01_4_ab	2.98	0.00	1.03	0.01	0.00	0.00	0.00	0.98	0.00	0.00	0.00	0.00	5.00	8
	01_6_chl	2.82	0.00	2.41	2.24	0.02	2.48	0.00	0.00	0.00	0.00	0.00	0.00	9.97	14
	04_ab	2.98	0.00	1.03	0.00	0.00	0.00	0.00	0.98	0.00	0.00	0.00	0.00	4.99	8
	04_2_phe	6.91	0.03	4.05	0.21	0.00	0.87	0.00	0.11	1.83	0.00	0.00	0.00	14.00	22
	04_2_ep	5.97	0.00	4.86	1.17	0.07	0.00	3.91	0.00	0.00	0.00	0.00	0.00	15.98	25
	05_phe	6.63	0.00	4.63	0.23	0.00	0.58	0.00	0.24	1.72	0.00	0.00	0.00	14.03	22
	02_2_phe	7.03	0.03	3.86	0.22	0.00	0.90	0.00	0.08	1.86	0.00	0.00	0.00	13.98	22
	07_phe	6.69	0.03	4.51	0.19	0.00	0.64	0.00	0.19	1.75	0.00	0.00	0.00	14.00	22
	06_amph	7.77	0.00	0.56	0.84	0.00	3.94	1.63	0.42	0.00	0.00	0.00	0.00	15.16	23
	03_3_cpx	2.00	0.00	0.38	0.17	0.00	0.49	0.57	0.42	0.00	0.00	0.00	0.00	4.03	6
	03_im14_phe	6.98	0.03	3.93	0.21	0.00	0.92	0.00	0.09	1.86	0.00	0.00	0.00	14.01	22
HA2	01_cpx1	1.99	0.00	0.06	0.13	0.00	0.85	0.92	0.07	0.00	0.00	0.00	0.00	4.02	6
	01_cpx2	1.99	0.00	0.06	0.13	0.00	0.85	0.92	0.05	0.00	0.00	0.00	0.00	4.00	6
	01_4_amph	6.36	0.03	2.45	1.50	0.00	2.81	1.87	0.76	0.00	0.00	0.00	0.00	15.77	23
	03_cpx	1.98	0.00	0.08	0.16	0.00	0.84	0.89	0.07	0.00	0.00	0.00	0.00	4.02	6
DC48B	01_2_pa	6.00	0.00	6.00	0.05	0.00	0.00	0.00	1.88	0.05	0.00	0.00	0.00	13.97	22
	01_3_ep	5.95	0.00	4.96	1.09	0.07	0.00	3.91	0.00	0.00	0.00	0.00	0.00	15.98	25
	01_4_gl	7.96	0.00	1.88	0.97	0.00	2.27	0.05	1.94	0.00	0.00	0.00	0.00	15.07	23
	01_6_pa	6.05	0.00	5.92	0.03	0.00	0.07	0.00	1.86	0.00	0.00	0.00	0.00	13.92	22
	02_2_gl	7.97	0.00	1.91	0.97	0.00	2.22	0.05	1.92	0.00	0.00	0.00	0.00	15.03	23
	03_2_pa	6.02	0.00	5.99	0.04	0.00	0.00	0.00	1.88	0.00	0.00	0.00	0.00	13.93	22
	03_3_pa	6.00	0.00	6.02	0.00	0.00	0.00	0.02	1.90	0.00	0.00	0.00	0.00	13.94	22
	03_3_cpx	2.00	0.00	0.48	0.17	0.00	0.39	0.45	0.53	0.00	0.00	0.00	0.00	4.02	6
	03_4_pa	5.98	0.00	6.04	0.03	0.00	0.00	0.00	1.89	0.00	0.00	0.00	0.00	13.95	22
	07_pa	6.00	0.00	5.94	0.04	0.00	0.07	0.00	1.87	0.07	0.00	0.00	0.00	13.99	22
	07_ep	5.95	0.00	5.45	0.63	0.07	0.00	3.88	0.00	0.00	0.00	0.00	0.00	15.98	25
	04_4_cpx	2.00	0.00	0.47	0.21	0.00	0.37	0.45	0.53	0.00	0.00	0.00	0.00	4.03	6
San1	01_im31_ab	2.99	0.00	1.02	0.00	0.00	0.00	0.00	0.99	0.00	0.00	0.00	0.00	4.99	8
	01_im32_ep	5.90	0.00	4.44	1.68	0.14	0.00	3.82	0.00	0.00	0.00	0.00	0.00	15.97	25
	01_im32_chl	2.85	0.00	2.35	1.67	0.02	3.09	0.00	0.00	0.00	0.00	0.00	0.00	9.98	14
	02_im34_chl	2.84	0.00	2.40	1.71	0.02	2.99	0.00	0.00	0.00	0.00	0.00	0.00	9.96	14
	02_im36_chl	2.76	0.00	2.44	1.66	0.03	3.12	0.00	0.00	0.00	0.00	0.00	0.00	10.02	14
	04_im39_phe	6.62	0.04	4.40	0.47	0.00	0.62	0.00	0.17	1.83	0.00	0.00	0.00	14.14	22
	04_40_phe	6.67	0.03	4.23	0.60	0.00	0.60	0.00	0.08	1.90	0.00	0.00	0.03	14.15	22
	05_im41_phe	6.90	0.00	3.93	0.48	0.00	0.74	0.00	0.00	1.87	0.00	0.00	0.10	14.02	22
	05_im42_ab	2.99	0.00	1.03	0.00	0.00	0.00	0.00	0.98	0.00	0.00	0.00	0.00	4.99	8
	06_44_phe	6.74	0.03	4.21	0.47	0.00	0.63	0.00	0.11	1.83	0.00	0.00	0.04	14.07	22
	07_im45_phe	6.70	0.03	4.32	0.47	0.00	0.61	0.00	0.12	1.83	0.00	0.00	0.00	14.08	22
	08_im46_phe	6.82	0.00	4.09	0.39	0.00	0.80	0.00	0.00	1.88	0.00	0.00	0.06	14.05	22
	03_im38_chl	2.84	0.00	2.40	1.68	0.00	3.05	0.00	0.00	0.00	0.00	0.00	0.00	9.97	14
	02_im35_amph	7.71	0.00	0.74	1.74	0.00	3.03	1.32	0.75	0.00	0.00	0.00	0.00	15.29	23

Table 36: EDS major element data for Chapter 5. *Fe and Mn are calculated as 2+ ions, except for epidote where they are calculated as 3+ ions.

Sample	Grain	Si	Ti	Al	Fe*	Mn*	Mg	Ca	Na	K	Ba	Ni	Cr	Total cations	Oxygens
San2	01_2_ep														
	01_2_chl	2.82	0.00	2.45	2.14	0.00	2.55	0.00	0.00	0.00	0.00	0.00	0.00	9.96	14
	01_4_chl	2.81	0.00	2.46	2.11	0.04	2.54	0.00	0.00	0.00	0.00	0.00	0.00	9.96	14
	01_5_ep	6.00	0.00	4.21	1.87	0.00	0.00	3.88	0.00	0.00	0.00	0.00	0.00	15.96	25
	01_6_ab	2.99	0.00	1.02	0.00	0.00	0.00	0.00	0.98	0.01	0.00	0.00	0.00	5.00	8
	02_5_amph	7.95	0.00	0.11	1.48	0.03	3.51	1.92	0.00	0.00	0.00	0.00	0.00	15.00	23
	02_3_ab	2.98	0.00	1.03	0.00	0.00	0.00	0.00	0.98	0.00	0.00	0.00	0.00	4.99	8
	03_3_chl	2.83	0.00	2.41	2.14	0.03	2.55	0.00	0.00	0.00	0.00	0.00	0.00	9.96	14
	04_2_amph	7.99	0.00	0.00	1.58	0.00	3.53	1.92	0.00	0.00	0.00	0.00	0.00	15.01	23
C13	01_3_law	2.02	0.00	1.96	0.04	0.00	0.00	0.98	0.00	0.00	0.00	0.00	0.00	5.00	8
	01_4_phe	7.03	0.00	3.78	0.43	0.00	0.89	0.00	0.00	1.93	0.00	0.00	0.00	14.05	22
	02_3_phe	7.00	0.00	3.90	0.35	0.00	0.85	0.00	0.00	1.93	0.00	0.00	0.00	14.02	22
	02_2_ep	6.02	0.00	4.43	1.61	0.00	0.00	3.89	0.00	0.00	0.00	0.00	0.00	15.96	25
	03_2_phe	7.03	0.00	3.84	0.36	0.00	0.84	0.00	0.00	1.96	0.00	0.00	0.00	14.03	22
	03_2_chl	2.86	0.00	2.35	1.94	0.04	2.78	0.00	0.00	0.00	0.00	0.00	0.00	9.96	14
	03_4_chl	2.83	0.00	2.38	1.94	0.02	2.81	0.00	0.00	0.00	0.00	0.00	0.00	9.98	14
	04_2_chl	2.88	0.00	2.27	1.92	0.03	2.90	0.00	0.00	0.00	0.00	0.00	0.00	9.99	14
	04_3_cpx_real														
122	04_2_ab														
	01_2_amph	7.29	0.14	0.51	1.11	0.00	3.26	2.99	0.00	0.00	0.00	0.00	0.00	15.31	23
	01_3_amph	7.25	0.15	0.64	1.09	0.00	3.06	2.97	0.25	0.00	0.00	0.00	0.00	15.40	23
	01_3_chl	2.87	0.00	2.36	1.79	0.04	2.88	0.00	0.00	0.00	0.00	0.00	0.00	9.95	14
	01_4_amph	7.57	0.11	0.76	1.64	0.00	2.01	2.05	1.61	0.00	0.00	0.00	0.00	15.75	23
	01_4_chl	2.93	0.00	2.30	1.80	0.03	2.84	0.00	0.00	0.00	0.00	0.00	0.00	9.91	14
	02_im22_amph	7.12	0.20	0.75	1.06	0.00	3.09	3.09	0.00	0.00	0.00	0.00	0.00	15.31	23
	02_im22_law	2.02	0.00	1.92	0.08	0.00	0.00	0.99	0.00	0.00	0.00	0.00	0.00	5.02	8
	02_im23_ab	2.98	0.00	1.03	0.00	0.00	0.00	0.00	0.99	0.00	0.00	0.00	0.00	5.00	8
	03_im24_amph	7.25	0.13	0.55	1.16	0.04	3.23	2.99	0.00	0.00	0.00	0.00	0.00	15.35	23
X1348	01_im4_amph	7.96	0.00	1.83	1.10	0.00	2.19	0.08	1.94	0.00	0.00	0.00	0.00	15.10	23
	01_im4_ep	5.95	0.00	4.95	1.19	0.00	0.00	3.89	0.00	0.00	0.00	0.00	0.00	15.98	25
	01_im5_ab	2.99	0.00	1.01	0.00	0.00	0.00	0.00	0.99	0.00	0.00	0.00	0.00	5.00	8
	01_im7_phe	6.76	0.00	4.34	0.36	0.00	0.61	0.00	0.15	1.85	0.00	0.00	0.00	14.07	22
	03_im15_pa	6.04	0.00	5.90	0.10	0.00	0.00	0.00	1.73	0.19	0.00	0.00	0.00	13.96	22

Table 37: EDS major element data for Chapter 5. *Fe and Mn are calculated as 2+ ions, except for epidote where they are calculated as 3+ ions.

Sample	Grain	Li (μg/g)	B	N	F	Cl	Rb	Sr	Cs	Na_2O (wt%)	MgO	Al_2O_3	K_2O
HA1	01_phe1	11	4.2	31	701	66	132	286	1.1	0.9	3.0	26	9.8
	01_cpx1	45	0.1	4.5	43	5.6	-0.3	22	0.1	7.5	6.8	10	0.0
	01_phe2	9.2	0.9	8.6	609	63	128	315	0.7	1.0	2.7	26	9.7
	02_phe1	8.3	1.7	28	574	64	126	280	0.9	0.8	2.7	25	9.6
	02_cpx1	38	0.2	4.8	33	22	0.0	34	0.1	7.0	6.7	10	0.0
	04_phe1	9.3	2.3	26	525	102	127	318	0.7	1.0	2.7	27	9.9
	04_cpx1	38	0.1	4.6	39.1	12	-0.5	42	0.1	6.7	7.2	9.8	0.0
	04_phe2	9.6	2.3	45	627	86	127	319	1.8	0.9	2.8	26	9.7
	04_cpx2	37	0.2	4.5	38	9.9	-0.4	40	0.5	7.1	7.0	10	0.0
	03_phe1	11	3.0	36	674	46	131	312	0.8	1.0	2.9	26	9.6
	03_cpx1	46	0.1	6.2	30	17	-0.3	20	0.1	7.4	6.7	9.8	0.0
	03_phe2	10	2.0	20	656	70	126	329	0.7	0.9	2.9	26	9.8
	03_cpx2	48	0.1	4.9	45	8.1	-0.5	26	0.1	7.4	6.8	10	0.0
DR10	01_2_chl1	82	1.3	1.9	2627	14	2.3	0.9	0.1	0.0	25	2.1	0.0
	01_2_amph1	1.7	2.5	3.5	3569	12	0.1	23	0.0	1.7	2.0	3.2	0.1
	01_4_phe1	37	49	418	1123	19	279	65	8.9	0.6	3.8	24	9.2
	01_4_phe2	44	38	250	1049	5.8	260	59	6.2	0.5	3.2	23	8.8
	01_5_chl1	76	0.7	1.4	2411	7.6	2.6	0.6	0.1	0.0	24	2.2	0.0
	02_2_phe1	34	51	269	1109	7.5	268	96	7.2	0.6	3.1	25	9.3
	02_2_amph1	0.9	3.5	6.4	3615	70	-0.2	18	0.2	1.1	2.1	1.8	0.1
	02_3_chl	79	2.3	4.6	2671	33	3.2	3.0	0.2	0.0	25	2.1	0.0
	02_4_phe	24	77	973	1022	3.1	272	51	12	0.4	3.6	23	8.8
	02_5_phe1	37	43	553	1055	3.8	298	33	10	0.4	3.5	23	9.1
	02_5_phe2	47	39	286	1028	29	271	56	6.6	0.5	3.3	23	8.9
	03_2_amph	1.7	4.4	6.6	2610	191	0.1	14	0.2	2.1	1.9	5.0	0.1
	03_3_phe	25	72	1034	1107	4.9	270	48	13	0.4	3.5	23	8.5
	03_4_chl	86	1.9	3.9	2475	34	2.5	3.8	0.2	0.0	24	2.2	0.0
	03_4_phe	40	40	260	999	7.0	264	66	7.2	0.5	3.1	23	8.9
	05_2_amph	1.6	4.2	5.9	3814	30	0.0	16	0.1	2.7	1.8	4.9	0.1
	05_2_chl	74	2.3	3.2	2268	16	3.6	3.7	0.2	0.0	25	2.2	0.0
	05_4_phe1	31	47	298	988	10	258	88	7.2	0.6	3.2	25	9.1
	05_4_phe2	27	55	490	946	11	245	50	8.1	0.6	3.0	23	8.6
275	01_2_amph	60	5.2	6.3	1795	42	1.3	12	0.1	4.7	1.3	10	0.1
	01_3_phe	89	13	197	710	18	432	211	16	0.9	3.4	26	9.9
	01_3_amph	40	5.0	5.3	2104	21	1.1	11	0.1	4.6	1.4	11	0.1
	01_4_phe	96	14	211	697	17	432	193	16	0.8	3.3	25	9.9
	01_4_ep	1.5	1.3	5.0	79	163	1.1	2904	0.5	0.1	0.4	27	0.0
	01_4_phe2	77	13	195	787	15	412	203	15	0.9	3.4	25	9.8
	02_3_pa	41	52	13	244	1.8	7.6	1291	0.4	6.9	0.2	38	0.8
	02_3_phe	60	35	212	628	37	407	79	12	0.6	2.8	26	10
	02_3_amph	13	2.0	1.8	2496	36	1.7	11	0.0	3.1	1.7	8.3	0.2
	02_4_phe	83	15	203	703	8.9	421	226	16	0.9	3.3	25	9.7
	02_4_pa	33	63	48	206	8.0	29.7	774	2.5	6.7	0.7	37	1.1
	03_2_cpx	108	0.4	2.9	32	6.4	0.1	46	0.1	6.0	7.6	11	0.0
	03_3_phe1	80	16	211	721	11	393	136	15	0.9	3.3	25	9.8
	03_3_phe2	88	17	201	677	12	416	186	16	0.8	3.2	25	9.7
	04_phe	76	13	183	698	11	398	223	15	0.9	3.3	25	9.8
	04_2_cpx	92	0.5	3.6	41	11	0.2	34	0.1	5.9	7.7	11	0.0
	04_phe2	86	12	176	740	7.6	427	210	16	0.8	3.4	25	9.8
DC46B	05_pa1	26	3.2	9.2	125	3.5	0.4	275	0.0	7.3	0.2	37	0.2
	05_pa2	30	4.9	89	113	36	1.4	260	0.5	7.3	0.2	38	0.1
	05_chl2	17	3.4	4.7	519	41	0.8	0.4	0.5	0.0	29	2.3	0.0
	05_2_pa	22	2.7	7.4	113	0.6	0.3	264	0.0	7.5	0.1	38	0.1
	05_2_chl	18	2.0	1.2	566	40	-0.1	0.2	0.1	0.0	28	2.2	0.0
	03_amph	88	0.4	2.7	331	2.0	0.5	0.2	0.1	6.8	1.3	10	0.0
	01_2_amph	84	0.4	3.2	383	1.6	0.6	0.4	0.0	6.3	1.3	10	0.0
	01_2_ctd	0.0	0.0	0.4	4.5	2.9	1.5	0.1	0.0	0.0	6.2	44	0.0
	01_3_amph	74	1.1	2.8	425	3.8	0.4	0.3	0.0	6.2	1.3	10	0.0
	01_3_ctd	0.0	0.0	0.3	3.0	1.1	0.7	0.1	0.0	0.0	6.7	44	0.0
	01_4_pa	46	11	19	89	1.2	0.6	364	0.2	7.1	0.1	37	0.2
	01_4_chl	12	0.3	1.1	538	15	0.6	0.1	0.2	0.0	28	2.3	0.0
	04_2_pa	44	2.3	9.0	95	0.6	0.3	370	0.1	7.4	0.1	38	0.1
	04_2_amph	85	0.8	8.6	375	11	0.0	0.4	0.0	6.8	1.4	11	0.0
	04_3_pa	65	69	34	80	9.7	1.8	653	0.2	7.1	0.3	38	0.3
	04_3_chl	17	2.6	2.1	545	23	0.9	0.3	0.2	0.0	30	2.3	0.0
	06_ab	0.0	2.6	1.3	1.5	2.3	0.0	232	0.1	10	0.0	16	0.0
	06_2_ab	0.0	2.2	1.4	2.1	2.7	0.1	253	0.1	8.1	0.0	16	0.0
DC46A	02_im26_amph	70	2.7	3.7	222	0.5	1.3	0.2	0.0	6.6	1.2	8.7	0.0
	02_im26_ep	0.2	0.6	2.8	14	39	-0.1	1241	0.0	0.0	0.1	27	0.0
	02_im26_pa1	11	225	46	98	19	15	140	0.7	6.4	0.4	35	1.5
	02_im26_pa2	19	160	13	81	2.3	2.5	163	0.1	7.2	0.2	37	0.6
	01_im21_amph	74	3.8	2.6	212	3.6	1.6	0.3	0.0	6.6	1.2	8.2	0.0
	01_im21_ep	0.2	0.2	1.0	14	13	0.0	1182	0.0	0.0	0.0	28	0.0
	03_im30_pa	19	152	11	104	2.5	2.2	133	0.1	7.1	0.3	37	0.5
	03_im30_chl	41	2.4	14	259	48	1.4	0.5	0.1	0.0	27	2.4	0.0
	03_im31_pa	28	115	16	84	0.0	0.8	158	0.0	7.2	0.1	37	0.4
	03_im31_chl	43	1.9	8.5	264	30	2.2	0.5	0.1	0.0	27	2.5	0.0
	03_chl	39	1.7	1.7	279	12	1.5	0.5	0.1	0.0	27	2.4	0.0

Table 38: SIMS trace element data for Chapter 5.

Sample	Grain	Li	B	N	F	Cl	Rb	Sr	Cs	Na_2O	MgO	Al_2O_3	K_2O
ZS15	02_2_pa	1.7	21	36	94	13	1.5	692	0.2	7.0	0.1	37	0.6
	02_2_ep	0.2	0.0	2.9	34	22	-0.7	2015	0.0	0.0	0.1	28	0.0
	02_3_cpx	31	1.6	13	23	49	-0.2	12	0.0	7.6	6.2	11	0.0
	02_4_pa	15	22	43	103	40	1.7	354	0.5	7.2	0.6	37	0.2
	02_5_pa	16	39	31	91	21	2.5	319	0.5	7.2	0.1	37	0.4
	01_2_cpx	38	1.3	11	39	57	-0.2	17	0.1	7.1	6.2	11	0.0
	01_3_amph	5.3	0.7	3.4	612	6.7	0.6	0.2	0.0	6.9	1.2	10	0.0
	01_3_ep	5.6	0.5	3.4	33	23	-0.3	2267	0.0	0.8	1.0	24	0.0
	03_2_pa	1.8	48	15	85	4.8	0.7	558.2	0.2	7.1	0.1	37.3	0.4
	03_3_cpx	36	1.7	6.5	21	13	-0.2	16	0.1	7.9	5.7	12	0.0
	03_3_ep	0.1	0.1	3.8	40	29	-0.1	3600	0.1	0.0	0.1	28	0.0
	03_4_pa	5.0	37	60	65	20	5.9	1333	0.2	6.8	0.1	37	0.9
	03_5_pa	3.8	27	14	73	9.3	0.4	311	0.1	7.3	0.1	38	0.2
	04_2_cpx	29	1.6	7.2	905	37	-0.1	49	0.2	7.1	5.4	11	0.0
	04_3_pa	41	1.1	20	29	89	0.8	8.6	0.1	7.1	6.6	11	0.0
X1008	03_gl	49	4.2	3.5	187	1.6	0.2	0.3	0.0	6.4	1.2	11	0.0
	04_phe	6.4	81	574	209	2.1	353	16	30	0.6	3.1	25	10
	04_2_phe1	8.2	79	555	230	4.6	353	10	32	0.5	3.2	25	10
	04_2_ep	0.2	0.3	14	15	52	-0.1	1646	0.1	0.0	0.1	26	0.0
	04_2_gl	69	3.6	8.0	163	15	1.1	0.3	0.0	6.5	1.2	11	0.0
	05_gl	59	4.8	2.6	191	4.9	1.2	0.5	0.0	6.2	1.2	10	0.0
	05_phe	62	3.9	3.0	163	2.2	1.3	0.2	0.1	6.4	1.2	11	0.0
	06_phe2	6.7	84	572	214	8.1	345	12	29	0.5	3.2	24	10
	06_2_phe	8.4	81	564	207	4.3	339	16	32	0.6	3.2	24	9.8
	opq_pa	12	82	19	27	8.6	2.4	176	0.1	7.3	0.1	37	0.4
	opq_pa2	12	96	27	27	6.5	3.1	389	0.1	7.1	0.1	37	0.6
VI1808	01_3_phe	0.2	7.8	34	588	2.9	27	7.2	0.7	0.1	5.4	18	12
	01_3_cpx	4.1	0.4	3.3	9.6	9.1	0.1	84	0.0	6.9	8.1	7.9	0.0
	01_4_phe	0.2	50	116	500	22	42	2.1	2.3	0.0	5.4	17	12
	01_4_cpx	4.2	0.5	3.7	7.7	18	0.8	76	0.0	7.2	7.7	8.0	0.0
	02_3_phe	0.2	29	101	535	9.6	42	3.2	1.8	0.0	5.6	18	12
	02_3_cpx	4.3	0.1	5.0	10	21	0.5	138	0.2	6.7	8.4	8.2	0.0
	02_4_phe	0.2	7.7	32	597	4.4	27	8.8	0.6	0.1	5.5	18	12
	02_4_cpx	0.4	2.8	5.9	71.7	36	-0.2	6416	0.1	0.2	0.0	31	0.0
	04_phe	0.3	57	144	551	20	60	3.3	3.1	0.0	5.4	17	11
	04_cpx	4.3	0.3	3.0	7.7	22	0.8	56	0.1	7.9	6.8	8.5	0.0
DR9	01_2_phe	33	90	271	277	9.6	223	22	6.9	0.3	3.8	21	10
	01_2_amph	7.4	2.9	2.7	876	18	0.7	2.1	0.1	2.3	1.7	5.7	0.1
	01_2_chl	2.8	1.5	2.6	638	8.8	0.0	1.5	0.1	1.3	8.2	2.9	0.1
	01_3_amph	7.9	6.6	19	820	78	4.2	6.2	1.1	2.0	1.7	5.7	0.2
	01_3_phe	37	77	307	214	16	231	15	6.8	0.5	3.5	23	10
	01_4_ab	0.0	0.3	2.1	7.9	9.6	0.1	3.9	0.0	11	0.0	16	0.0
	01_6_chl	111	1.6	5.0	168	57	4.2	8.8	1.6	0.0	21	2.4	0.0
	04_ab	0.1	0.7	0.9	3.3	19	0.2	4.8	0.0	11	0.0	16	0.0
	04_2_phe	20	137	347	274	21	240	9.3	7.2	0.2	4.1	21	11
	04_2_ep	0.3	0.2	0.7	46	10	-0.5	598	0.1	0.0	0.1	29	0.0
	05_phe	40	18	244	240	3.8	205	30	2.5	0.9	2.5	27	9.8
	05_2_phe	44	14	248	321	4.0	222	24	1.6	0.8	2.7	26	10
	02_2_phe	29	94	269	346	4.5	244	32	6.4	0.3	4.0	23	11
	05_2_cpx	79	3.6	11	22	102	0.6	20	0.4	6.1	7.4	9.2	0.0
	07_phe	36	13	267	267	4.3	229	16	2.6	0.8	2.8	26	10
	06_amph	3.1	5.0	3.8	2021	19	1.6	8.5	0.1	1.4	2.0	3.2	0.1
	03_3_cpx	52	2.4	1.9	12.5	3.6	0.1	21	0.0	5.2	8.5	8.2	0.0
	03_3_cpx2	54	2.6	2.2	11.8	10	0.1	23	0.0	5.4	8.1	8.5	0.0
	03_im14_phe	26	100	296	370	34	223	21	6.0	0.3	3.9	22	10
HA2	01_cpx1	3.4	3.6	2.0	6.8	17	-0.7	231	0.0	0.9	1.9	1.8	0.0
	01_cpx2	3.2	3.9	1.3	8.3	7.4	-1.2	218	0.0	0.9	1.9	1.5	0.0
	01_4_amph	6.0	17	4.4	64	802	2.6	14.0	0.0	2.4	1.6	15	0.1
	03_cpx	5.5	3.9	1.6	6.9	12.0	-1.0	259	0.0	0.9	1.9	2.1	0.0
	02_im14_chl	41	4.1	6.1	75	69	1.4	0.6	0.3	0.0	27	2.6	0.0
	02_cpx_bigmatrix	2.9	4.4	1.8	7.7	6.6	-0.5	249	0.0	0.9	1.9	1.7	0.0

Table 39: SIMS trace element data for Chapter 5.

Sample	Grain	Li	B	N	F	Cl	Rb	Sr	Cs	Na_2O	MgO	Al_2O_3	K_2O
DC48B	01_2_pa	17	18	31	71	9.8	3.5	137	0.4	7.5	0.7	38	0.3
	01_3_ep	0.1	0.7	3.0	16	12	0.0	1453	0.1	0.0	0.0	29	0.0
	01_4_gl	11	1.4	2.8	230	4.8	0.5	0.2	0.0	7.1	1.2	11	0.0
	01_6_pa	11	19	47	42	18	2.1	147	0.7	7.8	0.2	38	0.2
	02_2_gl	10	3.1	2.3	284	1.0	0.5	0.3	0.0	7.2	1.3	11	0.0
	03_2_pa	18	14	61	70	16	2.8	158	0.7	7.7	0.2	38	0.2
	03_3_pa	11	3.0	8.2	45	1.2	0.3	154	0.0	7.9	0.1	39	0.0
	03_3_cpx	18	1.1	8.0	25	22	0.1	24	0.4	7.3	6.6	11	0.0
	03_4_pa	20	4.0	7.2	45	0.6	0.4	166	0.0	7.9	0.1	39	0.1
	03_4_ab	0.0	0.1	2.4	4.5	12	0.0	4.7	0.0	1.4	0.0	16	0.0
	07_pa	13	12	30	42	2.8	4.2	116	0.3	7.6	0.6	37	0.4
	07_ep	1.7	0.3	1.4	20	9.8	0.2	550	0.1	0.6	0.6	28	0.0
	04_4_cpx	14	2.1	5.1	41	31	0.4	25	0.2	7.0	6.5	10	0.0
San1	01_im31_ab	0.0	0.1	0.1	0.8	1.1	0.1	3.4	0.0	11	0.0	15	0.0
	01_im32_ep	0.1	1.5	0.5	7.0	16	0.4	666	0.0	0.0	0.0	25	0.0
	01_im32_chl	95	1.3	4.4	248	12	1.6	0.4	0.2	0.0	23	2.6	0.0
	02_im34_chl	87	3.5	9.4	239	41	0.9	1.2	0.4	0.0	22	2.6	0.0
	02_im34_amph	4.8	4.3	11	472	31	0.3	1.3	0.1	2.7	14	5.0	0.1
	02_im36_chl	93	4.6	8.3	236	43	1.8	1.3	0.7	0.0	22	2.5	0.0
	04_im39_phe	33	53	12	148	9.0	226	2.7	5.6	0.5	2.8	24	11
	04_40_phe	31	48	6.8	152	1.1	227	2.9	2.9	0.5	2.8	24	11
	05_im41_phe	27	67	9.1	150	4.0	239	1.2	7.7	0.3	3.3	23	11
	05_im42_ab	0.0	0.2	0.2	0.7	1.6	0.0	4.7	0.0	11	0.0	16	0.0
	06_44_phe	34	48	18	153	9.0	228	2.4	4.9	0.4	3.0	24	11
	07_im45_phe	31	52	21	162	11	240	3.1	4.2	0.5	3.0	24	11
	08_im46_phe	33	57	12	174	9.7	229	1.9	5.8	0.3	4.0	24	11
	03_im38_chl	99	0.6	0.6	230	1.4	1.9	0.2	0.3	0.0	23	2.7	0.0
	02_im35_amph	2.9	3.5	2.1	509	6.6	0.3	16	0.0	2.8	13	5.5	0.1
	02_im34_amph_extra	2.1	3.2	14	422	50	-0.7	1.1	0.1	2.0	14	3.0	0.1
	02_im36_amph	3.0	1.5	91	162	117	0.0	1.6	0.0	7.1	6.0	10	0.1
San2	01_2_ep	0.1	2.8	1.6	10	23	-0.7	598	0.0	0.0	0.0	27	0.0
	01_2_chl	102	1.6	1.2	131	17	1.3	0.4	0.1	0.0	20	2.7	0.0
	01_4_chl	98	0.9	2.0	127	34	1.6	0.4	0.1	0.0	19	2.5	0.0
	01_5_ep	0.2	2.2	0.4	13	12	-1.0	584	0.0	0.0	0.2	27	0.0
	01_6_ab	0.0	0.6	3.4	1.5	1.9	0.1	1.5	0.0	11	0.0	16	0.0
	02_5_amph	3.8	2.1	4.8	188	21	-0.8	1.3	0.1	0.3	16	1.2	0.0
	02_4_amph	13	3.6	1.4	199	47	-0.2	1.2	0.1	0.2	16	3.5	0.0
	02_4_chl	43	2.5	0.6	122	7.9	0.7	4.2	0.1	0.1	12	9.9	0.0
	02_3_ab	0.0	0.3	0.3	1.0	0.0	0.0	0.5	0.0	11	0.0	15	0.0
	03_3_chl	101	1.8	2.6	127	7.2	0.9	7.3	0.3	0.0	19	2.7	0.0
	03_3_chl	86	1.7	1.1	119	14	0.0	0.4	0.2	0.1	19	2.7	0.0
	01_5_chl	9.5	7.6	31	225	439	0.0	1.4	0.2	0.3	17	1.8	0.1
	02_5_amph2	2.5	8.2	84	192	465	0.3	4.4	0.1	0.9	14	1.3	0.1
	04_2_amph	5.6	4.8	9.7	162	101	0.8	82	0.1	0.5	14	5.7	0.1
C13	01_3_law	0.2	3.5	0.4	168	1115	-0.2	306	0.1	0.1	0.0	29.28	0.0
	01_4_phe	3.2	96	88	262	55	247	1.7	6.4	0.1	3.7	21.35	12
	02_3_phe	2.5	100	65	270	33	247	1.2	5.1	0.1	3.6	22.28	12
	02_2_ep	0.2	1.8	0.7	19	16	0.1	4339	0.0	0.0	0.0	26.78	0.0
	03_2_phe	2.8	105	74	260	24	245	1.2	6.1	0.3	3.8	20.89	11
	03_2_chl	34	3.3	36	281	149	2.3	2.8	0.3	0.0	18.88	2.2	0.1
	03_4_chl	34	0.4	1.1	352	117	0.5	6.1	0.1	0.0	19.62	2.5	0.0
	04_2_chl	25	1.6	2.3	316	52	2.0	1.3	0.1	0.0	20.96	2.6	0.0
	04_3_cpx_real	20	3.7	1.8	5.2	104	-0.4	7.8	0.0	7.6	6.4	9.2	0.0
122	04_2_ab	40	4.4	0.7	17	7.2	0.1	8.8	0.0	10	2.7	14	0.0
	01_2_amph	4.1	0.6	0.5	40	14	-2.5	14	0.0	0.4	16	3.3	0.0
	01_3_amph	18	12	2.4	52	37	-0.3	7.3	0.1	7.1	9.4	6.1	0.0
	01_3_chl	145	1.7	11	86	32	0.9	0.6	0.2	0.0	21	2.5	0.0
	01_4_amph	14	5.9	4.9	44	55	-0.2	12	0.3	2.6	14	5.2	0.0
	01_4_chl	139	1.9	9.8	132	17	0.0	7.4	0.2	0.2	19	19	0.0
	02_im22_amph	13	3.2	2.7	133	24	-0.2	13	0.1	1.6	15	4.7	0.0
	02_im22_law	0.1	1.3	2.0	41	14	-0.1	191	0.1	0.1	0.0	28	0.0
	02_im22_chl	128	5.8	9.5	145	16	8.6	6.1	0.6	0.0	19	18	0.3
	02_im23_ab	0.0	0.0	1.1	0.8	0.0	0.0	1.1	0.0	11	0.0	15	0.0
	03_im24_ab	0.0	0.2	2.2	6.9	7.8	-0.1	75	0.1	9.6	0.0	19	0.0
	03_im24_amph	6.2	0.6	0.8	37	12	-0.3	14	0.0	1.0	15	4.3	0.0
X1348	01_im4_amph	28	3.7	2.0	147	5.4	-0.2	0.1	0.1	7.2	9.8	9.6	0.0
	01_im4_ep	0.2	0.1	0.8	15	11	-1.1	547	0.0	0.0	0.1	27	0.0
	01_im5_amph	23	1.6	2.5	165	4.2	0.8	0.1	0.0	7.3	9.3	9.5	0.0
	01_im5_ab	0.1	1.1	6.3	1.1	26	0.3	0.7	0.0	11	0.0	15	0.0
	01_im7_phe	4.7	72	39	178	1.1	200	2.8	11	0.6	2.7	24	11
	03_im15_pa	5.8	86	2.2	65	0.6	5.8	96	0.1	7.5	0.1	37	0.8
	03_im15_pa2	5.6	77	3.5	66	2.6	2.5	123	0.1	7.4	0.2	36	0.7
	03_im15_amph2	24	1.8	5.4	217	24	0.1	0.1	0.1	7.2	9.8	9.6	0.0
	01_im3_phe	10	137	1774	128	1440	202	1.5	12	0.4	3.0	24	12

Table 40: SIMS trace element data for Chapter 5.

Standard	Li (μg/g)	B	N	F	Cl	Rb	Sr	Cs	Na_2O (wt%)	MgO	Al_2O_3	K_2O
phe80-3	41	34	81	658	3.5	413	393	12	0.5	3.6	26	10
phe80-3	54	38	89	683	11	420	419	13	0.5	3.8	26	10
phe80-3	41	36	108	658	12	428	375	13	0.5	3.8	26	10
phe80-3	42	36	94	627	19	420	341	12	0.6	3.6	27	10
phe80-3	40	37	81	618	14	424	359	13	0.6	3.5	26	10
phe80-3	40	34	97	679	13	433	350	13	0.5	3.9	26	10
phe80-3	41	35	78	642	12	420	343	13	0.5	3.7	26	9.7
phe80-3	46	37	91	655	11	411	412	12	0.5	3.7	26	9.9
phe80-3	45	35	92	634	5.0	428	392	14	0.5	3.8	26	10
phe80-3	43	36	72	632	14	433	409	14	0.6	3.7	27	10
phe80-3	45	36	85	656	8.1	435	378	13	0.5	3.8	26	10
phe80-3	44	37	84	648	7.5	427	422	13	0.6	3.7	26	10
phe80-3	35	34	80	600	7.8	418	374	13	0.4	3.5	24	9.7
phe80-3	41	35	91	662	8.2	439	385	13	0.4	3.8	26	10
phe80-3	41	35	100	649	6.6	437	384	14	0.5	3.7	26	10
phe80-3	41	34	85	632	8.1	441	380	13	0.5	3.8	26	10
phe80-3	47	36	70	640	17	437	374	13	0.6	3.7	27	10
phe80-3	55	56	99	640	10	452	455	10	0.7	3.8	27	10
phe80-3	54	58	93	614	10	435	476	10	0.7	3.7	27	10
phe80-3	45	34	90	644	10	429	381	13	0.5	3.7	26	10
phe80-3	40	36	43	593	17	435	349	12	0.6	3.4	27	10
phe80-3	48	35	65	660	14	429	400	12	0.6	3.7	27	10
Average	44	38	85	642	11	429	389	13	0.5	3.7	26	10
rsd%	12%	17%	16%	3.5%	36%	2.3%	8.8%	7.7%	13%	3.2%	2.1%	1.8%
LMMN#1	1680	67	174	6237	9.2	876	4.3	15	0.6	0.7	33	11
LMMN#1	1335	73	184	6539	2.0	1092	2.5	21	0.6	0.7	33	11
LMMN#1	1339	45	185	6103	8.0	825	4.3	13	0.7	0.6	34	11
LMMN#1	1466	46	188	6343	5.3	794	4.5	15	0.7	0.6	33	10
LMMN#1	1686	57	201	6750	10	862	3.7	14	0.5	0.7	32	11
LMMN#1	1645	69	209	6518	12	1133	2.6	29	0.5	0.7	32	11
LMMN#1	1450	75	217	6184	7.2	1219	2.0	34	0.6	0.7	32	10
LMMN#1	1883	77	195	6239	24	973	3.2	28	0.5	0.8	32	11
LMMN#1	1799	86	198	6148	24	1127	2.2	31	0.5	0.8	32	11
LMMN#1	1600	65	213	5884	40	866	3.6	17	0.6	0.7	32	11
LMMN#1	1853	80	240	6203	24	922	3.5	25	0.4	0.8	32	11
LMMN#1	1376	72	248	6042	42	1169	2.0	22	0.6	0.7	33	11
Average	1593	68	204	6266	17	988	3.2	22	0.6	0.7	32	11
rsd%	12%	19%	11%	3.8%	77%	15%	29%	33%	15%	9.1%	2.0%	1.3%
LMMN#2	1530	42	148	6078	0.0	866	4.5	20	0.7	0.7	33	11
LMMN#2	1268	46	154	5800	1.6	831	4.3	12	0.6	0.6	33	11
LMMN#2	1626	51	154	5884	1.6	862	3.9	16	0.5	0.7	32	11
LMMN#2	1706	67	163	6387	1.1	1114	2.6	23	0.5	0.8	32	11
LMMN#2	1717	65	157	6288	0.5	1009	3.3	20	0.5	0.8	32	11
LMMN#2	1889	62	152	6350	0.5	1095	2.7	22	0.4	0.8	31	11
Average	1622	55	155	6131	0.9	963	3.5	19	0.5	0.7	32	11
rsd%	13%	19%	3.3%	4.1%	73%	13%	23%	21%	18%	10%	2.0%	0.6%

Table 41: SIMS trace element standards for Chapter 5.

Sample	Analysis	δ^{11}B (‰)	1sd (‰)	B (μg/g)	Sample	Analysis	δ^{11}B (‰)	1sd (‰)	B (μg/g)
DR10	03_3_phe	-5.6	0.4	53.7	DR9	03_im14_phe	-5.4	0.4	74.2
DR10	03_4_phe	-3.9	0.5	36.1	DR9	01_03_3_cpx	-12.7	1.7	1.7
DR10	02_4_phe	-5.5	0.4	65.1	DR9	03_3_cpx2	-13.0	1.4	2.2
DR10	02_5_phe	4.6	0.8	65.9	DR9	06_amph	-9.9	1.2	3.5
DR10	02_2_phe1	-3.1	0.5	41.1	DR9	02_05_phe	-10.7	0.4	17.5
DR10	01_4_phe1	-4.7	0.3	60.3	DR9	05_2_phe	-12.3	0.5	12.1
DR10	03_2_amph	-8.3	1.0	4.3	DR9	01_6_chl	0.9	1.5	3.4
DR10	03_4_chl	-1.2	2.2	2.0	DR9	01_2_phe	-7.9	0.3	46.6
DR10	02_2_amph1	-3.3	1.0	2.7	DR9	01_2_chl	-5.0	1.2	1.6
DR10	02_3_chl	1.8	1.5	2.6	DR9	01_3_amph	-5.9	0.8	6.3
DR10	01_2_amph1	-4.7	1.0	2.7	DR9	01_3_phe	-6.9	0.3	52.5
					DR9	04_2_phe	-7.1	0.3	65.9
DC46B	04_2_pa	5.7	1.2	3.8	275	02_3_pa	-7.1	0.3	54.8
DC46B	04_3_pa	3.1	0.3	61.5	275	02_3_phe	-6.2	1.0	35.4
DC46B	05_pa2	8.4	1.1	4.0	275	02_3_amph	-5.2	1.9	1.0
DC46B	05_pa1	4.5	1.2	3.3	275	01_3_phe	-6.0	0.5	11.8
DC46B	05_chl2	2.6	3.0	1.1	275	01_3_amph	-6.8	1.0	4.7
DC46B	04_2_amph	-6.5	2.5	0.4	275	04_phe	-8.0	0.6	12.7
DC46B	01_4_pa	-9.7	1.0	16.9	275	04_2_cpx	-10.8	2.5	0.8
DC46B	01_4_chl	-14.6	6.1	0.2	275	04_phe2	-6.1	0.6	10.7
DC46B	01_2_amph	3.5	3.2	0.3	275	02_4_phe	-4.4	0.5	13.7
DC46B	01_3_amph	-2.6	1.8	1.1	275	02_4_pa	-4.0	0.3	43.2
DC46B	05_2_pa	9.3	1.2	2.3	275	01_2_amph	-7.9	1.0	6.6
DC46A	02_im26_pa2	-3.1	0.2	140.5	122	01_3_amph	5.8	0.6	11.3
DC46A	03_im30_pa	-2.4	0.2	181.5	122	01_2_amph	2.5	2.1	1.2
DC46A	03_im31_pa	-2.1	0.3	146.2	122	01_4_amph	-1.3	0.9	7.3
DC46A	01_im21_amph	1.8	1.0	2.9	122	01_4_chl	3.3	1.1	6.0
DC46A	03_im30_chl	0.6	2.1	2.1	122	01_3_chl	-3.6	1.6	4.9
DC46A	03_im31_chl	3.8	2.6	1.0	122	02_im22_amph	3.6	1.3	4.7
DC46A	02_im26_amph2	-2.9	1.1	2.8	122	02_im22_chl	1.3	2.6	1.0
ZS15	01_3_amph	6.7	2.1	1.1	San1	04_im39_phe	-6.5	0.3	46.1
ZS15	01_2_cpx	2.2	2.3	0.7	San1	04_40_phe	-8.4	0.3	45.1
ZS15	02_2_pa	11.7	0.8	22.1	San1	05_im41_phe	-6.4	0.2	53.2
ZS15	02_4_pa	15.2	0.7	18.8	San1	08_im46_phe	-8.5	0.2	46.1
ZS15	5_02_5_pa	16.9	0.5	33.7	San1	07_im45_phe	-8.6	0.3	40.4
ZS15	03_2_pa	15.8	0.6	31.8	San1	01_im31_chl	0.1	1.9	1.5
ZS15	03_4_pa	9.4	0.6	29.0	San1	02_im34_chl	-2.5	1.4	5.8
ZS15	03_5_pa	12.4	0.7	20.2	San1	02_im34_amph	-9.3	1.6	0.4
ZS15	03_3_cpx	8.0	3.0	0.5	San1	02_im36_amph2	-3.9	1.3	8.2
DC48B	01_6_pa	5.3	0.6	16.6	C13	02_3_phe	-0.3	0.3	89.4
DC48B	01_2_pa	0.0	1.1	13.7	C13	01_phe_extra	-0.8	0.3	81.3
DC48B	03_2_pa	-0.4	1.2	8.9	C13	01_phe_extra2	-3.7	0.5	60.8
DC48B	03_3_pa	5.4	1.8	4.0	C13	03_2_phe	-0.3	0.4	82.6
DC48B	03_4_pa	-0.2	2.0	13.3	C13	03_2_phe_extra	-0.5	0.3	73.4
DC48B	01_4_gl	3.0	1.8	1.3	C13	03_4_chl	0.3	2.0	2.6
DC48B	02_2_gl	13.0	1.1	2.8	C13	04_2_chl	-3.0	1.8	2.7
DC48B	03_3_cpx	-11.0	2.1	1.2	C13	04_3_cpx_real	-5.3	1.5	2.6
X1008	04_phe	-7.7	0.3	70.5	San2	01_2_chl	1.6	2.6	2.3
X1008	04_2_phe1	-7.9	0.4	73.7	San2	01_4_chl	6.4	2.6	4.1
X1008	06_phe2	-2.7	0.4	58.3	San2	02_5_amph	-23.9	1.0	5.7
X1008	06_2_phe	-8.0	0.4	77.0	San2	02_5_amph_extra	-12.1	1.7	2.3
X1008	opq_pa	0.2	0.3	63.0	San2	02_4_amph	-6.2	1.5	4.7
X1008	opq_pa2	-2.7	0.4	94.2	San2	02_4_chl	-9.8	2.1	2.3
X1008	04_2_gl	-7.5	1.1	2.9	San2	03_4_amph	-10.6	1.3	4.2
X1008	03_gl	-6.2	0.9	3.4	San2	03_3_chl	-5.8	1.5	2.4
X1008	05_gl	-5.9	0.9	5.5	San2	03_3_chl_extra	-6.2	1.3	1.6
X1348	01_im7_phe	5.8	0.4	68.6 HA1	04_phe2	-7.4	1.7	1.7	
X1348	03_im15_pa	4.0	0.2	193.3 HA1	04_phe1	-5.1	1.5	1.4	
X1348	01_im4_amph	10.3	1.1	2.2 HA1	03_phe1	-7.2	1.4	1.4	
X1348	01_im5_amph	0.8	1.5	1.6 HA1	03_phe2	-12.0	1.6	1.2	
Vi1808	01_4_phe	13.2	0.4	42.2	HA2	01_4_amph	-3.8	1.1	3.4
Vi1808	01_3_phe	0.8	0.9	5.2	HA2	03_cpx	-8.3	1.2	2.3
Vi1808	02_3_phe	12.6	0.6	31.4	HA2	01_cpx1	-9.7	1.3	2.2
Vi1808	02_4_phe	0.1	1.1	6.1	HA2	01_cpx2	-10.3	1.4	2.3
Vi1808	04_phe	5.0	0.9	12.5	HA2	02_cpx_bigmatrix	-7.3	1.1	3.0
Vi1808	01_4_cpx	1.9	1.9	1.0					
Vi1808	02_4_cpx2	7.0	1.8	2.5					
Vi1808	01_3_cpx2	-2.5	4.9	0.3					

Table 42: SIMS B isotope data for Chapter 5.

Standard	$\delta^{11}B_{50c}$ (‰)	$\delta^{11}B_{100c}$ (‰)	$\delta^{11}B_{ref}$ (‰)	IMF_{50c} (‰)	IMF_{100c} (‰)	B_{50c} (μg/g)	B_{100c} (μg/g)	B_{ref} (μg/g)
GSD1-G								
Mean	10.6		10.2			65		65
2se	0.1							
n	33							
ARM-3								
Mean	-4.4		-3.8			48		61
2se	0.2							
n	15							
B6								
Mean	1.2		-1.8			182		204
2se	0.3							
n	5							
Phe80-3								
Mean	-17.4	-16.6	-13.5	-3.9	-3.1	22	24	27
2se	1.6	2.3						
n	13	10						
ms98973								
Mean	-24.7	-25.2	-20.0	-4.7	-5.2	37	39	44
2se	1.3	0.9						
n	3	3						
amph 21664								
Mean		-9.3	-6.1		-3.2		2.6	2.5
2se		1.2						
n		10						
amph 21805								
Mean		-4.7	-0.3		-4.4		9.1	14
2se		0.5						
n		15						
srp SY347								
Mean		-2.0	5.6		-7.6		3.9	5.5
2se		1.4						
n		6						

Table 43: SIMS B isotope standards for Chapter 5.

B Appendix B: Additional methods

B.1 Ellenbergerite mode calculation - Chapter 4

Here I include a description of the calculations used to constrain the modal abundance of ellenbergerite in whiteschists during prograde metamorphism. This was not included in the main text because it breaks up the flow of the argument there.

My data and previous studies (Chopin et al., 1986; Schertl et al., 1991) have broadly identified three end members of ellenbergerite in P-Ti-Zr space. P-rich ellenbergerites (>10 wt% P_2O_5) have low TiO2 (<0.5 wt%) and low to moderate ZrO2 (<2 wt%). P-poor ellenbergerites (<0.5 wt% P_2O_5) show substitution of Zr and Ti, forming an almost pure Ti endmember, and a mixed Ti, Zr endmember. ZrO_2 content ranges from 0-3.3 wt%, and TiO_2 from 1.8-4.2 wt%. I estimate the ellenbergerite mode present in the sample during prograde metamorphism by comparing ellenbergerite compositions with bulk P (c.a. 0.08 wt%), Zr (c.a. 200 µg/g) and Ti (c.a. 0.40 wt%) contents of whiteschists reported by Schertl and Schreyer, 2008. Using the maximum Zr and P contents observed in my ellenbergerites, and assuming all Zr and P is hosted in ellenbergerite, results in ellenbergerite modes of 0.83 and 0.63 % respectively. Incorporation of Zr in zircon and P in apatite, both of which are present as accessory minerals (Schertl et al., 1991) would reduce these modes. Lower P and Zr contents would result in higher modes. However, lower P and Zr requires higher Ti, and the availability of Ti is limited by the rutile mode, which dominates the Ti budget of the rock. If all ellenbergerite was the Ti-rich endmember, then rutile mode has to be <0.02 % in order to produce 5 % ellenbergerite. This does not include Ti in other phases, principally phengite and phlogopite, which would reduce rutile mode further. Rutile mode in the matrix was estimated at 0.7 % from point counting on sample DM5.2. The average ellenbergerite composition will not be any of these pure endmembers but even with intermediate compositions it is difficult to construct a situation where ellenbergerite mode can reasonably be >5 %. I therefore suggest that ellenbergerite mode during prograde metamorphism was between 1-5 %.

B.2 Grain boundary trace element calculation - Chapter 5

Here I include a description of the calculations used to assess the potential contribution of grain boundary hosted N to the total bulk N concentration in Section 5.6.4.

SIMS analyses of spots which overlapped grain boundaries (GB) have elevated N counts compared to analyses in the bulk minerals, which suggests that N concentrations in the GB region may be elevated. Since the GB width (~1–1000 nm) is much smaller than the size of the SIMS spot (~10 μm), I assume that the N concentration in the GB is equal to the N concentration determined across the whole spot divided by the ratio of the GB width/spot diameter. This will overestimate N concentrations in the GB somewhat, since some N in each spot resides in the bulk mineral, but as we will see, this does not affect the conclusions of the calculation. Taking the highest N concentration measured in one of these GB spots (91 μg/g) and GB thicknesses ranging from 1–1000 nm, gives a possible range of N concentrations in the GB from 91–0.091 wt% respectively. Next I estimate the GB porosity using Equation 9.6 of Turcotte and Schubert, 2002, which models the GB porosity as circular tubes bordering cubic grains (Figure 42), using a range of GB widths (1–1000 nm) and grain sizes (1–1000 μm). Combining these estimates for the porosity and GB N concentration gives the total GB N contribution to the bulk N concentration. This contribution increases with GB thickness since the linear reduction in GB N concentration is offset by the squared increase in porosity. Increasing grain size reduces the contribution since porosity is reduced.

696 *Flows in Porous Media*

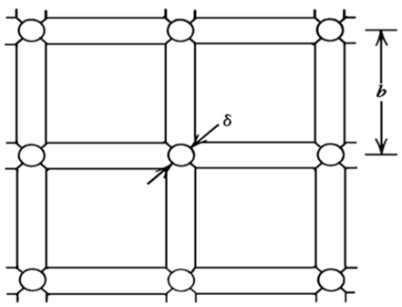


Figure 9.1 An idealized model of a porous medium. Circular tubes of diameter δ form a cubical matrix with dimensions b.

cube on each of these edges. Thus the equivalent of three tubes of diameter δ and length b lie within the cube. The porosity is therefore given by

$$\phi = 3\pi\left(\frac{\delta}{2}\right)^2 \frac{b}{b^3} = \frac{3\pi}{4}\frac{\delta^2}{b^2}. \tag{9.6}$$

Figure 42: Simplified model of grain boundary porosity from Turcotte and Schubert, 2002.

References

Adam, J., M. Locmelis, J. C. Afonso, T. Rushmer, and M. L. Fiorentini (2014). "The capacity of hydrous fluids to transport and fractionate incompatible elements and metals within the Earth's mantle". In: *Geochemistry, Geophysics, Geosystems* 15.6, pp. 2241–2253. DOI: https://doi.org/10.1002/2013GC005199.

Adler, J. F. and Q. Williams (2005). "A high-pressure X-ray diffraction study of iron nitrides: Implications for Earth's core". In: *Journal of Geophysical Research: Solid Earth* 110.B1. DOI: 10.1029/2004JB003103.

Agard, P. (2021). "Subduction of oceanic lithosphere in the Alps: Selective and archetypal from (slow-spreading) oceans". In: *Earth-Science Reviews* 214, p. 103517. DOI: 10.1016/j.earscirev.2021.103517.

Ahn, J. H., D. R. Peacor, and D. S. Coombs (1988). "Formation mechanisms of illite, chlorite and mixed-layer illite-chlorite in Triassic volcanogenic sediments from the Southland Syncline, New Zealand". In: *Contributions to Mineralogy and Petrology* 99.1, pp. 82–89. DOI: 10.1007/BF00399368.

Alard, O., A. Halimulati, and S. Demouchy (2022). "Look between the grains". In: *Nature Geoscience* 15.11. Number: 11 Publisher: Nature Publishing Group, pp. 856–857. DOI: 10.1038/s41561-022-01065-3.

Anczkiewicz, R., J. P. Platt, M. F. Thirlwall, and J. Wakabayashi (2004). "Franciscan subduction off to a slow start: evidence from high-precision Lu–Hf garnet ages on high grade-blocks". In: *Earth and Planetary Science Letters* 225.1, pp. 147–161. DOI: 10.1016/j.epsl.2004.06.003.

Andersen, T., H. Austrheim, and E. A. J. Burke (1991). "Mineral-fluid-melt interactions in high-pressure shear zones in the Bergen Arcs nappe complex, Caledonides of W. Norway: Implications for the fluid regime in Caledonian eclogite-facies metamorphism". In: *Lithos* 27.3, pp. 187–204. DOI: 10.1016/0024-4937(91)90012-A.

Andersen, T., E. A. J. Burke, and H. Austrheim (1989). "Nitrogen-bearing, aqueous fluid inclusions in some eclogites from the Western Gneiss Region of the Norwegian Caledonides". In: *Contributions to Mineralogy and Petrology* 103.2, pp. 153–165. DOI: 10.1007/BF00378501.

Angiboust, S., P. Agard, L. Jolivet, and O. Beyssac (2009). "The Zermatt-Saas ophiolite: the largest (60-km wide) and deepest (c. 70–80 km) continuous slice of oceanic lithosphere detached from a subduction zone?" In: *Terra Nova* 21.3, pp. 171–180. DOI: 10.1111/j.1365-3121.2009.00870.x.

Angiboust, S., R. Langdon, P. Agard, D. Waters, and C. Chopin (2012). "Eclogitization of the Monviso ophiolite (W. Alps) and implications on subduction dynamics". In: *Journal of Metamorphic Geology* 30.1, pp. 37–61. DOI: 10.1111/j.1525-1314.2011.00951.x.

Angiboust, S., T. Pettke, J. C. M. De Hoog, B. Caron, and O. Oncken (2014). "Channelized Fluid Flow and Eclogite-facies Metasomatism along the Subduction Shear Zone". In: *Journal of Petrology* 55.5, pp. 883–916. DOI: 10.1093/petrology/egu010.

Arculus, R. J., H. Lapierre, and Jaillard (1999). "Geochemical window into subduction and accretion processes: Raspas metamorphic complex, Ecuador". In: *Geology* 27.6, pp. 547–550. DOI: 10.1130/0091-7613(1999)027<0547:GWISAA>2.3.CO;2.

Avice, G., B. Marty, R. Burgess, A. Hofmann, P. Philippot, K. Zahnle, and D. Zakharov (2018). "Evolution of atmospheric xenon and other noble gases inferred from Archean to Paleoproterozoic rocks". In: *Geochimica et Cosmochimica Acta* 232, pp. 82–100. DOI: 10.1016/j.gca.2018.04.018.

Bach, W., N. Jöns, and F. Klein (2013). "Metasomatism Within the Ocean Crust". In: *Metasomatism and the Chemical Transformation of Rock: The Role of Fluids in Terrestrial and Extraterrestrial Processes*. Ed. by D. E. Harlov and H. Austrheim. Lecture Notes in Earth System Sciences. Berlin, Heidelberg: Springer, pp. 253–288. ISBN: 978-3-642-28394-9. DOI: 10.1007/978-3-642-28394-9_8.

Bach, W., B. Peucker-Ehrenbrink, S. R. Hart, and J. S. Blusztajn (2003). "Geochemistry of hydrothermally altered oceanic crust: DSDP/ODP Hole 504B – Implications for seawater-crust exchange budgets and Sr- and Pb-isotopic evolution of the mantle". In: *Geochemistry, Geophysics, Geosystems* 4.3. DOI: 10.1029/2002GC000419.

Barry, P. and D. R. Hilton (2016). "Release of subducted sedimentary nitrogen throughout Earth's mantle". In: *Geochemical Perspectives Letters* 2.2.

Beaudoin, G. M., J. D. Barnes, T. John, J. E. Hoffmann, R. Chatterjee, and D. F. Stockli (2022). "Global halogen flux of subducting oceanic crust". In: *Earth and Planetary Science Letters* 594, p. 117750. DOI: 10.1016/j.epsl.2022.117750.

Bebout, G., N. Banerjee, M. Izawa, K. Kobayashi, K. Lazzeri, L. Ranieri, and E. Nakamura (2018). "Nitrogen Concentrations and Isotopic Compositions of Seafloor-Altered Terrestrial Basaltic Glass: Implications for Astrobiology". In: *Astrobiology* 18.3, pp. 330–342. DOI: 10.1089/ast.2017.1708.

Bebout, G. E. (1997). "Nitrogen isotope tracers of high-temperature fluid-rock interactions: Case study of the Catalina Schist, California". In: *Earth and Planetary Science Letters* 151.1, pp. 77–90. DOI: 10.1016/S0012-821X(97)00117-9.

— (2007). "Metamorphic chemical geodynamics of subduction zones". In: *Earth and Planetary Science Letters* 260.3, pp. 373–393. DOI: 10.1016/j.epsl.2007.05.050.

Bebout, G. E., P. Agard, K. Kobayashi, T. Moriguti, and E. Nakamura (2013). "Devolatilization history and trace element mobility in deeply subducted sedimentary rocks: Evidence from Western Alps HP/UHP suites". In: *Chemical Geology* 342, pp. 1–20. DOI: 10.1016/j.chemgeo.2013.01.009.

Bebout, G. E., A. E. Bebout, and C. M. Graham (2007). "Cycling of B, Li, and LILE (K, Cs, Rb, Ba, Sr) into subduction zones: SIMS evidence from micas in high-P/T metasedimentary rocks". In: *Chemical Geology*. Geochemical processes responsible for element mobility from the slab to the surface 239.3, pp. 284–304. DOI: 10.1016/j.chemgeo.2006.10.016.

Bebout, G. E., D. C. Cooper, A. D. Bradley, and S. J. Sadofsky (1999). "Nitrogen-isotope record of fluid-rock interactions in the Skiddaw Aureole and granite, English Lake District". In: *American Mineralogist* 84.10, pp. 1495–1505. DOI: 10.2138/am-1999-1002.

Bebout, G. E. and M. L. Fogel (1992). "Nitrogen-isotope compositions of metasedimentary rocks in the Catalina Schist, California: Implications for metamorphic devolatilization history". In: *Geochimica et Cosmochimica Acta* 56.7, pp. 2839–2849. DOI: 10.1016/0016-7037(92)90363-N.

Bebout, G. E., K. E. Lazzeri, and C. A. Geiger (2016). "Pathways for nitrogen cycling in Earth's crust and upper mantle: A review and new results for microporous beryl and cordierite". In: *American Mineralogist* 101.1, pp. 7–24. DOI: 10.2138/am-2016-5363.

Bebout, G. E. and E. Nakamura (2003). "Record in metamorphic tourmalines of subduction-zone devolatilization and boron cycling". In: *Geology* 31.5, pp. 407–410. DOI: 10.1130/0091-7613(2003)031<0407:RIMTOS>2.0.CO;2.

Bebout, G. E., T. Ota, T. Kunihiro, W. D. Carlson, and E. Nakamura (2022). "Lithium in garnet as a tracer of subduction zone metamorphic reactions: The record in ultrahigh-pressure metapelites at Lago di Cignana, Italy". In: *Geosphere* 18.3, pp. 1020–1029. DOI: 10.1130/GES02473.1.

Bekaert, D. V., S. J. Turner, M. W. Broadley, J. D. Barnes, and S. A. Haldórsson (2021). "Subduction-Driven Volatile Recycling: A Global Mass Balance". In: *Annual Review of Earth and Planetary Sciences* 49.B1, pp. 37–70. ISSN: 1545-4495. DOI: 10.1146/annurev-earth-071620-055024.

Belgrano, T. M. and L. W. Diamond (2019). "Subduction-zone contributions to axial volcanism in the Oman–U.A.E. ophiolite". In: *Lithosphere* 11.3, pp. 399–411. DOI: 10.1130/L1045.1.

Berner, R. A. (2006). "Geological nitrogen cycle and atmospheric N2 over Phanerozoic time". In: *Geology* 34.5, pp. 413–415. DOI: 10.1130/G22470.1.

Biino, G. and R. Compagnoni (1992). "Very-high pressure metamorphism of the Brossasco coronite metagranite, southern Dora Maira Massif, Western Alps". In: *Schweiz. Mineral. Petrogr. Mitt.* 72, pp. 347–363.

Bobos, I. and L. B. Williams (2017). "Boron, lithium and nitrogen isotope geochemistry of NH4-illite clays in the fossil hydrothermal system of Harghita Bãi, East Carpathians, Romania". In: *Chemical Geology* 473, pp. 22–39. DOI: 10.1016/j.chemgeo.2017.10.005.

Boocock, T. J., S. Mikhail, A. J. Boyce, J. Prytulak, P. S. Savage, and E. E. Stüeken (2023a). "A primary magmatic source of nitrogen to Earth's crust". In: *Nature Geoscience* 16.6. Number: 6 Publisher: Nature Publishing Group, pp. 521–526. DOI: 10.1038/s41561-023-01194-3.

Boocock, T. J., S. Mikhail, J. Prytulak, T. Di Rocco, and E. E. Stüeken (2020). "Nitrogen Mass Fraction and Stable Isotope Ratios for Fourteen Geological Reference Materials: Evaluating the Applicability of Elemental Analyser Versus Sealed Tube Combustion Methods". In: *Geostandards and Geoanalytical Research* 44.3, pp. 537–551. DOI: 10.1111/ggr.12345.

Boocock, T. J., E. E. Stüeken, G. M. Bybee, R. König, A. J. Boyce, J. Prytulak, I. Buisman, and S. Mikhail (2023b). "Equilibrium partitioning and isotopic fractionation of nitrogen between biotite,

plagioclase, and K-feldspar during magmatic differentiation". In: *Geochimica et Cosmochimica Acta* 356, pp. 116–128. DOI: 10.1016/j.gca.2023.07.010.

Bos, A., W. Duit, A. M. J. van der Eerden, and J. B. H. Jansen (1988). "Nitrogen storage in biotite: An experimental study of the ammonium and potassium partitioning between 1M-phlogopite and vapour at 2 kb". In: *Geochimica et Cosmochimica Acta* 52.5, pp. 1275–1283. DOI: 10.1016/0016-7037(88)90281-5.

Bottrell, S. H., L. P. Carr, and J. Dubessy (1988). "A Nitrogen-Rich Metamorphic Fluid and Coexisting Minerals in Slates from North Wales". In: *Mineralogical Magazine* 52.367, pp. 451–457. DOI: 10.1180/minmag.1988.052.367.03.

Boutier, A., A. Vitale Brovarone, I. Martinez, O. Sissmann, and S. Mana (2021). "High-pressure serpentinization and abiotic methane formation in metaperidotite from the Appalachian subduction, northern Vermont". In: *Lithos* 396-397, p. 106190. DOI: 10.1016/j.lithos.2021.106190.

Brenan, J. M., F. J. Ryerson, and H. F. Shaw (1998). "The role of aqueous fluids in the slab-to-mantle transfer of boron, beryllium, and lithium during subduction: experiments and models". In: *Geochimica et Cosmochimica Acta* 62.19, pp. 3337–3347. DOI: 10.1016/S0016-7037(98)00224-5.

Bruno, M., R. Compagnoni, and M. Rubbo (2001). "The ultra-high pressure coronitic and pseudomorphous reactions in a metagranodiorite from the Brossasco-Isasca Unit, Dora-Maira Massif, western Italian Alps: a petrographic study and equilibrium thermodynamic modelling". In: *Journal of Metamorphic Geology* 19.1, pp. 33–43. DOI: 10.1046/j.1525-1314.2001.00291.x.

Busigny, V., P. Cartigny, C. Laverne, D. Teagle, M. Bonifacie, and P. Agrinier (2019). "A reassessment of the nitrogen geochemical behavior in upper oceanic crust from Hole 504B: Implications for subduction budget in Central America". In: *Earth and Planetary Science Letters* 525, p. 115735. DOI: 10.1016/j.epsl.2019.115735.

Busigny, V., P. Cartigny, and P. Philippot (2011). "Nitrogen isotopes in ophiolitic metagabbros: A re-evaluation of modern nitrogen fluxes in subduction zones and implication for the early Earth atmosphere". In: *Geochimica et Cosmochimica Acta* 75.23, pp. 7502–7521. DOI: 10.1016/j.gca.2011.09.049.

Busigny, V., P. Cartigny, P. Philippot, M. Ader, and M. Javoy (2003a). "Massive recycling of nitrogen and other fluid-mobile elements (K, Rb, Cs, H) in a cold slab environment: evidence from HP

to UHP oceanic metasediments of the Schistes Lustrés nappe (western Alps, Europe)". In: *Earth and Planetary Science Letters* 215.1, pp. 27–42. DOI: 10.1016/S0012-821X(03)00453-9.

Busigny, V., P. Cartigny, P. Philippot, and M. Javoy (2003b). "Ammonium quantification in muscovite by infrared spectroscopy". In: *Chemical Geology* 198.1, pp. 21–31. DOI: 10.1016/S0009-2541(02)00420-5.

— (2004). "Quantitative analysis of ammonium in biotite using infrared spectroscopy". In: *American Mineralogist* 89.11-12. Publisher: De Gruyter Section: American Mineralogist, pp. 1625–1630. DOI: 10.2138/am-2004-11-1206.

Busigny, V., C. Laverne, and M. Bonifacie (2005). "Nitrogen content and isotopic composition of oceanic crust at a superfast spreading ridge: A profile in altered basalts from ODP Site 1256, Leg 206". In: *Geochemistry, Geophysics, Geosystems* 6.12. DOI: https://doi.org/10.1029/2005GC001020.

Cann, J. R. (1969). "Spilites from the Carlsberg Ridge, Indian Ocean". In: *Journal of Petrology* 10.1, pp. 1–19. DOI: 10.1093/petrology/10.1.1.

Cannaò, E., M. Scambelluri, O. Müntener, B. Putlitz, and S. Agostini (2023). "Inheritance versus subduction-related δ^{11}B signatures of eclogites: Insights from the Voltri Massif (Ligurian Western Alps, Italy)". In: *Chemical Geology* 615, p. 121218. DOI: 10.1016/j.chemgeo.2022.121218.

Cartigny, P., J. W. Harris, D. Phillips, M. Girard, and M. Javoy (1998). "Subduction-related diamonds? - The evidence for a mantle-derived origin from coupled δ^{13}C–δ^{15}N determinations". In: *Chemical Geology* 147.1, pp. 147–159. DOI: 10.1016/S0009-2541(97)00178-2.

Castelli, D., F. Rolfo, C. Groppo, and R. Compagnoni (2007). "Impure marbles from the UHP Brossasco-Isasca Unit (Dora-Maira Massif, western Alps): evidence for Alpine equilibration in the diamond stability field and evaluation of the X(CO2) fluid evolution". In: *Journal of Metamorphic Geology* 25.6, pp. 587–603. DOI: 10.1111/j.1525-1314.2007.00716.x.

Chen, A., Y.-X. Chen, X. Gu, Z. Zeng, Z. Xiao, H.-P. Schertl, X. Han, Z.-F. Zhao, and F. Huang (2023a). "Barium isotope behavior during interaction between serpentinite-derived fluids and metamorphic rocks in the continental subduction zone". In: *Geochimica et Cosmochimica Acta* 353, pp. 61–75. DOI: 10.1016/j.gca.2023.05.016.

Chen, Q., Z. Zhang, Z. Wang, W.-C. Li, X.-Y. Gao, and H. Ni (2019a). "In situ Raman spectroscopic study of nitrogen speciation in aqueous fluids under pressure". In: *Chemical Geology* 506, pp. 51–57. DOI: 10.1016/j.chemgeo.2018.12.016.

Chen, X., S. Jiang, M. R.Palmer, H.-P. Schertl, A. Cambeses, D. Hernández-Uribe, K. Zhao, C. Lin, and Y. Zheng (2023b). "Tourmaline chemistry, boron, and strontium isotope systematics trace multiple melt–fluid–rock interaction stages in deeply subducted continental crust". In: *Geochimica et Cosmochimica Acta* 340, pp. 120–140. DOI: 10.1016/j.gca.2022.11.019.

Chen, Y.-X., W. Lu, Y. He, H.-P. Schertl, Y.-F. Zheng, J.-W. Xiong, and K. Zhou (2019b). "Tracking Fe mobility and Fe speciation in subduction zone fluids at the slab-mantle interface in a subduction channel: A tale of whiteschist from the Western Alps". In: *Geochimica et Cosmochimica Acta* 267, pp. 1–16. DOI: 10.1016/j.gca.2019.09.020.

Chen, Y.-X., H.-P. Schertl, Y.-F. Zheng, F. Huang, K. Zhou, and Y.-Z. Gong (2016). "Mg–O isotopes trace the origin of Mg-rich fluids in the deeply subducted continental crust of Western Alps". In: *Earth and Planetary Science Letters* 456, pp. 157–167. DOI: 10.1016/j.epsl.2016.09.010.

Chen, Y.-X., K. Zhou, Y.-F. Zheng, and H.-P. Schertl (2017). "Zircon geochemical constraints on the protolith nature and metasomatic process of the Mg-rich whiteschist from the Western Alps". In: *Chemical Geology* 467, pp. 177–195. DOI: 10.1016/j.chemgeo.2017.08.013.

Chopin, C. (1984). "Coesite and pure pyrope in high-grade blueschists of the Western Alps: a first record and some consequences". In: *Contributions to Mineralogy and Petrology* 86.2, pp. 107–118. DOI: 10.1007/BF00381838.

Chopin, C., R. Klaska, O. Medenbach, and D. Dron (1986). "Ellenbergerite, a new high-pressure Mg-Al-(Ti,Zr)-silicate with a novel structure based on face-sharing octahedra". In: *Contributions to Mineralogy and Petrology* 92.3, pp. 316–321. DOI: 10.1007/BF00572160.

Clarke, E., J. C. M. De Hoog, L. Kirstein, J. Harvey, and B. Debret (2020). "Metamorphic olivine records external fluid infiltration during serpentinite dehydration". In: *Geochemical Perspectives Letters* 16, pp. 25–29. DOI: 10.7185/geochemlet.2039.

Codeço, M. S., P. Weis, R. B. Trumbull, J. Glodny, M. Wiedenbeck, and R. L. Romer (2019). "Boron Isotope Muscovite-Tourmaline Geothermometry Indicates Fluid Cooling During Magmatic-Hydrothermal

W-Sn Ore Formation". In: *Economic Geology* 114.1, pp. 153–163. DOI: 10.5382/econgeo.2019.4625.

Coggon, R. and T. J. B. Holland (2002). "Mixing properties of phengitic micas and revised garnet-phengite thermobarometers". In: *Journal of Metamorphic Geology* 20.7, pp. 683–696. DOI: 10.1046/j.1525-1314.2002.00395.x.

Collins, N. C., G. E. Bebout, S. Angiboust, P. Agard, M. Scambelluri, L. Crispini, and T. John (2015). "Subduction zone metamorphic pathway for deep carbon cycling: II. Evidence from HP/UHP metabasaltic rocks and ophicarbonates". In: *Chemical Geology* 412, pp. 132–150. DOI: 10.1016/j.chemgeo.2015.06.012.

Compagnoni, R., B. Messiga, and D. Castelli (1994). "High pressure metamorphism in the Western Alps. Guide-book to the field excursion of the 16th meeting of the IMA, September 10–15, 2004, Pisa, 148 p." In.

Compagnoni, R. and T. Hirajima (2001). "Superzoned garnets in the coesite-bearing Brossasco-Isasca Unit, Dora-Maira massif, Western Alps, and the origin of the whiteschists". In: *Lithos* 57.4, pp. 219–236. DOI: 10.1016/S0024-4937(01)00041-X.

Compagnoni, R. and F. Rolfo (2003). "UHPM units in the Western Alps". In: *Ultrahigh Pressure Metamorphism*. Ed. by G. Papp, T. G. Weiszburg, D. A. Carswell, R. Compagnoni, and F. Rolfo. Budapest: Mineralogical Society of Great Britain and Ireland, pp. 13–49. ISBN: 978-963-463-646-5 978-0-903056-54-0. DOI: 10.1180/EMU-notes.5.2.

Connolly, J. A. D. and M. E. Galvez (2018). "Electrolytic fluid speciation by Gibbs energy minimization and implications for subduction zone mass transfer". In: *Earth and Planetary Science Letters* 501, pp. 90–102. DOI: 10.1016/j.epsl.2018.08.024.

Coogan, L. A., K. M. Gillis, M. Pope, and J. Spence (2017). "The role of low-temperature (off-axis) alteration of the oceanic crust in the global Li-cycle: Insights from the Troodos ophiolite". In: *Geochimica et Cosmochimica Acta* 203, pp. 201–215. DOI: 10.1016/j.gca.2017.01.002.

Corno, A., C. Groppo, A. Borghi, P. Mosca, and M. Gattiglio (2023). "To be or not to be Alpine: New petrological constraints on the metamorphism of the Chenaillet Ophiolite (Western Alps)". In: *Journal of Metamorphic Geology* 41.6, pp. 745–765. DOI: 10.1111/jmg.12716.

Cottrell, E. and K. A. Kelley (2011). "The oxidation state of Fe in MORB glasses and the oxygen fugacity of the upper mantle". In: *Earth and Planetary Science Letters* 305.3-4, pp. 270–282. DOI: 10.1016/j.epsl.2011.03.014.

Dachs, E. (1990). "Geothermobarometry in metasediments of the southern Grossvenediger area (Tauern Window, Austria)". In: *Journal of Metamorphic Geology* 8.2, pp. 217–230. DOI: 10.1111/j.1525-1314.1990.tb00467.x.

Dal Piaz, G. V, G. Venturelli, P. Spadea, and G. Di Battistini (1981). "Geochemical features of metabasalts and metagabbros from the Piemonte ophiolite nappe, Italian Western Alps". In: *Geochemical features of metabasalts and metagabbros from the Piemonte ophiolite nappe, Italian Western Alps* 142.3. Place: Stuttgart Publisher: Schweizerbart, pp. 248–269.

De Capitani, C. and K. Petrakakis (2010). "The computation of equilibrium assemblage diagrams with Theriak/Domino software". In: *American Mineralogist* 95, pp. 1006–1016. DOI: 10.2138/am.2010.3354.

De Capitani, C. and T. H. Brown (1987). "The computation of chemical equilibrium in complex systems containing non-ideal solutions". In: *Geochimica et Cosmochimica Acta* 51.10, pp. 2639–2652. DOI: 10.1016/0016-7037(87)90145-1.

De Hoog, J. C. M., K. Hattori, and H. Jung (2014). "Titanium- and water-rich metamorphic olivine in high-pressure serpentinites from the Voltri Massif (Ligurian Alps, Italy): evidence for deep subduction of high-field strength and fluid-mobile elements". In: *Contributions to Mineralogy and Petrology* 167.3, p. 990. DOI: 10.1007/s00410-014-0990-x.

De Hoog, J. C. M. and I. P. Savov (2018). "Boron Isotopes as a Tracer of Subduction Zone Processes". In: *Boron Isotopes: The Fifth Element*. Ed. by H. Marschall and G. Foster. Advances in Isotope Geochemistry. Cham: Springer International Publishing, pp. 217–247. ISBN: 978-3-319-64666-4. DOI: 10.1007/978-3-319-64666-4_9.

Debret, B., K. T. Koga, F. Cattani, C. Nicollet, G. Van den Bleeken, and S. Schwartz (2016). "Volatile (Li, B, F and Cl) mobility during amphibole breakdown in subduction zones". In: *Lithos* 244, pp. 165–181. DOI: 10.1016/j.lithos.2015.12.004.

Demény, A., Z. D. Sharp, and H.-R. Pfeifer (1997). "Mg-metasomatism and formation conditions of Mg-chlorite-muscovite-quartzphyllites (leucophyllites) of the Eastern Alps (W. Hungary) and

their relations to Alpine whiteschists". In: *Contributions to Mineralogy and Petrology* 128.2, pp. 247–260. DOI: 10.1007/s004100050306.

Deschamps, F., M. Godard, S. Guillot, C. Chauvel, M. Andreani, K. Hattori, B. Wunder, and L. France (2012). "Behavior of fluid-mobile elements in serpentines from abyssal to subduction environments: Examples from Cuba and Dominican Republic". In: *Chemical Geology* 312-313, pp. 93–117. DOI: 10.1016/j.chemgeo.2012.04.009.

Di Vincenzo, G., S. Tonarini, B. Lombardo, D. Castelli, and L. Ottolini (2006). "Comparison of 40Ar–39Ar and Rb–Sr Data on Phengites from the UHP Brossasco–Isasca Unit (Dora Maira Massif, Italy): Implications for Dating White Mica". In: *Journal of Petrology* 47.7, pp. 1439–1465. DOI: 10.1093/petrology/egl018.

Dobrzhinetskaya, L. F., R. Wirth, J. Yang, I. D. Hutcheon, P. K. Weber, and H. W. Green (2009). "High-pressure highly reduced nitrides and oxides from chromitite of a Tibetan ophiolite". In: *Proceedings of the National Academy of Sciences* 106.46, pp. 19233–19238. DOI: 10.1073/pnas.0905514106.

Domanik, K. J., R. L. Hervig, and S. M. Peacock (1993). "Beryllium and boron in subduction zone minerals: An ion microprobe study". In: *Geochimica et Cosmochimica Acta* 57.21, pp. 4997–5010. DOI: 10.1016/S0016-7037(05)80005-5.

Domanik, K. J. and J. R. Holloway (1996). "The stability and composition of phengitic muscovite and associated phases from 5.5 to 11 GPa: Implications for deeply subducted sediments". In: *Geochimica et Cosmochimica Acta* 60.21, pp. 4133–4150. DOI: 10.1016/S0016-7037(96)00241-4.

Duit, W., J. B. H. Jansen, A. v. Breemen, and A. Bos (1986). "Ammonium micas in metamorphic rocks as exemplified by Dome de l'Agout (France)". In: *American Journal of Science* 286.9, pp. 702–732. DOI: 10.2475/ajs.286.9.702.

Dyar, M. D., M. Wiedenbeck, D. Robertson, L. R. Cross, J. S. Delaney, K. Ferguson, C. A. Francis, E. S. Grew, C. V. Guidotti, R. L. Hervig, J. M. Hughes, J. Husler, W. Leeman, A. V. McGuire, D. Rhede, H. Rothe, R. L. Paul, I. Richards, and M. Yates (2001). "Reference Minerals for the Microanalysis of Light Elements". In: *Geostandards Newsletter* 25.2-3, pp. 441–463. DOI: 10.1111/j.1751-908X.2001.tb00616.x.

Elkins, L. J., T. P. Fischer, D. R. Hilton, Z. D. Sharp, S. McKnight, and J. Walker (2006). "Tracing nitrogen in volcanic and geothermal volatiles from the Nicaraguan volcanic front". In: *Geochimica et Cosmochimica Acta* 70.20, pp. 5215–5235. DOI: 10.1016/j.gca.2006.07.024.

Enami, M., S. R. Wallis, and Y. Banno (1994). "Paragenesis of sodic pyroxene-bearing quartz schists: implications for the P-T history of the Sanbagawa belt". In: *Contributions to Mineralogy and Petrology* 116.1, pp. 182–198. DOI: 10.1007/BF00310699.

Epstein, G. S., G. E. Bebout, and S. Angiboust (2021). "Fluid and mass transfer along transient subduction interfaces in a deep paleo-accretionary wedge (Western Alps)". In: *Chemical Geology* 559, p. 119920. DOI: 10.1016/j.chemgeo.2020.119920.

Errico, J., J. Barnes, A. Strickland, and J. Valley (2013). "Oxygen isotope zoning in garnets from Franciscan eclogite blocks: evidence for rock-buffered fluid interaction in the mantle wedge". In: *Contributions to Mineralogy & Petrology* 166.4, pp. 1161–1176. DOI: 10.1007/s00410-013-0915-0.

Erzinger, J., W. Bach, J. C. Alt, H. Kinoshita, L. B. Stokking, and P. J. Michael (1996). "Downhole variation of molecular nitrogen in DSDP/ODP Hole 504B: preliminary results". In: *Proceedings of the Ocean Drilling Program : Scientific Results* 148, pp. 3–8. DOI: 10.2973/odp.proc.sr.148.156.1996.

Feininger, T. (1980). "Eclogite and Related High-Pressure Regional Metamorphic Rocks from the Andes of Ecuador". In: *Journal of Petrology* 21.1, pp. 107–140. DOI: 10.1093/petrology/21.1.107.

Ferrando, S., M. L. Frezzotti, M. Petrelli, and R. Compagnoni (2009). "Metasomatism of continental crust during subduction: the UHP whiteschists from the Southern Dora-Maira Massif (Italian Western Alps)". In: *Journal of Metamorphic Geology* 27.9, pp. 739–756. DOI: 10.1111/j.1525-1314.2009.00837.x.

Ferrando, S. (2012). "Mg-metasomatism of metagranitoids from the Alps: genesis and possible tectonic scenarios". In: *Terra Nova* 24.6, pp. 423–436. DOI: 10.1111/j.1365-3121.2012.01078.x.

Ferrando, S., C. Groppo, M. L. Frezzotti, D. Castelli, and A. Proyer (2017). "Dissolving dolomite in a stable UHP mineral assemblage: Evidence from Cal-Dol marbles of the Dora-Maira Massif (Italian Western Alps)". In: *American Mineralogist* 102.1, pp. 42–60. DOI: 10.2138/am-2017-5761.

Ferraris, C., D. Castelli, and B. Lombardo (2005). "SEM/TEM-AEM characterization of micro- and nano-scale zonation in phengite from a UHP Dora-Maira marble petrologic significance of armoured Si-rich domains". In: *European Journal of Mineralogy* 17.3, pp. 453–464. DOI: 10.1127/0935-1221/2005/0017-0453.

Fischer, T. P., W. F. Giggenbach, Y. Sano, and S. N. Williams (1998). "Fluxes and sources of volatiles discharged from Kudryavy, a subduction zone volcano, Kurile Islands". In: *Earth and Planetary Science Letters* 160.1, pp. 81–96. DOI: 10.1016/S0012-821X(98)00086-7.

Fischer, T. P., D. R. Hilton, M. M. Zimmer, A. M. Shaw, Z. D. Sharp, and J. A. Walker (2002). "Subduction and Recycling of Nitrogen Along the Central American Margin". In: *Science* 297.5584, pp. 1154–1157. DOI: 10.1126/science.1073995.

Frezzotti, M. L. and S. Ferrando (2015). "The chemical behavior of fluids released during deep subduction based on fluid inclusions†". In: *American Mineralogist* 100.2-3, pp. 352–377. DOI: 10.2138/am-2015-4933.

Fu, B., J. L. R. Touret, Y.-F. Zheng, and B.-m. Jahn (2003). "Fluid inclusions in granulites, granulitized eclogites and garnet clinopyroxenites from the Dabie–Sulu terranes, eastern China". In: *Lithos*. 6th International Eclogite Conference: Eclogites and Related High and Ultrahigh Pressure Metamorphic Rocks 70.3, pp. 293–319. DOI: 10.1016/S0024-4937(03)00103-8.

Förster, M. W., S. F. Foley, O. Alard, and S. Buhre (2019). "Partitioning of nitrogen during melting and recycling in subduction zones and the evolution of atmospheric nitrogen". In: *Chemical Geology* 525, pp. 334–342. DOI: 10.1016/j.chemgeo.2019.07.042.

Füri, E., E. Deloule, and C. Dalou (2018). "Nitrogen abundance and isotope analysis of silicate glasses by secondary ionization mass spectrometry". In: *Chemical Geology* 493, pp. 327–337. DOI: 10.1016/j.chemgeo.2018.06.008.

Füri, E., M. Portnyagin, N. Mironov, C. Deligny, A. Gurenko, R. Botcharnikov, and F. Holtz (2021). "In situ quantification of the nitrogen content of olivine-hosted melt inclusions from Klyuchevskoy volcano (Kamchatka): Implications for nitrogen recycling at subduction zones". In: *Chemical Geology* 582, p. 120456. DOI: 10.1016/j.chemgeo.2021.120456.

Gabriele, P., M. Ballèvre, E. Jaillard, and J. Hernandez (2003). "Garnet-chloritoid-kyanite metapelites from the Raspas Complex (SW Ecuador) a key eclogite-facies assemblage". In: *European Journal of Mineralogy* 15.6, pp. 977–989. DOI: 10.1127/0935-1221/2003/0015-0977.

Gale, A., C. A. Dalton, C. H. Langmuir, Y. Su, and J.-G. Schilling (2013). "The mean composition of ocean ridge basalts". In: *Geochemistry, Geophysics, Geosystems* 14.3, pp. 489–518. DOI: https://doi.org/10.1029/2012GC004334.

Galvez, M. E., J. A. D. Connolly, and C. E. Manning (2016). "Implications for metal and volatile cycles from the pH of subduction zone fluids". In: *Nature* 539.7629. Number: 7629 Publisher: Nature Publishing Group, pp. 420–424. DOI: 10.1038/nature20103.

Gauthiez-Putallaz, L., D. Rubatto, and J. Hermann (2016). "Dating prograde fluid pulses during subduction by in situ U–Pb and oxygen isotope analysis". In: *Contributions to Mineralogy and Petrology* 171.2, p. 15. DOI: 10.1007/s00410-015-1226-4.

Gebauer, D., H. P. Schertl, M. Brix, and W. Schreyer (1997). "35 Ma old ultrahigh-pressure metamorphism and evidence for very rapid exhumation in the Dora Maira Massif, Western Alps". In: *Lithos* 41.1, pp. 5–24. DOI: 10.1016/S0024-4937(97)82002-6.

Gerya, T. V., B. Stöckhert, and A. L. Perchuk (2002). "Exhumation of high-pressure metamorphic rocks in a subduction channel: A numerical simulation". In: *Tectonics* 21.6, pp. 6–1–6–19. DOI: 10.1029/2002TC001406.

Gillis, K. M. and P. T. Robinson (1990). "Patterns and processes of alteration in the lavas and dykes of the Troodos Ophiolite, Cyprus". In: *Journal of Geophysical Research: Solid Earth* 95.B13, pp. 21523–21548. DOI: 10.1029/JB095iB13p21523.

Goldblatt, C., M. W. Claire, T. M. Lenton, A. J. Matthews, A. J. Watson, and K. J. Zahnle (2009). "Nitrogen-enhanced greenhouse warming on early Earth". In: *Annual Review of Earth and Planetary Sciences* 12.B1, pp. 891–896. ISSN: 1752-0908. DOI: 10.1038/ngeo692.

Goncalves, P., S. Guillot, J.-M. Lardeaux, C. Nicollet, and B. Mercier de Lepinay (2000). "Thrusting and sinistral wrenching in a pre-Eocene HP-LT Caribbean accretionary wedge (Samaná Peninsula, Dominican Republic)". In: *Geodinamica Acta* 13.2-3. Publisher: Taylor & Francis _eprint: https://doi.org/10.1080/09853111.2000.11105368, pp. 119–132. DOI: 10.1080/09853111.2000.11105368.

Green, E. C. R., R. W. White, J. F. A. Diener, R. Powell, T. J. B. Holland, and R. M. Palin (2016). "Activity–composition relations for the calculation of partial melting equilibria in metabasic rocks". In: *Journal of Metamorphic Geology* 34.9, pp. 845–869. DOI: 10.1111/jmg.12211.

Groppo, C., M. Beltrando, and R. Compagnoni (2009). "The P–T path of the ultra-high pressure Lago Di Cignana and adjoining high-pressure meta-ophiolitic units: insights into the evolution of the subducting Tethyan slab". In: *Journal of Metamorphic Geology* 27.3, pp. 207–231. DOI: 10.1111/j.1525-1314.2009.00814.x.

Groppo, C., B. Lombardo, D. Castelli, and P. Cadoppi (2005). "Decompressional P-T Path in the Albite-Stability Field of Orthogneiss from the Uhp Unit of the Dora-Maira Massif". In: *Abstracts*. Graz.

Groppo, C., D. Castelli, and F. Rolfo (2007a). "HT, pre-Alpine relics in a spinel-bearing dolomite marble from the UHP Brossasco-Isasca Unit (Dora-Maira Massif, western Alps, Italy)". In: *Periodico di Mineralogia* 76, pp. 155–168. DOI: 10.2451/2007PM0022.

Groppo, C., S. Ferrando, M. Gilio, S. Botta, F. Nosenzo, G. Balestro, A. Festa, and F. Rolfo (2019). "What's in the sandwich? New P–T constraints for the (U)HP nappe stack of southern Dora-Maira Massif (Western Alps)". In: *European Journal of Mineralogy* 31.4, pp. 665–683. DOI: 10.1127/ejm/2019/0031-2860.

Groppo, C., B. Lombardo, D. Castelli, and R. Compagnoni (2007b). "Exhumation History of the UHPM Brossasco-Isasca Unit, Dora-Maira Massif, as Inferred from a Phengite-Amphibole Eclogite". In: *International Geology Review* 49.2, pp. 142–168. DOI: 10.2747/0020-6814.49.2.142.

Guggino, S. N. and R. L. Hervig (2011). "Synthesis and Characterization of Five New F-bearing Basalt Reference Materials (Fba Glasses): Quantifying the Fluorine Content of the Basaltic Glass Standards BCR-2G, BHVO-2G. GSA-1G, GSC-1G, GSD-1G, GSE-1G, ML3B-G, KL2-G, and ALV-519-4". In: *AGU Fall Meeting Abstracts* 31, pp. V31C–2535.

Guidotti, C. V. and F. P. Sassi (1976). "Muscovite as a petrogenetic indicator mineral in pelitic schists". In: *Neues Jahrbuch fur Mineralogie, Abhandlungen* 127, pp. 97–142.

Guo, S., B. Su, T. John, K. Zhao, P. Tang, Y. Chen, and Y. Li (2022). "Boron release and transfer induced by phengite breakdown in subducted impure metacarbonates". In: *Lithos* 408-409, p. 106548. DOI: 10.1016/j.lithos.2021.106548.

Gyomlai, T., P. Agard, H. R. Marschall, L. Jolivet, and A. Gerdes (2021). "Metasomatism and deformation of block-in-matrix structures in Syros: The role of inheritance and fluid-rock interactions along the subduction interface". In: *Lithos* 386-387, p. 105996. DOI: 10.1016/j.lithos.2021.105996.

Hacker, B. R. (2008). "H2O subduction beyond arcs". In: *Geochemistry, Geophysics, Geosystems* 9.3. DOI: 10.1029/2007GC001707.

Haendel, D., K. Mühle, H.-M. Nitzsche, G. Stiehl, and U. Wand (1986). "Isotopic variations of the fixed nitrogen in metamorphic rocks". In: *Geochimica et Cosmochimica Acta* 50.5, pp. 749–758. DOI: 10.1016/0016-7037(86)90351-0.

Halama, R. and G. Bebout (2021). "Earth's Nitrogen and Caron Cycles". In: *Space Science Reviews* 217.B1. ISSN: 1572-9672. DOI: 10.1007/s11214-021-00826-7.

Halama, R., G. E. Bebout, T. John, and M. Scambelluri (2014). "Nitrogen recycling in subducted mantle rocks and implications for the global nitrogen cycle". In: *International Journal of Earth Sciences* 103.7, pp. 2081–2099. DOI: 10.1007/s00531-012-0782-3.

Halama, R., G. E. Bebout, T. John, and V. Schenk (2010). "Nitrogen recycling in subducted oceanic lithosphere: The record in high- and ultrahigh-pressure metabasaltic rocks". In: *Geochimica et Cosmochimica Acta* 74.5, pp. 1636–1652. DOI: 10.1016/j.gca.2009.12.003.

Halama, R., G. E. Bebout, H. R. Marschall, and T. John (2017). "Fluid-induced breakdown of white mica controls nitrogen transfer during fluid–rock interaction in subduction zones". In: *International Geology Review* 59.5-6, pp. 702–720. DOI: 10.1080/00206814.2016.1233834.

Halama, R., M. Konrad-Schmolke, and J. C. M. De Hoog (2020). "Boron isotope record of peak metamorphic ultrahigh-pressure and retrograde fluid–rock interaction in white mica (Lago di Cignana, Western Alps)". In: *Contributions to Mineralogy and Petrology* 175.3, p. 20. DOI: 10.1007/s00410-020-1661-8.

Hall, A. (1989). "Ammonium in spilitized basalts of southwest England and its implications for the recycling of nitrogen". In: *Geochemical Journal* 23.1, pp. 19–23. DOI: 10.2343/geochemj.23.19.

Hanyu, T., I. Kaneoka, and K. Nagao (1999). "Noble gas study of HIMU and EM ocean island basalts in the Polynesian region". In: *Geochimica et Cosmochimica Acta* 63.7, pp. 1181–1201. DOI: 10.1016/S0016-7037(99)00044-7.

Harris, B. J. R., J. C. M. de Hoog, and R. Halama (2022). "The behaviour of nitrogen during subduction of oceanic crust: Insights from in situ SIMS analyses of high-pressure rocks". In: *Geochimica et Cosmochimica Acta* 321, pp. 16–34. DOI: 10.1016/j.gca.2022.01.018.

Harvey, J., C. J. Garrido, I. Savov, S. Agostini, J. A. Padrón-Navarta, C. Marchesi, V. López Sánchez-Vizcaíno, and M. T. Gómez-Pugnaire (2014). "11B-rich fluids in subduction zones: The role of antigorite dehydration in subducting slabs and boron isotope heterogeneity in the mantle". In: *Chemical Geology* 376, pp. 20–30. DOI: 10.1016/j.chemgeo.2014.03.015.

Heft, K. L., K. M. Gillis, M. A. Pollock, J. A. Karson, and E. M. Klein (2008). "Role of upwelling hydrothermal fluids in the development of alteration patterns at fast spreading ridges: Evidence from the sheeted dike complex at Pito Deep". In: *Geochemistry, Geophysics, Geosystems* 9.5. DOI: 10.1029/2007GC001926.

Hermann, J. (2003). "Experimental evidence for diamond-facies metamorphism in the Dora-Maira massif". In: *Lithos*. 6th International Eclogite Conference: Eclogites and Related High and Ultra-high Pressure Metamorphic Rocks 70.3, pp. 163–182. DOI: 10.1016/S0024-4937(03)00097-5.

Hernández-Uribe, D. and R. M. Palin (2019). "A revised petrological model for subducted oceanic crust: Insights from phase equilibrium modelling". In: *Journal of Metamorphic Geology* 37.6, pp. 745–768. DOI: 10.1111/jmg.12483.

Hernández-Uribe, D., R. M. Palin, K. A. Cone, and W. Cao (2020). "Petrological Implications of Seafloor Hydrothermal Alteration of Subducted Mid-Ocean Ridge Basalt". In: *Journal of Petrology* 61.9, egaa086. DOI: 10.1093/petrology/egaa086.

Herviou, C., A. Verlaguet, P. Agard, M. Locatelli, H. Raimbourg, B. Lefeuvre, and B. Dubacq (2021). "Along-dip variations of subduction fluids: The 30–80 km depth traverse of the Schistes Lustrés complex (Queyras-Monviso, W. Alps)". In: *Lithos* 394-395, p. 106168. DOI: 10.1016/j.lithos.2021.106168.

Holland, T. J. B. and R. Powell (2011). "An improved and extended internally consistent thermodynamic dataset for phases of petrological interest, involving a new equation of state for solids". In: *Journal of Metamorphic Geology* 29.3, pp. 333–383. DOI: 10.1111/j.1525-1314.2010.00923.x.

Honma, H. and Y. Itihara (1981). "Distribution of ammonium in minerals of metamorphic and granitic rocks". In: *Geochimica et Cosmochimica Acta* 45.6, pp. 983–988. DOI: 10.1016/0016-7037(81)90122-8.

Hughes, L., S. Cuthbert, A. Quas-Cohen, L. Ruzié-Hamilton, A. Pawley, G. Droop, I. Lyon, R. Tartèse, and R. Burgess (2021). "Halogens in Eclogite Facies Minerals from the Western Gneiss Region, Norway". In: *Minerals* 11.7. Number: 7 Publisher: Multidisciplinary Digital Publishing Institute, p. 760. DOI: 10.3390/min11070760.

Ishikawa, T. and E. Nakamura (1993). "Boron isotope systematics of marine sediments". In: *Earth and Planetary Science Letters* 117.3, pp. 567–580. DOI: 10.1016/0012-821X(93)90103-G.

— (1994). "Origin of the slab component in arc lavas from across-arc variation of B and Pb isotopes". In: *Nature* 370.6486, pp. 205–208. DOI: 10.1038/370205a0.

Jackson, C. R. M., E. Cottrell, and B. Andrews (2021). "Warm and oxidizing slabs limit ingassing efficiency of nitrogen to the mantle". In: *Earth and Planetary Science Letters* 553, p. 116615. DOI: 10.1016/j.epsl.2020.116615.

Jia, Y. (2006). "Nitrogen isotope fractionations during progressive metamorphism: A case study from the Paleozoic Cooma metasedimentary complex, southeastern Australia". In: *Geochimica et Cosmochimica Acta* 70.20, pp. 5201–5214. DOI: 10.1016/j.gca.2006.08.004.

Jochum, K. P. and B. Stoll (2008). "Reference materials for elemental and isotopic analyses by LA-(MC)-ICP-MS: Successes and outstanding needs". In: *Laser Ablation ICP-MS in the Earth Sciences: Current practices and outstanding issues* 40, pp. 147–168.

Jochum, K. P., M. Willbold, I. Raczek, B. Stoll, and K. Herwig (2005). "Chemical Characterisation of the USGS Reference Glasses GSA-1G, GSC-1G, GSD-1G, GSE-1G, BCR-2G, BHVO-2G and BIR-1G Using EPMA, ID-TIMS, ID-ICP-MS and LA-ICP-MS". In: *Geostandards and Geoanalytical Research* 29.3, pp. 285–302. DOI: https://doi.org/10.1111/j.1751-908X.2005.tb00901.x.

John, T., E. E. Scherer, K. Haase, and V. Schenk (2004). "Trace element fractionation during fluid-induced eclogitization in a subducting slab: trace element and Lu–Hf–Sm–Nd isotope systematics". In: *Earth and Planetary Science Letters* 227.3, pp. 441–456. DOI: 10.1016/j.epsl.2004.09.009.

John, T., E. E. Scherer, V. Schenk, P. Herms, R. Halama, and D. Garbe-Schönberg (2010). "Subducted seamounts in an eclogite-facies ophiolite sequence: the Andean Raspas Complex, SW Ecuador". In: *Contributions to Mineralogy and Petrology* 159.2, pp. 265–284. DOI: 10.1007/s00410-009-0427-0.

Johnson, B. and C. Goldblatt (2015). "The nitrogen budget of Earth". In: *Earth-Science Reviews* 148, pp. 150–173. DOI: 10.1016/j.earscirev.2015.05.006.

Kelley, K. A., T. Plank, J. Ludden, and H. Staudigel (2003). "Composition of altered oceanic crust at ODP Sites 801 and 1149". In: *Geochemistry, Geophysics, Geosystems* 4.6. DOI: 10.1029/2002GC000435.

Kerrick, D. M. and J. A. D. Connolly (2001). "Metamorphic devolatilization of subducted oceanic metabasalts: implications for seismicity, arc magmatism and volatile recycling". In: *Earth and Planetary Science Letters* 189.1, pp. 19–29. DOI: 10.1016/S0012-821X(01)00347-8.

Kessel, R., P. Ulmer, T. Pettke, M. W. Schmidt, and A. B. Thompson (2005). "The water–basalt system at 4 to 6 GPa: Phase relations and second critical endpoint in a K-free eclogite at 700 to 1400 °C". In: *Earth and Planetary Science Letters* 237.3, pp. 873–892. DOI: 10.1016/j.epsl.2005.06.018.

King, R. L., G. E. Bebout, M. Grove, T. Moriguti, and E. Nakamura (2007). "Boron and lead isotope signatures of subduction-zone mélange formation: Hybridization and fractionation along the slab–mantle interface beneath volcanic arcs". In: *Chemical Geology*. Geochemical processes responsible for element mobility from the slab to the surface 239.3, pp. 305–322. DOI: 10.1016/j.chemgeo.2007.01.009.

Klemme, S., H. R. Marschall, D. E. Jacob, S. Prowatke, and T. Ludwig (2011). "Trace-element partitioning and boron isotope fractionation between white mica and tourmaline". In: *The Canadian Mineralogist* 49.1, pp. 165–176. DOI: 10.3749/canmin.49.1.165.

Kodolányi, J., T. Pettke, C. Spandler, B. S. Kamber, and K. Gméling (2012). "Geochemistry of Ocean Floor and Fore-arc Serpentinites: Constraints on the Ultramafic Input to Subduction Zones". In: *Journal of Petrology* 53.2, pp. 235–270. DOI: 10.1093/petrology/egr058.

Konrad-Schmolke, M. and R. Halama (2014). "Combined thermodynamic–geochemical modeling in metamorphic geology: Boron as tracer of fluid–rock interaction". In: *Lithos* 208-209, pp. 393–414. DOI: 10.1016/j.lithos.2014.09.021.

Konrad-Schmolke, M., P. J. O'Brien, and T. Zack (2011). "Fluid Migration above a Subducted Slab—Constraints on Amount, Pathways and Major Element Mobility from Partially Overprinted Eclogite-facies Rocks (Sesia Zone, Western Alps)". In: *Journal of Petrology* 52.3, pp. 457–486. DOI: 10.1093/petrology/egq087.

Konrad-Schmolke, M., R. Halama, and V. C. Manea (2016). "Slab mantle dehydrates beneath Kamchatka—Yet recycles water into the deep mantle". In: *Geochemistry, Geophysics, Geosystems* 17.8, pp. 2987–3007. DOI: 10.1002/2016GC006335.

Kouketsu, Y. and M. Enami (2011). "Calculated stabilities of sodic phases in the Sambagawa metapelites and their implications". In: *Journal of Metamorphic Geology* 29.3, pp. 301–316. DOI: 10.1111/j.1525-1314.2010.00919.x.

Kowalski, P. M., B. Wunder, and S. Jahn (2013). "Ab initio prediction of equilibrium boron isotope fractionation between minerals and aqueous fluids at high P and T". In: *Geochimica et Cosmochimica Acta* 101, pp. 285–301. DOI: 10.1016/j.gca.2012.10.007.

Krogh, E. J., C. W. Oh, and J. C. Liou (1994). "Polyphase and anticlockwise P-T evolution for Franciscan eclogites and blueschists from Jenner, California, USA". In: *Journal of Metamorphic Geology* 12.2, pp. 121–134. DOI: 10.1111/j.1525-1314.1994.tb00008.x.

Kruhl, J. H., E. Griesshaber, W. W. Schmahl, and R. Wirth (2024). "Fracturing and widening of grain boundary networks in quartz, plagioclase and olivine crystal aggregates during exhumation at low P-T conditions". In: *Journal of Structural Geology* 179, p. 105032. DOI: 10.1016/j.jsg.2023.105032.

Kruhl, J. H., R. Wirth, and L. F. G. Morales (2013). "Quartz grain boundaries as fluid pathways in metamorphic rocks". In: *Journal of Geophysical Research: Solid Earth* 118.5, pp. 1957–1967. DOI: 10.1002/jgrb.50099.

Kupriyanov, I. N., A. G. Sokol, Y. V. Seryotkin, A. N. Kruk, A. A. Tomilenko, and T. A. Bul'bak (2023). "Nitrogen fractionation in mica metapelite under hot subduction conditions: Implications

for nitrogen ingassing to the mantle". In: *Chemical Geology* 628, p. 121476. DOI: 10.1016/j.chemgeo.2023.121476.

Labidi, J., E. D. Young, T. P. Fischer, P. H. Barry, C. J. Ballentine, and J. M. de Moor (2021). "Recycling of nitrogen and light noble gases in the Central American subduction zone: Constraints from 15N15N". In: *Earth and Planetary Science Letters* 571, p. 117112. DOI: 10.1016/j.epsl.2021.117112.

Lafay, R., F. Deschamps, S. Schwartz, S. Guillot, M. Godard, B. Debret, and C. Nicollet (2013). "High-pressure serpentinites, a trap-and-release system controlled by metamorphic conditions: Example from the Piedmont zone of the western Alps". In: *Chemical Geology* 343, pp. 38–54. DOI: 10.1016/j.chemgeo.2013.02.008.

Lardeaux, J. M., S. Schwartz, P. Tricart, A. Paul, S. Guillot, N. Béthoux, and F. Masson (2006). "A crustal-scale cross-section of the south-western Alps combining geophysical and geological imagery". In: *Terra Nova* 18.6, pp. 412–422. DOI: 10.1111/j.1365-3121.2006.00706.x.

Lee, J. H., D. R. Peacor, D. D. Lewis, and R. P. Wintsch (1984). "Chlorite-illite/muscovite interlayered and interstratified crystals: A TEM/STEM study". In: *Contributions to Mineralogy and Petrology* 88.4, pp. 372–385. DOI: 10.1007/BF00376762.

Leeman, W. and V. Sisson (1996). "Geochemistry of boron and its implications for crustal and mantle processes". In: *Boron. Rev. Mineral.* Vol. 33, pp. 645–707.

Lesne, P., S. C. Kohn, J. Blundy, F. Witham, R. E. Botcharnikov, and H. Behrens (2011). "Experimental Simulation of Closed-System Degassing in the System Basalt–H2O–CO2–S–Cl". In: *Journal of Petrology* 52.9, pp. 1737–1762. DOI: 10.1093/petrology/egr027.

Li, H., J. Hermann, and L. Zhang (2022). "Melting of subducted slab dictates trace element recycling in global arcs". In: *Science Advances* 8.2, eabh2166. DOI: 10.1126/sciadv.abh2166.

Li, J.-L., R. Klemd, J. Gao, and M. Meyer (2012). "Coexisting carbonate-bearing eclogite and blueschist in SW Tianshan, China: Petrology and phase equilibria". In: *Journal of Asian Earth Sciences* 60, pp. 174–187. DOI: 10.1016/j.jseaes.2012.08.015.

Li, K., G.-Y. Li, Y.-F. Du, W. Han, J. Zhang, L.-H. Chen, J.-B. Zhou, and L. Li (2021a). "Intraslab remobilization of nitrogen during early subduction facilitates deep nitrogen recycling: Insights

from the blueschists in the Heilongjiang Complex in NE China". In: *Chemical Geology* 583, p. 120474. DOI: 10.1016/j.chemgeo.2021.120474.

Li, K. and L. Li (2022). "Nitrogen enrichments in sheeted dikes and gabbros from DSDP/ODP/IODP Hole 504B and 1256D: Insights into nitrogen recycling in Central America and global subduction zones". In: *Geochimica et Cosmochimica Acta* 335, pp. 197–210. DOI: 10.1016/j.gca.2022.08.036.

— (2023a). "Alteration enrichment of nitrogen in the gabbroic oceanic crust: Implications for global subducting nitrogen budget and subduction-zone nitrogen recycling". In: *Geochimica et Cosmochimica Acta* 351, pp. 96–107. DOI: 10.1016/j.gca.2023.04.029.

— (2023b). "Nitrogen enrichment in the altered upper oceanic crust: A new perspective on constraining the global subducting nitrogen budget and implications for subduction-zone nitrogen recycling". In: *Earth and Planetary Science Letters* 602, p. 117960. DOI: 10.1016/j.epsl.2022.117960.

Li, K., A. J. Yu, P. H. Barry, and L. Li (2023a). "Oceanic serpentinites: A potentially critical reservoir for deep nitrogen recycling". In: *Geology*. DOI: 10.1130/G51464.1.

Li, L. and G. E. Bebout (2005). "Carbon and nitrogen geochemistry of sediments in the Central American convergent margin: Insights regarding subduction input fluxes, diagenesis, and paleoproductivity". In: *Journal of Geophysical Research: Solid Earth* 110.B11. DOI: 10.1029/2004JB003276.

Li, L., G. E. Bebout, and B. D. Idleman (2007). "Nitrogen concentration and δ^{15}N of altered oceanic crust obtained on ODP Legs 129 and 185: Insights into alteration-related nitrogen enrichment and the nitrogen subduction budget". In: *Geochimica et Cosmochimica Acta* 71.9, pp. 2344–2360. DOI: 10.1016/j.gca.2007.02.001.

Li, L., K. Li, Y. Li, J. Zhang, Y. Du, and M. Labbe (2021b). "Recommendations for offline combustion-based nitrogen isotopic analysis of silicate minerals and rocks". In: *Rapid Communications in Mass Spectrometry* 35.10, e9075. DOI: 10.1002/rcm.9075.

Li, L., Y. Qi, Y. Chen, K. Li, F. Huang, and P. Cartigny (2023b). "Nitrogen isotopic insight into sediment recycling in the southern Lesser Antilles arc: Implication to subduction-zone nitrogen recycling". In: *Earth and Planetary Science Letters* 619, p. 118307. DOI: 10.1016/j.epsl.2023.118307.

Li, L., Y.-F. Zheng, P. Cartigny, and J. Li (2014). "Anomalous nitrogen isotopes in ultrahigh-pressure metamorphic rocks from the Sulu orogenic belt: Effect of abiotic nitrogen reduction during fluid–rock interaction". In: *Earth and Planetary Science Letters* 403, pp. 67–78. DOI: 10.1016/j.epsl.2014.06.029.

Li, Y., R. Huang, M. Wiedenbeck, and H. Keppler (2015). "Nitrogen distribution between aqueous fluids and silicate melts". In: *Earth and Planetary Science Letters* 411, pp. 218–228. DOI: 10.1016/j.epsl.2014.11.050.

Liu, H., Y.-Y. Xue, T. Yang, X. Jin, C.-F. You, C.-T. Lin, W.-D. Sun, and J. Deng (2022). "Fluid-rock interactions at shallow depths in subduction zone: Insights from trace elements and B isotopic composition of metabasites from the Mariana forearc". In: *Lithos* 422-423, p. 106730. DOI: 10.1016/j.lithos.2022.106730.

Luisier, C., L. P. Baumgartner, B. Putlitz, and T. Vennemann (2021). "Whiteschist genesis through metasomatism and metamorphism in the Monte Rosa nappe (Western Alps)". In: *Contributions to Mineralogy and Petrology* 176.1, p. 10. DOI: 10.1007/s00410-020-01759-0.

Maffeis, A., S. Ferrando, J. A. D. Connolly, C. Groppo, M. L. Frezzotti, and D. Castelli (2021). "Thermodynamic analysis of HP-UHP fluid inclusions: The solute load and chemistry of metamorphic fluids". In: *Geochimica et Cosmochimica Acta* 315, pp. 207–229. DOI: 10.1016/j.gca.2021.08.044.

Mallik, A., Y. Li, and M. Wiedenbeck (2018). "Nitrogen evolution within the Earth's atmosphere–mantle system assessed by recycling in subduction zones". In: *Earth and Planetary Science Letters* 482, pp. 556–566. DOI: 10.1016/j.epsl.2017.11.045.

Mallik, A., A. M. Rebaza, P. Kapp, L. Li, Y. Du, A. Al Shams, and E. H. G Cooperdock (2023). "Metabasic Rocks as Important Nitrogen Carriers to Forearc Depths: Implications for Deep Nitrogen Cycling". In: *Geochimica et Cosmochimica Acta*. DOI: 10.1016/j.gca.2023.10.007.

Manatschal, G. and O. Müntener (2009). "A type sequence across an ancient magma-poor ocean–continent transition: the example of the western Alpine Tethys ophiolites". In: *Tectonophysics*. Tethyan tectonics of the Mediterranean region: some recent advances 473.1, pp. 4–19. DOI: 10.1016/j.tecto.2008.07.021.

Manning, C. E. (2004). "The chemistry of subduction-zone fluids". In: *Earth and Planetary Science Letters* 223.1, pp. 1–16. DOI: 10.1016/j.epsl.2004.04.030.

Marger, K., C. Luisier, L. P. Baumgartner, B. Putlitz, B. L. Dutrow, A.-S. Bouvier, and A. Dini (2019). "Origin of Monte Rosa whiteschist from in-situ tourmaline and quartz oxygen isotope analysis by SIMS using new tourmaline reference materials". In: *American Mineralogist* 104.10, pp. 1503–1520. DOI: 10.2138/am-2019-7012.

Marschall, H. R. (2005). "Lithium, Beryllium and Boron in High-Pressure Metamorphic Rocks from Syros (Greece)". Thesis. DOI: 10.11588/heidok.00005634.

— (2018). "Boron Isotopes in the Ocean Floor Realm and the Mantle". In: *Boron Isotopes: The Fifth Element*. Ed. by H. Marschall and G. Foster. Advances in Isotope Geochemistry. Cham: Springer International Publishing, pp. 189–215. ISBN: 978-3-319-64666-4. DOI: 10.1007/978-3-319-64666-4_8.

Marschall, H. R., R. Altherr, T. Ludwig, A. Kalt, K. Gméling, and Z. Kasztovszky (2006a). "Partitioning and budget of Li, Be and B in high-pressure metamorphic rocks". In: *Geochimica et Cosmochimica Acta* 70.18, pp. 4750–4769. DOI: 10.1016/j.gca.2006.07.006.

Marschall, H. R., R. Altherr, and L. Rüpke (2007). "Squeezing out the slab — modelling the release of Li, Be and B during progressive high-pressure metamorphism". In: *Chemical Geology*. Geochemical processes responsible for element mobility from the slab to the surface 239.3, pp. 323–335. DOI: 10.1016/j.chemgeo.2006.08.008.

Marschall, H. R., T. Ludwig, R. Altherr, A. Kalt, and S. Tonarini (2006b). "Syros Metasomatic Tourmaline: Evidence for Very High-δ^{11}B Fluids in Subduction Zones". In: *Journal of Petrology* 47.10, pp. 1915–1942. DOI: 10.1093/petrology/egl031.

Marschall, H. R., V. D. Wanless, N. Shimizu, P. A. E. Pogge von Strandmann, T. Elliott, and B. D. Monteleone (2017). "The boron and lithium isotopic composition of mid-ocean ridge basalts and the mantle". In: *Geochimica et Cosmochimica Acta* 207, pp. 102–138. DOI: 10.1016/j.gca.2017.03.028.

Martin, C., K. E. Flores, A. Vitale-Brovarone, S. Angiboust, and G. E. Harlow (2020). "Deep mantle serpentinization in subduction zones: Insight from in situ B isotopes in slab and mantle wedge serpentinites". In: *Chemical Geology* 545, p. 119637. DOI: 10.1016/j.chemgeo.2020.119637.

Martin, C., E. Ponzevera, and G. Harlow (2015). "In situ lithium and boron isotope determinations in mica, pyroxene, and serpentine by LA-MC-ICP-MS". In: *Chemical Geology* 412, pp. 107–116. DOI: 10.1016/j.chemgeo.2015.07.022.

Martin, S., G. Rebay, J.-R. Kienast, and C. Mével (2008). "An eclogitised oceanic palaeo-hydrothermal field from the St. Marcel Valley (Italian Western Alps)". In: *Ofioliti* 33.1, pp. 49–63. DOI: 10.4454/ofioliti.v33i1.359.

Marty, B., L. Zimmermann, M. Pujol, R. Burgess, and P. Philippot (2013). "Nitrogen Isotopic Composition and Density of the Archean Atmosphere". In: *Science* 342.6154. Publisher: American Association for the Advancement of Science Section: Report, pp. 101–104. DOI: 10.1126/science.1240971.

Massonne, H. J. and W. Schreyer (1987). "Phengite geobarometry based on the limiting assemblage with K-feldspar, phlogopite, and quartz". In: *Contributions to Mineralogy and Petrology* 96.2, pp. 212–224. DOI: 10.1007/BF00375235.

Massonne, H.-J. and M. Sobiech (2007). "Paragonite: Why Is It So Rare in Medium-Temperature High-Pressure Rocks?" In: *International Geology Review* 49.4. Publisher: Taylor & Francis _eprint: https://doi.org/10.2747/0020-6814.49.4.301, pp. 301–312. DOI: 10.2747/0020-6814.49.4.301.

Melzer, S. and B. Wunder (2000). "Island-arc basalt alkali ratios: Constraints from phengite-fluid partitioning experiments". In: *Geology* 28.7, pp. 583–586. DOI: 10.1130/0091-7613(2000)28<583:IBARCF>2.0.CO;2.

Menold, C. A., M. Grove, N. E. Sievers, C. E. Manning, A. Yin, E. D. Young, and K. Ziegler (2016). "Argon, oxygen, and boron isotopic evidence documenting 40ArE accumulation in phengite during water-rich high-pressure subduction metasomatism of continental crust". In: *Earth and Planetary Science Letters* 446, pp. 56–67. DOI: 10.1016/j.epsl.2016.04.010.

Mikhail, S., P. H. Barry, and D. A. Sverjensky (2017). "The relationship between mantle pH and the deep nitrogen cycle". In: *Geochimica et Cosmochimica Acta* 209, pp. 149–160. DOI: 10.1016/j.gca.2017.04.007.

Mikhail, S. and D. A. Sverjensky (2014). "Nitrogen speciation in upper mantle fluids and the origin of Earth's nitrogen-rich atmosphere". In: *Nature Geoscience* 7.11. Number: 11 Publisher: Nature Publishing Group, pp. 816–819. DOI: 10.1038/ngeo2271.

Mingram, B. and K. Bräuer (2001). "Ammonium concentration and nitrogen isotope composition in metasedimentary rocks from different tectonometamorphic units of the European Variscan Belt". In: *Geochimica et Cosmochimica Acta* 65.2, pp. 273–287. DOI: 10.1016/S0016-7037(00)00517-2.

Mitchell, E., T. Fischer, D. Hilton, E. Hauri, A. Shaw, J. De Moor, Z. Sharp, and K. Kazahaya (2010). "Nitrogen sources and recycling at subduction zones: Insights from the Izu-Bonin-Mariana arc". In: *Geochemistry, Geophysics, Geosystems* 11.2. DOI: 10.1029/2009GC002783.

Miyamoto, A., M. Enami, M. Tsuboi, and K. Yokoyama (2007). "Peak conditions of kyanite-bearing quartz eclogites in the Sanbagawa metamorphic belt, central Shikoku, Japan". In: *Journal of Mineralogical and Petrological Sciences* 102.6, pp. 352–367. DOI: 10.2465/jmps.070120.

Mohapatra, R. K. and S. V. S. Murty (2000). "Origin of air-like noble gases in oceanic basalts". In: *Geophysical Research Letters* 27.11, pp. 1583–1586. DOI: 10.1029/1999GL008465.

Moine, B., C. Guillot, and F. Gibert (1994). "Controls of the composition of nitrogen-rich fluids originating from reaction with graphite and ammonium-bearing biotite". In: *Geochimica et Cosmochimica Acta* 58.24, pp. 5503–5523. DOI: 10.1016/0016-7037(94)90246-1.

Molina, J. F. and S. Poli (2000). "Carbonate stability and fluid composition in subducted oceanic crust: an experimental study on H2O–CO2-bearing basalts". In: *Earth and Planetary Science Letters* 176.3, pp. 295–310. DOI: 10.1016/S0012-821X(00)00021-2.

Moores, E. M., F. J. Vine, P. W. Gast, E. C. Bullard, J. R. Cann, and D. H. Matthews (1997). "The Troodos Massif, Cyprus and other ophiolites as oceanic crust: evaluation and implications". In: *Philosophical Transactions of the Royal Society of London. Series A, Mathematical and Physical Sciences* 268.1192, pp. 443–467. DOI: 10.1098/rsta.1971.0006.

Morgan, G. B. and D. London (1989). "Experimental reactions of amphibolite with boron-bearing aqueous fluids at 200 MPa: implications for tourmaline stability and partial melting in mafic rocks". In: *Contributions to Mineralogy and Petrology* 102.3, pp. 281–297. DOI: 10.1007/BF00373721.

Nabelek, P. I. (1987). "General equations for modeling fluid/rock interaction using trace elements and isotopes". In: *Geochimica et Cosmochimica Acta* 51.6, pp. 1765–1769. DOI: 10.1016/0016-7037(87)90354-1.

Nagurney, A. B., M. J. Caddick, R. D. Law, N. L. Ross, and S. C. Kruckenberg (2021). "Crystallographically controlled void space at grain boundaries in the Harkless quartzite". In: *Journal of Structural Geology* 143, p. 104235. DOI: 10.1016/j.jsg.2020.104235.

Nakano, T. and E. Nakamura (2001). "Boron isotope geochemistry of metasedimentary rocks and tourmalines in a subduction zone metamorphic suite". In: *Physics of the Earth and Planetary Interiors*. Processes and Consequences of Deep Subduction 127.1, pp. 233–252. DOI: 10.1016/S0031-9201(01)00230-8.

Nehlig, P., T. Juteau, V. Bendel, and J. Cotten (1994). "The root zones of oceanic hydrothermal systems: Constraints from the Samail ophiolite (Oman)". In: *Journal of Geophysical Research: Solid Earth* 99.B3, pp. 4703–4713. DOI: 10.1029/93JB02663.

Nishizawa, M., Y. Sano, Y. Ueno, and S. Maruyama (2007). "Speciation and isotope ratios of nitrogen in fluid inclusions from seafloor hydrothermal deposits at 3.5 Ga". In: *Earth and Planetary Science Letters* 254.3, pp. 332–344. DOI: 10.1016/j.epsl.2006.11.044.

Nowlan, E. U, H. P Schertl, and W Schreyer (2000). "Garnet–omphacite–phengite thermobarometry of eclogites from the coesite-bearing unit of the southern Dora-Maira Massif, Western Alps". In: *Lithos* 52.1, pp. 197–214. DOI: 10.1016/S0024-4937(99)00091-2.

Ota, T., K. Kobayashi, T. Kunihiro, and E. Nakamura (2008). "Boron cycling by subducted lithosphere; insights from diamondiferous tourmaline from the Kokchetav ultrahigh-pressure metamorphic belt". In: *Geochimica et Cosmochimica Acta* 72.14, pp. 3531–3541. DOI: 10.1016/j.gca.2008.05.002.

Otsuki, M. and S. Banno (1990). "Prograde and retrograde metamorphism of hematitebearing basic schists in the Sanbagawa belt in central Shikoku". In: *Journal of Metamorphic Geology* 8.4, pp. 425–439. DOI: 10.1111/j.1525-1314.1990.tb00629.x.

Pabst, S., T. Zack, I. P. Savov, T. Ludwig, D. Rost, S. Tonarini, and E. P. Vicenzi (2012). "The fate of subducted oceanic slabs in the shallow mantle: Insights from boron isotopes and light element composition of metasomatized blueschists from the Mariana forearc". In: *Lithos* 132-133, pp. 162–179. DOI: 10.1016/j.lithos.2011.11.010.

Padrón-Navarta, J. A., V. L. Sánchez-Vizcaíno, J. Hermann, J. A. D. Connolly, C. J. Garrido, M. T. Gómez-Pugnaire, and C. Marchesi (2013). "Tschermak's substitution in antigorite and

consequences for phase relations and water liberation in high-grade serpentinites". In: *Lithos. Serpentinites from mid-oceanic ridges to subduction* 178, pp. 186–196. DOI: 10.1016/j.lithos.2013.02.001.

Pagé, L., K. Hattori, J. C. M. de Hoog, and A. I. Okay (2016). "Halogen (F, Cl, Br, I) behaviour in subducting slabs: A study of lawsonite blueschists in western Turkey". In: *Earth and Planetary Science Letters* 442, pp. 133–142. DOI: 10.1016/j.epsl.2016.02.054.

Palya, A. P., I. S. Buick, and G. E. Bebout (2011). "Storage and mobility of nitrogen in the continental crust: Evidence from partially melted metasedimentary rocks, Mt. Stafford, Australia". In: *Chemical Geology* 281.3, pp. 211–226. DOI: 10.1016/j.chemgeo.2010.12.009.

Pawlig, S. and L. P. Baumgartner (2001). "Geochemistry of a talc-kyanite-chloritoid shear zone within the Monte Rosa granite, Val d'Ayas, Italy". In: *Schweizerische Mineralogische und Petrographische Mitteilungen* 81, pp. 329–346. DOI: 10.5169/seals-61696.

Peacock, S. A. (1990). "Fluid Processes in Subduction Zones". In: *Science* 248.4953. Publisher: American Association for the Advancement of Science Section: Articles, pp. 329–337. DOI: 10.1126/science.248.4953.329.

Peacock, S. M. (2020). "Advances in the thermal and petrologic modeling of subduction zones". In: *Geosphere* 16.4, pp. 936–952. DOI: 10.1130/GES02213.1.

Peacock, S. M. and R. L. Hervig (1999). "Boron isotopic composition of subduction-zone metamorphic rocks". In: *Chemical Geology* 160.4, pp. 281–290. DOI: 10.1016/S0009-2541(99)00103-5.

Pearce, J. (1996). "A User's Guide to Basalt Discrimination Diagrams". In: *Geol. Assoc. Canada Short Course Notes* 12, pp. 79–113.

Penniston-Dorland, S. C., M. J. Kohn, and C. E. Manning (2015). "The global range of subduction zone thermal structures from exhumed blueschists and eclogites: Rocks are hotter than models". In: *Earth and Planetary Science Letters* 428, pp. 243–254. DOI: 10.1016/j.epsl.2015.07.031.

Penniston-Dorland, S. C., S. S. Sorensen, R. D. Ash, and S. V. Khadke (2010). "Lithium isotopes as a tracer of fluids in a subduction zone mélange: Franciscan Complex, CA". In: *Earth and Planetary Science Letters* 292.1, pp. 181–190. DOI: 10.1016/j.epsl.2010.01.034.

Perfit, M. R., D. A. Gust, A. E. Bence, R. J. Arculus, and S. R. Taylor (1980). "Chemical characteristics of island-arc basalts: Implications for mantle sources". In: *Chemical Geology*. 17th Meeting

of the International Union of Geodesy and Geophysics 30.3, pp. 227–256. DOI: 10.1016/0009-2541(80)90107-2.

Philippot, P., V. Busigny, M. Scambelluri, and P. Cartigny (2007). "Oxygen and nitrogen isotopes as tracers of fluid activities in serpentinites and metasediments during subduction". In: *Mineralogy and Petrology* 91.1, pp. 11–24. DOI: 10.1007/s00710-007-0183-7.

Philippot, P., P. Chevallier, C. Chopin, and J. Dubessy (1995). "Fluid composition and evolution in coesite-bearing rocks (Dora-Maira massif, Western Alps): implications for element recycling during subduction". In: *Contributions to Mineralogy and Petrology* 121.1, p. 29. DOI: 10.1007/s004100050088.

Philippot, P. and J. Selverstone (1991). "Trace-element-rich brines in eclogitic veins: implications for fluid composition and transport during subduction". In: *Contributions to Mineralogy and Petrology* 106.4, pp. 417–430. DOI: 10.1007/BF00321985.

Piccoli, F., J. J. Ague, X. Chu, M. Tian, and A. Vitale Brovarone (2021). "Field-Based Evidence for Intra-Slab High-Permeability Channel Formation at Eclogite-Facies Conditions During Subduction". In: *Geochemistry, Geophysics, Geosystems* 22.3, e2020GC009520. DOI: 10.1029/2020GC009520.

Pitcairn, I. K., D. A. H. Teagle, R. Kerrich, D. Craw, and T. S. Brewer (2005). "The behavior of nitrogen and nitrogen isotopes during metamorphism and mineralization: Evidence from the Otago and Alpine Schists, New Zealand". In: *Earth and Planetary Science Letters* 233.1, pp. 229–246. DOI: 10.1016/j.epsl.2005.01.029.

Plank, T. (2014). "The Chemical Composition of Subducting Sediments". In: *Treatise on Geochemistry (Second Edition)*. Ed. by H. D. Holland and K. K. Turekian. Oxford: Elsevier, pp. 607–629. ISBN: 978-0-08-098300-4. DOI: 10.1016/B978-0-08-095975-7.00319-3.

Plank, T. and C. H. Langmuir (1993). "Tracing trace elements from sediment input to volcanic output at subduction zones". In: *Nature* 362.6422. Number: 6422 Publisher: Nature Publishing Group, pp. 739–743. DOI: 10.1038/362739a0.

Plessen, B., D. E. Harlov, D. Henry, and C. V. Guidotti (2010). "Ammonium loss and nitrogen isotopic fractionation in biotite as a function of metamorphic grade in metapelites from western Maine, USA". In: *Geochimica et Cosmochimica Acta* 74.16, pp. 4759–4771. DOI: 10.1016/j.gca.2010.05.021.

Plümper, O., T. John, Y. Y. Podladchikov, J. C. Vrijmoed, and M. Scambelluri (2017). "Fluid escape from subduction zones controlled by channel-forming reactive porosity". In: *Nature Geoscience* 10.2. Number: 2 Publisher: Nature Publishing Group, pp. 150–156. DOI: 10.1038/ngeo2865.

Poli, S. and M. W. Schmidt (2002). "Petrology of Subducted Slabs". In: *Annual Review of Earth and Planetary Sciences* 30.1, pp. 207–235. DOI: 10.1146/annurev.earth.30.091201.140550.

Powell, R. and T. J. B. Holland (1988). "An internally consistent dataset with uncertainties and correlations: 3. Applications to geobarometry, worked examples and a computer program". In: *Journal of Metamorphic Geology* 6.2, pp. 173–204. DOI: 10.1111/j.1525-1314.1988.tb00415.x.

Pöter, B., M. Gottschalk, and W. Heinrich (2004). "Experimental determination of the ammonium partitioning among muscovite, K-feldspar, and aqueous chloride solutions". In: *Lithos* 74.1, pp. 67–90. DOI: 10.1016/j.lithos.2004.01.002.

Ravna, E. J. K. and M. P. Terry (2004). "Geothermobarometry of UHP and HP eclogites and schists – an evaluation of equilibria among garnet–clinopyroxene–kyanite–phengite–coesite/quartz". In: *Journal of Metamorphic Geology* 22.6, pp. 579–592. DOI: 10.1111/j.1525-1314.2004.00534.x.

Raymond, L. A. (2017). "A metasomatic setting, the Russian River Arch, and gravitational emplacement in the history of eclogites at the classic eclogite locality of Jenner, California, USA". In: *International Geology Review* 59.5-6. Publisher: Taylor & Francis _eprint: https://doi.org/10.1080/00206814.2016 pp. 577–598. DOI: 10.1080/00206814.2016.1213143.

Reinecke, T. (1998). "Prograde high- to ultrahigh-pressure metamorphism and exhumation of oceanic sediments at Lago di Cignana, Zermatt-Saas Zone, western Alps". In: *Lithos* 42.3, pp. 147–189. DOI: 10.1016/S0024-4937(97)00041-8.

Rieder, M., G. Cavazzini, Y. S. D'yakonov, V. A. Frank-Kamenetskii, G. Gottardi, S. Guggenheim, P. W. Koval', G. Müller, A. M. R. Neiva, E. W. Radoslovich, J.-L. Robert, F. P. Sassi, H. Takeda, Z. Weiss, and D. R. Wones (1998). "Nomenclature of the Micas". In: *Clays and Clay Minerals* 46.5, pp. 586–595. DOI: 10.1346/CCMN.1998.0460513.

Romer, R. L., A. Meixner, and K. Hahne (2014). "Lithium and boron isotopic composition of sedimentary rocks — The role of source history and depositional environment: A 250Ma record from the Cadomian orogeny to the Variscan orogeny". In: *Gondwana Research* 26.3, pp. 1093–1110. DOI: 10.1016/j.gr.2013.08.015.

Rubatto, D. (2017). "Zircon: The Metamorphic Mineral". In: *Reviews in Mineralogy and Geochemistry* 83.1, pp. 261–295. DOI: 10.2138/rmg.2017.83.9.

Rubatto, D., D. Gebauer, and M. Fanning (1998). "Jurassic formation and Eocene subduction of the Zermatt–Saas-Fee ophiolites: implications for the geodynamic evolution of the Central and Western Alps". In: *Contributions to Mineralogy and Petrology* 132.3, pp. 269–287. DOI: 10.1007/s004100050421.

Rubatto, D. and J. Hermann (2001). "Exhumation as fast as subduction?" In: *Geology* 29.1, pp. 3–6. DOI: 10.1130/0091-7613(2001)029<0003:EAFAS>2.0.CO;2.

Ryan, J. G. and C. H. Langmuir (1993). "The systematics of boron abundances in young volcanic rocks". In: *Geochimica et Cosmochimica Acta* 57.7, pp. 1489–1498. DOI: 10.1016/0016-7037(93)90008-K.

Sadofsky, S. J. and G. E. Bebout (2000). "Ammonium partitioning and nitrogen-isotope fractionation among coexisting micas during high-temperature fluid-rock interactions: examples from the New England Appalachians". In: *Geochimica et Cosmochimica Acta* 64.16, pp. 2835–2849. DOI: 10.1016/S0016-7037(00)00393-8.

Sadofsky, S. J. and G. E. Bebout (2004). "Nitrogen geochemistry of subducting sediments: New results from the Izu-Bonin-Mariana margin and insights regarding global nitrogen subduction". In: *Geochemistry, Geophysics, Geosystems* 5.3. DOI: 10.1029/2003GC000543.

Sasaki, A. and S. Ishihara (1979). "Sulfur isotopic composition of the magnetite-series and ilmenite-series granitoids in Japan". In: *Contributions to Mineralogy and Petrology* 68.2, pp. 107–115. DOI: 10.1007/BF00371893.

Scambelluri, M., O. Müntener, L. Ottolini, T. T. Pettke, and R. Vannucci (2004). "The fate of B, Cl and Li in the subducted oceanic mantle and in the antigorite breakdown fluids". In: *Earth and Planetary Science Letters* 222.1, pp. 217–234. DOI: 10.1016/j.epsl.2004.02.012.

Scambelluri, M., T. Pettke, and E. Cannaò (2015). "Fluid-related inclusions in Alpine high-pressure peridotite reveal trace element recycling during subduction-zone dehydration of serpentinized mantle (Cima di Gagnone, Swiss Alps)". In: *Earth and Planetary Science Letters* 429, pp. 45–59. DOI: 10.1016/j.epsl.2015.07.060.

Schertl, H.-P., W. Schreyer, and C. Chopin (1991). "The pyrope-coesite rocks and their country rocks at Parigi, Dora Maira Massif, Western Alps: detailed petrography, mineral chemistry and PT-path". In: *Contributions to Mineralogy and Petrology* 108.1, pp. 1–21. DOI: 10.1007/BF00307322.

Schertl, H.-P. and W. Schreyer (2008). "Geochemistry of coesite-bearing pyrope quartzite and related rocks from the Dora-Maira Massif, Western Alps". In: *Eur.J.Mineral.* 20, pp. 791–809. DOI: 10.1127/0935-1221/2008/0020-1862.

Schmidt, C., R. Thomas, and W. Heinrich (2005). "Boron speciation in aqueous fluids at 22 to 600°C and 0.1 MPa to 2 GPa". In: *Geochimica et Cosmochimica Acta* 69.2, pp. 275–281. DOI: 10.1016/j.gca.2004.06.018.

Schmidt, M. W. and S. Poli (2014). "Devolatilization During Subduction". In: *Treatise on Geochemistry (Second Edition)*. Ed. by H. D. Holland and K. K. Turekian. Oxford: Elsevier, pp. 669–701. ISBN: 978-0-08-098300-4. DOI: 10.1016/B978-0-08-095975-7.00321-1.

Schmidt, M. W. (1996). "Experimental Constraints on Recycling of Potassium from Subducted Oceanic Crust". In: *Science* 272.5270, pp. 1927–1930. DOI: 10.1126/science.272.5270.1927.

Schmidt, M. W. and S. Poli (1998). "Experimentally based water budgets for dehydrating slabs and consequences for arc magma generation". In: *Earth and Planetary Science Letters* 163.1, pp. 361–379. DOI: 10.1016/S0012-821X(98)00142-3.

Schmidt, M. W., D. Vielzeuf, and E. Auzanneau (2004). "Melting and dissolution of subducting crust at high pressures: the key role of white mica". In: *Earth and Planetary Science Letters* 228.1, pp. 65–84. DOI: 10.1016/j.epsl.2004.09.020.

Schramm, B., C. W. Devey, K. M. Gillis, and K. Lackschewitz (2005). "Quantitative assessment of chemical and mineralogical changes due to progressive low-temperature alteration of East Pacific Rise basalts from 0 to 9 Ma". In: *Chemical Geology* 218.3, pp. 281–313. DOI: 10.1016/j.chemgeo.2005.01.011.

Schreyer, W. (1973). "Whiteschist: A High-Pressure Rock and its Geologic Significance". In: *The Journal of Geology* 81.6, pp. 735–739. DOI: 10.1086/627926.

Schroeder, P. A. and E. D. Ingall (1994). "A method for the determination of nitrogen in clays, with application to the burial diagenesis of shales". In: *Journal of Sedimentary Research* 64.3a, pp. 694–697. DOI: 10.1306/D4267E79-2B26-11D7-8648000102C1865D.

Shannon, R. D. (1976). "Revised effective ionic radii and systematic studies of interatomic distances in halides and chalcogenides". In: *Acta Crystallographica Section A: Crystal Physics, Diffraction, Theoretical and General Crystallography* 32.5. Number: 5 Publisher: International Union of Crystallography, pp. 751–767. DOI: 10.1107/S0567739476001551.

Sharp, Z. D. and J. D. Barnes (2004). "Water-soluble chlorides in massive seafloor serpentinites: a source of chloride in subduction zones". In: *Earth and Planetary Science Letters* 226.1, pp. 243–254. DOI: 10.1016/j.epsl.2004.06.016.

Sharp, Z. D., E. J. Essene, and J. C. Hunziker (1993). "Stable isotope geochemistry and phase equilibria of coesite-bearing whiteschists, Dora Maira Massif, western Alps". In: *Contributions to Mineralogy and Petrology* 114.1, pp. 1–12. DOI: 10.1007/BF00307861.

Sidey, V. (2016). "On the effective ionic radii for ammonium". In: *Acta Crystallographica Section B: Structural Science, Crystal Engineering and Materials* 72.4. Number: 4 Publisher: International Union of Crystallography, pp. 626–633. DOI: 10.1107/S2052520616008064.

Sievers, N. E., C. A. Menold, M. Grove, and M. A. Coble (2017a). "White mica trace element and boron isotope evidence for distinctive infiltration events during exhumation of deeply subducted continental crust". In: *International Geology Review* 59.5-6, pp. 621–638. DOI: 10.1080/00206814.2016.1219881.

Sievers, N. E., J. Tenore, S. C. Penniston-Dorland, and G. E. Bebout (2017b). "Fingerprints of forearc element mobility in blueschist-facies metaconglomerates, Catalina Schist, California". In: *International Geology Review* 59.5-6. Publisher: Taylor & Francis _eprint: https://doi.org/10.1080/00206814.2016.12 pp. 741–752. DOI: 10.1080/00206814.2016.1253038.

Simon, G., C. Chopin, and V. Schenk (1997). "Near-end-member magnesiochloritoid in prograde-zoned pyrope, Dora-Maira massif, western Alps". In: *Lithos* 41.1, pp. 37–57. DOI: 10.1016/S0024-4937(97)82004-X.

Smith, H. J., A. J. Spivack, H. Staudigel, and S. R. Hart (1995). "The boron isotopic composition of altered oceanic crust". In: *Chemical Geology*. The Mantle-Ocean connection 126.2, pp. 119–135. DOI: 10.1016/0009-2541(95)00113-6.

Som, S. M., R. Buick, J. W. Hagadorn, T. S. Blake, J. M. Perreault, J. P. Harnmeijer, and D. C. Catling (2016). "Earth's air pressure 2.7 billion years ago constrained to less than half of modern

levels". In: *Nature Geoscience* 9.6. Number: 6 Publisher: Nature Publishing Group, pp. 448–451. DOI: 10.1038/ngeo2713.

Som, S. M., D. C. Catling, J. P. Harnmeijer, P. M. Polivka, and R. Buick (2012). "Air density 2.7 billion years ago limited to less than twice modern levels by fossil raindrop imprints". In: *Nature* 484.7394. Number: 7394 Publisher: Nature Publishing Group, pp. 359–362. DOI: 10.1038/nature10890.

Sorensen, J. N. Grossman, and M. R. Perfit (1997). "Phengite-hosted LILE Enrichment in Eclogite and Related Rocks: Implications for Fluid-Mediated Mass Transfer in Subduction Zones and Arc Magma Genesis". In: *Journal of Petrology* 38.1, pp. 3–34. DOI: 10.1093/petroj/38.1.3.

Spandler, C., J. Hermann, R. Arculus, and J. Mavrogenes (2004). "Geochemical heterogeneity and element mobility in deeply subducted oceanic crust; insights from high-pressure mafic rocks from New Caledonia". In: *Chemical Geology* 206.1, pp. 21–42. DOI: 10.1016/j.chemgeo.2004.01.006.

Spandler, C., T. Pettke, and J. Hermann (2014). "Experimental study of trace element release during ultrahigh-pressure serpentinite dehydration". In: *Earth and Planetary Science Letters* 391, pp. 296–306. DOI: 10.1016/j.epsl.2014.02.010.

Spránitz, T., J. A. Padrón-Navarta, C. Szabó, Szabó, and M. Berkesi (2022). "Abiotic passive nitrogen and methane enrichment during exhumation of subducted rocks: Primary multiphase fluid inclusions in high-pressure rocks from the Cabo Ortegal Complex, NW Spain". In: *Journal of Metamorphic Geology* 40.8, pp. 1291–1319. DOI: 10.1111/jmg.12666.

Starr, P. G. and D. R. M. Pattison (2019). "Metamorphic devolatilization of basalts across the greenschist-amphibolite facies transition zone: insights from isograd mapping, petrography and thermodynamic modelling". In: *Lithos* 342-343, pp. 295–314. DOI: 10.1016/j.lithos.2019.05.020.

Staudacher, T. and C. J. Allègre (1988). "Recycling of oceanic crust and sediments: the noble gas subduction barrier". In: *Earth and Planetary Science Letters* 89.2, pp. 173–183. DOI: 10.1016/0012-821X(88)90170-7.

Staudigel, H. (2014). "Chemical Fluxes from Hydrothermal Alteration of the Oceanic Crust". In: *Treatise on Geochemistry (Second Edition)*. Ed. by H. D. Holland and K. K. Turekian. Oxford: Elsevier, pp. 583–606. ISBN: 978-0-08-098300-4. DOI: 10.1016/B978-0-08-095975-7.00318-1.

Staudigel, H., T. Plank, B. White, and H.-U. Schmincke (1996). "Geochemical Fluxes During Seafloor Alteration of the Basaltic Upper Oceanic Crust: DSDP Sites 417 and 418". In: *Subduction*. American Geophysical Union (AGU), pp. 19–38. ISBN: 978-1-118-66457-5. DOI: 10.1029/GM096p0019.

Sun, S.-s and W. F. McDonough (1989). "Chemical and isotopic systematics of oceanic basalts: implications for mantle composition and processes". In: 42, pp. 313–345.

Svensen, H., B. Jamtveit, D. A. Banks, and H. Austrheim (2001). "Halogen contents of eclogite facies fluid inclusions and minerals: Caledonides, western Norway". In: *Journal of Metamorphic Geology* 19.2, pp. 165–178. DOI: 10.1046/j.0263-4929.2000.00301.x.

Syracuse, E. M., P. E. van Keken, and G. A. Abers (2010). "The global range of subduction zone thermal models". In: *Physics of the Earth and Planetary Interiors*. Special Issue on Deep Slab and Mantle Dynamics 183.1, pp. 73–90. DOI: 10.1016/j.pepi.2010.02.004.

Tian, Y., Y. Xiao, Y.-X. Chen, H. Sun, H. Liu, F. Tong, J.-H. Yang, and H.-P. Schertl (2019). "Serpentinite-derived low δ^7Li fluids in continental subduction zones: Constraints from the fluid metasomatic rocks (whiteschist) from the Dora-Maira Massif, Western Alps". In: *Lithos* 348-349, p. 105177. DOI: 10.1016/j.lithos.2019.105177.

Tonarini, S., W. P. Leeman, and P. T. Leat (2011). "Subduction erosion of forearc mantle wedge implicated in the genesis of the South Sandwich Island (SSI) arc: Evidence from boron isotope systematics". In: *Earth and Planetary Science Letters* 301.1, pp. 275–284. DOI: 10.1016/j.epsl.2010.11.008.

Trumbull, R. B. and J. F. Slack (2018). "Boron Isotopes in the Continental Crust: Granites, Pegmatites, Felsic Volcanic Rocks, and Related Ore Deposits". In: *Boron Isotopes: The Fifth Element*. Ed. by H. Marschall and G. Foster. Advances in Isotope Geochemistry. Cham: Springer International Publishing, pp. 249–272. ISBN: 978-3-319-64666-4. DOI: 10.1007/978-3-319-64666-4_10.

Turcotte, D. L. and G. Schubert (2002). *Geodynamics*. 2nd ed. Cambridge: Cambridge University Press. DOI: 10.1017/CBO9780511807442.

Turner, S. J., M. H. Barickman, J. Rodriguez, D. A. Fike, C. M. Jones, K. Wang, I. P. Savov, S. Agostini, M. J. Krawczynski, and R. Parai (2023). "Boron isotopes in Central American volcanics indicate a key role for the subducting oceanic crust". In: *Earth and Planetary Science Letters* 619, p. 118289. DOI: 10.1016/j.epsl.2023.118289.

Turner, S. J. and C. H. Langmuir (2022). "An Evaluation of Five Models of Arc Volcanism". In: *Journal of Petrology* 63.3, egac010. DOI: 10.1093/petrology/egac010.

Ulmer, P. and V. Trommsdorff (1995). "Serpentine Stability to Mantle Depths and Subduction-Related Magmatism". In: *Science* 268.5212, pp. 858–861. DOI: 10.1126/science.268.5212.858.

Urann, B. M., V. L. Roux, T. John, G. M. Beaudoin, and J. D. Barnes (2020). "The distribution and abundance of halogens in eclogites: An in situ SIMS perspective of the Raspas Complex (Ecuador)". In: *American Mineralogist* 105.3, pp. 307–318. DOI: 10.2138/am-2020-6994.

Van Keken, P. E., B. R. Hacker, E. M. Syracuse, and G. A. Abers (2011). "Subduction factory: 4. Depth-dependent flux of H2O from subducting slabs worldwide". In: *Journal of Geophysical Research: Solid Earth* 116.B1. ISSN: 2156-2202. DOI: 10.1029/2010JB007922.

Van Keken, P. E., I. Wada, G. A. Abers, B. R. Hacker, and K. Wang (2018). "Mafic High-Pressure Rocks Are Preferentially Exhumed From Warm Subduction Settings". In: *Geochemistry, Geophysics, Geosystems* 19.9, pp. 2934–2961. DOI: 10.1029/2018GC007624.

Van der Straaten, F., R. Halama, T. John, V. Schenk, F. Hauff, and N. Andersen (2012). "Tracing the effects of high-pressure metasomatic fluids and seawater alteration in blueschist-facies overprinted eclogites: Implications for subduction channel processes". In: *Chemical Geology* 292-293, pp. 69–87. DOI: 10.1016/j.chemgeo.2011.11.008.

Varekamp, J., R. Kreulen, R. Poorter, and M. Van Bergen (1992). "Carbon sources in arc volcanism, with implications for the carbon cycle". In: *Terra Nova* 4.3, pp. 363–373. DOI: 10.1111/j.1365-3121.1992.tb00825.x.

Vils, F., L. Pelletier, A. Kalt, O. Müntener, and T. Ludwig (2008). "The Lithium, Boron and Beryllium content of serpentinized peridotites from ODP Leg 209 (Sites 1272A and 1274A): Implications for lithium and boron budgets of oceanic lithosphere". In: *Geochimica et Cosmochimica Acta* 72.22, pp. 5475–5504. DOI: 10.1016/j.gca.2008.08.005.

Vitale Brovarone, A., D. A. Sverjensky, F. Piccoli, F. Ressico, D. Giovannelli, and I. Daniel (2020). "Subduction hides high-pressure sources of energy that may feed the deep subsurface biosphere". In: *Nature Communications* 11.1. Number: 1 Publisher: Nature Publishing Group, p. 3880. DOI: 10.1038/s41467-020-17342-x.

Vitale Brovarone, A., O. Beyssac, J. Malavieille, G. Molli, M. Beltrando, and R. Compagnoni (2013). "Stacking and metamorphism of continuous segments of subducted lithosphere in a high-pressure wedge: The example of Alpine Corsica (France)". In: *Earth-Science Reviews* 116, pp. 35–56. DOI: 10.1016/j.earscirev.2012.10.003.

Vitale Brovarone, A., C. Groppo, G. Hetényi, R. Compagnoni, and J. Malavieille (2011). "Coexistence of lawsonite-bearing eclogite and blueschist: phase equilibria modelling of Alpine Corsica metabasalts and petrological evolution of subducting slabs". In: *Journal of Metamorphic Geology* 29.5, pp. 583–600. DOI: 10.1111/j.1525-1314.2011.00931.x.

Walowski, K. J., L. A. Kirstein, J. C. M. De Hoog, T. R. Elliott, I. P. Savov, and R. E. Jones (2019). "Investigating ocean island mantle source heterogeneity with boron isotopes in melt inclusions". In: *Earth and Planetary Science Letters* 508, pp. 97–108. DOI: 10.1016/j.epsl.2018.12.005.

Watenphul, A., B. Wunder, R. Wirth, and W. Heinrich (2010). "Ammonium-bearing clinopyroxene: A potential nitrogen reservoir in the Earth's mantle". In: *Chemical Geology* 270.1, pp. 240–248. DOI: 10.1016/j.chemgeo.2009.12.003.

Weber, S., L. W. Diamond, P. Alt-Epping, and A. C. Brett-Adams (2021). "Reaction Mechanism and Water/Rock Ratios Involved in Epidosite Alteration of the Oceanic Crust". In: *Journal of Geophysical Research: Solid Earth* 126.6, e2020JB021540. DOI: 10.1029/2020JB021540.

White, R. W., R. Powell, T. J. B. Holland, T. E. Johnson, and E. C. R. Green (2014). "New mineral activity–composition relations for thermodynamic calculations in metapelitic systems". In: *Journal of Metamorphic Geology* 32.3, pp. 261–286. DOI: 10.1111/jmg.12071.

Whitney, D. L. and B. W. Evans (2010). "Abbreviations for names of rock-forming minerals". In: *American Mineralogist* 95.1, pp. 185–187. DOI: 10.2138/am.2010.3371.

Wirth, R., J. H. Kruhl, L. F. G. Morales, and A. Schreiber (2022). "Partially open grain and phase boundaries as fluid pathways in metamorphic and magmatic rocks". In: *Journal of Metamorphic Geology* 40.1, pp. 67–85. DOI: 10.1111/jmg.12610.

Wordsworth, R. D. (2016). "Atmospheric nitrogen evolution on Earth and Venus". In: *Earth and Planetary Science Letters* 447, pp. 103–111. DOI: 10.1016/j.epsl.2016.04.002.

Wunder, B., E. Berryman, B. Plessen, D. Rhede, M. Koch-Müller, and W. Heinrich (2015). "Synthetic and natural ammonium-bearing tourmaline". In: *American Mineralogist* 100.1, pp. 250–256. DOI: 10.2138/am-2015-5055.

Wunder, B., A. Meixner, R. L. Romer, R. Wirth, and W. Heinrich (2005). "The geochemical cycle of boron: Constraints from boron isotope partitioning experiments between mica and fluid". In: *Lithos* 84.3, pp. 206–216. DOI: 10.1016/j.lithos.2005.02.003.

Wyllie, P. J. (1988). "Magma genesis, plate tectonics, and chemical differentiation of the Earth". In: *Reviews of Geophysics* 26.3, pp. 370–404. DOI: 10.1029/RG026i003p00370.

Xiong, J.-W., Y.-X. Chen, H.-Z. Ma, H.-P. Schertl, Y.-F. Zheng, and K.-D. Zhao (2022). "Tourmaline boron isotopes trace metasomatism by serpentinite-derived fluid in continental subduction zone". In: *Geochimica et Cosmochimica Acta* 320, pp. 122–142. DOI: 10.1016/j.gca.2022.01.003.

Xiong, J.-W., Y.-X. Chen, K. Zhou, H.-P. Schertl, Y.-F. Zheng, F. Huang, X.-P. Xia, and Z.-W. Chen (2021). "Fe and O isotopes in coesite-bearing jadeite quartzite from the Western Alps record multistage fluid-rock interactions in a continental subduction zone". In: *Geochimica et Cosmochimica Acta* 312, pp. 1–24. DOI: 10.1016/j.gca.2021.08.006.

Xu, J., G. B. Zhang, H. R. Marschall, J. B. Walters, S. Q. Liu, Z. Lü, L. F. Zhang, H. Hu, and N. Li (2022). "Boron isotopes of white mica and tourmaline in an ultra-high pressure metapelite from the western Tianshan, China: dehydration and metasomatism during exhumation of subducted ocean-floor sediments". In: *Contributions to Mineralogy and Petrology* 177.4, p. 46. DOI: 10.1007/s00410-022-01916-7.

Yamada, C., T. Tsujimori, Q. Chang, and J.-I. Kimura (2019). "Boron isotope variations of Franciscan serpentinites, northern California". In: *Lithos* 334-335, pp. 180–189. DOI: 10.1016/j.lithos.2019.02.004.

Yamaoka, K., T. Ishikawa, O. Matsubaya, D. Ishiyama, K. Nagaishi, Y. Hiroyasu, H. Chiba, and H. Kawahata (2012). "Boron and oxygen isotope systematics for a complete section of oceanic crustal rocks in the Oman ophiolite". In: *Geochimica et Cosmochimica Acta* 84, pp. 543–559. DOI: 10.1016/j.gca.2012.01.043.

Yu, A. J., X. Lin, J. Zhu, H. He, and L. Li (2023). "Environmental effects on ammonium adsorption onto clay minerals: Experimental constraints and applications". In: *Applied Clay Science* 246, p. 107165. DOI: 10.1016/j.clay.2023.107165.

Zellmer, G. F., M. Edmonds, and S. M. Straub (2015). "Volatiles in subduction zone magmatism". In: *Geological Society, London, Special Publications* 410.1, pp. 1–17. DOI: 10.1144/SP410.13.

Zimmer, M. M., T. P. Fischer, D. R. Hilton, G. E. Alvarado, Z. D. Sharp, and J. A. Walker (2004). "Nitrogen systematics and gas fluxes of subduction zones: Insights from Costa Rica arc volatiles". In: *Geochemistry, Geophysics, Geosystems* 5.5. DOI: 10.1029/2003GC000651.

Zucali, M., M. Spalla, and G. Gosso (2002). "Strain partitioning and fabric evolution as a correlation tool: The example of the Eclogitic Micaschists Complex in the Sesia-Lanzo Zone (Monte Mucrone-Monte Mars, Western Alps, Italy)". In: *Schweizerische Mineralogische und Petrographische Mitteilungen* 82, pp. 429–454.